THE UNIVERSITY
of EDINBURGH

Establishing a Human Cell-Based Model System for Macular Degeneration

Almar Neiteler

PhD

The University of Edinburgh

2019

Declaration

I declare that this thesis was composed by myself and that all experiments in this thesis were performed by myself unless otherwise indicated in the text. This work has not been submitted for any other degree or professional qualification.

Almar Neiteler

2019

Acknowledgements

I would like to thank Prof James Ross, Prof Baljean Dhillon, and Prof Siddharthan Chandran for giving me the opportunity to carry out this work.

I would like to thank all the members of Prof Ross' Tissue Injury and Repair Group, and in particular Kathryn Sangster and James Black for their technical support, Dr Anwar Palakkan for his technical advice, especially regarding flow cytometry and qPCR, and his help with the stem cell cultures, and Kevin Gallagher for his advice on the cell viability assays.

I would also like to thank all the members of Prof Chandran's group, and in particular Dr Bhuvaneish Thangaraj Selvaraj for all his technical advice and especially regarding gene editing, Dr Karen Burr for her help with the stem cell cultures and her advice on differentiation protocols, James Cooper for his help with the gene editing, Dr James Longden for his help with systems biology analysis of the RNA-seq data, and David Story for his technical support.

I am grateful for all the technical advice provided by Dr Shyamanga Borooah (University of California, San Diego), especially regarding L-ORD and the complement system.

Furthermore, I would like to thank Prof David Hay and Prof Sarah Howie (The University of Edinburgh) for their advice and support; I would like to thank Dr Owen Dando and Prof Giles Hardingham (The University of Edinburgh) for their help with the RNA-seq data analysis and all their advice regarding the RNA-seq; I would like to thank Graham Anderson and Dr Pierre Bagnaninchi (The University of Edinburgh) for their collaboration on the UV and ECIS experiments; and I would like to thank Dr Widad Dantoft (Cardiff University) and Callum Idle for proofreading this thesis.

Finally, I would like to thank my family, who have supported me in every way possible throughout this whole experience.

Abstract

Age-related macular degeneration (AMD) is the most common cause of visual loss amongst the elderly in developed countries. AMD is a complex disease with a highly variable phenotype, which makes generating reliable disease models difficult. In addition, lack of knowledge of the underlying pathological mechanisms makes development of an effective treatment difficult. To address the lack of knowledge of the molecular mechanisms affected in AMD a robust cell-based model system is needed. Late-onset retinal degeneration (L-ORD) is a rare autosomal dominant disorder caused by a p.S163R, p.P188T, or p.G216C missense mutation in the C1q and tumor necrosis factor-related protein 5 (*C1QTNF5*) gene. L-ORD has a very similar phenotype to AMD, including sub-RPE deposit formation, the hallmark of AMD. Studying L-ORD could therefore potentially reveal common molecular pathways affected in macular degenerations. Here, I used CRISPR/Cas9 gene editing to correct the p.S163R mutation in *C1QTNF5* in patient-derived induced pluripotent stem cells (iPSCs) and generated *C1QTNF5* null iPSCs. The iPSC lines were differentiated into retinal pigment epithelium (RPE), the cell type that highly expresses C1QTNF5 and is severely affected in macular degenerations. RNA sequencing of L-ORD and control iPSC-RPE revealed that the extracellular matrix, complement system, lipid and general cell metabolism, and oxidative stress pathways are affected in L-ORD. $C1QTNF5^{S163R}$ in L-ORD iPSC-RPE was found to form less high molecular weight multimeric structures compared to its isogenic gene-corrected control. In addition, L-ORD iPSC-RPE were also found to phagocytose and possibly adhere differently compared to their isogenic controls. Both oxidative stress and the complement system play an important role in the pathology of macular degenerations. RPE were found to undergo regulated necrosis in response to oxidative stress and L-ORD iPSC-RPE were found to be more sensitive to UV light-induced oxidative stress. In addition, the terminal complement system complex C5b-9 was found to bind more frequently to L-ORD iPSC-RPE and colocalises with APOE in sub-RPE drusen-like deposits after human serum exposure. Together, the results in this thesis reveal that L-ORD iPSC-RPE have a molecular phenotype that could explain part of the clinical presentation of this disease and possibly of AMD. Further study of the affected molecular mechanisms could potentially lead to therapies for both L-ORD and AMD.

Lay Summary

Age-related macular degeneration (AMD) is the most common cause of visual loss amongst the elderly in developed countries. AMD is a complex disease with a highly variable clinical presentation which inevitably leads to difficulty when studying this disease. AMD always leads to the degeneration of the macula, the most light-sensitive part of the retina and is responsible for sharp central vision. Lack of knowledge of this disease is one of the main reasons why there is currently no effective treatment. Related diseases with similar characteristics to AMD, are caused by one mutation. Unlike AMD, these are much easier to study and could potentially provide more information about shared macular degeneration-causing mechanisms. One of these diseases is late-onset retinal degeneration (L-ORD), which is a rare disorder caused by a mutation in the gene *C1QTNF5*. L-ORD has a noticeably similar clinical presentation to AMD, and therefore the mutation in *C1QTNF5* is likely to affect the same molecular mechanisms involved in causing AMD. Here, I used gene editing to correct the *C1QTNF5* mutation in patient-derived stem cells. These stem cells were then converted into retinal pigment epithelial (RPE) cells, the type of eye cells most affected in macular degenerations. Comparison of gene-corrected RPE and uncorrected RPE from patients revealed some key differences. The protein encoded by the *C1QTNF5* gene was found to have a different shape caused by the mutation, which likely affects its function. Moreover, RPE from patients had greater sensitivity to light-induced stress and increased accumulation of immune system proteins compared to the gene-corrected cells. Together, the results in this thesis reveal some of the molecular mechanisms affected in L-ORD that could explain part of the clinical presentation of this disease and possibly also of AMD. Further study of the affected molecular mechanisms could potentially lead to a therapy for both L-ORD and AMD.

Table of Contents

List of Figures

List of Tables

List of Abbreviations

4-HNE 4-hydroxynonenal

β-HB . . . . . β-hydroxybutyrate

A2E . . . . . .

2-[2,6-dimethyl-8-(2,6,6-trimethyl-1-cyclohexen-1-yl)-1E,3E,5E,7E-octatetraenyl]-1-(2-hydroxyethyl)-4-[4-methyl-6-(2,6,6-trimethyl-1-cyclohexen-1-yl)-1E,3E,5E-hexatrienyl]-pyridinium

Aβ . . . . . Amyloid β

AAV . . . . . Adeno-associated virus

ABCA4 . . . . . ATP Binding Cassette Subfamily A Member 4

ACC . . . . . Acetyl Coenzyme A Carboxylase

ACSL4 . . . . Acyl-CoA Synthetase Long Chain Family Member 4

ADAM . . . . . A Disintegrin And Metalloproteinase Domain

ADAMTS . . . . . ADAM With Thrombospondin Motifs

ADAMTSL . . . . . ADAMTS-Like

ADIPOR . . . . . Adiponectin Receptor

ADRP . . . . . Adipose Differentiation-Related Protein

AMD . . . . . Age-related macular degeneration

AMP . . . . . Adenosine Monophosphate

AMPK . . . . . 5’-AMP-Activated Protein Kinase

APOE . . . . . Apolipoprotein E

APP . . . . . Amyloid β Precursor Protein

ARMS2 . . . . . Age-Related Maculopathy Susceptibility 2

ATP . . . . . Adenosine triphosphate

BAK1 . . . . . BCL2 Antagonist/Killer 1

BAX . . . . . BCL2 Associated X

BCL2 . . . . . B-Cell CLL/Lymphoma 2

BER . . . . . Base excision repair

BEST1 . . . . . Bestrophin 1

bFGF . . . . . . Basic FGF

Bp . . . . . Base pairs

BrdU . . . . . Bromodeoxyuridine

BSA . . . . . Bovine serum albumin

C11-BODIPY$^{581/591}$ . . . . . .

4,4-difluoro-5-(4-phenyl-1,3-butadienyl)-4-bora-3a,4a-diaza-s-indacene-3-undecanoic acid

C1q . . . . . Complement Component 1q

C1r . . . . . Complement Component 1r

C1s . . . . . Complement Component 1s

C2 . . . . . Complement Component 2

C3 . . . . . Complement Component 3

C4 . . . . . Complement Component 4

C5 . . . . . Complement Component 5

C6 . . . . . Complement Component 6

C7 . . . . . Complement Component 7

C8 . . . . . Complement Component 8

C9 . . . . . Complement Component 9

C1QL C1q-like

C1QTNF . . . . . C1q And TNF Related Protein

Cas . . . . . CRISPR-associated protein

Cas9n . . . . . Cas9 nickase

CAT . . . . . Catalase

CCL2 . . . . . C-C Motif Chemokine Ligand 2

CCP . . . . . Complement control protein

CCR2 . . . . . C-C Motif Chemokine Receptor 2

CDKN2A . . . . . Cyclin Dependent Kinase Inhibitor 2A

cDNA . . . . . Complementary DNA

CFB . . . . . Complement Factor B

CFD . . . . . Complement Factor D

CFH . . . . . Complement Factor H

CFHR . . . . . CFH-related

CFI . . . . . Complement Factor I

CNTF . . . . . Ciliary Neurotrophic Factor

CNV . . . . . Choroidal neovascularisation

CNS . . . . . Central nervous system

CR1 . . . . . Complement Receptor Type 1

CRALBP . . . . . Cellular Retinaldehyde-Binding Protein

CRISPR . . . . Clustered regularly interspaced short palindromic repeats

crRNA . . . . . CRISPR RNA

CX3CL1 . . . . . C-X3-C Motif Chemokine Ligand 1

CX3CR1 . . . . . C-X3-C Motif Chemokine Receptor 1

DAF . . . . . Decay Accelerating Factor

DAPI . . . . . 4’,6-diamidino-2-phenylindole

DDM . . . . *n*-Dodecyl β-D-maltoside

DHRD . . . . . Doyne honeycomb retinal dystrophy

DFO . . . . . Deferoxamine

DHA . . . . . Docosahexaenoic acid

DMEM . . . . . Dulbecco's Modified Eagle Medium

DMSO . . . . . Dimethyl sulfoxide

DNA . . . . . Deoxyribonucleic acid

DSB . . . . . Double-stranded break

dsDNA . . . . . Double-stranded DNA

DTT . . . . . Dithiothreitol

ECIS . . . . . Electric cell-substrate impedance sensing

ECL . . . . . Enhanced chemiluminescence

ECM . . . . . Extracellular matrix

EDTA . . . . . Ethylenediaminetetraacetic acid

EFEMP1 . . . EGF-Containing Fibrillin-like Extracellular Matrix Protein 1

EGF . . . . . epidermal growth factor

ELISA . . . . . Enzyme-linked immunosorbent assay

ELM . . . . . External limiting membrane

ER . . . . . Endoplasmic reticulum

ERK . . . . . Extracellular Signal Regulated Kinase

ESC . . . . . Embryonic stem cell

ETC . . . . . Electron transport chain

FCS . . . . . Foetal calf serum

Fer-1 . . . . . Ferrostatin-1

FGF . . . . . Fibroblast Growth Factor

FITC Fluorescein-5-Isothiocyanate

FPKM . . . Fragments per kilobase of transcript per million mapped reads

fRPE . . . . . Foetal RPE

gaAMD . . . . . Geographic atrophy AMD

GAG . . . . . Glycosaminoglycan

gDNA . . . . . Genomic DNA

GCL . . . . . Ganglion cell layer

GCLM . . . . . Glutamate-Cysteine Ligase Modifier Subunit

GFP . . . . . Green fluorescent protein

GO . . . . . Gene Ontology

GPX . . . . . Glutathione Peroxidase

GSH . . . . . Glutathione

GSK'840B GSK2791840B

gRNA . . . . . Guide RNA

HEK . . . . . Human embryonic kidney

HDR . . . . . Homology directed repair

HMW . . . . . High molecular weight

HOHA . . . . . 4-hydroxy-7-oxohept-5-enoic acid

HRP . . . . . Horse radish peroxidase

Hsp70 . . . . . Heat Shock Protein 70

HSPA1B. . . . . Heat Shock Protein Family A (Hsp70) Member 1B

HTRA1 . . . . High-Temperature Requirement A Serine Peptidase 1

IGF-1 . . . . . Insulin-like Growth Factor-1

IgG . . . . . Immunoglobulin G

IL . . . . . Interleukin

ILM . . . . . Inner limiting membrane

Indel . . . . . Insertion or deletion

INL . . . . . Inner nuclear layer

IPA . . . . . Ingenuity Pathway Analysis

IPL . . . . . Inner plexiform layer

iPSC . . . . . Induced pluripotent stem cell

IRBP . . . . . Interstitial Retinal Binding Protein

JNK . . . . . c-Jun N-Terminal Kinase

KLF4 . . . . . Kruppel Like Factor 4

KO . . . . . Knockout

LAZ . . . . . Long anteriorly inserted lens zonules

LCA . . . . . Leber's congenital amaurosis

LC-PUFA . . . . . Long-chain PUFA

LD . . . . . Lipid droplet

LEDGF . . . . . Lens Epithelium-Derived Growth Factor

L-ORD . . . . . Late-onset retinal degeneration

LPAAT . . . . . Lysophosphatidic Acid Acyltransferase

LPCAT3 . . . . . Lysophosphatidylcholine Acyltransferase 3

LPS . . . . . Lipopolysaccharide

LRAT . . . . . Lecithin retinol acyltransferase

MAC . . . . . Membrane attack complex

MAPK . . . . . Mitogen-Activated Protein Kinase

MASP . . . . . MBL-Associated Serine Protease

MBL . . . . . Mannose-Binding Lectin

MCP . . . . . Membrane Cofactor Protein

MCP-1 . . . . . Monocyte Chemoattractant Protein-1

MDA . . . . . Malondialdehyde

MERTK . . . . . MER Proto-Oncogene, Tyrosine Kinase

MFRP . . . . . Membrane Frizzled-Related Protein

MITF . . . . . Melanogenesis Associated Transcription Factor

ML . . . . . Malattia Leventinese

MLKL . . . . . Mixed Lineage Kinase Domain-Like Protein

MMP . . . . . Matrix Metalloproteinase

mTOR . . . . . Mechanistic Target Of Rapamycin Kinase

NEAA . . . . . Non-essential amino acids

Nec-1 . . . . . Necrostatin-1

NFE2L2 . . . . . Nuclear Factor, Erythroid 2 Like 2

NFL . . . . . Nerve fibre layer

NHEJ . . . . . Non-homologous end joining

NPD1 . . . . . Neuroprotection D1

NSA . . . . . Necrosulfonamide

Nt . . . . . Nucleotides

nvAMD . . . . . Neovascular AMD

Oct-3/4 . . . . . Octamer-Binding Protein 3/4

ONL . . . . . Outer nuclear layer

OPC . . . . . Optic progenitor cell

OPL . . . . . Outer plexiform layer

PA . . . . . Palmitic acid

PAGE . . . . . Polyacrylamide gel electrophoresis

PAM . . . . . Protospacer adjacent motif

PAX6 . . . . . Paired Box 6

PBS . . . . . Phosphate-buffered saline

PC . . . . . Phosphatidylcholine

PCR . . . . . Polymerase chain reaction

PDGF . . . . . Platelet-Derived Growth Factor

PDLIM2 . . . . . PDZ And LIM Domain 2

PE . . . . . Phosphatidylethanolamine

PEDF . . . . . Pigment Epithelium-Derived Factor

PFA . . . . . Paraformaldehyde

PI . . . . . Propidium iodide

PIM . . . . . Pro-neural induction medium

PIS . . . . . Photoreceptor inner segments

PLIN . . . . . Perilipin

PMEL . . . . . Premelanosome Protein

POS . . . . . Photoreceptor outer segments

PPAR . . . . . Peroxisome Proliferator-Activated Receptor

PPARA . . . . . PPAR Alpha

PPARG . . . . . PPAR Gamma

PRKAA1 . . . . Protein Kinase AMP-Activated Catalytic Subunit Alpha 1

PUFA . . . . . Polyunsaturated fatty acid

PVDF . . . . . Polyvinylidene difluoride

qPCR . . . . . Quantitative PCR

RCS . . . . . Royal College of Surgeons

RDH . . . . . Retinol Dehydrogenase

RDM . . . . . Retinal differentiation medium

Rds . . . . . Retinal degeneration slow

RFLP . . . . . Restriction fragment length polymorphism

RGC . . . . . Retinal ganglion cell

RIPK . . . . . Receptor-Interacting Protein Kinase

RNA . . . . . Ribonucleic acid

RNA-seq . . . . . RNA sequencing

RNP . . . . . Ribonuclear protein

ROS . . . . . Reactive oxygen species

RPC . . . . . Retinal progenitor cells

RPE . . . . . Retinal pigment epithelium

RPE65 . . . . . RPE-Specific 65 KDa Protein

SD . . . . . Standard deviation

SDS . . . . . Sodium dodecyl sulphate

SFD . . . . . Sorsby's fundus dystrophy

sgRNA . . . . . Single-guide RNA

SIFT . . . . . Sorting intolerant from tolerant

SNP . . . . . Single nucleotide polymorphism

SOD . . . . . Superoxide Dismutase

SOX2 . . . . . Sex Determining Region Y-Box 2

SQSTM1 . . . . . Sequestosome 1

ssDNA . . . . . Single-stranded DNA

ssODN . . . . . Single-stranded oligodeoxy-nucleotides

STGD3 . . . . . Stargardt-like macular dystrophy type 3

tBHP . . . . . *Tert*-butyl hydroperoxide

TBP . . . . . TATA-Box Binding Protein

TBS . . . . . Tris-buffered saline

TCA . . . . . Tricarboxylic acid

TEER . . . . . Transepithelial electrical resistance

TBF-β . . . . . Transforming Growth Factor-β

TIMP3 . . . . . Tissue Inhibitor Of Metalloproteinases 3

TNF . . . . . Tumor Necrosis Factor

TNFR . . . . . TNF Receptor

TRA-1-60 . . . . . T Cell Receptor Alpha Locus

tracrRNA . . . . . Trans-activating crRNA

UV . . . . . Ultraviolet

VEGF . . . . . Vascular Endothelial Growth Factor

VLC-PUFA . . . . . Very long-chain PUFA

VSX2 . . . . . Visual System Homeobox 2

Wt . . . . . Wildtype

ZO-1 . . . . . Zona Occludens 1

Chapter 1 Introduction

1.1 The retina

The retina is the light-sensitive tissue in the back of the eye, and it consists of retinal neurons, retinal glial cells, and the retinal pigment epithelium (RPE). Six types of retinal neurons form the neural retina: rod and cone photoreceptors, horizontal cells, bipolar cells, amacrine cells, and retinal ganglion cells (RGCs). The retinal macroglia are the Müller glia and retinal astrocytes and the retina also contains retinal microglia. Together, these cell types capture, process, and transfer light signals to the brain.

The retina has multiple different regions. Light is focused by the lens on the centre of the retina, termed the macula lutea. In the centre of the macula is the fovea, a small pit structure of about 1.5 mm in diameter that contains the highest density of cone photoreceptor cells and is therefore responsible for central, high-resolution, colour vision. The region of the retina towards the nose is called the optic disc, or the blind spot, and contains no photoreceptor cells. Here, the RGCs form the optic nerve that extents from the eye to the brain.

The retina has a multi-layered structure and light can pass though most of the layers[1,2]. The retina has ten distinct layers (Fig. 1.1). Anterior, adjacent to the vitreous body, is the inner limiting membrane (ILM) which serves as a basement membrane. Adjacent to the ILM is the nerve fibre layer (NFL), which contains the axonal fibres of the RGCs that run bundled together radially towards the optic disc, where they leave the eye into the optic nerve. Adjacent to the NFL is the ganglion cell layer (GCL) where the cell bodies of the RGCs are located. The dendritic processes of the RGCs extend into the adjacent inner plexiform layer (IPL), where they synapse with the processes of the bipolar and amacrine cells. The next layer, the inner nuclear layer (INL), is the location of the cell bodies of the bipolar, horizontal, and amacrine cells. Adjacent is the outer plexiform layer (OPL) where again mostly synaptic connections take place, but this time between photoreceptor cells and bipolar and horizontal cells. The cell bodies of the photoreceptor cells are located in the adjacent outer nuclear layer (ONL). The external limiting membrane (ELM) separates the photoreceptor cell bodies from the disposable light-sensitive photoreceptor outer segments (POS), which have their own

layer. Here, the used POS are shed from the photoreceptors. RPE, in the final layer, phagocytose the POS.

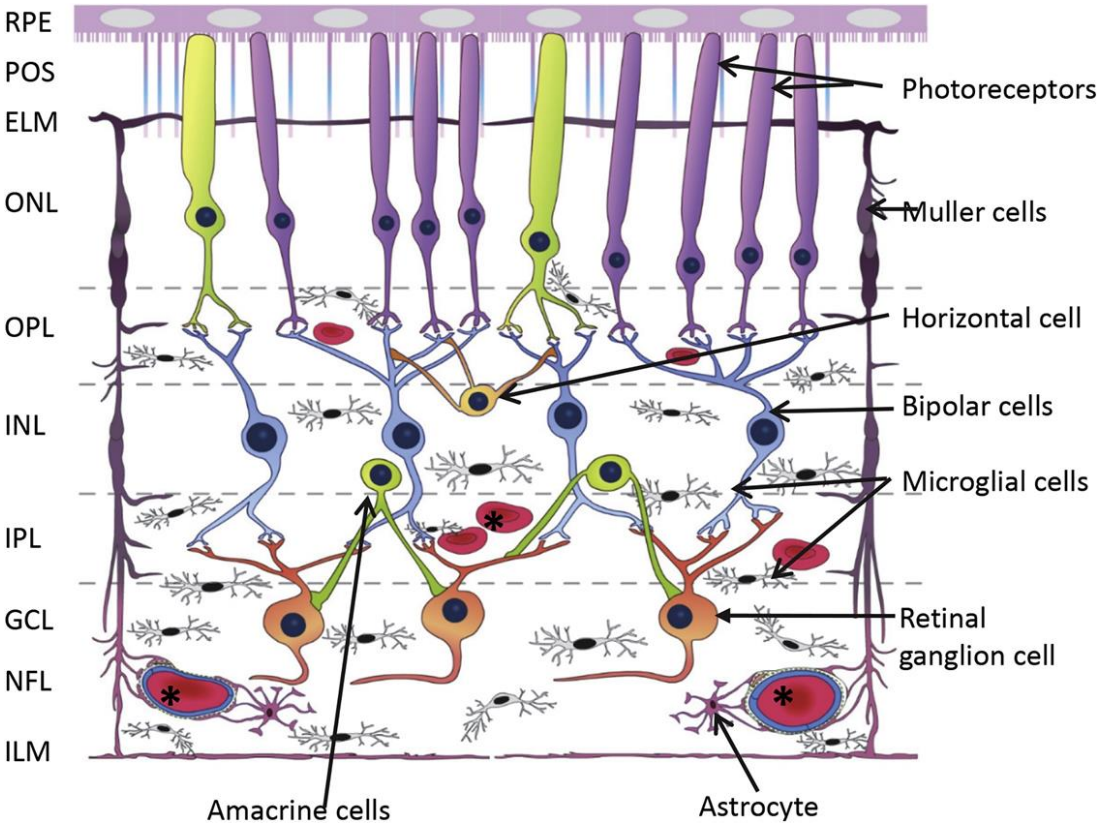

Figure 1.1 | The layers and cell types of the retina. The layers of the retina, and the position of the retinal cells within these layers, under normal physiological conditions. ILM = inner limiting membrane; NFL = nerve fibre layer; GCL = ganglion cell layer; IPL = inner plexiform layer; INL = inner nuclear layer; OPL = outer plexiform layer; ONL = outer nuclear layer; ELM = external limiting membrane; POS = photoreceptor outer segments; RPE = retinal pigment epithelium; asterisk (*) = blood vessel. Reproduced from Rathnasamy et al. (2019)[3].

Retinal neurons have a variety of functions[4]. They are relatively very small but numerous. The rod photoreceptor is the second most numerous neuronal type in the human body after cerebellar granule cells[4]. Rod photoreceptors are specialised for dim light vision and outnumber cone photoreceptors about 20-fold[4]. Rod photoreceptors contain the light-sensitive pigment rhodopsin in the POS, whereas each cone photoreceptors contains a different cone opsin. Each cone opsin absorbs a different spectrum of light, forming the basis

for colour vision. Photoreceptors can absorb photons from light with their light-sensitive pigment situated in the POS and converts this into a biochemical signal. Photo-oxidative damage causes inactivation of POS and are therefore shed from the photoreceptors. Because of continuous photo-oxidative damage, POS are constantly shed and new POS are constantly regrown, a process that is light-dependent[5]. Shed POS are phagocytosed by RPE.

Before POS are shed, the light-induced biochemical signal in the POS is transduced back through the layers of the retina, via horizontal, bipolar and amacrine cells, to the RGCs. Horizontal cells provide direct inhibitory feedback to the photoreceptors, by adjusting the output, and therefore can adjust the brightness locally in the image[4]. Rod photoreceptors are connected to rod bipolar cells, whereas cone photoreceptors are connected to 11 different types of cone bipolar cells[6]. Each different bipolar cell extracts different information from the photoreceptor output to transmit to the inner retina[4]. There are around 30 types of amacrine cells that modulate the output of bipolar cells[4]. Amacrine cells receive input from bipolar cells and feed this signal back to the bipolar cells, forward to the RGCs, and lateral to other amacrine cells. Amacrine cells help RGCs to detect motion, vertically integrate signals to allow for signal crossover, and regulate the output of other retinal neurons[4]. There are around 20 types of RGCs, each transducing different signals obtained from the input of different bipolar and amacrine cells[4]. RGCs extent through the optic nerve to the various visual centres in the brain. About 20-30% of the human cerebral cortex is devoted to vision[7]. Here, the processing of light signals continues.

The retinal glial cells have a supportive function in the retina. Retinal astrocytes and Müller glia are the macroglia of the retina[8]. Macroglia provide metabolic and functional support, protect from oxidative stress, and maintain a homeostatic environment for retinal neurons. In addition, macroglia are also involved in regulating local blood flow. Müller glia are long radially oriented cells that span the entire width of the retina (Fig. 1.1). Müller glia are typically the first glial cells to detect and respond to retinal injury because of their radially distribution in the retina[9]. Retinal astrocytes are mainly located in the NFL of the retina (Fig. 1.1)[10]. Retinal microglia are the immune cells of the retina[3,11,12]. Under normal physiological conditions microglia are in a resting state and can be found in the inner layers of the retina, but not beyond the OPL (Fig. 1.1). In this state, microglia survey their microenvironment and release neuroprotective and anti-inflammatory factors[13]. Microglia become activated in the

event of an injury or in disease, resulting in a change of morphology and migration to the site of injury[14,15].

The retina has a dual vascular supply. The retinal vasculature supplies the inner layers of the retina, whilst the choroid supplies the outer layers of the retina. The retina, and specifically the macula, is considered the most metabolic active tissue in the body[16]. The choroid has fenestrated capillaries, allowing for leakage of proteins and other molecules from circulation into the Bruch's membrane. The Bruch's membrane is a layer of extracellular matrix (ECM) and separates the RPE from the endothelium of the choroid. Large macromolecules cannot pass through the Bruch's membrane. The RPE forms a barrier with its tight junctions between the fluid of the choroid and the rest of the retina.

1.2 Retinal pigment epithelium

The most posterior layer of the retina is the RPE. The RPE is a pigmented monolayer that has several important roles to fulfil to ensure correct functioning of the retina[17]. The apical and basal sides of the RPE faces the photoreceptors and Bruch's membrane of the choroid respectively. RPE have tight junctions that form a narrow barrier between the subretinal space and the choriocapillaris[17,18]. This forms the blood-retina barrier and is of importance for the immune privilege of the eye and for the highly selective transport between the choroid and the retina.

One important function of RPE is to absorb light focused on the retina by the lens[17]. The retina has a high blood perfusion, creating an oxygen-rich environment. Light focussed on the macula lutea thus enables photo-oxidation, leading to the production of radical oxygen species (ROS) and subsequent oxidative damage. RPE therefore have melanosomes, a lysosome-related organelle, which produce and store melanin pigments[19]. Scattered light is filtered and absorbed by the melanin in melanosomes of the RPE to improve the image quality and to limit oxidative damage.

RPE also participate in the visual cycle together with the photoreceptors[17,20]. Photoreceptors catch light in the visual pigments situated in the POS with the molecule 11-*cis* retinal bound to the protein opsin, forming photopsin. 11-*cis* retinal forms all-*trans* retinal after photon absorption. Photoreceptors are unable to re-isomerise all-*trans* retinal back to 11-*cis* retinal. All-*trans* retinal is transported to the cytoplasm by ATP Binding Cassette Subfamily A Member

4 (ABCA4) and reduced by all-*trans* retinol dehydrogenase (RDH12) to all-*trans* retinol, also known as vitamin A. All-*trans* retinol is transported through the subretinal space via interstitial retinal binding protein (IRBP) to the RPE for re-isomerisation to 11-*cis* retinal. In RPE, lecithin retinol acyltransferase (LRAT) esterifies all-*trans* retinol to phosphatidylcholine to form all-*trans* retinyl esters. Retinoid isomerase and retinoid isomerohydrolase RPE-specific 65 KDa protein (RPE65) isomerise all-*trans* retinyl esters to 11-*cis* retinol. Finally, 11-*cis* retinol is converted to 11-*cis* retinal by 11-*cis* retinol dehydrogenase (RDH5), a process accelerated by cellular retinaldehyde-binding protein (CRALBP). 11-*cis* retinal is then released from CRALBP and transported back to the photoreceptors via IRBP.

RPE are also important for photoreceptor maintenance[17]. RPE secrete growth factors that promote photoreceptor survival[21] and phagocytose POS to maintain photoreceptor excitability[22,23]. RPE have microvilli on their apical surface that physically associate with POS and use these microvilli to phagocytose POS as they are shed. Two RPE receptors are mainly involved in the phagocytosis of POS: $\alpha_V\beta_5$ integrin and MER proto-oncogene tyrosine kinase (MERTK)[23-25]. $\alpha_V\beta_5$ integrin is necessary for the binding of RPE microvilli to the POS. Bound $\alpha_V\beta_5$ integrin activates two intracellular signalling cascades that causes phosphorylation and activation of Rac1 GTPase and MERTK[23]. Rac1 GTPase is required for the recruitment of F-actin for the formation of phagocytic cups and MERTK is in part required for the contraction of the phagocytic cup during phagocytosis[26]. Mutations in *MERTK* were found to be the cause of recessive retinitis pigmentosa[27,28], a form of hereditary retinal degeneration. Mutated orthologue *Mertk* was also found to be the cause of retinal degeneration in Royal College of Surgeons (RCS) rats[27], an important model system for hereditary retinal degeneration. Activation of MERTK also results into an intracellular signalling cascade leading to increased levels of free Ca^{2+} which is necessary for regulating phagocytic activity[17]. In addition to the $\alpha_V\beta_5$/MERTK pathway, CD36 can bind to oxidised phospholipids on POS and facilitate increased phagocytic capacity of RPE, possibly to prevent oxidative damage[24,29]. After phagocytosis by RPE, POS components are either marked for degradation or recycled for transport back to the photoreceptors.

RPE also secretes a variety of growth factors, vital for the adjacent endothelium and photoreceptors[17,21,30], as well as complement components for a local immune response[31]. Some important factors that RPE secrete to adjacent cells include ATP, fas-ligand (fas-L), fibroblast growth factors, transforming growth factor-β (TGF-β), insulin-like growth factor-1

(IGF-1), platelet-derived growth factor (PDGF), vascular endothelial growth factor (VEGF), lens epithelium-derived growth factor (LEDGF), ciliary neurotrophic factor (CNTF), members of the interleukin family, pigment epithelium-derived factor (PEDF), tissue inhibitor of matrix metalloprotease 3 (TIMP3), complement factor H (CFH), and C-C motif chemokine ligand 2 (CCL2)[17,30,32].

Some critical functions of the RPE are regulated by intracellular free Ca^{2+} concentration changes[33,34]. Bestrophin-1 (BEST1) is an important regulator of intracellular Ca^{2+} homeostasis in RPE and functions as both a Ca^{2+}-activated anion channel and a regulator of intracellular Ca^{2+} signalling[35,36]. BEST1 is predominantly expressed in the RPE and is an integral membrane protein localised to the basolateral plasma membrane[37]. It functions as a Ca^{2+}-activated anion channel in the ER, where it regulates the levels of the Ca^{2+} stores[38]. In addition, BEST1 can also function as a regulator for Ca^{2+} channel activity[39]. Ion channels like BEST1 were found to regulate RPE phagocytosis of POS[40]. Ca^{2+} is also important for regulation of VEGF secretion by RPE[41]. There are over 200 mutations found in the gene *BEST1*, causing at least five clinically distinct forms of retinal degeneration, of which Best vitelliform macular dystrophy is the most common[42,43].

The RPE maintains ion homeostasis in the subretinal space[17]. Photo-activation of the photoreceptors and the activity of retinal neurons causes changes in the subretinal space[44]. The RPE provides a fast compensation for these changes. In particular, K^+ concentrations in the subretinal space can change rapidly because of photoreceptor activity. In the dark, there is an influx of K^+ into the POS from the subretinal space, which is compensated by an efflux of K^+ from the photoreceptor inner segments (PIS) into the subretinal space. When light strikes the photoreceptors, the ion channels on the POS closes and the efflux of K^+ from the PIS decreases. This leads to decrease of K^+ concentrations in the subretinal space and subsequent depolarisation of the RPE apical membrane. Depolarisation of the RPE apical membrane induces transport of K^+ from the RPE to the subretinal space. This compensation of K^+ concentration is required to maintain photoreceptor and retinal neuron excitability.

The RPE plays an important role in the pathology of many retinal degenerations when compromised. The most common form of retinal degeneration is age-related macular degeneration (AMD).

1.3 Age-related macular degeneration

AMD is the most common cause of visual loss in the elderly in developed countries[45-47]. It is estimated that 8.7% of all blindness worldwide is caused by AMD and this is expected to increase to 196 million people affected in 2020, and 288 million in 2040[48]. AMD is a major public health problem costing annually at least $30 billion in the United States alone[49] and has a significant impact on the quality of life, making a person with AMD less active[50] with a higher risk of depression[51] and anxiety[52].

AMD is a complex multifactorial chronic disease that typically occurs after the sixth decade of life[53] and has a highly variable phenotype which makes generating reliable disease models difficult. In addition, lack of knowledge of the underlying pathological mechanisms makes development of a treatment difficult[54]. Risk factors for AMD include age, ethnicity, smoking, light exposure, hypertension, high body mass index, cataract surgery, and genetic predisposition[55]. AMD has a strong genetic component, as a number of susceptibility variants of loci are implicated to contribute to AMD[56,57]. This wide range of risk factors lead to a diverse disease phenotype.

About 52 single nucleotide polymorphisms (SNPs) have been found at 34 loci that have been associated with late stage AMD in a large genome-wide association study[57]. The most important susceptibility loci for AMD are in a cluster on chromosome 1 which includes *CFH* and *CFHRs* and on chromosome 10 near age-related maculopathy susceptibility 2 (*ARMS2*) and high-temperature requirement A serine peptidase 1 (*HTRA1*)[58]. Loci conferring moderate risk to AMD are on chromosome 6 near *C2* and *CFB* and on chromosome 19 near *C3*[58]. It is still unclear what the underlying molecular mechanisms are that are affected by *ARMS2* and *HTRA1* in AMD. Nonetheless, *ARMS2* has been associated with an increase in systemic complement system activation in AMD[59]. *HTRA1* encodes for a serine protease that is thought to play a role in the processing of amyloid β precursor protein (APP)[60], the precursor for amyloid β (Aβ), a component of sub-RPE deposits found in AMD[61,62]. CFH, CFHRs, CFB, C2, and C3 are components of the complement system, which is thought to play a major role in the pathology of AMD (see Chapter 5).

AMD can be characterised by sub-RPE deposit formation[63], accumulation of lipofuscin in RPE (see Chapter 4), RPE senescence[64], detachment of RPE from the Bruch's membrane and subsequent cell death[65], chronic oxidative injury (see Chapter 4), chronic complement system activation (see Chapter 5), and chronic inflammation in the retina. Transcriptome analysis of

patients with AMD revealed the involvement of inflammatory genes in the onset and progression of AMD[66].

AMD can be classified as early, intermediate, and late stage disease, based on clinical presentation[67]. One of the earliest manifestations of AMD is deposit formation between the RPE and the Bruch's membrane, termed drusen[68]. Medium (63–125 μm) to large (≥125 μm) soft drusen can be found in early and intermediate stage AMD and these stages have little to no vision loss. Soft drusen are pale yellow deposits visible upon fundoscopic examination and are located between the basal lamina of the RPE and the Bruch's membrane. The amount and size of soft drusen are associated with an increased risk of AMD[69]. In early AMD, also pigmentary changes can be observed in the macula, such as hyperpigmentation or hypopigmentation[67]. Intermediate AMD is defined by the extensive presence of medium-sized drusen[67].

There are two variants of late stage AMD: exudative "wet" or neovascular AMD (nvAMD) and "dry" or geographic atrophy AMD (gaAMD). nvAMD is responsible for around 85% of the legal blindness caused by AMD[70]. In nvAMD, choroidal neovascularisation (CNV) leads to neovascular tuft growth through the Bruch's membrane into the sub-RPE space or between the RPE and the neural retina. Vessels produced in nvAMD haemorrhage or leak fluid more often, leading to rapid loss of vision. In contrast, vision loss in gaAMD is more gradual. In gaAMD, geographic atrophy causes loss of the choroid, RPE, and neural retina. Areas with confluent drusen are typically where geographic atrophy develops.

nvAMD can be treated with VEGF inhibitors which slows down loss in visual acuity[71]. Continued loss of visual acuity with anti-VEGF therapy is attributed to retinal thinning, an increase in geographic atrophy, and an increase in lesion size. Anti-VEGF therapy requires multiple injections per year for at least five years. About one fifth of the patients treated with anti-VEGF therapy develop gaAMD within two years of treatment[72]. There is still no treatment for gaAMD. Anti-VEGF therapy is therefore not a good treatment for AMD.

Drusen are considered to be a hallmark of AMD[63]. Whilst it is believed that drusen are associated with pathological processes, it is still not understood how these deposits develop and what role they have in the pathology. The content of drusen has been analysed with immunohistochemistry and proteomics[73]. Drusen have been found to contain cholesterol[74], and over 129 different proteins[73] including, TIMP3[75], vitronectin[76], inflammatory proteins of the complement system (see Chapter 5), the Alzheimer's Aβ, apolipoprotein E (APOE)[77],

clusterin, and immunoglobulins. The proportion of inflammatory proteins found in drusen suggest a role for local inflammation in the biogenesis of drusen[63].

Cellular senescence is thought to play a causative role in age-related diseases and aging in general[78]. Similarly, RPE senescence has been suggested to play a role in the aetiology of AMD[64]. Senescence of RPE can be induced by oxidative stress[79]. However, the precise mechanisms on how RPE senescence contributes to AMD pathology on a molecular level have not been uncovered yet.

To address the lack of knowledge of the molecular mechanisms affected in AMD a robust model system is needed. There are a number of very rare diseases that resemble AMD but are caused by a single mutation. It is thought that studying these diseases would lead to a better understanding of AMD and could potentially function as models for AMD. There is especially not much know about the early stages of AMD when drusen are formed. Late-onset retinal degeneration (L-ORD), Malattia Leventinese (ML) / Doyne honeycomb retinal dystrophy (DHRD), and Sorsby's fundus dystrophy (SFD) are diseases causing macular degeneration that closely resemble the early stages of AMD and form sub-RPE drusen-like deposits. Therefore, these diseases could potentially form model systems of early stage AMD.

1.4 Late-onset retinal degeneration

L-ORD is a rare autosomal dominant disorder caused by a mutation in the complement component 1q (C1q) and tumor necrosis factor (TNF)-related protein 5 (*C1QTNF5*) gene, also known as *CTRP5*[80] (see Chapter 3). The founder mutation in *C1QTNF5* is thought to originate from the south-east of Scotland[81]. Patients often have increased difficulty with dark adaptation in their fourth decade of life and progresses to sudden loss of central vision in their sixth decade of life. Eventually the progressive symptoms lead to total loss of vision.

L-ORD has a very similar clinical and pathological phenotype compared to AMD and has therefore been suggested as a model for AMD[81]. Given its rarity and similarity to AMD, L-ORD is often misdiagnosed as AMD[81]. L-ORD can be characterised by bilateral loss of vision, delayed dark adaptation, fundus drusen-like yellow spots, midperipheral pigmentation, CNV, chorioretinal atrophy, and long anteriorly inserted lens zonules (LAZ)[81].

There are three stages recognised in L-ORD progression[81]. Stage one (age 0-40) is often asymptomatic with normal visual acuity. However, LAZ may be found on pupil dilatation tests[82]. LAZ are characterised by zonular fibres that extend more central than usual on the anterior lens capsule and can be already found in the third decade of life in patients with L-ORD[83]. Stage two (age 40-60) is characterised with increased difficulty adapting to dark[84]. Patients still have normal visual acuity, but fundus examination reveals yellow dots and pigmentary changes. Stage three (age 60 and older) is characterised by CNV, resulting in sudden central vision loss. CNV areas rapidly increase and leave retinal scarring and atrophy. Early stage three mostly resembles AMD but the same visual changes in AMD typically occur later than in L-ORD[81].

High doses of vitamin A have led to some improvements in dark adaptation in patients with early stage L-ORD[83,84]. However, vitamin A treatment does not affect disease progression and only has a short- to medium-term beneficial effect[81]. Anti-VEGF treatment has not been tested yet on patients with L-ORD to treat the CNV. There is therefore no effective treatment yet for this disease.

1.5 Malattia Leventinese / Doyne honeycomb retinal dystrophy and Sorsby's fundus dystrophy

ML/DHRD and SFD are rare hereditary macular degenerations with many phenotypical similarities compared to early stage AMD and L-ORD but also have distinct differences. Nonetheless, common molecular pathways are likely to be affected amongst these diseases.

A p.R345W mutation in epidermal growth factor (EGF)-containing fibrillin-like extracellular matrix protein 1 (EFEMP1), also known as fibulin-3, causes ML and DHRD[85]. ML/DHRD is also known as autosomal dominant radial drusen. ML and DHRD are both autosomal dominant diseases. *EFEMP1* is located on chromosome 2 (2p16.1) and encodes for a 55 kDa protein that is normally secreted into the ECM. *EFEMP1* is most commonly expressed in the RPE and the lung[85,86].

EFEMP1 is a member of the fibulin family of glycoproteins. Fibulins are secreted into the ECM and are involved in basement membrane formation and stabilisation[87,88]. EFEMP1 belongs to the short fibulins subgroup. Short fibulins are involved in the formation and homeostasis of

elastic tissue. EFEMP1 is therefore thought to be a component of the elastic fiber/microfibril system[89]. EFEMP1 can bind to TIMP3[90] and CFH[91].

Short fibulins are proteolysed by matrix metalloproteinases (MMPs). Specifically, the a disintegrin and metalloproteinase domain (ADAM) family of proteins and the ADAM with thrombospondin motifs (ADAMTS) family of proteins are thought to be involved in specific short fibulin proteolysis[89]. Interestingly, a homozygous p.C1079R missense mutation in *ADAMTS18* was shown to cause early-onset retinal dystrophy[92].

The p.R345W mutation was found to cause misfolding of EFEMP1 and therefore reduced secretion and thus retention of this protein in the RPE[93]. In addition, EFEMP1 is also found between the RPE and drusen in both ML and AMD[93]. This aberrant accumulation of EFEMP1 is thought to be the cause of drusen formation in ML, DHRD and AMD. Moreover, mice with a *EFEMP1*$^{R345W/\ R345W}$ knock-in mutation were found to develop basal deposits resembling those found in AMD[94,95]. Furthermore, deposits formed by *EFEMP1*^{R345W} RPE *in vitro* were shown to induce a complement response by these cells[31]. Complement factors produced by RPE were shown to contribute to the deposit formation. Drusen found in ML and DHRD often closely resemble those found in AMD, but also have some distinct differences[96]. Mutations in fibulin-5[97,98] and fibulin-6/hemicentin 1[99] (HMCN1) are also implicated to be involved in AMD. In addition, mutation p.Q5345R in *HMCN1* leads to dominant macular dystrophy[100,101].

Sorsby's fundus dystrophy (SFD) is a rare autosomal dominant disorder[102]. SFD is characterised by bilateral deposition of yellow drusen-like material and extensive CNV occurring between the third and fifth decades of life. SFD closely resembles stage 2 L-ORD but has an earlier onset[81] and is caused by mutations in the *TIMP3* gene[103-105]. In addition, a rare mutation in *TIMP3* has also been associated with AMD[57]. *TIMP3* is located on chromosome 22 (22q12.3) and encodes for a 24 kDa glycosylated protein that binds to EFEMP1[90]. *TIMP3* mRNA is expressed in the RPE[106] and the protein localises to the ECM component of Bruch's membrane[107].

The TIMP family of proteins inhibit MMPs to regulate ECM renewal. The ECM is constantly remodelled in healthy tissue. Synthesis and degradation of ECM components are in a dynamic equilibrium. MMPs degrade specific components in the ECM and are tightly regulated[108]. The N-terminal domain of TIMPs is responsible for MMP inhibition. Of all the TIMPs, TIMP3 inhibits the most MMPs, including multiple ADAMs and ADAMTSs[109].

Multiple different mutations in *TIMP3* can lead to SFD, especially missense mutations in exon 5 of *TIMP3*. This leads to a cysteine transition in TIMP3 that causes SFD, such as p.S156C[110], p.G166C[111], p.G167C[112], p.Y168C[103], p.S170C[113], p.Y172C[114], p.S181C[103], and p.Y191C[115]. It was found that most of these mutated proteins had normal TIMP3 characteristics and localisation to the ECM, but also form dimers unlike the wildtype TIMP3[105,116]. Each of these mutations are thought to lead to an unpaired cysteine at a different site in the protein. The unpaired cysteine at different locations could potentially explain the different TIMP3 dimers found to predominate for each mutation[105]. Unpaired cysteines can create additional intermolecular disulphide bonds. In addition, mutations near the C-terminus could also interfere with the TIMP3 binding site to EFEMP1, which is located here[90].

TIMP3 is found to inhibit angiogenesis and neovascularisation[117-119]. It inhibits angiogenesis by blocking VEGF from binding to the VEGF receptor 2[120]. It is therefore likely that *TIMP3* mutations lead to a loss of function causing the extensive CNV in SFD. Treatment of patients with anti-VEGF has therefore been proposed[121]. Furthermore, delayed dark adaptation in SFD was found to be reversible with vitamin A treatment[112].

1.6 Aims of this study

There is a lack of knowledge of the molecular mechanisms affected in AMD, especially in the early stages of AMD. Formation of the sub-RPE drusen, the hallmark of AMD, is not well understood. Rare hereditary sub-RPE drusen-like deposit-forming macular degenerations, such as L-ORD, ML/DHRD, and SFD, closely resemble early stage AMD. Shared molecular pathways could be affected between these diseases that lead to the sub-RPE deposit formation. Studying these rare hereditary macular degenerations could therefore possibly provide valuable knowledge about shared early-disease mechanisms. Knowledge of early-disease mechanisms could lead to the development of treatment before the onset of severe disease symptoms and could possibly prevent disease progression.

Studying hereditary macular degenerations provides the advantage of a single mutation leading to the disease phenotype, whereas in AMD a combination of multiple genetic and environmental risk factors leads to the disease phenotype. Hereditary macular degenerations therefore allow for the generation of patient-specific induced pluripotent stem cells (iPSCs) bearing the gene mutation of interest. Gene editing can subsequently be

used to correct the mutation, generating isogenic pairs, where only the mutation of interest is the difference. This allows precise studying of the effect of a single mutation. Furthermore, these cells allow for the investigation of two cellular processes commonly affected in macular degenerations: oxidative stress and the complement system.

In order to study the molecular mechanisms affected in L-ORD, iPSCs had previously been generated from patients. These iPSCs were used in this work to achieve the following aims:

- Gene-correction of L-ORD iPSC lines using CRISPR/Cas9 gene editing. In addition, generation of C1QTNF5 knockout (KO) iPSC line using the same gene editing tools.
- Generation of RPE to study the C1QTNF5 protein function and what effects the L-ORD mutation has on the protein.
- Investigation of the effects of oxidative stress on RPE and how this contributes to the macular degeneration phenotype, all using the generated L-ORD iPSC RPE and RPE cell lines.
- Investigate how the complement system contributes to the macular degeneration phenotype using L-ORD iPSC RPE.

Chapter 2 Gene Editing *C1QTNF5*

2.1 Introduction

2.1.1 Induced pluripotent stem cells

Stem cells are self-renewing cells that can differentiate into more specialised cells. Stem cells found in the inner cell mass of developing embryos are said to be pluripotent. Pluripotent cells have the ability to differentiate into the different cell types that comprise the endoderm, mesoderm, and ectoderm germ layers. Embryonic stem cells (ESCs) can be isolated and maintained in *in vitro* culture[122]. Moreover, it has been found that human somatic cells can be reprogrammed to pluripotent stem cells through the addition of four transcription factors: Oct-3/4, SOX2, KLF4, and c-Myc[123] or Oct-3/4, SOX2, NANOG, and LIN28[124]. These induced pluripotent stem cells (iPSCs) have the same ability to self-renew and differentiate into the three germ layers as ESCs. The ability of pluripotent stem cells to become most cell types and their ability to self-renew provides for a virtually unlimited supply of a cell type of choice. Both ESCs and iPSCs are now routinely used for fundamental cell research, disease modelling, and drug development.

iPSCs hold several important advantages over ESCs. Most significantly, iPSCs do not require the need for embryos but can be generated from most cell types taken directly from patients. This allows for the generation of patient-specific stem cells that have the same genotype as the patient and could therefore be transplanted back to the patient without risking immune rejection. This is an important consideration for regenerative medicine. Patient-derived iPSCs could be used to correct a genetic defect via gene editing, differentiated to the affected cell type, and then transplanted back to the patient to restore the affected tissue. In addition, gene correction of patient-derived iPSCs and their comparison with uncorrected iPSCs allows for the study of the effect of a single gene mutation with an otherwise identical genetic background. Furthermore, the study of isogenic iPSC pairs allows for more precise disease modelling and drug development.

2.1.2 CRISPR/Cas9 gene editing

Gene editing tools can be used to introduce or correct SNPs. In addition, these tools can also be used to introduce short sequences or delete parts of a sequence. This allows for the introduction of one of the macular degeneration-causing mutations into wildtype (wt) iPSC lines and the correction of the mutation in patient-derived iPSC lines. Moreover, KO lines can be generated with these gene editing tools to investigate the function of the protein of interest.

Clustered regularly interspaced short palindromic repeats (CRISPR), in association with the nuclease CRISPR-associated protein (Cas), is an RNA-guided nuclease system that is used for gene editing[125,126]. In this system the nuclease Cas is guided by a specific RNA guide to a specific locus where it can introduce a double-stranded break (DSB). The DSB is subsequently repaired by one of two endogenous DNA repair mechanisms: homology directed repair (HDR) or non-homologous end joining (NHEJ) (Fig. 2.1). NHEJ occurs in the absence of a repair template. This process is highly error-prone and therefore introduces insertion or deletion (indel) mutations. In contrast, by providing a repair template HDR can fully repair the DSB.

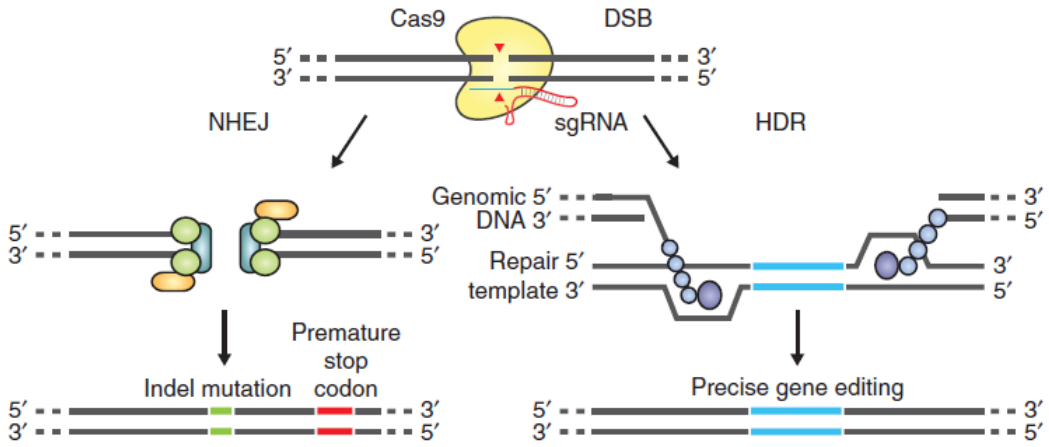

Figure 2.1 | Cas9 creates a DSB that can be resolved by HDR or NHEJ. Cas9 is directed to the locus of interest by the gRNA where it will create a DSB. Endogenous DNA repair mechanisms HDR or NHEJ can repair the break. Only HDR uses a template to repair the break and normally this is the other allele. For gene editing purposes a template can be added instead, with the edit of interest. NHEJ typically causes indel mutations resulting in a premature stop codon. DSB = double-stranded break; HDR = homology directed repair; NHEJ = non-homologous end joining. Reproduced from Ran et al. (2013)[127].

The CRISPR/Cas systems originated as an acquired defence system in bacteria and archaea[128-131]. This multistep process is executed by *cas* genes and non-coding RNA. Small invading foreign DNA fragments are recognised as non-self and subsequently incorporated into the host CRISPR loci between repetitive elements. These incorporated foreign DNA fragments, now termed protospacers, are then transcribed and processed into CRISPR RNA (crRNA) used for targeting foreign DNA. Downstream of a protospacer is a conserved 5'-NGG sequence, termed protospacer adjacent motif (PAM). In the Type II CRISPR system, targeting crRNA anneals to trans-activating crRNA (tracrRNA) to form guide RNA (gRNA). gRNA forms a ribonuclear protein (RNP) with Cas9 and can bind and neutralise complementary invading viral and plasmid DNA. After the gRNA binds to a 20-base pair (bp) target sequence, Cas9 induces a DSB ~3 bp upstream of the PAM. The resulting DNA fragments can again be incorporated into the CRISPR loci.

The CRISPR/Cas systems have been repurposed and modified to allow efficient gene editing in a variety of species[125]. For biotechnology purposes, targeting crRNA and tracrRNA can be fused together to form a chimeric single-guide RNA (sgRNA)[132] and, to improve specificity of gene editing, a D10A nickase mutant of Cas9 (Cas9n) was generated that introduces nicks in the DNA instead of DSBs[133]. By using a pair of offset sgRNAs complementary to opposite strands of the target site, site-specific DSBs can be generated with Cas9n. Off-target individual single strand DNA nicks would be repaired by the endogenous base excision repair (BER) system. A CRISPR/Cas system can be leveraged into editing a specific locus if a repair template is provided for HDR. Plasmids or single-stranded oligodeoxy-nucleotides (ssODNs) containing homology arms flanking the insertion sequence can be used as HDR templates.

Recent advances in stem cell technologies combined with advances in gene editing tools provides an unprecedented opportunity to develop new experimental models to study macular degeneration. However, background genetic variation among different patient-derived iPSC lines leads to confounding results, presenting a challenge to disease modelling. Generation of isogenic pairs, using CRISPR/Cas9, allows for the study of the effect of a single gene mutation, since the only difference between the parental line and the gene-corrected line is the mutation. Therefore, correcting the *C1QTNF5*^{S163R} mutation in L-ORD patient-derived stem cells should provide a basis for modelling L-ORD and likely macular degeneration in general.

2.1.3 Aims and objectives

In order to study the function of C1QTNF5 and the effect of the *C1QTNF5*^{S163R} mutation on the protein, the following was carried out in this chapter:

1. The *C1QTNF5*^{S163R} mutation in patient-derived iPSCs was gene-corrected by using CRISPR/Cas9 gene editing to generate an isogenic pair for disease modelling
2. A biallelic KO of the *C1QTNF5* gene was generated in an iPSC line by using CRISPR/Cas9 gene editing to study the function of C1QTNF5
3. The gene editing strategies used were investigated if they resulted in off-target editing by Sanger sequencing

2.2 Materials and methods

2.2.1 Cell culture

iPSCs were cultured in Essential 8 medium (Gibco, Loughborough, UK) on 6-well plates coated with growth factor-reduced matrigel (Corning, New York, NY) by Dr Burr (The University of Edinburgh) and Almar Neiteler. L-ORD case iPSC lines LORD3 and LORD4 were previously generated from male patient-derived fibroblasts through episomal reprogramming by Dr Borooah (The University of Edinburgh) with Dr Burr (The University of Edinburgh) (PhD thesis, Dr Borooah, The University of Edinburgh). The control wt iPSC line used, CS02iCTR-NTn1, was previously generated from peripheral blood mononuclear cells from a wt male through episomal reprogramming (Cedars-Sinai, Los Angeles, CA).

HEK 293T cells were cultured in DMEM/F-12 (Gibco) supplemented with 10% foetal calf serum (FCS; Gibco) and 2 mM L-glutamine (Gibco).

2.2.2 Pluripotency staining

The iPSC lines were washed with PBS and fixed with 4% paraformaldehyde (PFA) for 10 minutes. After another two washes with PBS the cells were permeabilised with 0.1% TritonX-100 (Sigma-Aldrich, Dorset, UK) for 10 minutes and subsequently blocked with 3% normal goat serum for 1 hour. The fixed cells were incubated with the primary antibody overnight at 4 °C. The cells were washed twice with PBS and subsequently incubated with a secondary Alexa Fluor®-conjugated antibody for 30 minutes and counterstained with 300 nM DAPI (Biotium, Fremont, CA) for 10 minutes. After another three washes with PBS, the cells were mounted in Fluorsave mounting medium (Merck Millipore, Nottingham, UK) and imaged with a Leica DM IRB fluorescence microscope (Leica Microsystems, Milton Keynes, UK). The antibodies and concentrations used are listed in Table S8.

2.2.3 Karyotyping

The iPSC lines were arrested in metaphase and labelled with a 10 µM bromodeoxyuridine (BrdU; Sigma-Aldrich) and 10 µg/ml colcemid (Sigma-Aldrich) solution for 15 hours. The cells

were then enlarged with a hypotonic 0.56% potassium chloride (Sigma-Aldrich) and 0.4% sodium citrate solution (Fisher Scientific UK Ltd., Loughborough, UK) for 25 minutes to facilitate the spreading of metaphase chromosomes. The cells were then fixed in a methanol and glacial acetic acid fixative solution and send for karyotyping (TDL Genetics, London, UK).

2.2.4 Designing CRISPR/Cas9(n) constructs and cloning

Targeting crRNA pairs to use in conjunction with Cas9n to target the *C1QTNF5*^{S163R} mutation site were designed as 20-bp sequences directly upstream of a 5'-NGG PAM sequence according to specifications previously described[127,133]. In short, the pairs were designed to generate 5' overhangs and at least one of the pairs nicks within 22 bp of the HDR insertion site. The targeting crRNA pair offset gap for use with Cas9n was designed to be between 0-20 bp and pairs nick in opposite strands.

The L-ORD *C1QTNF5*^{S163R} mutation itself is part of a 5'-NGG PAM. Therefore, another targeting crRNA was designed by Dr Selvaraj (The University of Edinburgh) to specifically target this site to use in conjunction with wt Cas9.

To generate a C1QTNF5 KO iPSC line, Dr Selvaraj (The University of Edinburgh) designed a targeting crRNA pair that, in conjunction with wt Cas9, creates a deletion in exon one and thereby creating an in-frame stop codon.

Targeting crRNA pairs to use in conjunction with Cas9n to edit *C1QTNF5* were ligated into a plasmid containing Cas9n, pSpCas9n(BB)-2A-Puro (PX462) V2.0 (Addgene, Middlesex, UK). The targeting crRNA pairs for *C1QTNF5* repair and C1QTNF5 KO were ligated into a plasmid containing wt Cas9, pSpCas9(BB)-2A-Puro (PX459) V2.0 (Addgene). Both plasmids already contain the tracrRNA. Targeting crRNAs and repair templates were ordered as ssODNs (IDT, Leuven, Belgium), see Table S1. After annealing, the targeting crRNA ODNs were ligated into the pSpCas9n vector cut open with *BbsI* (Thermo Scientific, Paisley, UK), upstream of the tracrRNA, for co-expression of Cas9 or Cas9n with sgRNA. The ligation mix was treated with PlasmidSafe Exonuclease (Epicentre, Madison, WI) to remove any linear DNA from the mix. pSpCas9 vectors with correction and KO crRNAs were obtained from Dr Selvaraj (The University of Edinburgh), see Table S2. All plasmids were cloned in One Shot® TOP10 Chemically Competent *E. coli* (Invitrogen, Paisley, UK) according to the manufacturer's instructions.

The *C1QTNF5* targeting crRNA for L-ORD repair was also ordered for an Alt-R CRISPR/Cas9 system (IDT) transfection. For this system, crRNA, tracrRNA and Cas9 protein were ordered separately. Targeting crRNA and tracrRNA oligomers were resuspended to 200 µM in TE buffer, mixed together in equimolar concentrations, and annealed together at 95 °C for 2 minutes to generate the gRNA duplex. To 200 pmol gRNA, 137.25 pmol of Cas9 protein was added and incubated for 10-20 minutes to generate the RNP for transfection. For RNA sequences used in the RNP complex see Table S3.

The HDR templates were designed as ssODNs with homology arms of at least 70 nucleotides (nt) on either side[127]. One or both PAM sequences were mutated in the repair template to prevent sequential editing and therefore lowering the chance of NHEJ events. For HDR template sequences see Table S4.

2.2.5 Transfection

The pSpCas9(n)-sgRNA constructs were first tested on HEK 293T cells. HEK 293T cells were seeded in a 12-well plate well ($2*10^5$ cells/well) a day prior to transfection. Cells were transfected once 80-90% confluent with Lipofectamine 2000 (Invitrogen) according to the manufacturer's protocol. The pSpCas9(n)-sgRNA constructs were co-transfected with pmaxGFP (Lonza Ltd., Basel, Switzerland) to check transfection efficiency. Transfection efficiency was observed with a fluorescence microscope (Carl Zeiss Ltd., Cambridge, UK) the day after transfection.

iPSCs were transfected once 80-90% confluent. Cells were washed with PBS and dissociated to single cells with Accutase (Stemcell Technologies, Vancouver, Canada). The single cell suspension was washed again with PBS and the cells were counted. $8*10^5$ cells were nucleofected using a P3 Primary Cell 4D-Nucleofector X Kit (Lonza Ltd.) in combination with a 4D-Nucleofector™ Core Unit and X Unit (Lonza Ltd.) with program CA-137 according to the manufacturer's protocol. 2 µg per pSpCas9(n)-sgRNA or 9 µl of RNP complex and 2.5 µl of 200 µM HDR template were used for nucleofection. In all nucleofections 1 µg pEGFP/Puromycin was co-transfected for selection. Nucleofected cells were seeded in a Matrigel-coated 6-well plate well in E8 medium supplemented with 10 µM ROCK-inhibitor Y-27632 (Stemcell Technologies). Transfection efficiency was observed with a fluorescence microscope (Carl Zeiss Ltd.) the day after transfection. Nucleofected cells were selected with

10 µM puromycin (Gibco) for 24 hours. The cells were allowed to recover from selection and were passaged at very low density ($5*10^3$ and $1*10^4$) as single cells onto a Matrigel-coated 10 cm dish in E8 with ROCK-inhibitor. Single colonies were picked and transferred to a Matrigel-coated 96-well plate. Duplicate plates were made for maintenance and restriction fragment length polymorphism (RFLP) screening. Nucleofection of pSpCas9 constructs for gene correction, selection, and the maintenance of single cell-derived clones was performed in collaboration with James Cooper (The University of Edinburgh).

2.2.6 PCR

Plasmids ligated with targeting crRNAs were validated using GoTaq Flexi polymerase (Promega, Southampton, UK). The PCR program had an initial denaturation step at 95 ˚C for 2 minutes. After the initial denaturation step the program continued with 21 cycles of denaturation at 95 ˚C for 15 seconds, annealing at 57.5 ˚C for 30 seconds, and extension at 73 ˚C for 30 seconds. The final extension was at 73 ˚C for 5 minutes. PCR products were run on a 2% agarose gel. PCR primers were designed with the primer design tool Primer3[134-136] and are listed in Table S6.

The *C1QTNF5* mutation region was PCR amplified using Q5® High-Fidelity DNA Polymerase (New England Biolabs, Ipswich, MA). The PCR program had an initial denaturation step at 98 ˚C for 30 seconds. After the initial denaturation step the program continued with 34 cycles of denaturation at 98 ˚C for 10 seconds, annealing at 66 ˚C for 30 seconds, and extension at 72 ˚C for 30 seconds. The final extension was at 72 ˚C for 2 minutes. PCR products were run on a 2% agarose gel. PCR of the *C1QTNF5* mutation region was performed in collaboration with James Cooper (The University of Edinburgh).

The *C1QTNF5* KO region was PCR amplified using the QIAGEN Multiplex PCR Kit (Qiagen, Manchester, UK). The PCR program had an initial denaturation step at 95 ˚C for 15 minutes. After the initial denaturation step the program continued with 34 cycles of denaturation at 94 ˚C for 30 seconds, annealing at 55 ˚C for 30 seconds, and extension at 72 ˚C for 30 seconds. The final extension was at 72 ˚C for 10 minutes. PCR products were run on a 2% agarose gel.

2.2.7 Restriction fragment length polymorphism screening and Sanger sequencing

For restriction fragment length polymorphism (RFLP) screening and Sanger sequencing, genomic DNA (gDNA) was isolated from transfected cells, using a Wizard® Genomic DNA Purification Kit (Promega), according to the manufacturer's instructions. Isolated gDNA was used for PCR amplification of the mutation region. PCR products were purified using the ChargeSwitch PCR Clean-Up Kit (Invitrogen), according to the manufacturer's instructions. Purified PCR products were normalised to 200 ng and used to generate heteroduplexes by denaturing and slowly reannealing the DNA strands[127,137]. The slow annealing program had an initial denaturation step at 95 ˚C for 5 minutes. After the initial denaturation step the program continued by reannealing slowly by lowering the temperature 2 ˚C/second to 85 ˚C. After 1 minutes at 85 ˚C the program lowered the temperature 0.1 ˚C/second to 25 ˚C followed by 30 seconds at 25 ˚C. The formed heteroduplexes were then digested with T7 Endonuclease I (New England Biolabs) at 37 ˚C for 15 minutes. Digested products were run on a 2% agarose gel.

PCR products of the mutation region were also used for restriction digestion. The L-ORD *C1QTNF5*^{S163R} mutation site generates a *BstNI* restriction site. To 15 µl of PCR product 2 µl of NEBuffer 3.1 (New England Biolabs), 2 µl of dH_2O, and 1 µl of *BstNI* (New England Biolabs) was added. This was incubated at 60 °C for 1 hour. Digested products were run on a 2% agarose gel. Restriction digestions were performed in collaboration with James Cooper (The University of Edinburgh).

Purified PCR products were also sent for Sanger sequencing (Source Bioscience, Nottingham, UK).

2.2.8 Off-target screening

Top five possible off-target sites for each targeting crRNA were selected through the Sanger Find Off-Targets by Sequence tool[138] and are listed in Table S5. Primers for each possible off-target site were designed with the primer design tool Primer3[134-136] and are listed in Table S6. Each possible off-target site was PCR amplified as described above in each edited line (see section 2.2.6). PCR products were purified using the ChargeSwitch PCR Clean-Up Kit, according to the manufacturer's instructions. Purified PCR products were sent for Sanger sequencing (Source Bioscience).

2.2.9 C1QTNF5 variant effect prediction

The Ensembl Variant Effect Predictor tool[139] was used to predict the effects of the p.S163R and the p.A154T missense mutations on the structure and function of C1QTNF5. The algorithms SIFT and PolyPhen were used.

2.3 Results

2.3.1 iPSC lines have normal stem cell characteristics

Several different iPSC lines were used in this study and were tested for their stem cell qualities. All iPSC lines used grew as typical iPSC colonies (Fig. 2.2a). The iPSC lines were immunostained for known pluripotency markers NANOG, Oct-3/4, and TRA-1-60. All three pluripotency markers were found to be expressed in the iPSC lines (Fig. 2.2b). The karyotype was analysed for the iPSC lines to check for possible chromosomal abnormalities that can be introduced by iPSC propagation and by freezing and thawing of the cells. Karyotyping of the lines revealed no chromosomal abnormalities (Fig. 2.2c). Gene correction was performed on the L-ORD case iPSC lines LORD3 and LORD4 (see sections 2.3.5, 2.3.6, and 2.3.7), harbouring the heterozygous *C1QTNF5*^{S163R} mutation causative for L-ORD, and were named LORD3C and LORD4C respectively. The wt control iPSC line CS02iCTR-NTn1 was used to create a biallelic KO of C1QTNF5 (see section 2.3.11).

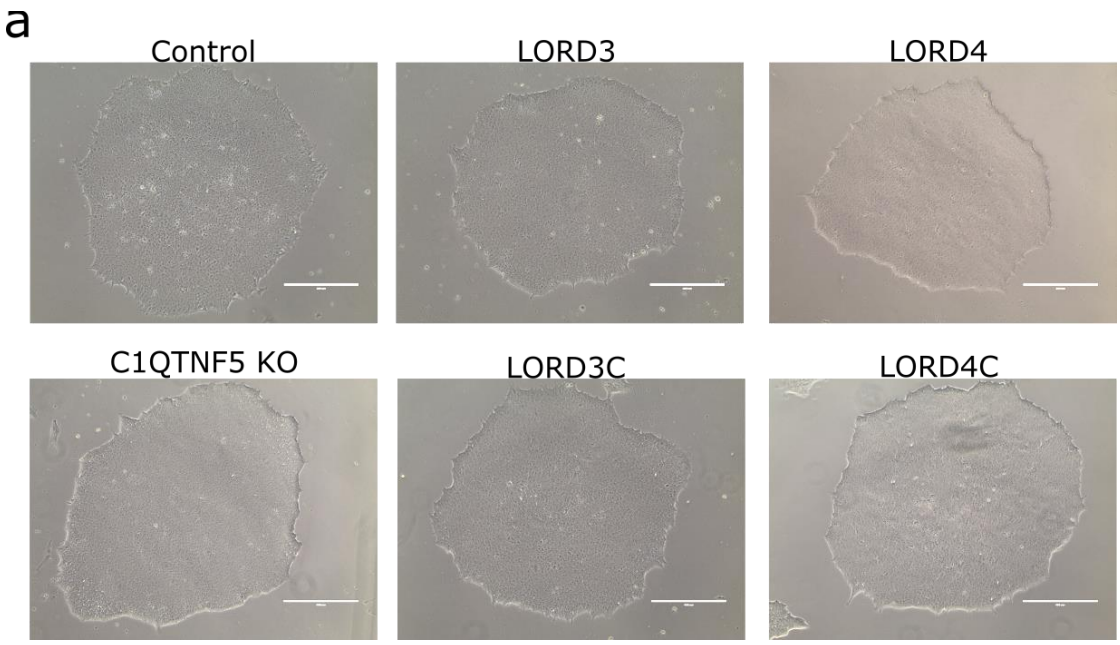

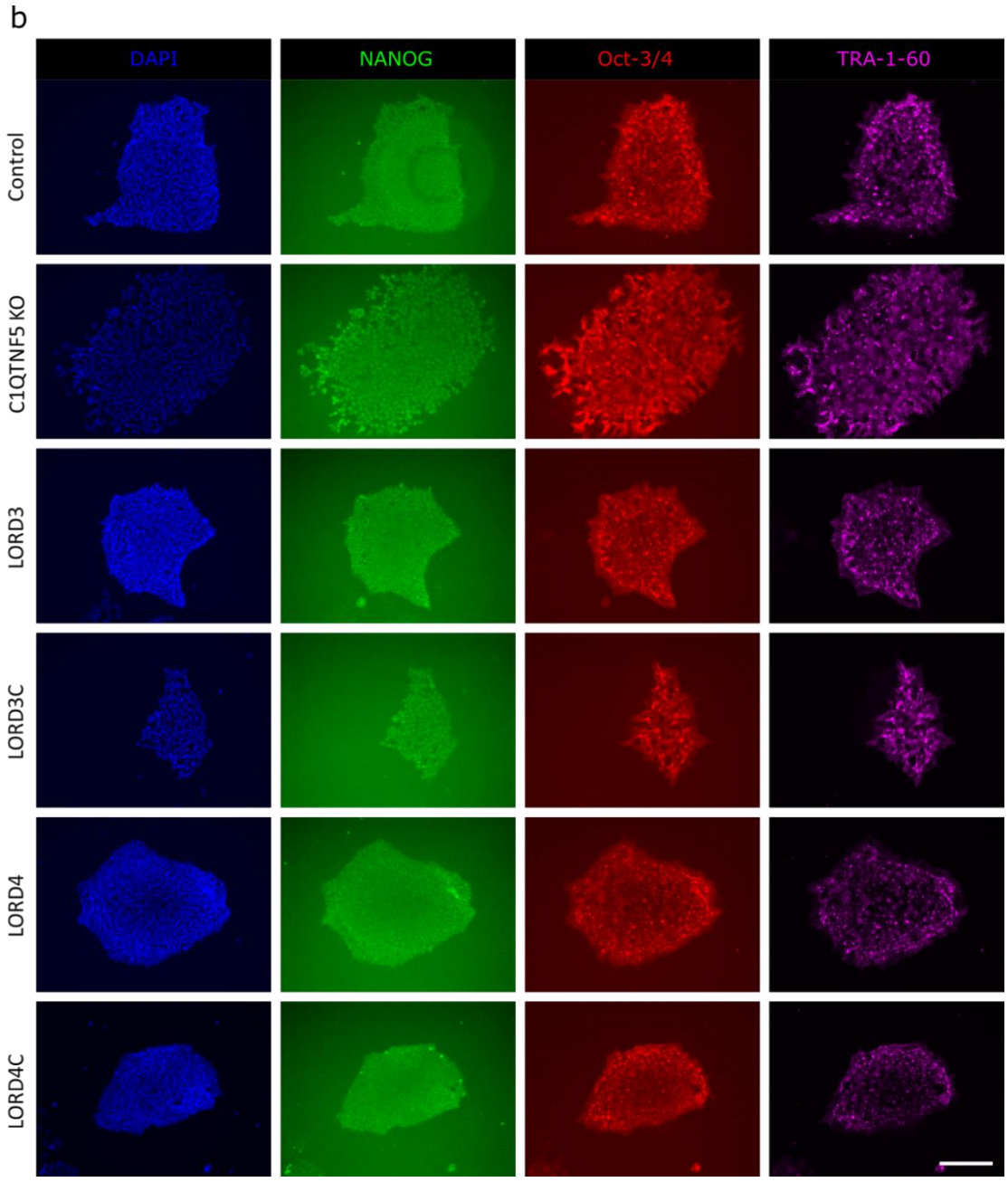
b
DAPI
NANOG
Oct-3/4
TRA-1-60
Control
C1QTNF5 KO
LORD3
LORD3C
LORD4
LORD4C

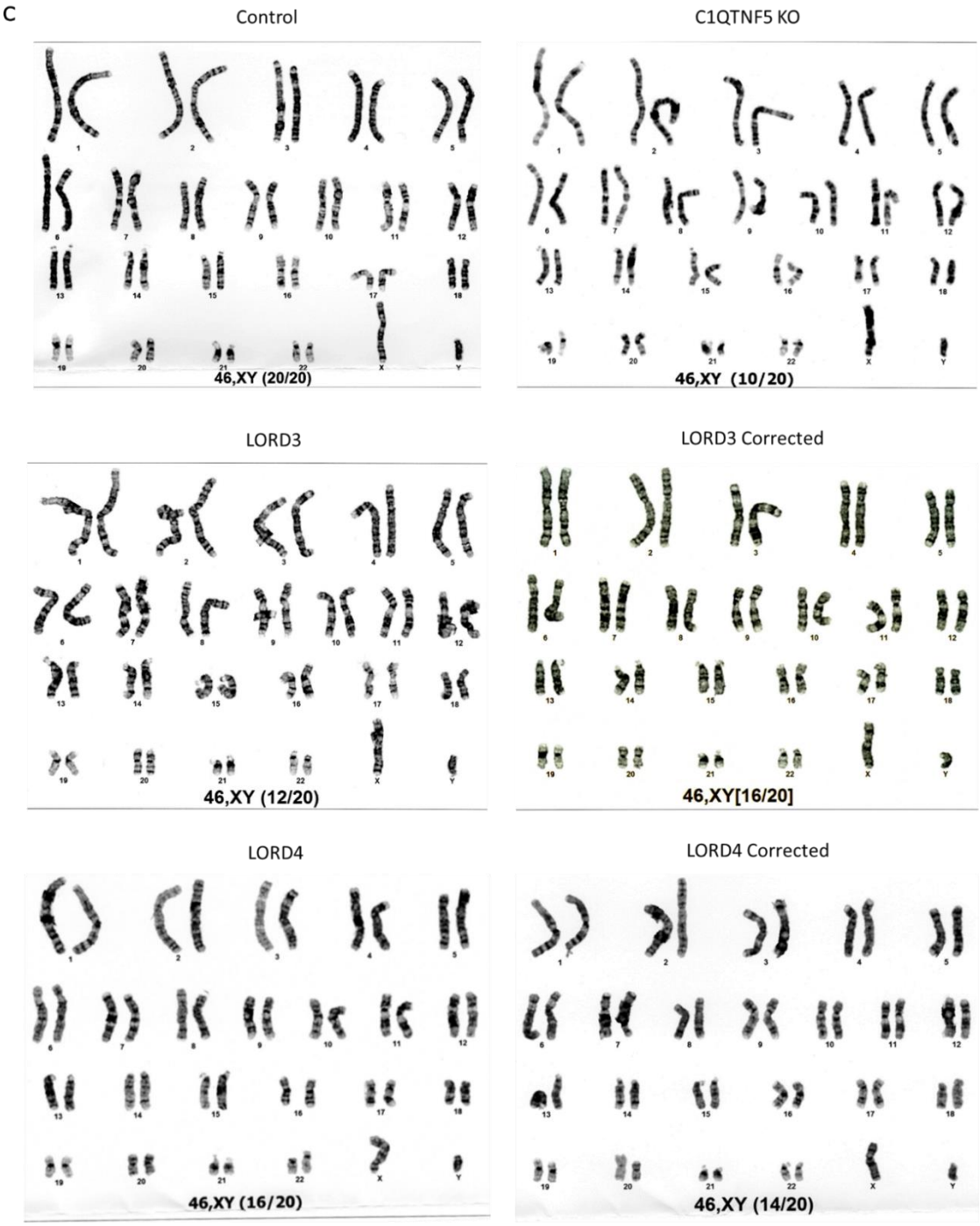

Figure 2.2 | The iPSC lines used had normal iPSC characteristics. The iPSC lines grew in normal iPSC colonies (**a**), expressed the pluripotency markers NANOG, Oct3/4, and TRA-1-60 (**b**), and had a normal 46,XY karyotype (**c**). Scale bars equal 400 µm (**a**) and 200 µm (**b**).

2.3.2 Design and construction of *C1QTNF5*^{S163R} gene correction plasmids

To target the *C1QTNF5*^{S163R} mutation site, gRNA pairs were designed that in conjunction with Cas9n can generate a DSB near the mutation site (Fig. 2.3a). When transfected in conjunction with an HDR template, the *C1QTNF5*^{S163R} mutation can be corrected. A separate HDR template was designed for each gRNA pair to introduce a silent mutation in the PAM sites of their respective gRNA pair to prevent subsequent editing. The gRNA pairs here could also be used to introduce the *C1QTNF5*^{S163R} mutation in a wt iPSC line. Both gRNAs of a pair were cloned in a plasmid containing Cas9n for co-expression.

In addition, a gRNA was designed to target only the *C1QTNF5*^{S163R} mutation (gRNA Correction). The *C1QTNF5*^{S163R} mutation itself generates a PAM sequence and therefore this was leveraged to design this gRNA that can only target the L-ORD allele (Fig. 2.3b). This gRNA was cloned in a plasmid containing Cas9 for co-expression after transfection. As an alternative, gRNA Correction was also used in conjunction with tracrRNA and Cas9 to form an RNP for transfection.

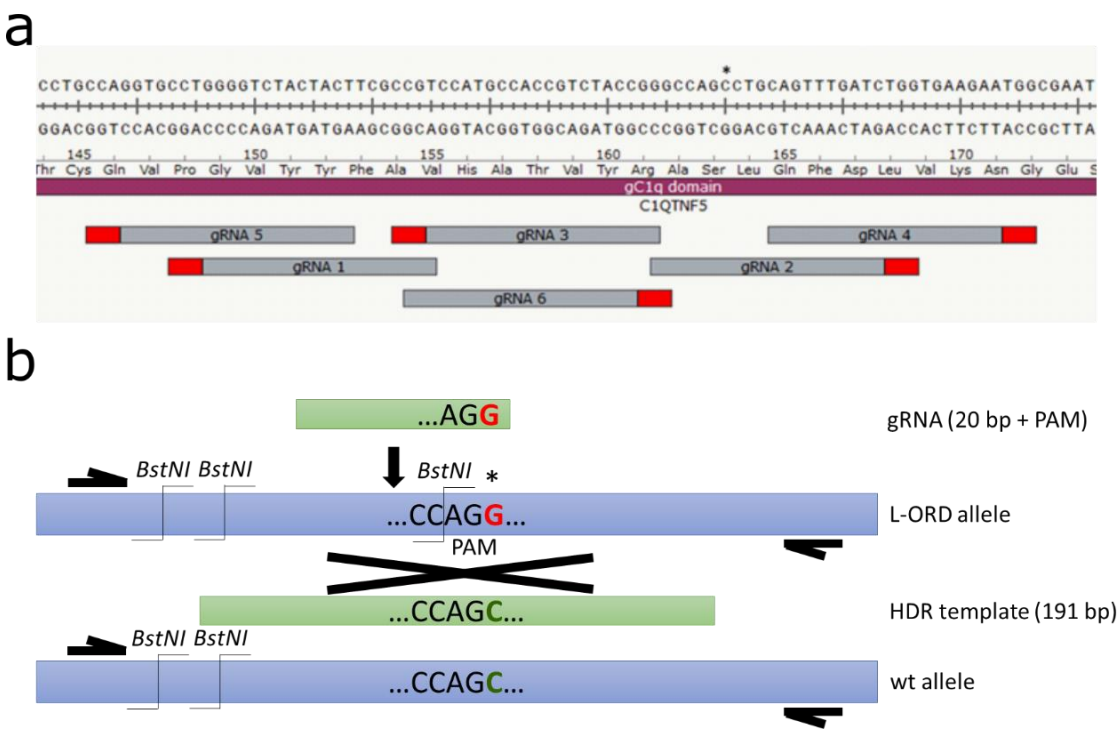

Figure 2.3 | Strategies used for targeting the *C1QTNF5* mutation site. The *C1QTNF5*^{S163R} mutation site (asterisk) was targeted with gRNA pairs (1 and 2, 3 and 4, 5 and 6) in conjunction with Cas9n to generate a DSB (**a**). An HDR template was designed per gRNA pair to introduce or correct the *C1QTNF5*^{S163R} mutation and to create a silent mutation in one or both PAM sites of the gRNAs to prevent sequential editing. The *C1QTNF5*^{S163R} mutation (red, asterisk) also generates a PAM site (**b**). Thus, a gRNA designed with this PAM would only target the *C1QTNF5*^{S163R} mutation. A wt HDR template with 95 bp homology arms was used to repair the mutation (G>C) in a scarless-fashion. The *C1QTNF5*^{S163R} mutation also generates an extra *BstNI* restriction site (5'-CCWGG-3'). This allows for the screening for successfully edited clones. PAM = protospacer adjacent motif; HDR = homology directed repair; wt = wildtype.

gRNA1 and gRNA2 were cloned into a plasmid containing Cas9n for co-expression. gRNA Correction was previously cloned into a plasmid containing wildtype Cas9 and validated by Dr Selvaraj (The University of Edinburgh). Successful cloning of gRNA1 and gRNA2 was determined by PCR amplification of the plasmid with the forward primer annealing to the gRNA insert and the reverse primer annealing to the plasmid backbone. PCR amplification only worked when the gRNA-specific primer was able to anneal to its respective gRNA insert (Fig. 2.4), indicating that the gRNA was successfully cloned into the plasmid with Cas9n.

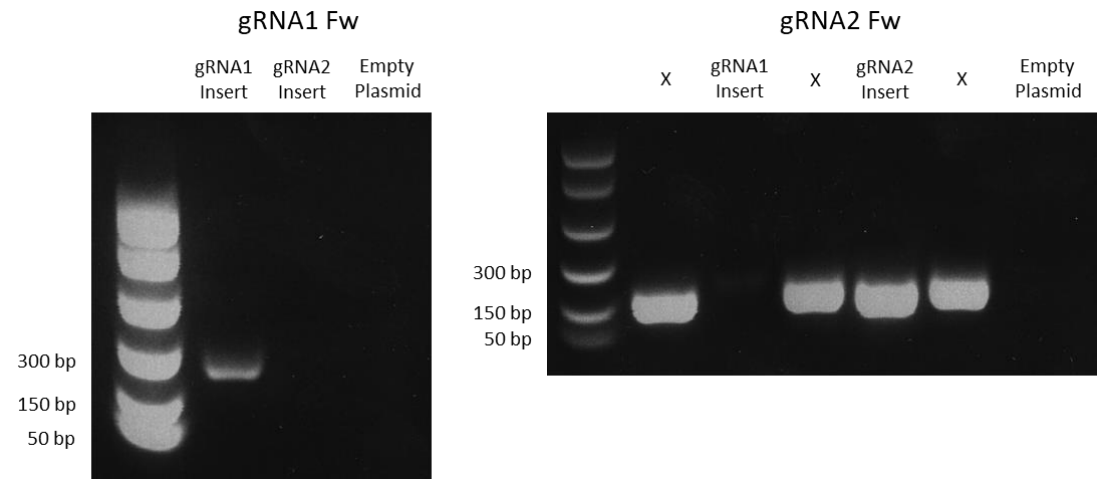

Figure 2.4 | gRNA1 and gRNA2 were successfully cloned into plasmids containing Cas9n. gRNA1 and gRNA2 were cloned into plasmids containing Cas9n. Forward primers specifically designed to anneal to gRNA1 or gRNA2 were used to test correct insertion of the gRNA into the Cas9n plasmids in conjunction with a reverse primer annealing to the plasmid backbone. The Cas9n plasmid with gRNA1, gRNA2, or empty were PCR amplified with the gRNA1-specific forward primer (left) or the gRNA2-specific forward primer (right) and only showed a PCR band of 177 bp or 167 bp respectively when their specific insert was successfully cloned into the plasmid.

2.3.3 Gene correction gRNA specificity test transfection of HEK 293T cells

HEK 293T cells were transfected with gRNA1, gRNA2, both gRNA1 and gRNA2, or gRNA Correction plasmids, in order to determine if the gRNAs are able to target the site of interest, and to assess the cutting efficiency of Cas9 in the site of interest. The *C1QTNF5* mutation locus was subsequently PCR amplified from isolated gDNA. The PCR products were subjected to a denaturing and slow reannealing process that allows for the formation of heteroduplex double-stranded DNA (dsDNA). The T7 endonuclease specifically recognises and cleaves the resulting mismatched dsDNA. Plasmids containing gRNA1 and gRNA2 also contain Cas9n and therefore on their own would not generate a DSB but a nick in the DNA. Therefore, gRNA1 and gRNA2 were each co-transfected with a plasmid containing Cas9. The plasmid containing gRNA Correction already has Cas9 in it.

Transfection of HEK 293T cells with gRNA1 or gRNA2 in combination with Cas9 causes a DSB near the mutation site in *C1QTNF5*. The DSB is then repaired by endogenous NHEJ, resulting in random indel mutations. Transfection with gRNA1 and Cas9 resulted in an undigested PCR

product band at 300 bp and bands underneath indicating NHEJ events have taken place which were digested by T7 (Fig. 2.5). Therefore, gRNA1 targets the correct locus. The specificity of gRNA2 on its own with Cas9 could not be shown (Fig. 2.5). However, gRNA1 and gRNA2 combined also showed NHEJ multiple bands (Fig. 2.5), indicating that both gRNAs bind to the right site in *C1QTNF5* and efficiently cause DSBs with Cas9n. Transfection with the plasmid containing gRNA Correction did not generate any NHEJ bands (Fig. 2.5), indicating that gRNA Correction with Cas9 cannot target the wt HEK 293T cell line. This is expected as gRNA Correction has a PAM site that can only recognise the L-ORD mutant allele which is absent in the wt HEK 293T cell line (Fig. 2.3b).

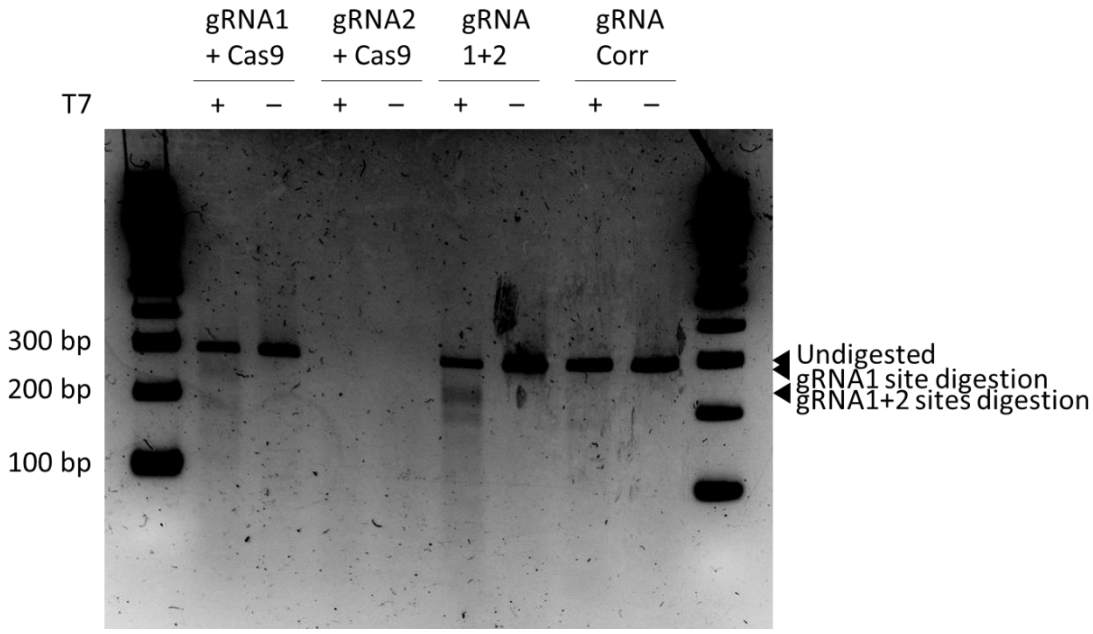

Figure 2.5 | T7 endonuclease assay test on HEK 293T transfected with gRNA constructs. HEK 293T cells were transfected with gRNA1 with wt Cas9 plasmid, gRNA2 with wt Cas9 plasmid, gRNA1 and 2, or gRNA correction. gRNA1 in combination with Cas9 would generate 245 and 56 bp bands. gRNA2 in combination with Cas9 would generate 193 and 108 bp bands. gRNA1 and gRNA2 together would generate 194, 56 and 52 bp bands. The undigested PCR product is 301 bp.

2.3.4 Gene correction gRNA specificity test transfection of L-ORD iPSCs

gRNA Correction could not be tested on the wt HEK 293T cell line because it lacks the required PAM site for the gRNA to bind to. This gRNA was therefore tested on the case iPSC line LORD4

in combination with the HDR template. In a T7 assay the untransfected case cells show the predicted digestion bands (Fig. 2.6a), since it is a heterozygous mutation. The transfected case cells also show these bands when not selected for transfection, indicating that there are still mutant cells in the population (Fig. 2.6a). However, this assay was not sensitive enough to determine if there was a subpopulation of successfully edited cells (Fig. 2.6a).

Another method to check successful editing is through restriction digestion. The *C1QTNF5*^{S163R} mutation in the L-ORD case generates a *BstNI* restriction site (Fig. 2.3b). The untransfected case cells show the predicted digestion bands, because two restriction sites are already in the amplicon (Fig. 2.6b). Case cells would show these bands in addition to extra fragments due to the extra restriction site caused by the *C1QTNF5*^{S163R} mutation. Correction of the *C1QTNF5*^{S163R} mutation should make these extra bands fainter compared to the case, but unfortunately this is not clear (Fig. 2.6b). Nonetheless, since this gRNA is expected to be L-ORD allele-specific, gRNA Correction was used for the subsequent L-ORD mutation correction experiments.

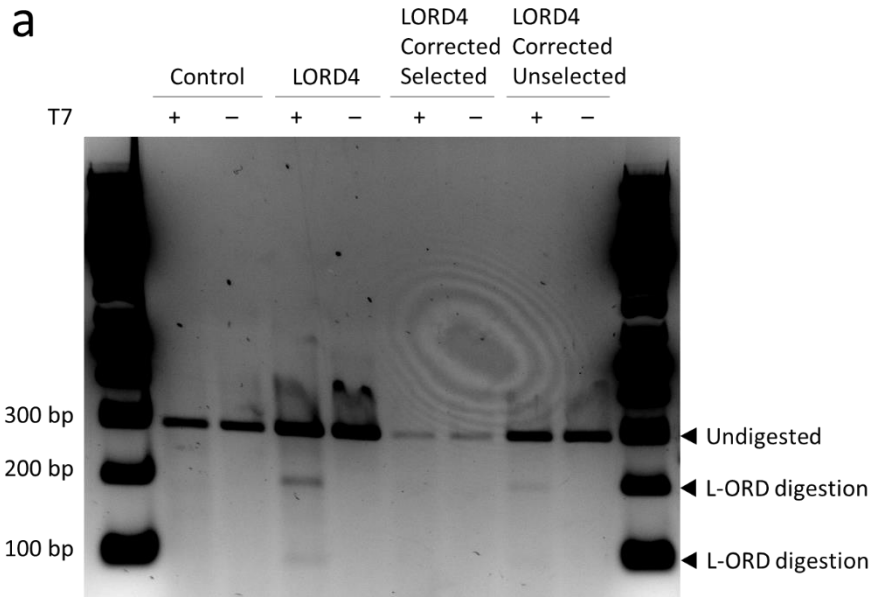

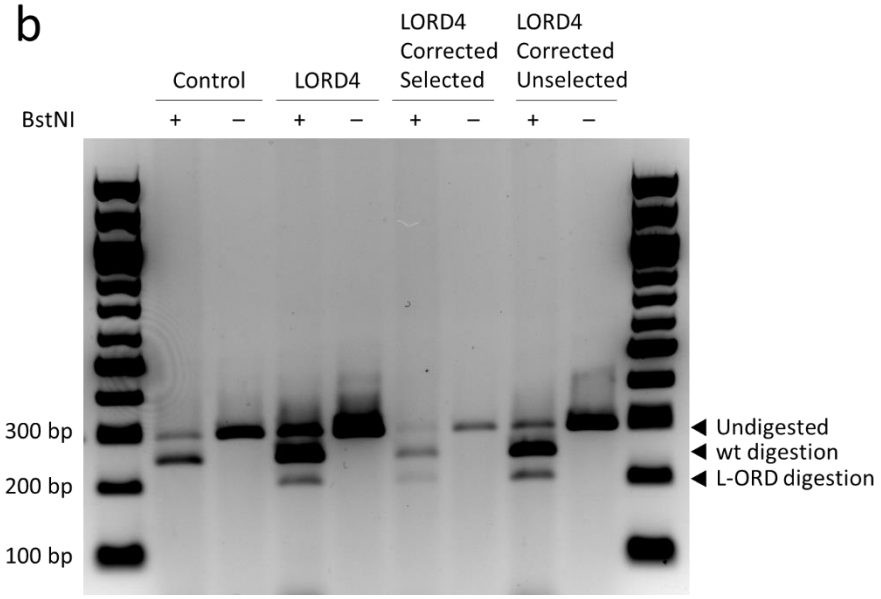

Figure 2.6 | RFLP assays L-ORD case iPSCs transfected with *C1QTNF5* correction RNP and HDR template on population level. LORD4 case iPSCs were transfected with *C1QTNF5* correction RNP with HDR template and selected with puromycin for successful transfection. Control iPSCs (CS02iCTR-NTn1), LORD4, and transfected LORD4 without puromycin selection were used as controls. The *C1QTNF5* mutation region was PCR amplified and subsequently digested with T7 endonuclease (**a**) or *BstNI* restriction enzyme (**b**). In the T7 assay the wt control iPSCs would generate no extra bands, untransfected LORD4 iPSCs would generate 209 and 92 bp digestion bands, LORD4 corrected and selected would still generate fainter 209 and 92 bp bands, and LORD4 corrected and not selected would still generate the 209 and 92 bp bands in the T7 assay (**a**). In the *BstNI* assay the wt control iPSCs would generate 249, 45 and 7 bp bands, untransfected LORD4 iPSCs would generate the same bands in addition to 206 and 43 bp bands, LORD4 corrected and selected would still generate the additional 206 and 43 bp bands but fainter, and LORD4 corrected and not selected would also still generate the additional 206 and 43 bp bands (**b**). The undigested PCR product is 301 bp for both assays.

2.3.5 Gene correction of LORD4 using the RNP method

LORD4 was transfected with gRNA Correction using the RNP method. gRNA Correction was chosen because it should only edit the L-ORD allele and not the wt allele (Fig. 2.3b). This was confirmed in wt HEK 293T cells because gRNA Correction was unable to edit these cells (Fig. 2.5).

From the transfected and puromycin-selected LORD4 population of cells, 240 single cell-derived clones were screened and one *C1QTNF5* corrected clone (clone 3-41) was found via *BstNI* restriction digestion (Fig. 2.7a). Sanger sequencing of clone 3-41 confirms that this clone has *C1QTNF5* successfully gene-corrected (Fig. 2.7b). Although the *C1QTNF5*^{S163R} mutation was corrected, it seemed that the gene editing introduced a new *C1QTNF5*^{A154T} mutation (Fig. 2.7c).

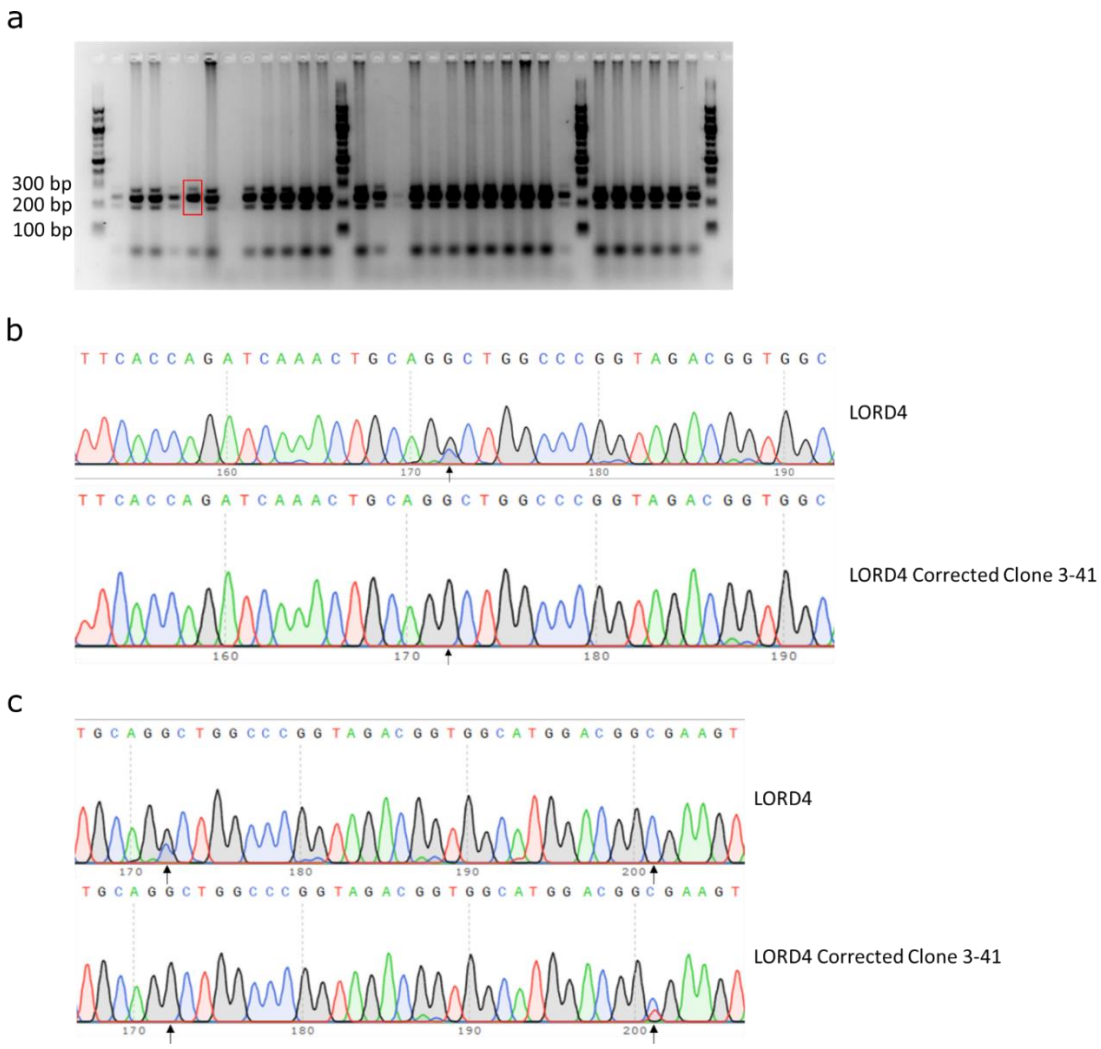

Figure 2.7 | *BstNI* restriction digestion on 240 case iPSC single cell-derived LORD4 clones transfected with *C1QTNF5* correction RNP and wt HDR template and Sanger sequencing. LORD4 iPSCs were transfected with *C1QTNF5* correction RNP and 240 single cell-derived clones were screened by PCR and subsequent *BstNI* restriction digestion after selection with puromycin (not all shown) (**a**). The wt control iPSCs were expected to generate 249, 45 and 7 bp bands whereas LORD4 case iPSCs were expected to generate additional 206 and 43 bp digestion bands. One out of 240 clones showed the

expected loss of the 206 bp band for a successful correction of the L-ORD allele (clone 3-41; red box). Sanger sequencing of the antisense strand of LORD4 showed a double peak; a G for the wt allele, and a C for the L-ORD allele (arrow) (**b**). In contrast, clone 3-41 showed a single G peak, indicating successful gene correction. However, gene editing introduced a new C>T (p.A154T) mutation upstream in the corrected allele (right arrows) (**c**). The left arrows indicate the L-ORD mutation site.

2.3.6 Gene correction of LORD4 using the plasmid method

LORD4 was corrected again because of the introduced *C1QTNF5*^{A154T} mutation (Fig. 2.7c). The gRNA Correction in the Cas9 plasmid was used, because the RNP method used previously was very inefficient. 192 single cell-derived clones were screened and 36 clones seemed to be successfully edited (Fig. 2.8).

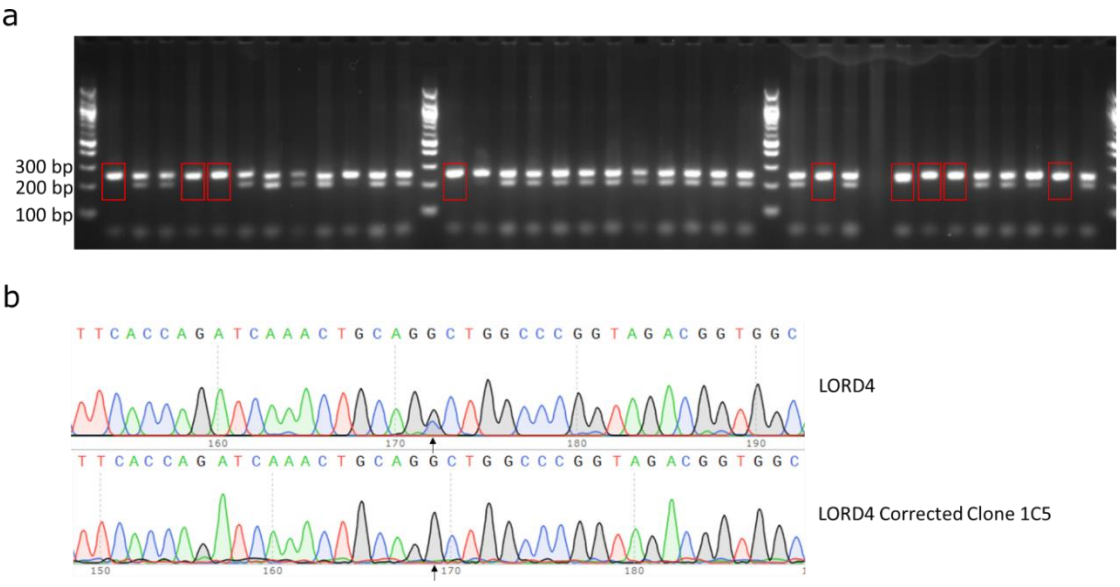

Figure 2.8 | *BstNI* restriction digestion on 192 case iPSC single cell-derived LORD4 clones transfected with *C1QTNF5* correction plasmid and wt HDR template and Sanger sequencing. LORD4 iPSCs were transfected with *C1QTNF5* correction plasmid and 192 single cell-derived clones were screened by PCR and subsequent *BstNI* restriction digestion after selection with puromycin (not all shown) (**a**). The wt control iPSCs were expected to generate 249, 45 and 7 bp bands whereas LORD4 case iPSCs were expected to generate additional 206 and 43 bp digestion bands. 36 out of 192 clones showed the expected loss of the 206 bp band for a successful correction of the L-ORD allele (red boxes). Sanger sequencing of the antisense strand of LORD4 showed a double peak; a G for the wt allele, and a C for the L-ORD allele (arrow) (**b**). In contrast, corrected clones showed a single G peak, indicating successful gene correction.

2.3.7 Gene correction of LORD3 using the plasmid method

For the correction of LORD3 the gRNA Correction in the Cas9 plasmid was used again. 192 single cell-derived clones were screened and 35 clones seemed to be successfully edited (Fig. 2.9).

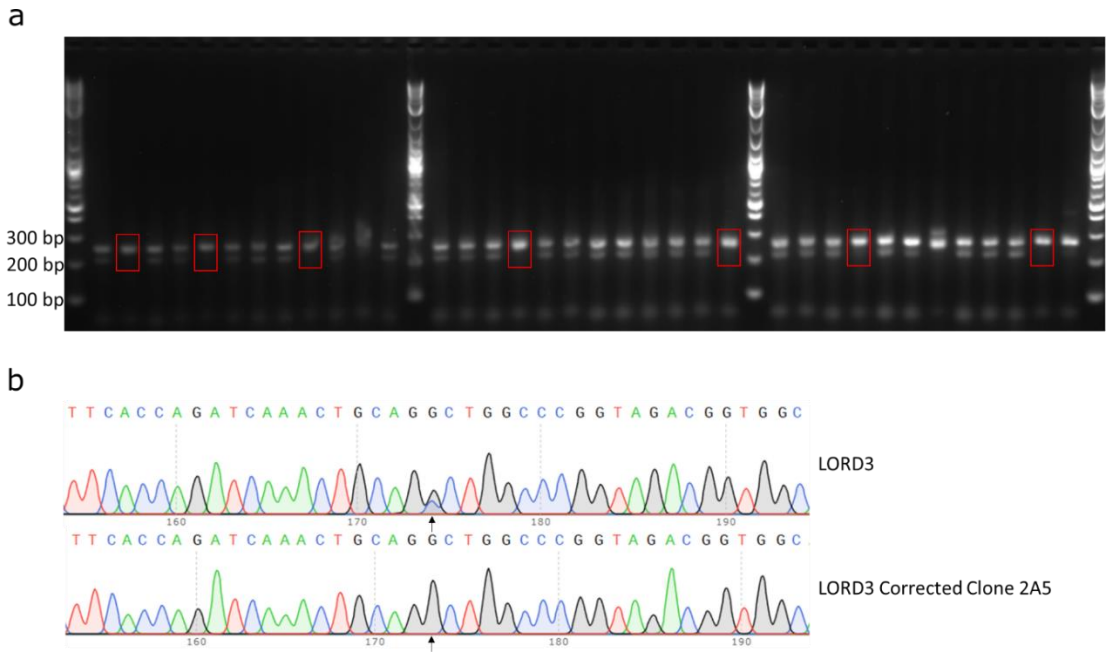

Figure 2.9 | *BstNI* restriction digestion on 192 case iPSC single cell-derived LORD3 clones transfected with *C1QTNF5* correction plasmid and wt HDR template and Sanger sequencing. LORD3 iPSCs were transfected with *C1QTNF5* correction plasmid and 192 single cell-derived clones were screened by PCR and subsequent *BstNI* restriction digestion after selection with puromycin (not all shown) (**a**). The wt control iPSCs were expected to generate 249, 45 and 7 bp bands whereas LORD3 case iPSCs were expected to generate additional 206 and 43 bp digestion bands. 35 out of 192 clones showed the expected loss of the 206 bp band for a successful correction of the L-ORD allele (red boxes). Sanger sequencing of the antisense strand of LORD3 showed a double peak; a G for the wt allele, and a C for the L-ORD allele (arrow) (**b**). In contrast, corrected clones showed a single G peak, indicating successful gene correction.

2.3.8 Checking gene-corrected LORD3 and LORD4 clones for off-target activity

Even though gRNA Correction was designed to only target the L-ORD allele, and the gRNA did not cause any editing activity in wt HEK 293T cells, edited iPSC clones were checked for off-allele editing. To check if the gRNA is specific for the L-ORD allele, multiple edited clones were sequenced. Loss of the *BstNI* restriction site is either due to HDR-mediated correction of the L-ORD allele or due to NHEJ-mediated generation of indels in the L-ORD allele. It is possible that, if the wt allele is targeted, indels are introduced in the wt allele. Even in clones that lost the *BstNI* restriction site due to indels generated by NHEJ, the wt trace could be observed in the background (Fig. S1a). This suggests that NHEJ only occurred in the L-ORD allele and that the wt allele was spared. Therefore, only the L-ORD allele was found to be targeted and edited with gRNA Correction.

The CRISPR/Cas9 system is highly efficient is generating DSBs. However, the downside of such high activity is that there is an increased propensity for off-target activity at sites highly homologous to the gRNA. Sanger sequencing was performed on top five potential off-target sites for gRNA Correction in LORD3 and LORD4 gene-corrected clones to assess for potential off-target deleterious mutations. The sequence of all top five loci were found to be unaltered in both LORD3 and LORD4 gene-corrected clones (Fig. S1b), suggesting that the off-target activity of gRNA Correction is minimal.

2.3.9 Strategy for generating C1QTNF5 KO lines

To generate a C1QTNF5 KO line, a gRNA pair was previously designed and cloned into plasmids containing Cas9 and validated by Dr Selvaraj (The University of Edinburgh). The gRNA pair was designed to create two DSBs in exon 1 of *C1QTNF5* in conjunction with Cas9 (Fig. 2.10). The 107 bp fragment between the DSBs would be deleted and the remaining ends would be joined by NHEJ to introduce an in-frame stop codon.

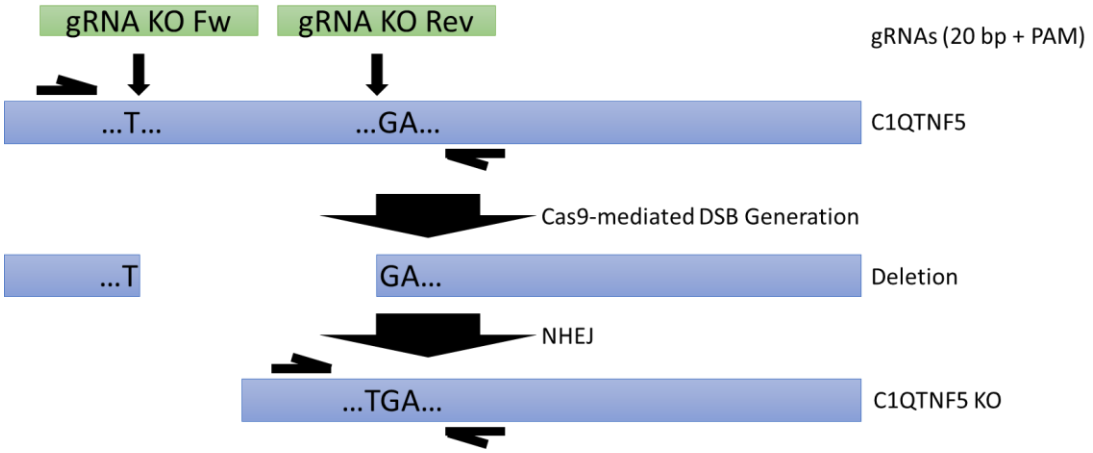

Figure 2.10 | Strategy for generating C1QTNF5 KO lines. A gRNA pair was designed to generate two DSBs (arrows) in exon 1 of *C1QTNF5* in conjunction with Cas9. The 107 bp region between the DSBs is subsequently deleted and the remaining ends are ligated together via NHEJ. Thus, the 3' T of the upstream fragment would join with the 5' GA of the downstream fragment, forming an in-frame TGA stop codon.

2.3.10 KO gRNAs test transfection of HEK 293T cells

The designed gRNAs for generating a C1QTNF5 KO line were first tested on a wt HEK 293T cell line. HEK 293T cells were therefore transfected with the C1QTNF5 KO gRNA pair in plasmids containing Cas9. The transfected cells show a smaller size 387 bp band when the KO region in *C1QTNF5* was PCR amplified because of the 107 bp deletion (Fig. 2.11). Therefore, the gRNA pair can target and edit the correct site in *C1QTNF5* in conjunction with Cas9.

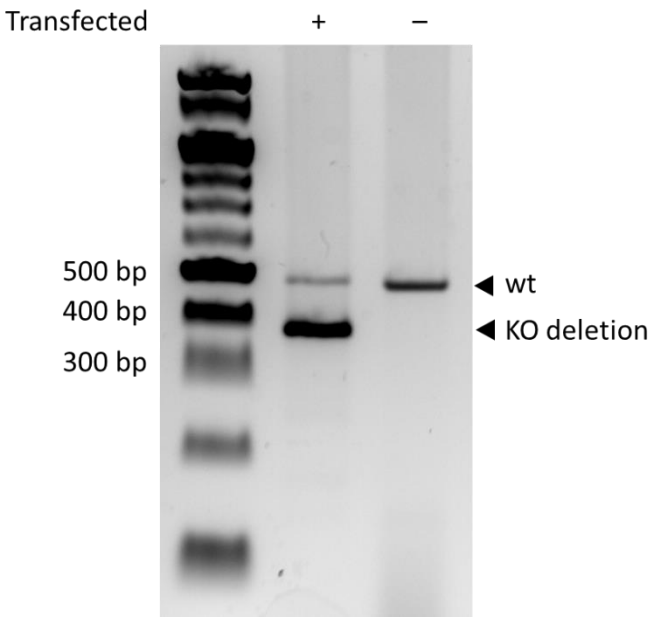

Figure 2.11 | PCR test on HEK293T transfected with C1QTNF5 KO constructs on population level. HEK 293T cells were transfected with the C1QTNF5 KO gRNA pair in plasmids containing Cas9. PCR amplification of the targeted KO region in *C1QTNF5* would result in a 494 bp band, but when successfully edited in a 387 bp PCR band. Transfected cells had a mixed population with the expected 107 bp deletion.

2.3.11 Generation of C1QTNF5 KO iPSC line

The control wt iPSC line CS02iCTR-NTn1 was transfected with the C1QTNF5 KO gRNA pair. Transfected cells showed the expected 107 bp deletion band after PCR amplification of the C1QTNF5 target locus (Fig. 2.12). Moreover, the transfected cells that were also selected with puromycin show a thicker deletion band than the unselected cells, indicating enrichment of transfected clones via antibiotic selection.

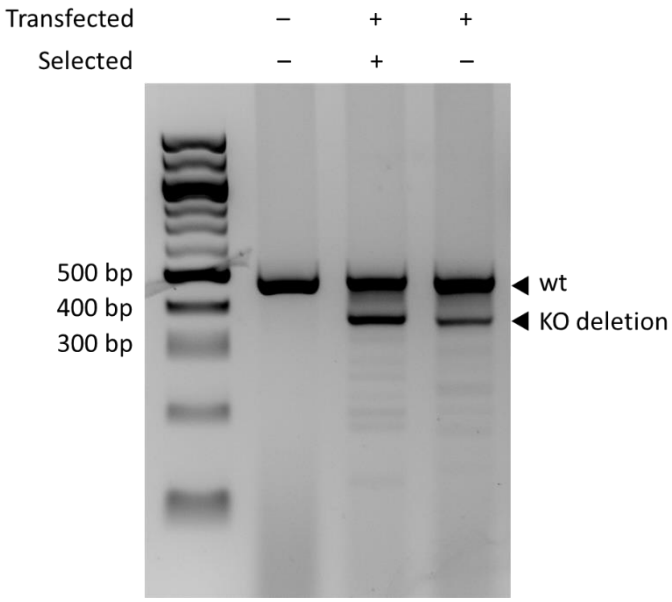

Figure 2.12 | PCR on wt iPSCs transfected with C1QTNF5 KO constructs on population level. Control wt iPSCs were transfected with a C1QTNF5 KO gRNA pair in plasmids containing Cas9. When transfected with these plasmids it would result in a 387 bp PCR band. Untransfected cells would have a 494 bp band. Treatment with puromycin should select for cells transfected with the gRNA pair.

From the transfected population of cells 70 single cell-derived clones were screened and three *C1QTNF5*$^{-/-}$ clones were found in addition to seven possible *C1QTNF5*$^{+/-}$ clones (Fig. 2.13a). Sanger sequencing of clone 36 showed that this clone had a successful biallelic deletion in *C1QTNF5* resulting in an in-frame TGA stop codon (Fig. 2.13b and c).

a

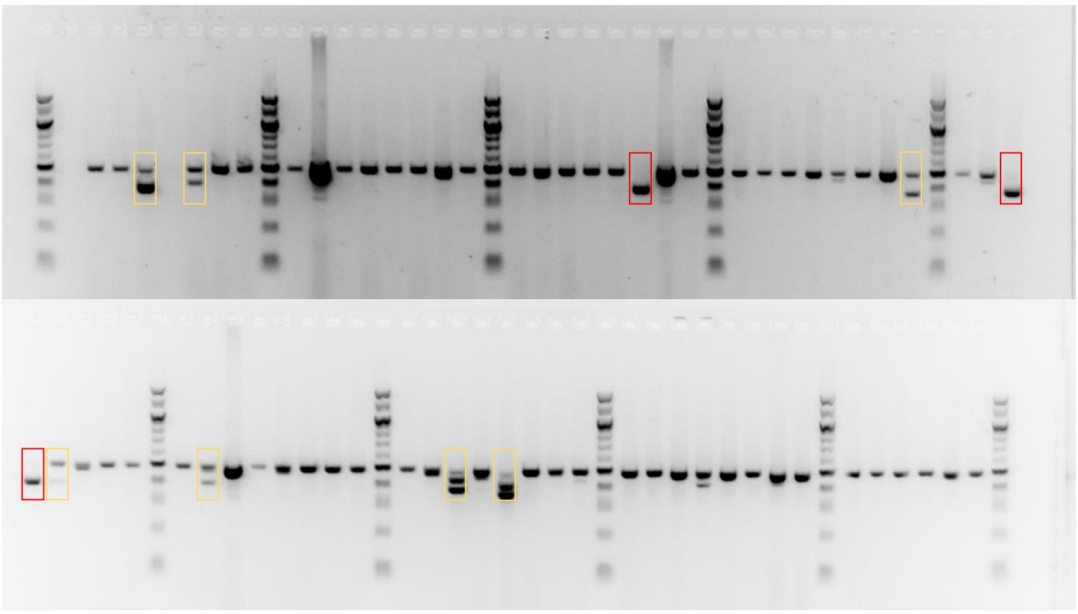

b

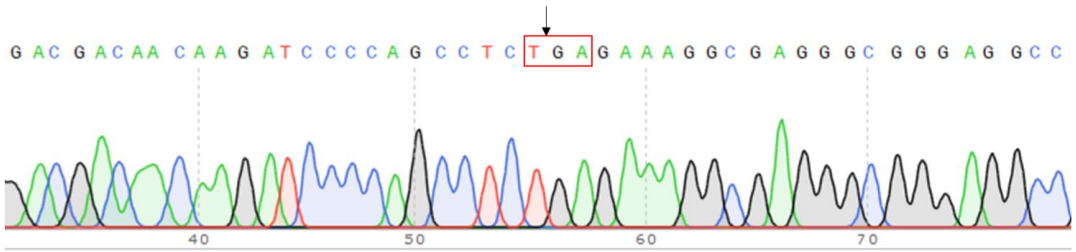

c

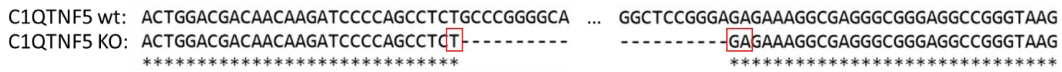

Figure 2.13 | PCR on 70 wt iPSC single cell-derived clones transfected with C1QTNF5 KO constructs and Sanger sequencing. Control wt iPSCs were transfected with a C1QTNF5 KO gRNA pair in plasmids containing Cas9 and 70 single cell-derived clones were screened by PCR after puromycin selection (**a**). Three out of 70 clones showed the expected single 387 bp PCR band for a successful biallelic KO deletion (red boxes). Seven out of 70 clones showed the 387 bp PCR band in addition to the 494 bp PCR band indicating possible monoallelic KO deletion (yellow boxes). Sanger sequencing of clone 36 showed a missing 107 bp at the predicted location (arrow), resulting in a TGA stop codon (red box) (**b**). Alignment of the *C1QTNF5* sequence of clone 36 with wt *C1QTNF5* sequence showed the 107 bp deletion, resulting in a TGA stop codon (red boxes) (**c**).

2.3.12 Checking C1QTNF5 KO clones for off-target activity

Sanger sequencing was performed on the C1QTNF5 null clone 36 for the top four potential off-target sites for both the upstream and downstream gRNA to assess for deleterious mutations. None of these loci were changed in C1QTNF5 KO compared to its isogenic control (Fig. S2). However, both lines did have some SNPs compared to the reference sequence in one of the predicted off-target loci which were therefore already present before editing.

2.4 Discussion

The ability to use L-ORD patient-derived stem cells in combination with gene editing allows for a unique way to investigate the function of C1QTNF5, as well as the effects of the L-ORD mutation on the protein function. Here, I showed the gene correction of the L-ORD-causing *C1QTNF5*^{S163R} mutation in two different patient-derived iPSC lines. In addition, I generated a biallelic KO of the C1QTNF5 in a wt iPSC line.

One of the L-ORD iPSC lines, LORD4, was edited using a relatively new CRISPR/Cas9 editing method. With this method, the gRNA, tracrRNA, and the Cas9 protein are incubated together to form an RNP prior to transfection. This method yielded a very low successful editing efficiency of 0.42% (Fig. 2.7a). The low efficiency could be due to inefficient assembly of the RNP, degradation of RNA, inefficient transfection of the RNP, or the length of the HDR repair template. Further experiments are needed to address the low efficiency of the RNP method. A new, shorter HDR template was designed and used for the plasmid-based editing experiments.

Even though the L-ORD mutation was corrected in LORD4 using the RNP method (Fig. 2.7b), a new *C1QTNF5*^{A154T} mutation was introduced in the same corrected allele (Fig. 2.7c). Sanger sequencing indicates that an HDR event resulted in the correction of the *C1QTNF5*^{S163R} mutation. Correction of the *C1QTNF5*^{S163R} mutation removes the PAM site, making subsequent editing of this site as unlikely as editing the wt allele (Fig. 2.5 and 2.10a). The new *C1QTNF5*^{A154T} mutation was therefore most likely introduced in the same HDR event as the *C1QTNF5*^{S163R} mutation was corrected. It is possible that the HDR repair template used to correct the *C1QTNF5*^{S163R} mutation had a mutation in it.

LORD4 was edited again using a different CRISPR/Cas9 editing method. An additional L-ORD iPSC line, LORD3, was also edited using this method. With this method, the gRNA is cloned into a vector containing the tracrRNA and Cas9. Transfection of iPSCs with this vector results in co-expression of these three components and subsequent assembly of the RNP inside the cell. The *C1QTNF5*^{S163R} mutation was successfully gene-corrected in LORD3 and LORD4 using this method (Fig. 2.8 and 2.9). Successful gene editing of the *C1QTNF5*^{S163R} mutation site was screened by the absence of the *BstNI* restriction site in *C1QTNF5*^{S163R}. The *BstNI* restriction site in *C1QTNF5*^{S163R} can be lost by either a successful HDR event in conjunction with the

repair template or a NHEJ event introducing an indel mutation at the site. Gene editing using the plasmid-based method yielded about a 18% efficiency. Of this successful targeting and editing, about 50% resulted in NHEJ and about 50% in HDR. Even though HDR always resulted in the correction of the L-ORD mutation, some corrected clones had a different SNP introduced. This was again possibly due to the purity of the HDR template. The efficiency for complete HDR-mediated gene correction was 7.8%. The gRNA Correction did not cause off-target editing in the wt allele nor off-target editing in top five predicted loci that are highly homologous to gRNA Correction (Fig. S1). However, whole genome sequencing would need to be performed to completely exclude any off-target editing.

An alternative way to potentially correct the *C1QTNF5*^{S163R} (c.686C>G) L-ORD mutation could be through base editing. Base editing is a relatively new gene editing technique relying on deaminases in conjunction with CRISPR/Cas9 but does not cause DSBs[140,141]. Therefore, no NHEJ could occur and no indel mutations could take place during gene editing. This could improve the efficiency of gene editing and could make gene editing directly in patients safer. Unfortunately, base editors can currently only do C-to-T and A-to-G conversions. There are currently no base pair editors that can change transversions[142], such as G-to-C, necessary to correct the c.686C>G L-ORD mutation. Hypothetically, a C-to-G base editor can be designed[143]. Alternatively, a G-to-T base editor could also be used to change the L-ORD arginine codon back to the wildtype serine, resulting in a silent mutation. A-to-C and T-to-G base editors would be needed to repair the L-ORD *C1QTNF5*^{P188T} (c.562C>A) and *C1QTNF5*^{G216C} (c.646G>T) mutations respectively. Base editors will need to be designed regardless because deaminases have been found recently to edit off-target in RNA[144]. It might be possible to at least gene correct the c.686C>G L-ORD mutation through base editing in the near future.

A C1QTNF5 KO iPSC line was generated using the CRISPR/Cas9 plasmid-based method with an upstream and a downstream gRNA. This method relies on NHEJ generating two DSB close together in exon 1 of *C1QTNF5*, resulting in a small deletion that leads to the generation of an in-frame stop codon. This strategy is highly efficient and precise compared to a single gRNA strategy that relies on HDR repair, because NHEJ events occur more often than HDR events. Therefore, fewer clones would need to be screened for the C1QTNF5 KO generation. Ten out of 70 clones were found to have the 107 bp deletion caused by the gene editing. Of these clones, three were found to have the deletion in both alleles, resulting in *C1QTNF5* null

iPSC lines (Fig. 2.13). Neither of the two gRNAs caused off-target editing in top four predicted loci that are highly homologous to the respective gRNA (Fig. S2). However, whole genome sequencing would need to be performed to completely exclude any off-target editing.

Together, these results show that the *C1QTNF5* gene can be successfully targeted and edited for both gene correction of the *C1QTNF5*^{S163R} L-ORD mutation, as well as gene KO. Gene correction was designed to be L-ORD allele-specific, which was confirmed by Sanger sequencing all edited clones. Correction and KO gRNAs were found to cause no off-target editing in loci highly homologous to the gRNAs. The isogenic lines generated here could be differentiated to iPSC-RPE and could provide new insights in the function of the C1QTNF5 protein and the effect of the *C1QTNF5*^{S163R} mutation leading to L-ORD.

Chapter 3 Characteristics of L-ORD iPSC-RPE and C1QTNF5

3.1 Introduction

3.1.1 Differentiation of iPSC to RPE

During human embryonic development optic progenitor cells (OPCs) form in the primitive forebrain[145]. The OPCs evaginate on both sides of the forebrain to form two bulges termed optic vesicles. OPCs of the optic vesicle are competent to become neural retina, optic stalk, or RPE. The optic vesicles undergo a process of cavitation, rotation, and invagination to form optic cups. RPE progenitor cells originate from the dorsal side of the optic cups and spread to surround the prospective neural retina.

Retinal progenitor cells (RPCs) are derived of the neuroblastic layer of the optic cup. The RPCs divide symmetrically to increase the progenitor pool size. In addition, the RPCs eventually give rise to the seven mature cell types of the neural retina: RGCs, amacrine cells, bipolar cells, horizontal cells, rod and cone photoreceptors, and Müller glia. This requires the downregulation of the transcription factor MITF and upregulation of the transcription factor VSX2[146], also known as CHX10. Conversely, if MITF is upregulated and VSX2 is downregulated, RPCs instead give rise to the RPE[147].

Multiple methods are reported in literature to emulate the different steps of retinal development in order to differentiate ESCs or iPSCs to RPE. The two main differentiation protocols are the continuous adherent culture method and the embryoid body (EB) method.

The continuous adherent culture method relies on the removal of basic fibroblast growth factor (bFGF, also known as FGF2) from the stem cell culture. bFGF is an essential growth factor necessary for both pluripotency and self-renewal of human ESCs and iPSCs, and is therefore part of stem cell maintenance medium[148-150]. Moreover, bFGF is known to repress RPE specification[145]. In the continuous adherent culture method bFGF is removed after the cells reach confluence[151-156], resulting in default differentiation. Initial pigmentation could be observed 1-8 weeks after bFGF removal. Pigmented foci grow over time and can be mechanically dissected after about 6-14 weeks. These isolated pigmented patches can then be cultured to generate an enriched population of RPE cells.

The EB method relies on the culturing of the stem cell colonies in suspended aggregates[147,157]. The EBs are maintained in a pro-neural induction medium (PIM) containing N-2 supplement, providing optimal growth conditions for neuronal cell types, accelerating the formation of neuroectoderm, and promoting retinal differentiation[158]. EBs are then allowed to attach to the culture dish which then forms neuroepithelial rosettes. The medium was then replaced with a retinal differentiation medium (RDM) containing B-27 supplement, known to enhance and accelerate retinal differentiation[158].

The continuous adherent culture method and the EB method both generate cells that have important RPE characteristics, in addition to the typical RPE cobble stone-like morphology and pigmentation. RPE generated in this way express typical RPE markers, including RPE65 and CRALBP, which have a function in the visual cycle; MITF and PMEL, which are involved in melanosome development for pigmentation; BEST1, an ion channel regulator; MERTK, which is involved in phagocytosis; and ZO-1, a tight-junction marker for epithelial cells. Furthermore, RPE generated in this way establish apical/basal polarity and have the typical RPE ability to phagocytose POS. Stem cell-derived RPE generated by these protocols have also been shown to rescue visual function in RCS rats[152,154].

Both protocols can be combined to utilise the ease of the continuous adherent culture method and the accelerated RPE-generation of the EB method, without the need of additional cytokines. For this, bFGF is removed to induce default differentiation. Subsequent replacement of medium with PIM with N-2 supplement leads eventually to the formation of neuroepithelial rosettes after about two weeks. Neuroepithelial rosettes represent the early neural plate or neural tube stage at which cells have committed to the neural lineage and can be directed to differentiate to more specific neuronal fates[159]. At this point activin A can be added to favour specific differentiation towards RPE. Activin A is known to efficiently induce differentiation to RPE[160]. Pigmented foci would form and, once grown large enough, can be dissected out and replated to a new dish for further enrichment and expansion. The medium can then be replaced with RDM with B-27 supplement without retinoic acid, because retinoic acid is known to promote the growth of rod photoreceptors[161,162] and delays RPE maturation[163]. iPSC-RPE can be serially expanded at least three times[164].

3.1.2 C1QTNF5

A p.S163R (c.686C>G) missense mutation is found in *C1QTNF5* in patients with L-ORD[80,83]. Recently, the mutations p.P188T (c.562C>A) and p.G216C (c.646G>T) were also found to cause L-ORD[165]. *C1QTNF5* is located on chromosome 11 (11q23.3), encodes for a 25 kDa secretory glycoprotein, and belongs to the C1QTNF family of secretory proteins[166]. The function of C1QTNF5 is still unclear.

The C1QTNF family is involved in cellular metabolism and immunity[167-169]. Thus far, 17 members of this protein family have been discovered. C1QTNF proteins are comprised of four domains: a N-terminal signal peptide domain, a short variable domain, a collagen G-X-Y repeat domain, and a C-terminal globular C1q (gC1q) domain (Fig. 3.1). The gC1q domain is homologous to C1q, which is a component of the classical complement pathway (see Chapter 5). A, B, and C chains of C1q form a trimer that resembles a bouquet-like structure. Similarly, C1QTNF proteins form stable homotrimers and some members can also form heterotrimers[168]. C1QTNF trimers often assemble into higher order structures such as nonamers and dodecamers. The 3D structure of the gC1q domain is also very similar to the C-terminal region of the TNF homology domain[167]. This domain is a common feature in the TNF family of proteins.

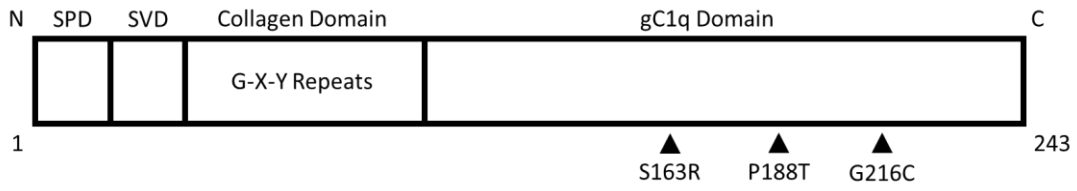

Figure 3.1 | The protein domains of C1QTNF5. All C1QTNF family members have a signal peptide domain (SPD), a short variable domain (SVD), a collagen domain consisting of G-X-Y repeats, and a globular C1q (gC1q) domain. Relative domain sizes and length of protein depicted here are from C1QTNF5. The three mutations known to cause L-ORD are located in the gC1q domain (arrows).

C1QTNFs undergo several post-translational modifications that influence their stability and function[169]. Proline residues in the third position of the collagen G-X-Y repeat sequence can be hydroxylated. Furthermore, one or more G-X-K-G-(E/D) sequences are present in the collagen domain of C1QTNFs, except for C1QTNF4, C1QTNF12, and

C1QTNF15/erythroferrone. The G-X-K-G-(E/D) consensus sequence can be sequentially hydroxylated and glycosylated. These post-translational modifications potentially influence the assembly of higher-order C1QTNF structures. As recombinant C1QTNF expressed by bacterial systems does not have these modifications, C1QTNFs are therefore best studied in mammalian model systems.

One of the best characterised members of the C1QTNF family is adiponectin. Adiponectin is a protein hormone exclusively expressed in adipocytes and is important for regulating cellular energy homeostasis, as well as glucose and lipid metabolism[170,171]. Adiponectin is also known to have anti-inflammatory functions by inhibiting macrophage phagocytic activity and lipopolysaccharide (LPS)-induced inflammation[172]. Furthermore, AMPK activation is known to prevent apoptosis in different cell types[173-175]. Adiponectin circulates in human plasma at relatively high concentrations, whereas other C1QTNFs are found at 1-2 orders of magnitude less in human circulation[169]. Adiponectin induces phosphorylation and activation of 5'-AMP-activated protein kinase (AMPK) and thereby increases glucose uptake, reduces glucose serum levels, and increases lactate production in myocytes. Adiponectin also induces phosphorylation and inhibition of acetyl-CoA carboxylase (ACC) and thereby increasing fatty acid oxidation in myocytes and hepatocytes.

Whilst related to adiponectin in sequence and structure, each C1QTNF member has a distinct tissue expression profile and function related to cellular metabolism and immunity. Similarly to adiponectin, C1QTNF1 and C1QTNF2 also induce phosphorylation of both AMPK and ACC, increase glucose uptake, reduce glucose serum levels, and promote fatty acid oxidation[176,177]. C1QTNF9 and C1QTNF13/C1QL3 also induce phosphorylation of AMPK and subsequent glucose uptake[178,179]. C1QTNF3 and C1QTNF12 have an anti-inflammatory function and, like adiponectin, also reduce LPS-induced inflammation in macrophages[180,181]. Homozygous missense mutations in *C1QTNF4* lead to retinal degeneration, but not much is known about its function[182]. C1QTNF6 also has anti-inflammatory functions and is found to suppress the alternative complement pathway[183,184]. Mutations in *C1QTNF7* were found to cause conduct disorder, one of the most prevalent childhood psychiatric conditions[185]. C1QTNF11/C1QL4 and C1QTNF14/C1QL1 promote angiogenesis of endothelial cells[186] and C1QTNF11/C1QL4 is also thought to regulate adipogenesis[187]. C1QTNF15/erythroferrone promotes iron and fatty acid uptake[188,189]. C1QTNF16/otolin-1 is part of otoconia crystals in vestibule of the inner ear

necessary for maintaining balance[190]. Not much is known yet about the function of C1QTNF8 and C1QTNF10/C1QL2.

The *C1QTNF5* gene encodes a short-chain collagen that is highly expressed in the RPE and is also expressed at a lower level in adipose tissue, testes, skeletal muscle, brain, spleen, and uterus[169]. C1QTFN5 is also found in human circulation[191,192]. C1QTNF5 is secreted and associates with the cell membrane in RPE[193]. Monomers of C1QTNF5 assemble into trimers and six trimers assemble into a bouquet-like shaped octadecamer (Fig. 3.2)[194,195]. The localisation of C1QTNF5 to the cell membrane and the structural similarities with collagens VIII and X suggests that C1QTNF5 could also have a role in cell adhesion, cell polarisation, and cell-cell communication. Another possible function of C1QTNF5 is regulation of the complement system, like C1QTNF6, because it has a gC1q domain. The complement system is dysregulated in AMD (see Chapter 5). C1QTNF5 could also have a role in cellular metabolism like adiponectin.

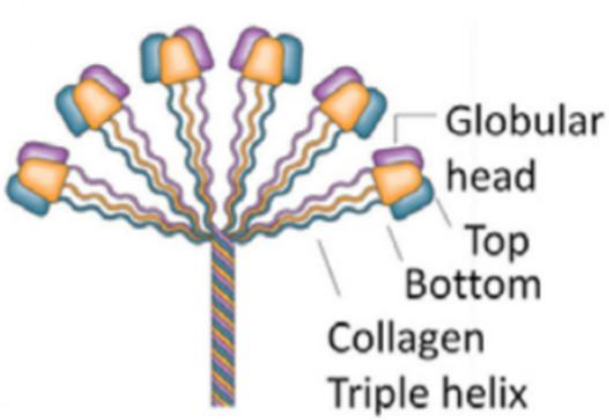

Figure 3.2 | Quaternary structure of C1QTNF5. C1QTNF5 forms trimers which assemble into a bouquet-like shaped octadecamer. Reproduced from Tu and Palczewski (2014)[195].

The globular domain of C1QTNF5 is about 40% homologous to that of adiponectin[196]. C1QTNF5 could therefore also have a role in the cellular response to oxidative damage and energy homeostasis. Recombinant C1QTNF5 is found to induce phosphorylation and activation of AMPK which led to an increased uptake of glucose in myocytes, similar to adiponectin, C1QTNF1, C1QTNF2, C1QTNF9, and C1QTNF13/C1QL3[196,197]. Similar to adiponectin, recombinant C1QTNF5 was found to inhibit reactive oxygen species (ROS) accumulation and caspase-3 activation, and thereby apoptosis, through activation of AMPK in myocytes[197]. Furthermore, C1QTNF5 was found to promote phosphorylation of ACC and

stimulate fatty acid oxidation. C1QTNF5 and C1qtnf5 expression in humans and mice respectively were found to be dependent on diet[198]. Moreover, decrease in circulating C1QTNF5 was found to be associated with metabolic syndrome in humans[192]. It is not yet known if C1QTNF5 also activates AMPK and regulates metabolism in RPE and the rest of the retina.

The p.S163R, p.P188T, and p.G216C mutations causing L-ORD are located in the gC1q domain of C1QTNF5 (Fig. 3.1)[165]. These mutations prevent multimerisation of C1QTNF5 to octadecamers[165,195]. Moreover, the secretion of mutated protein was found to be impaired[193]. The mutated protein is retained in the endoplasmic reticulum and can still interact with the wild-type protein[199]. These changes are thought to lead to the abnormal changes in the extracellular matrix between the RPE and Bruch's membrane found in patients with L-ORD[200,201].

Several mouse models have been generated to investigate the function of C1qtnf5. Mice with a *C1qtnf5*$^{+/S163R}$ knock-in show retinal abnormalities between 12 and 21 months of age, including RPE abnormalities, accumulation of drusen, Bruch's membrane abnormalities, loss of photoreceptors, and retinal vascular leakage[202]. However, another *C1qtnf5*$^{+/S163R}$ knock-in mouse model did not recapitulate the same retinal degenerative phenotype even up to two years[203]. *C1qtnf5*$^{-/-}$ KO mice have also been generated but had no apparent retinal defects between four and ten months of age, the time period in which this study was conducted[198]. C1qtnf5-deficient mice had reduced fasting insulin on standard diet and had attenuated hepatic steatosis and improved insulin action on a high-fat diet.

The entire *C1QTNF5* gene is located within the 3' untranslated region of the membrane frizzled-related protein (*MFRP*) gene and is co-transcribed with *MFRP*[80,204]. Dicistronic transcripts, like *C1QTNF5* and *MFRP*, typically encode proteins that are involved in the same molecular pathways[205]. It is thought that 5' cap-independent ribosome recruitment and translation initiation has evolved to allow the cell to deal with physiological stress conditions, where cap-mediated initiation is repressed[206]. A promoter sequence has been found that potentially allows *C1QTNF5* expression independently of *MFRP*[207]. C1QTNF5 is also found to interact with MFRP[199,208]. MFRP is a type II membrane protein with an unknown function[209]. It is thought that MFRP could be involved in lipid transport or lipid sensing in the sub-retinal space. Mutations in *MFRP* cause nanophthalmos and posterior microphthalmia[210], indicating

that *MFRP* has a role in ocular development. *Mfrp* is mutated in the *rd6* mouse model for retinal degeneration[204]. However, mutations in *MFRP* do not cause L-ORD.

An important receptor for adiponectin is adiponectin receptor 1 (ADIPOR1)[211,212]. ADIPOR1 is important for the activation of the AMPK pathway and DHA transport into RPE and photoreceptors[213]. ADIPOR1 KO causes retinal degeneration, whereas adiponectin KO does not[213]. Absence of Mfrp in the *rd6* mouse model for retinal degeneration causes loss of Adipor1 expression, specifically in the RPE and not in the photoreceptors[214]. It is not known what effect MFRP KO has on the expression of C1QTNF5. Furthermore, it is thought that one of the functions of C1QTNF5 is to block ADIPOR1. ADIPOR1 regulation could therefore have an important role in L-ORD.

It is still not clear what the function is of C1QTNF5 and what the consequences are of the *C1QTNF5*^{S163R} mutation on a cellular level. Studying RPE differentiated from the previously gene-corrected patient-derived iPSCs as well as the previously generated C1QTNF5 KO iPSCs (see Chapter 2) should give a better insight into the function of C1QTNF5 and how it contributes to macular degeneration when mutated.

3.1.3 Aims and objectives

In order to study iPSC-RPE, C1QTNF5, and the effect of the *C1QTNF5*^{S163R} mutation, the following was carried out in this chapter:

1. Different iPSC lines were differentiated into RPE by using a previously established protocol
2. iPSC-RPE were phenotypically and functionally characterised by immunostaining for RPE markers, measuring their transepithelial electrical resistance, and investigating their capability to phagocytose POS
3. C1QTNF5 expression, secretion, and structure in L-ORD and wt iPSC-RPE was studied by using qPCR and western blotting
4. The transcriptome of L-ORD iPSC-RPE compared to its isogenic gene-corrected control was studied by using RNA sequencing followed by Gene Ontology enrichment analysis and Ingenuity Pathway Analysis

3.2 Materials and methods

3.2.1 Cell culture

iPSCs were cultured by Dr Burr (The University of Edinburgh) and Almar Neiteler as described in Chapter 2 (2.2.1).

3.2.2 Differentiation towards iPSC-RPE

Differentiation was similar as described before[164]. The medium of the iPSCs was replaced with Essential 6 medium (Gibco) on day one. On day three the medium was replaced with PIM, consisting of Advanced DMEM/F-12 (Gibco), 2 mM GlutaMAX, and 1% N-2 supplement (Gibco). The medium was replaced every two to three days. PIM was supplemented with 100 ng/ml Activin A (Peprotech, London, UK) when neural epithelia appeared around day 14. Medium was replaced with PIM without Activin A once pigmentation started around day 20. Pigmented patches were dissected with needles, digested to single cells with trypsin/EDTA, and transferred to a new plate coated with 1 µg/cm^2 of Laminin-521 (BioLamina, Sundbyberg, Sweden) seven to ten days after pigmentation started. The cells were then maintained in RDM, consisting of 75% DMEM (Gibco), 25% F-12 (Gibco), and 2% B-27 supplement minus vitamin A (Gibco). The medium was replaced twice a week. RDM was supplemented with 10% FCS for two days and was then reduced to 2% FCS until confluent. Once confluent, RDM without FCS was used. iPSC-RPE were used for experiments three weeks after reaching confluency and having regained pigmentation.

iPSC-derived cortical astrocytes, spinal astrocytes, oligodendrocytes, and motor neurons were generated by Tuula Ritakari (The University of Edinburgh), Maria Stavrou (The University of Edinburgh), Leoli Telford-Cooke (The University of Edinburgh), and Arpan Mehta (The University of Edinburgh), respectively.

3.2.3 Immunocytochemistry

iPSC-RPE were washed with PBS and fixed with 4% PFA for 10 minutes. After another two washes with PBS the cells were permeabilised with 0.1% TritonX-100 (Sigma-Aldrich) for 15

minutes and subsequently blocked with 3% normal goat serum for 1 hour. Staining with the primary antibody was at 4 °C overnight. The cells were washed twice with PBS and subsequently stained with a secondary Alexa Fluor®-conjugated antibody for 30 minutes and counterstained with 5 µM DRAQ5™ (Abcam, Cambridge, UK) for 10 minutes. After another three washes with PBS, the cells were mounted in Fluorsave mounting medium (Merck Millipore) and imaged with a Leica DMi8 inverted microscope (Leica Microsystems). The antibodies and concentrations used are listed in Table S8.

3.2.4 Electric cell-substrate impedance sensing

Electric cell-substrate impedance sensing (ECIS) was performed as described before[215]. Briefly, iPSC-RPE were seeded onto ECIS® Cultureware 96-well plates (Applied BioPhysics Inc, Troy, NY) coated with 1 µg/cm^2 of Laminin-521. The ECIS plate with iPSC-RPE was placed in an array holder in a humidified incubator at 37 °C with 5% CO_2. iPSC-RPE were allowed to reach confluency and maturity as described above (see section 3.2.2) whilst impedance was being measured and recorded. Multiple frequency impedance measurements were recorded using an ECIS® Zθ instrument (Applied BioPhysics Inc) by Graham Anderson (The University of Edinburgh) and Dr Bagnaninchi (The University of Edinburgh).

3.2.5 Transepithelial electrical resistance measurements

The transepithelial electrical resistance (TEER) of confluent iPSC-RPE grown on transwell membranes with 0.4 µm pore size (Corning) coated with 1 µg/cm^2 of Laminin-521 in a 12-well plate was measured using an epithelial voltohmmeter (EVOM2; World Precision Instruments, Sarasota, USA) according to manufacturer's instruction and as previously described[216]. Briefly, the electrode was sterilised with 70% ethanol prior to measurement with the shorter end of the electrode submerged in the medium in the cell compartment and the longer end of the electrode submerged in the medium outside the cell compartment. The net TEER was calculated by subtracting the background resistance measurement obtained from wells containing just medium and then multiplying the difference by the area of the transwell membrane (1.12 cm^2) to obtain values in Ω*cm^2.

3.2.6 Phagocytosis assay

The phagocytosis assay was performed as described before[217], with some modifications. Bovine rod POS (InVision BioResources, Seattle, USA) were washed three times with and resuspended in wash solution, consisting of 10% sucrose, 20 mM sodium phosphate buffer pH 7.2, and 5 mM taurine. To obtain a 2 mg/ml working solution of fluorescein-5-Isothiocyanate (FITC), 10 mg of FITC (Invitrogen) was dissolved in 0.1 M sodium-carbonate buffer pH 9.5. To conjugate POS with FITC, 1.5 ml of FITC working solution was added to 5 ml of POS suspension and incubated at 21 °C for 1 hour whilst rotating in the dark. The POS-FITC conjugate was then washed twice with and resuspended in DMEM with 2.5% sucrose.

iPSC-RPE were seeded at $7.5*10^3$ cells/well in a 96-well plate and cultured for four weeks until mature and confluent. The iPSC-RPE were fed 50 POS-FITC/cell for 0.5, 1, 2, 3, or 4 hours. Phagocytosis was terminated by washing three times with PBS. The iPSC-RPE were then fixed with pre-warmed 4% PFA for 10 minutes and subsequently counterstained with 300 nM DAPI for 10 minutes. After three washes with PBS the cells were imaged with a Zeiss Axio Observer Z1 motorised inverted microscope with an automatic stage (Carl Zeiss Ltd.).

3.2.7 qPCR

iPSC-RPE cell lines were seeded at $3*10^5$ cells/well in a 6-well plate and allowed to reach confluence and to mature for four weeks. RNA was extracted using TRIzol® Reagent (Ambion, Waltham, MA) according to manufacturer's instructions. cDNA was made using the High Capacity cDNA Reverse Transcription Kit (Applied Biosystems, Foster City, CA) according to manufacturer's instructions and primers were designed by Primerdesign Ltd. (Southampton, UK), see Table S7 for sequences. DyNAmo ColorFlash SYBR Green kit (Thermo Scientific) was used in combination with a CFX96 Touch™ Real-Time PCR Detection System (Bio-Rad, Hercules, CA).

3.2.8 Denaturing and non-denaturing PAGE gels and western blotting

For denaturing gels, confluent mature iPSC-RPE were lysed in RIPA buffer supplemented with Complete Mini protease inhibitor cocktail (Sigma-Aldrich) and PhosSTOP phosphatase inhibitor (Roche, Basel, Switzerland) and passed through a 21-gauge needle (Sterican,

Hessen, Germany) to shear the DNA. For non-denaturing gels confluent mature iPSC-RPE were lysed in Native PAGE™ Sample Buffer (Invitrogen) with 10% DDM (Invitrogen) to solubilise the proteins. Conditioned medium containing the secreted C1QTNF5 protein was also taken from mature iPSC-RPE. Cell lysate concentration was determined with a *DC*™ Protein Assay (Bio-Rad) and conditioned medium protein concentration was determined with a Pierce™ BCA Protein Assay Kit (Thermo Scientific).

For denaturing gels, 20 µg of cell lysate or conditioned medium in Laemmli sample buffer (Bio-Rad) supplemented with 50 mM DTT was heated to 98 °C for 5 minutes and subsequently loaded and ran on a 12% SDS-PAGE gel. For non-denaturing gels, NativePAGE™ 5% G-250 Sample Additive (Invitrogen) was added just before loading the samples onto the gel. 20 µg of cell lysate or conditioned medium were then loaded and run on a NativePAGE™ 3-12% Bis-Tris Protein Gel (Invitrogen).

Gels were blotted onto a polyvinylidene difluoride (PVDF) membrane (Bio-Rad), blocked with TBS with 5% Marvel for 1 hour at room temperature, and incubated with 1:1,000 C1QTNF5 antibody (R&D Systems, Minneapolis, MN) overnight at 4 °C. The following day the membrane was incubated with 1:2,000 HRP-conjugated secondary antibody (Merck Millipore) for 30 minutes at room temperature. After incubation with Amersham ECL reagent (GE Healthcare, Little Chalfont, UK), an Amersham Hyperfilm (GE Healthcare) was exposed to the membrane. The same membrane was reprobed with 1:5,000 β-actin antibody (Abcam) for 1 hour at room temperature followed by 1:4,000 HRP-conjugated secondary antibody (Merck Millipore) for 30 minutes at room temperature to check for loading control. Exposed films were developed in a Mi-5 X-ray developer machine (Jet Xray, London, UK). The antibodies and concentrations used are listed in Table S9.

3.2.9 RNA-seq

For RNA sequencing (RNA-seq), total RNA was extracted from iPSC-RPE using TRIzol® reagent (Ambion) and the quality and quantity was assessed using RNA ScreenTape (Agilent) with a 2200 TapeStation system (Agilent). The RNA samples were sent to Edinburgh Genomics (Edinburgh, UK) for RNA library preparation and sequencing. Illumina mRNA-seq libraries were prepared from 1 µg of total RNA using TruSeq RNA Sample Prep Kit v2 (Illumina, Cambridge, UK) with a 10-cycle enrichment step according to manufacturer's protocol. Final

libraries were sequenced on a NovaSeq 6000 Sequencing System (Illumina) at a target depth of ~50 million read pairs per sample with 150 base paired-end reads.

Reads were mapped to the primary assembly of the human (hg38) reference genome contained in Ensembl release 92[218]. Alignment was performed with STAR (version 2.5.3a)[219]. Tables of per-gene read counts were generated from the mapped reads with featureCounts (version 1.5.2)[220]. Differential expression analysis was then performed using DESeq2 (R package version 1.18.1)[221]. Sample heatmaps and PCA plots were produced using variance-stabilized per-gene read counts. Gene ontology enrichment analysis was performed using topGO (R package version 2.30.1)[222] and gene set analysis with the "camera" function[223] from the R package "limma" (version 3.34.9). RNA-seq data analysis was performed by Dr Dando (The University of Edinburgh) and Prof Hardingham (The University of Edinburgh).

The list of differentially expressed genes (LORD4 versus LORD4 corrected) with an adjusted *p*-value of less than 0.05 was subjected to Ingenuity Pathway Analysis (IPA; build version 49309495; Qiagen)[224] against the Ingenuity Knowledge Base, considering only relationships where confidence was classified as "Experimentally Observed" and species was "Human". Canonical pathways enriched in the differentially expressed genes and the list of predicted upstream regulators was exported. Due to the high number of differentially expressed transcripts networks were only drawn for connected genes with a fragments per kilobase of transcript per million mapped reads (FPKM) of at least 10 and adjusted *p*-value of less than 0.01. For the network linking C1QTNF5 to differentially expressed genes ($p < 0.05$) the network was first grown using the Ingenuity Knowledge Base considering only relationships where confidence was classified as either "Experimentally Observed" or "High (predicted)" as there were no direct connections found between the differentially expressed genes and C1QTNF5. RNA-seq network analysis by IPA was performed by Dr James Longden (The University of Edinburgh).

3.2.10 Statistics

Experiments were repeated at least three times. Statistical analysis was performed using Microsoft Excel version 1905 and GraphPad Prism 6 software. Student's *t*-tests were used to determine statistical significance between groups. *P*-values of less than 0.05 were considered to be statistically significant.

3.3 Results

3.3.1 iPSC-RPE pigment and express RPE markers

In order to study the function of C1QTNF5 and its role in macular degeneration, iPSC lines from two patients harbouring the heterozygous *C1QTNF5*^{S163R} mutation, the corresponding isogenic gene-corrected lines (see Chapter 2), a healthy control line, and a C1QTNF5 KO line (see Chapter 2) were differentiated to RPE.

Differentiation of iPSCs to RPE was similar to a previously published protocol[164], but with some modifications (Fig. 3.3a). Briefly, bFGF was removed from the standard iPSC medium to initiate default differentiation towards neuroectoderm. The medium was replaced with PIM after two days. When neuroepithelial rosettes appeared, activin A was added to the medium until pigmentation started. Pigmented foci were mechanically dissected and transferred to a new plate for further enrichment in RDM.

The resulting iPSC-RPE had a typical RPE cobble stone-like morphology and were pigmented (Fig. 3.3b). The iPSC-RPE also expressed typical RPE markers, including MITF, ZO-1, BEST1, and CRALBP (Fig. 3.3c).

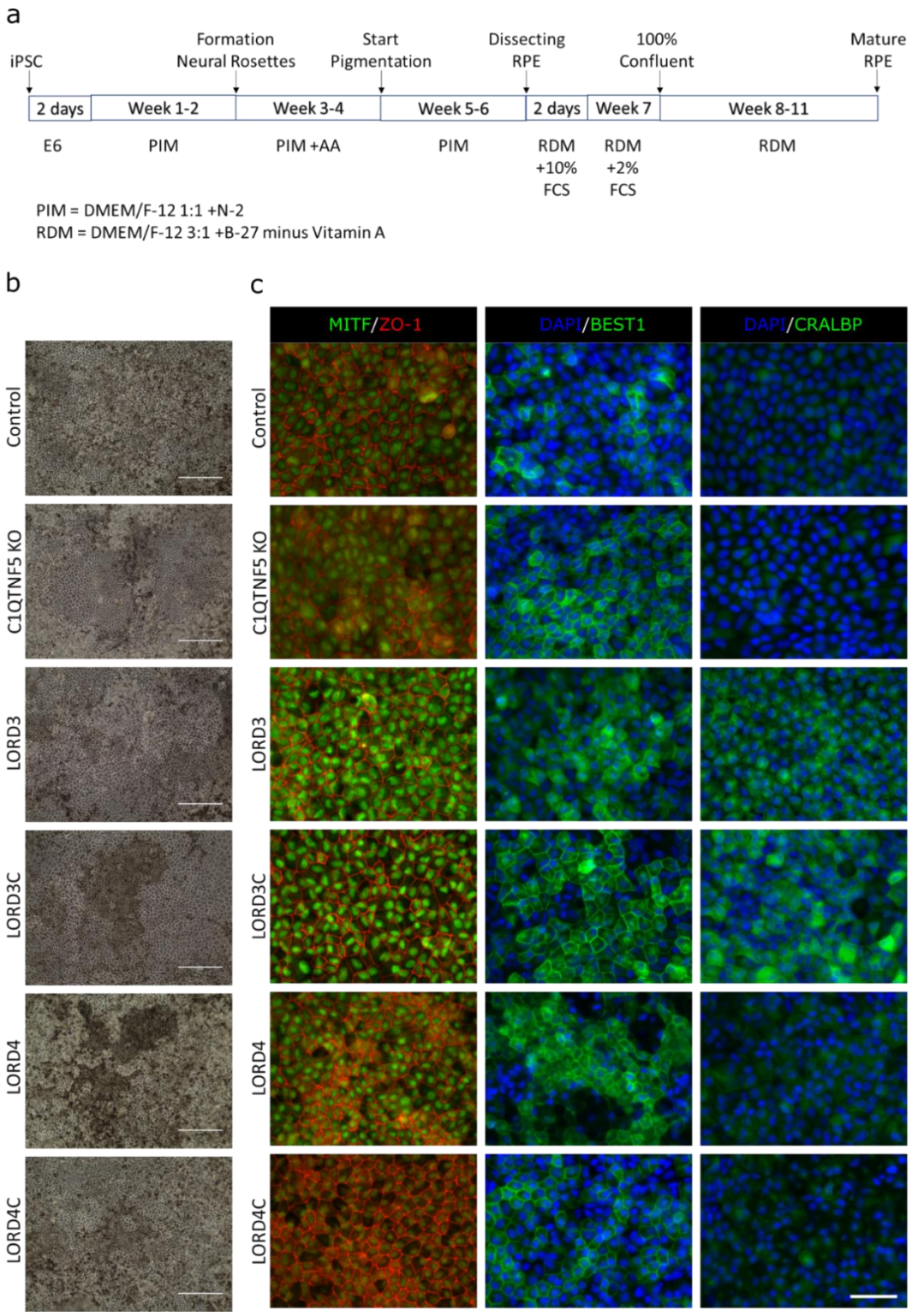

Figure 3.3 | iPSC-RPE lines pigment and express RPE markers. iPSC to RPE protocol (**a**). All iPSC-RPE lines showed pigmentation and cobble stone morphology (**b**). The iPSC-RPE lines also expressed the RPE markers MITF, ZO-1, BEST1, and CRALBP (**c**). Scale bars equal 200 µm (**b**) and 50 µm (**c**). PIM = pro-neural induction medium; RMD = retinal differentiation medium; AA = activin A; FCS = foetal calf serum.

3.3.2 ECIS and TEER

ECIS was employed to investigate if there was any difference in cell proliferation between wt and L-ORD iPSC-RPE during growth and maturation. With ECIS, a small non-invasive alternating current (1 μA) was applied to the cells using gold microelectrodes[225,226]. Electrical impedance increases as more cells attach and spread on the ECIS array microelectrodes[226]. L-ORD iPSC-RPE seemed to have a higher impedance on the ECIS array during the first 160 hours of growth and maturation compared to its isogenic gene-corrected control (Fig. 3.4a). However, the impedance was found to be similar after 160 hours of cell growth. This difference in impedance in the initial growth phase of the L-ORD iPSC-RPE could reflect a difference in cell proliferation or cell adhesion to the microelectrodes. Although this experiment has only been performed once, it is in line with previous findings showing a difference in impedance between L-ORD iPSC-RPE and a non-isogenic control line[215].

iPSC-RPE were grown on porous filter supports which allows nutrient supply to the basolateral side and therefore promotes epithelial differentiation closer to native epithelium[227,228]. TEER can be measured to analyse the epithelial barrier function which reflects the quality and functional polarity of epithelial cells grown on porous filter supports[229]. The TEER for the iPSC-RPE lines was similar to human foetal RPE and iPSC-RPE previously described, with a TEER over 150 $\Omega*cm^2$ (Fig. 3.4b), the proposed functional threshold[164,216,230]. This indicates that the iPSC-RPE generated have a normal epithelial barrier function.

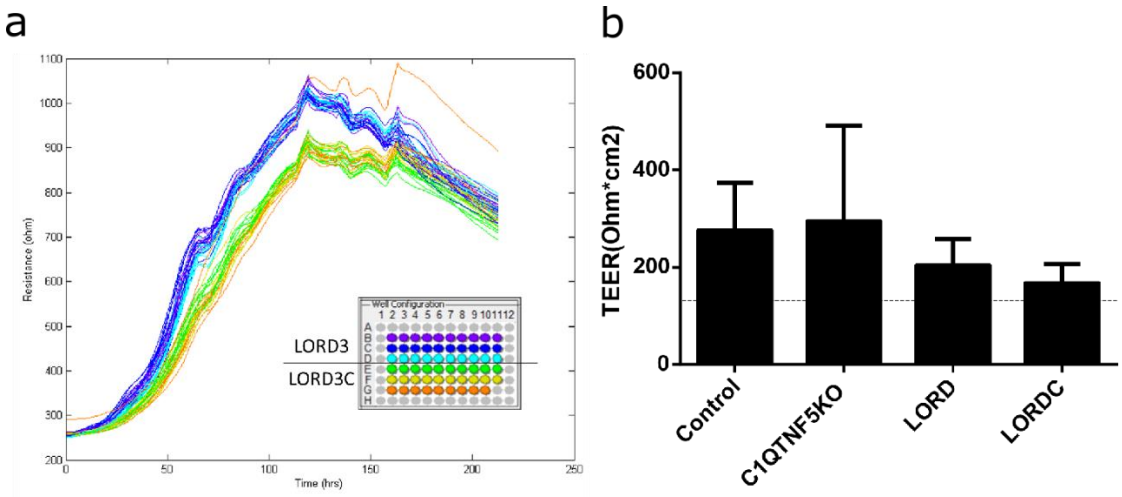

Figure 3.4 | ECIS and TEER measurements of iPSC-RPE lines. ECIS (**a**) and TEER (**b**) was measured of control, C1QTNF5 KO, LORD, and LORDC iPSC-RPE grown on ECIS arrays and transwell membranes respectively. Dotted line demarcates proposed functional threshold. Error bars represent standard deviation (SD) of at least six independent experiments.

3.3.3 Phagocytosis

An important function of RPE is to phagocytose POS. iPSC-RPE were therefore tested for their capability to phagocytose POS. All lines used were able to phagocytose POS (Fig. 3.5). However, when normalised for the total number of cells, C1QTNF5 KO iPSC-RPE phagocytosed relatively more POS than their isogenic control (Fig. 3.5b). Moreover, also L-ORD iPSC-RPE phagocytose more POS compared to their isogenic gene-corrected control (Fig. 3.5a and b).

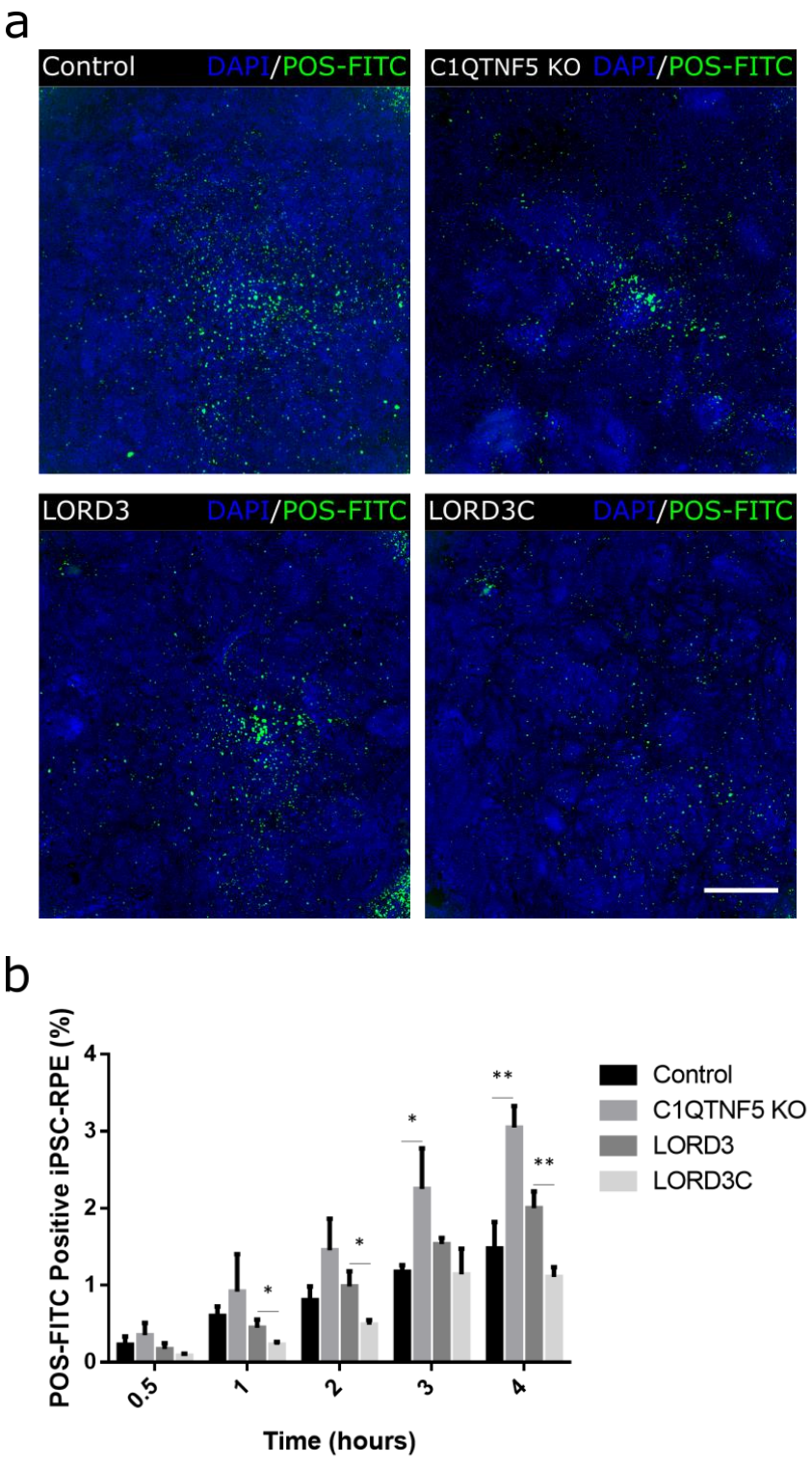

Figure 3.5 | C1QTNF5 KO and L-ORD iPSC-RPE phagocytose more POS. Control, C1QTNF5 KO, LORD3, and LORD3C iPSC-RPE were fed with 50 POS-FITC/cell for 0.5, 1, 2, 3, or 4 hours. After washing and fixation the iPSC-RPE were imaged (**a**). POS-FITC was quantified and divided by cell count (**b**). Scale bar equals 200 µm. Error bars represent SD of at least three independent experiments. **P*<0.05 and ***P*<0.005, determined by *t*-test compared to respective isogenic control line.

3.3.4 iPSC-RPE express C1QTNF5

All iPSC-RPE lines were found to express *C1QTNF5* mRNA (Fig. 3.6). C1QTNF5 KO iPSC-RPE expressed significantly less *C1QTNF5* mRNA, most likely due to nonsense-mediated decay caused by the premature in-frame stop codon.

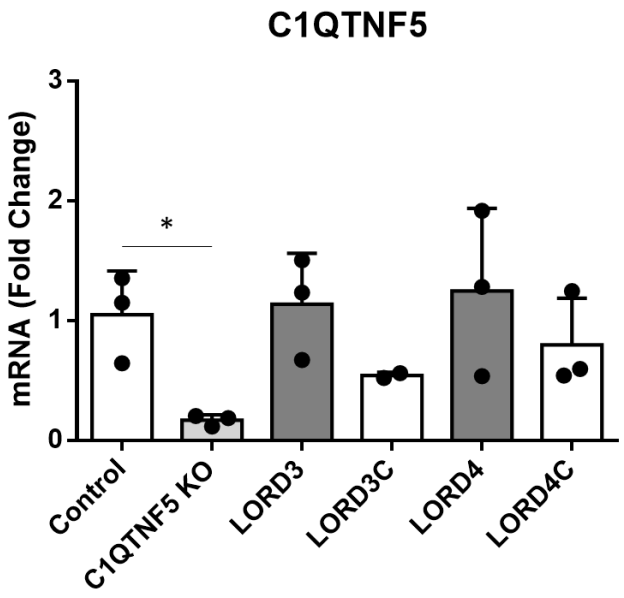

Figure 3.6 | C1QTNF5 mRNA expression in iPSC-RPE lines. Control, C1QTNF5 KO, LORD3, LORD3C, LORD4, and LORD4C iPSC-RPE all express *C1QTNF5* mRNA. C1QTNF5 KO iPSC-RPE express significantly less *C1QTNF5* mRNA. Error bars represent SD of at least three independent experiments. **P*<0.05, determined by *t*-test on ΔCT compared to isogenic control line.

Similarly, C1QTNF5 protein was expressed in all iPSC-RPE lines, except in the C1QTNF5 KO line, and was also found secreted into the medium (Fig. 3.7a). C1QTNF5 was found to be expressed both on the apical and basal side of C1QTNF5-expressing iPSC-RPE when grown on transwell membranes (Fig. 3.7b). Under native physiological conditions, C1QTNF5 multimerises into an octadecamer high molecular weight (HMW) structure and the C1QTNF5^{S163R} mutant is known to destabilise this structure[165,195]. To investigate if the gene correction corrects the HMW C1QTNF5 structure, cell lysates of the iPSC-RPE lines were run on a native PAGE gel. L-ORD iPSC-RPE expressed less HMW C1QTNF5 and especially more trimer C1QTNF5 under native conditions, which was corrected in their respective gene edited isogenic controls (Fig. 3.7c). This indicates that the gene correction of *C1QTNF5^{S163R}* does correct the quaternary structure of the protein.

C1QTNF5 is also known to be expressed in the brain[169]. To investigate which type of cells in the brain express C1QTNF5, cell lysates of iPSC-derived cortical and spinal astrocytes,

oligodendrocytes, and motor neurons were analysed. C1QTNF5 was found to be expressed in cortical astrocytes and oligodendrocytes, albeit in smaller quantities than in RPE (Fig. 3.7d). This indicates that C1QTNF5 also has a function in these cell types.

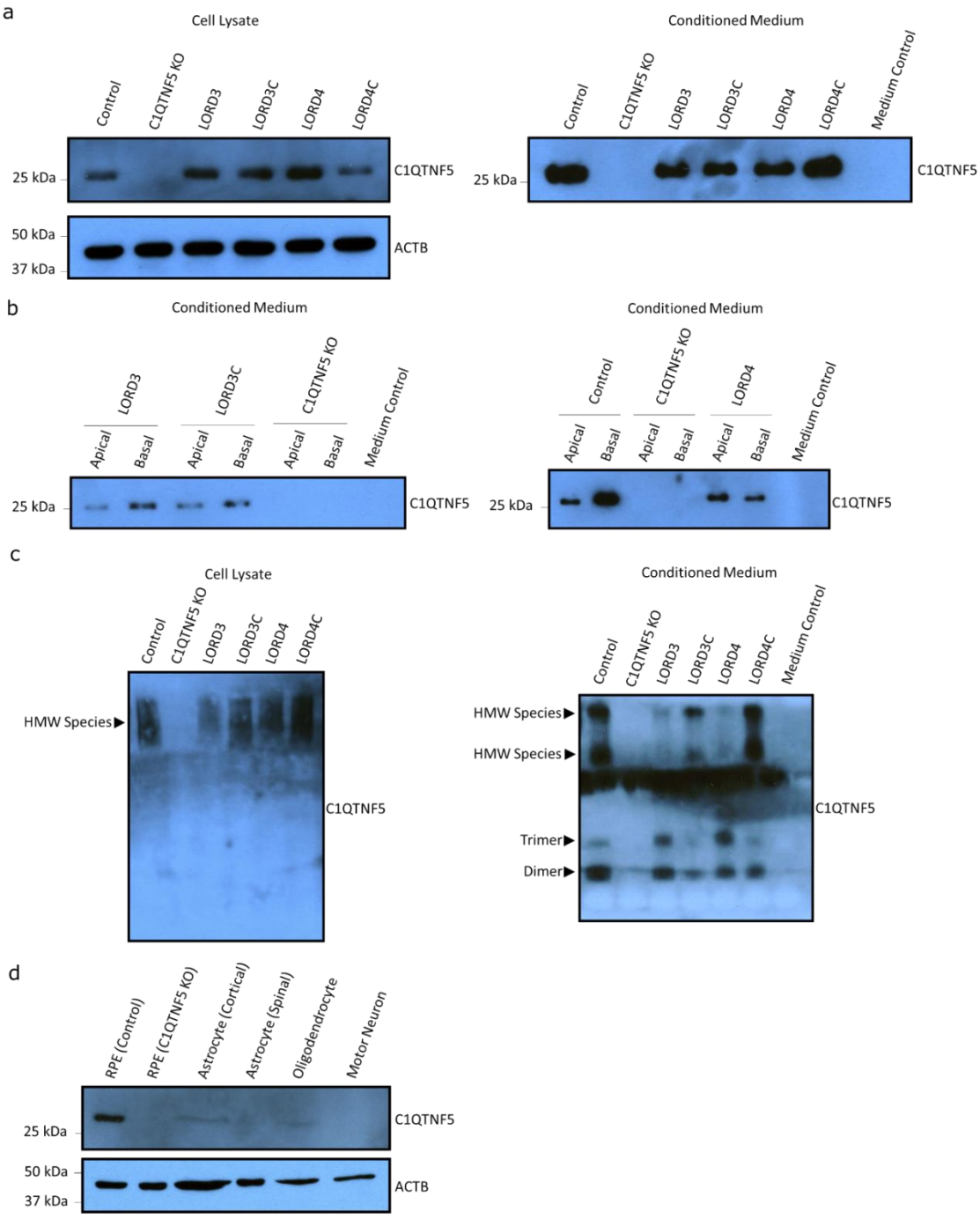

Figure 3.7 | iPSC-RPE express C1QTNF5 protein and L-ORD iPSC-RPE express less HMW C1QTNF5. iPSC-RPE express and secrete C1QTNF5 into the medium, as shown on a denaturing gel (**a**). All iPSC-

RPE lines, except for C1QTNF5 KO, secrete C1QTNF5 both on the apical and basal side when grown on transwell membranes, as shown on a denaturing gel (**b**). L-ORD iPSC-RPE lines express less HMW C1QTNF5 in both cell lysate and in medium, as shown on a non-denaturing gel (**c**). C1QTNF5 was also found to be expressed in iPSC-cortical astrocytes, iPSC-oligodendrocytes, and iPSC-motor neurons, as shown on a denaturing gel (**d**). HMW = high molecular weight.

3.3.5 RNA-seq of L-ORD iPSC-RPE

The transcriptome of the LORD4 iPSC-RPE line was compared to its isogenic gene-corrected control LORD4C iPSC-RPE line using RNA-seq on three biological repeats of each. Hierarchical clustering and heat map analysis showed segregation between most LORD4 and LORD4C iPSC-RPE biological repeats (Fig. 3.8a). Principal component analysis shows the variance among the gene-corrected controls and the mutants and between these two groups (Fig. 3.8b). Although PCA does not show clear grouping of the biological replicates, due to the variability between the biological replicates, numerous significantly differentially expressed genes were still found between the mutant iPSC-RPE biological replicates and their isogenic gene-corrected control biological replicates. In LORD4 iPSC-RPE 203 genes were found to be significantly upregulated and 342 genes downregulated compared to its isogenic gene-corrected control (Fig. 3.8c and Table S10).

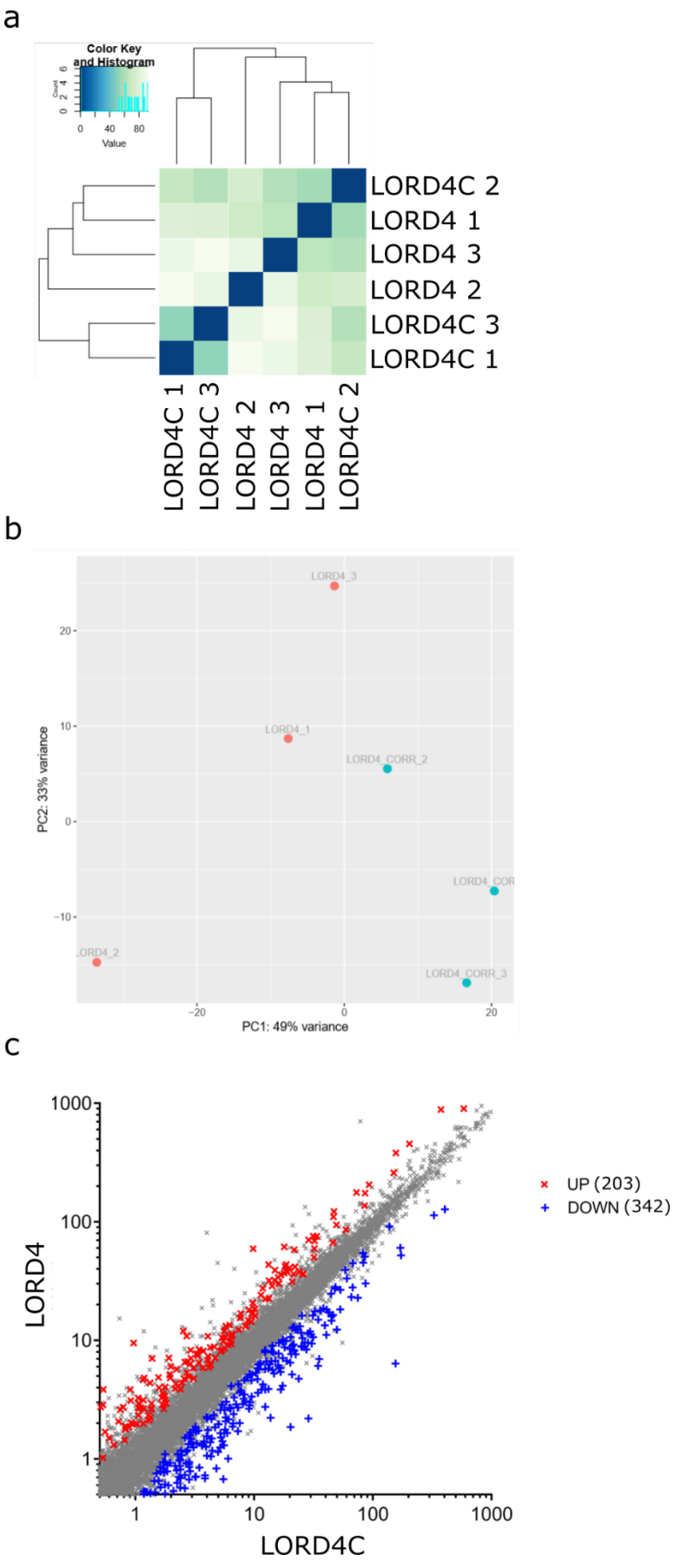

Figure 3.8 | RNA-seq analysis of L-ORD iPSC-RPE. Heat map and dendrogram depicting hierarchical clustering of RNA-seq reads from L-ORD iPSC-RPE line LORD4 and its isogenic corrected control LORD4C (**a**). PCA plot depicting the variance in transcription profile between the iPSC-RPE lines and biological replicates (**b**). Scatter plot showing transcriptome reads of LORD4 compared to LORD4C. Red crosses denote significantly upregulated genes and blue crosses denote significantly downregulated genes (P<0.05, analysis performed using DESeq2) (**c**).

Out of the 545 significantly differentially expressed genes (Table S10), several genes were found in literature to be involved in RPE functioning related to macular degeneration (Table 3.1).

Table 3.1 | RNA-seq Gene Ontology enrichment analysis – genes.

a. Gene Ontology enrichment LORD4 upregulated genes

Gene	Average FPKM LORD4	Average FPKM LORD4C	Log2 Fold Change	*p*-value
PLIN4	3.2753	1.0561	1.3987	5.86E-05
CAT	27.5871	11.8302	1.1229	2.22E-04
COL8A1	175.0595	86.0702	1.0040	7.88E-04
SULF1	177.2071	72.8288	1.1408	0.0010
CD55	9.9747	6.3601	0.6683	0.0063
MYRIP	38.6003	18.7759	0.9516	0.0092
ADAMTSL1	2.7051	1.1107	1.0004	0.0100
PTGDS	122.3596	47.1128	1.0844	0.0163
TIMP3	903.7854	583.5120	0.6459	0.0179
PLAG1	2.1174	1.3035	0.7152	0.0200
SLC6A20	94.5036	49.2990	0.8831	0.0207
C1QTNF1	8.5826	5.6379	0.6261	0.0342
MMP17	3.5626	1.6971	0.9069	0.0356
SGK3	11.3845	6.4815	0.7874	0.0382
NAV3	7.3550	4.0755	0.8122	0.0400
PLIN2	35.7211	16.8457	0.9027	0.0470
HMGCS2	4.6424	1.1531	1.0859	0.0481

b. Gene Ontology enrichment LORD4 downregulated genes

Gene	Average FPKM LORD4	Average FPKM LORD4C	Log2 Fold Change	*p*-value
ADAMTS16	27.9936	67.5930	-1.0924	2.82E-07
LINC00461	0.5997	1.8959	-1.4268	9.45E-07
ADAMTS18	0.6287	2.2417	-1.3336	3.02E-05
ANO4	0.9417	2.8428	-1.1219	0.0050
SLC6A15	27.3346	47.8335	-0.6978	0.0055
GPM6B	9.8805	18.6140	-0.7383	0.0177
MMP11	9.8984	18.5679	-0.7388	0.0251
CFI	0.1006	0.4898	-1.1668	0.0271
CCL2	16.3755	46.3386	-1.0169	0.0298
DDR1	54.6464	82.4894	-0.5002	0.0473

Using the Gene Ontology (GO) enrichment database, significantly differentially expressed genes between L-ORD iPSC-RPE and its isogenic gene-corrected control were found to differentially regulate several cellular pathways. GO gene set analysis was performed revealing changed cellular pathways between L-ORD iPSC-RPE and its isogenic gene-corrected control by looking at genes that individually may not be significantly differentially expressed but as part of a gene set or pathway have a coherent shift in expression. Upregulated gene sets in L-ORD iPSC-RPE were found to have a function in the ECM, lipid metabolism, and cell death (Table 3.2a). In L-ORD iPSC-RPE downregulated genes were found to be involved in the ECM and calcium regulation (Table 3.2b).

Table 3.2 | RNA-seq Gene Ontology enrichment analysis – gene sets.

a. Gene Ontology enrichment LORD4 upregulated pathways

Notable GO terms	# of genes	*p*-value
Basement membrane	7	0.00091
Sterol metabolic process	5	0.00862
Adipose tissue development	3	0.0091
Extracellular space	60	0.01044
Regulation of CAMKK-AMPK signaling cascade	1	0.01201
Regulation of programmed cell death	15	0.01222

b. Gene Ontology enrichment LORD4 downregulated pathways

Notable GO terms	# of genes	*p*-value
Extracellular space	81	0.000012
Extracellular matrix organization	18	0.00019
Cell surface	28	0.00034
Cellular response to calcium ion	5	0.00357
Extracellular region	115	0.00718
Calcium ion binding	20	0.01151

Analysis of the cellular upstream regulator network, by using IPA, revealed the transcriptional regulators and other important pathway regulators that control the differentially expressed genes between L-ORD iPSC-RPE and its isogenic gene-corrected control (Table S11). The *p*-value of overlap measures whether there is a statistically significant overlap between the significantly differentially expressed genes and all genes that could be regulated by the upstream regulator of interest.

Network analysis, by using IPA, of the differentially expressed genes between L-ORD iPSC-RPE and its isogenic gene-corrected control also revealed the variety of canonical pathways

affected (Fig. S3). In order to reveal the most affected pathways, a subset of significantly differentially expressed genes was created with a FPKM of at least 10 in all biological repeats and an adjusted *p*-value of less than 0.01. This revealed two highly connected networks: a network enriched with genes associated with cellular metabolism (Fig. 3.9a) and a network enriched with genes associated with cell migration, development, and cell death and survival (Fig. 3.9b).

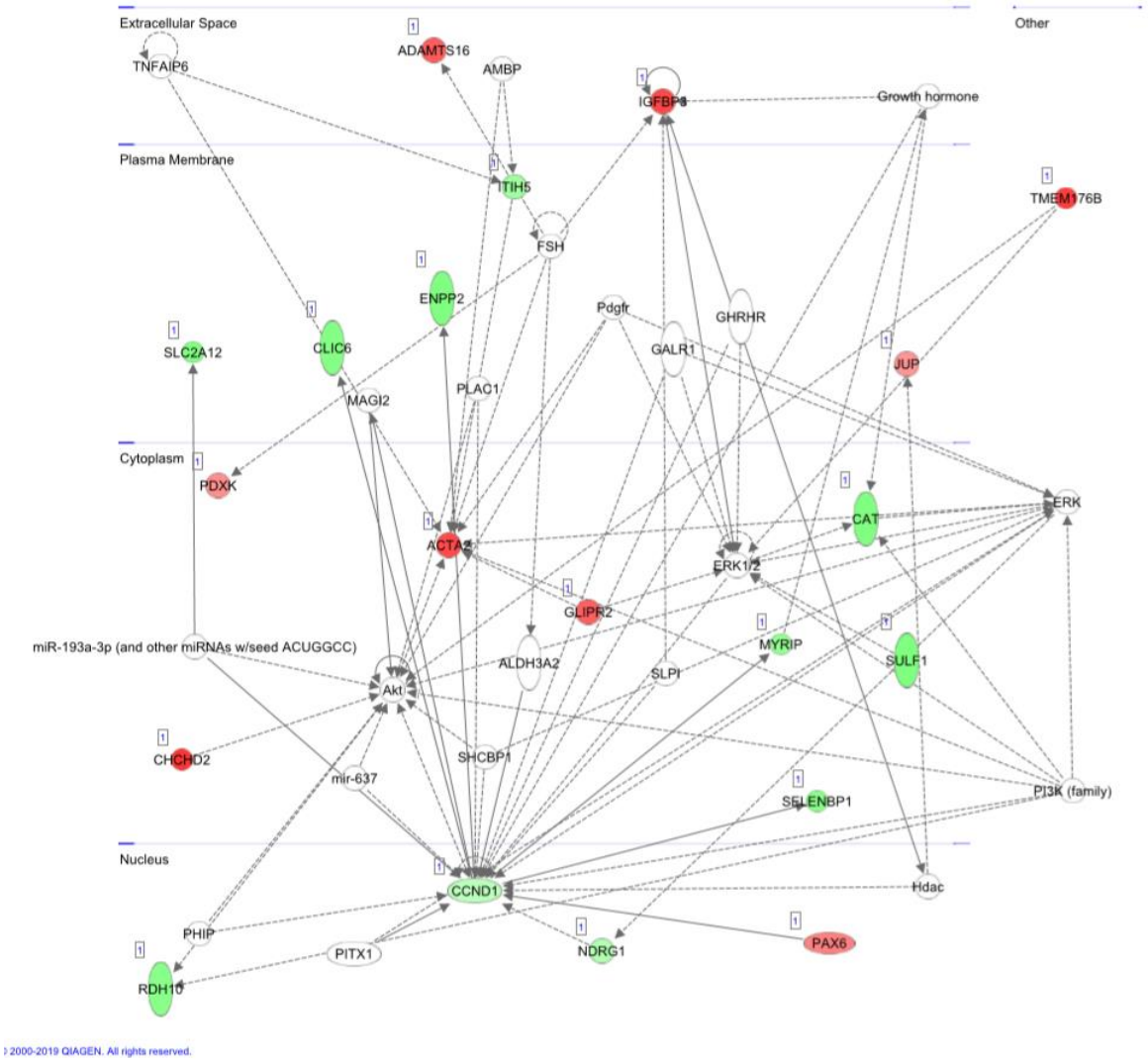

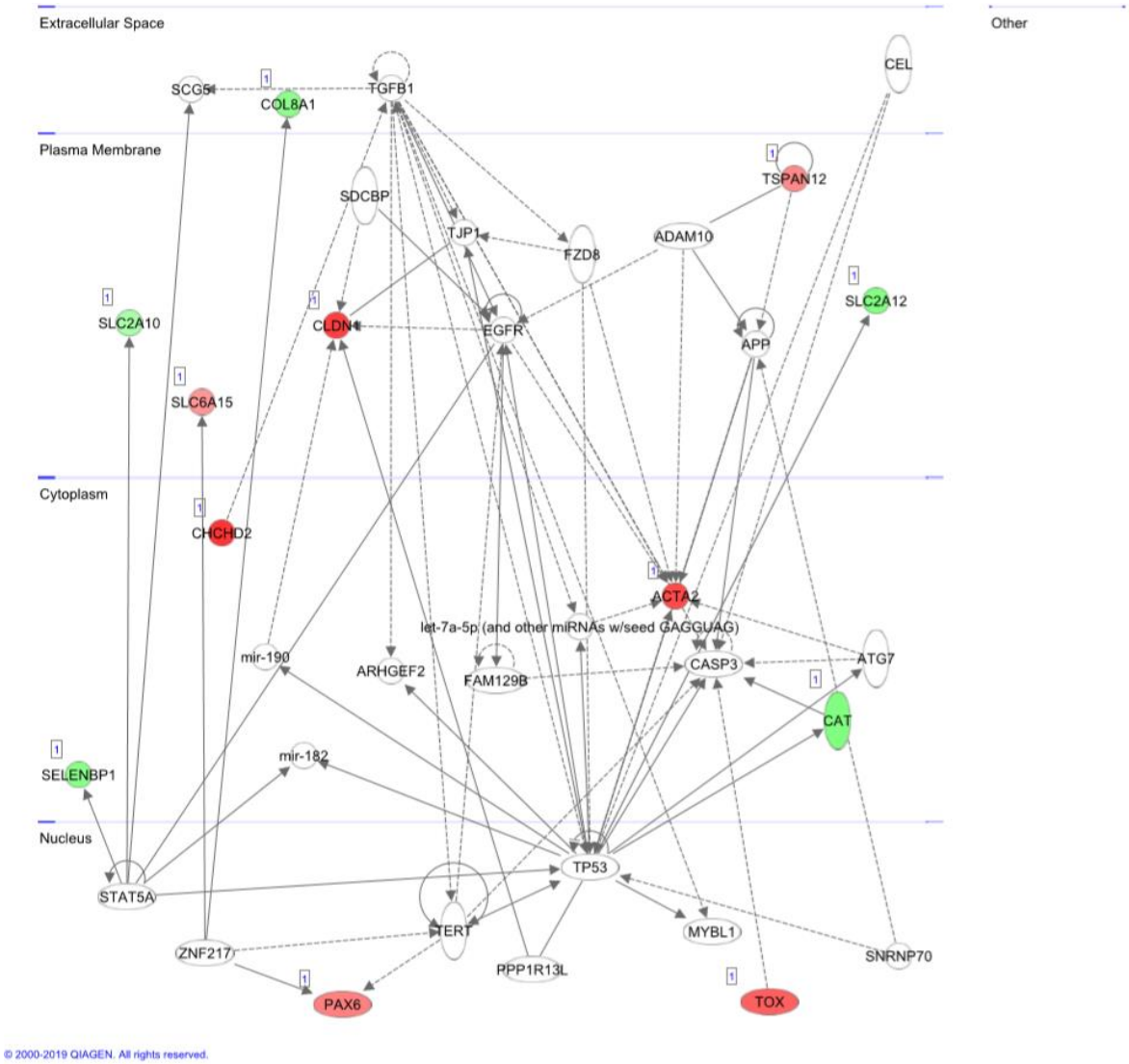

Figure 3.9 | RNA-seq Ingenuity Pathway Analysis – highly connected pathways differentially regulated in LORD4 and LORD4C. A subset of significantly differentially expressed genes between L-ORD iPSC-RPE and its isogenic gene-corrected control was created with at least 10 FPKM in all biological repeats and an adjusted *p*-value of less than 0.01. This revealed two highly connected networks: a network enriched with genes associated with cellular metabolism (**a**) and a network enriched with genes associated with cell migration, development, and cell death and survival (**b**). Green shows upregulated and red shows downregulated significantly differentially expressed genes between LORD4 and LORD4C. White genes are predicted by IPA to be present in the network. Transcriptional regulators are indicated by a horizontal oval, receptors/enzymes/ion channels are indicated by a vertical oval, and all other genes were circles.

Next, it was investigated how C1QTNF5 could contribute to the differences in gene expression between L-ORD iPSC-RPE and its isogenic gene-corrected control. Based on IPA, C1QTNF5 does not seem to directly regulate any of the significantly differentially expressed

genes (Fig. 3.10). However, some miRNAs are predicted to regulate both C1QTNF5 as well as some of the significantly differentially expressed genes.

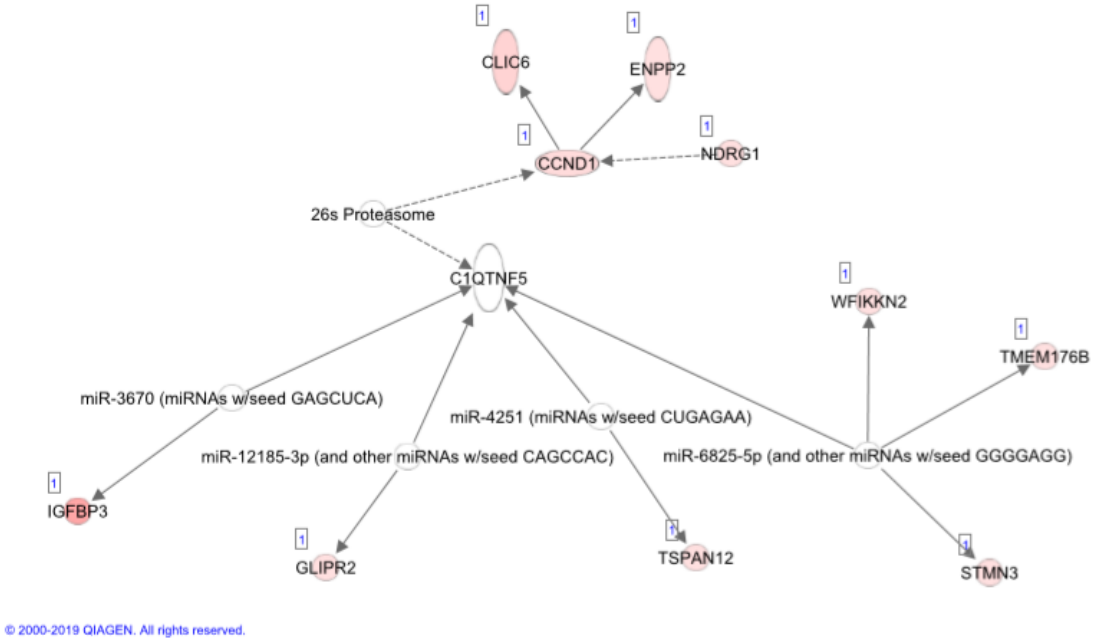

Figure 3.10 | RNA-seq Ingenuity Pathway Analysis – C1QTNF5 network. A network depicting C1QTNF5 and how it relates to some of the significantly differentially expressed genes between L-ORD iPSC-RPE and its isogenic gene-corrected control. Green shows upregulated and red shows downregulated significantly differentially expressed genes between LORD4 and LORD4C. White genes are predicted by IPA to be present in the network. Transcriptional regulators are indicated by a horizontal oval, receptors/enzymes/ion channels are indicated by a vertical oval, and all other genes were circles.

3.4 Discussion

RPE generated from patient-derived stem cells are a valuable model system to study genetic diseases affecting the RPE. Here, I showed relatively fast and efficient generation of RPE from L-ORD patient-derived iPSCs and other iPSC lines. L-ORD iPSC-RPE showed differences in adherence to substrate, phagocytosis capability, C1QTNF5 protein structure, and gene expression, compared to its isogenic gene-corrected control. In addition, C1QTNF5 KO iPSC-RPE also showed a difference in phagocytosis capability.

iPSC-RPE were found to have a typical RPE morphology, including pigmentation, and expressed RPE markers (Fig. 3.3). Furthermore, iPSC-RPE also showed functional similarities to RPE, including having RPE-like TEER (Fig. 3.4b) and the capability to phagocytose POS (Fig. 3.5). Therefore, iPSC-RPE resemble RPE in morphology and function.

ECIS of iPSC-RPE revealed that L-ORD iPSC-RPE had a higher impedance during growth and maturation compared to its isogenic gene-corrected control (Fig. 3.4a). The higher impedance measured could reflect a difference in cell proliferation or cell adherence of the L-ORD iPSC-RPE to the ECIS microelectrodes. Although this was performed only once, the impedance measurements show a similar trend as what has been found before between a L-ORD iPSC-RPE line and a non-isogenic iPSC-RPE control line[215]. Furthermore, it was suggested that the increased impedance initially measured, primarily reflected that the L-ORD iPSC-RPE spread and adhered more readily to the ECIS microelectrodes than the wt iPSC-RPE as the cells were seeded at confluence[215]. It is possible that the similar higher initial impedance measured in L-ORD iPSC-PRE and its isogenic gene-corrected control also reflects adherence differences rather than proliferation differences. In addition, one of the cellular pathways most affected in L-ORD iPSC-RPE is involved in cell migration (Fig. 3.9b). Moreover, the second most significant predicted upstream regulator of the differentially expressed genes in L-ORD iPSC-RPE, PDLIM2, regulates cell adhesion and migration (Table S11). Additional experiments will need to confirm the adherence and migration differences in L-ORD iPSC-RPE. It was previously suggested that C1QTNF5^{S163R} could lead to abnormal adhesion of RPE to the Bruch's membrane because of its structural similarities with collagens[80]. However, it was found that HEK 293 EBNA cells stably transfected with either His-tagged wt C1QTNF5 or C1QTNF5^{S163R} adhered less to laminin-coated plates when transfected with the latter[199]. It is possible that the cell line used is unable to properly fold C1QTNF5^{S163R}. It is also possible that

the His-tag prevents proper folding of the protein or the protein adherence function. In addition, the His-tag could also possibly influence the assembly of C1QTNF5 into multimeric structures, influencing the adherence properties of C1QTNF5.

L-ORD iPSC-RPE phagocytosed more POS (Fig. 3.5), similar to what has been found before (PhD thesis, Dr Borooah, The University of Edinburgh). Gene correction of *C1QTNF5* reduced the amount of POS phagocytosed. Interestingly, C1QTNF5 KO iPSC-RPE also phagocytosed more POS compared to its isogenic control line. C1QTNF5 could therefore have a function in regulating phagocytosis. Altered phagocytosis in L-ORD RPE could influence the photoreceptors. Slightly increased phagocytosis could damage rod photoreceptors over the years and possibly cause the delayed dark adaptation in patients.

C1QTNF5 was found to be expressed and secreted in equal amounts in both L-ORD and control iPSC-RPE (Fig. 3.7a). In contrast, it has been shown previously that C1QTNF5^{S163R} is strongly reduced in expression and secretion in a *C1QTNF5*^{S163R}-transfected cell lines[165,193,199]. L-ORD and control iPSC-RPE also both secreted C1QTNF5 in equal amounts both apically and basally (Fig. 3.7b). In contrast, it was previously found that C1QTNF5^{S163R} was preferentially basolaterally secreted in *C1QTNF5*^{S163R}-transfected mouse RPE[231] and the human hTERT RPE-1 cell line[165]. These differences in protein expression and secretion could be due to the difference between the iPSC-RPE used in this study and cell lines used in the previous studies. Another explanation could be that the polyclonal antibody used in this study recognises more C1QTNF5 epitopes than the monoclonal antibody for C1QTNF5 or tagged C1QTNF5 used in the previous studies. Furthermore, C1QTNF5 was tagged in these studies, which could influence proper folding of the protein and the assembly into multimeric structures.

The destabilisation of the C1QTNF5 multimeric structure in L-ORD iPSC-RPE was similar as what has been predicted before *in silico* and has been found before in a hTERT RPE-1 C1QTNF5-transfected cell line[165]. L-ORD iPSC-RPE showed a marked reduction in HMW C1QTNF5 oligomers caused by C1QTNF5^{S163R} (Fig. 3.7c). Furthermore, there was a notable increase in C1QTNF5 trimers in L-ORD iPSC-RPE. This could indicate that wt C1QTNF5 and C1QTNF5^{S163R} were still able to oligomerise with the collagen domain to form trimers, but assembly of the HMW octadecamer structure seems to be impaired by the p.S163R mutation in the gC1q domain. The octadecamer is predicted to be the functional unit of C1QTNF5[195] and therefore the destabilisation of the octadecamer by C1QTNF5^{S163R} could affect the function of C1QTNF5.

C1QTNF5 was also found to be expressed in iPSC-derived cortical astrocytes and oligodendrocytes, but not in spinal astrocytes and motor neurons (Fig. 3.7d). Interestingly, of these cell types found in the brain, astrocytes and oligodendrocytes can also be found in the eye. Oligodendrocytes are also part of the optic nerve. Retinal astrocytes mature from astrocyte progenitor cells and immature astrocytes that migrate into the neural retina from the optic disc[232]. C1QTNF5 could have a similar function in cortical astrocytes and oligodendrocytes as in RPE. Moreover, the C1QTNF5^{S163R} mutation could possibly also affect these cell types.

Retinal astrocytes and Müller glia are the macroglia of the retina[8]. Macroglia provide metabolic and functional support, protect from oxidative stress, and maintain a homeostatic environment for retinal neurons. In the retina, astrocytes are essential for the development of retinal vasculature through angiogenesis[233]. In the brain, astrocytes are an important source of inflammatory chemokines[234] and likely also in the retina. Astrocytes can become activated, called reactive astrogliosis, which can be triggered by injury. In AMD human retinal tissue, hypertrophic astrocytes were found to have phagocytosed RGCs, and astrocytes were found to pass through the inner limiting membrane and form a glial membrane in the vitreous humour of the eye together with Müller glia[235]. Like Müller glia, reactive astrogliosis can contribute to angiogenesis and CNV by increased expression of VEGF[236]. Astrocytes are also known to express various complement system proteins[8,237] and express C5a receptor[238]. Therefore, retinal astrocytes play an important role in AMD pathology and possibly also in L-ORD. Expression of C1QTNF5^{S163R} by retinal astrocytes possibly affects their function which could contribute to the L-ORD phenotype.

The RNA-seq data revealed that the iPSC-RPE expressed all the 154 RPE signature genes[239] and most of them at relatively high levels. Nine out of 154 signature genes were found to be differentially expressed between the L-ORD iPSC-RPE and its isogenic gene-corrected control (Table 3.1). *GPM6B* has been associated with X-linked retinitis pigmentosa[239]. *MYRIP* is involved in melanosome transport[239]. SNPs in *NAV3* and *SLC6A20* have been associated with AMD as well as a SNP in *NAV3* is associated with dominant cavitary optic disc anomalies and a SNP in *SLC6A20* is associated with dominant hereditary vascular retinopathy[239]. *PTGDS* is a melanocyte marker[239]. The other four genes *PLAG1*, *SGK3*, *SLC6A15*, and *SULF1* have no known function in RPE yet.

Some genes typically associated with AMD were also found to be differentially expressed in L-ORD iPSC-RPE. SNPs near *COL8A1* and *DDR1* have been associated with AMD[58] and these genes were found to be respectively significantly upregulated and downregulated in L-ORD iPSC-RPE (Table 3.1). However, their role in AMD pathology is still unclear.

GO gene set enrichment analysis and IPA of the RNA-seq data revealed various significant ECM (Table 3.2) as well as cell migration (Fig. 3.9b and Table S11) changes respectively in L-ORD iPSC-RPE compared to its isogenic gene-corrected control. This is consistent with the ECIS recordings that show that L-ORD iPSC-RPE possibly adhere differently to the substrate compared to its isogenic gene-corrected control (Fig. 3.4a). Several ECM remodelling proteins in particular were found to be significantly differentially expressed in L-ORD iPSC-RPE. It is therefore possible that C1QTNF5^{S163R} causes changes in the ECM that change the adhesion properties of RPE.

In particular, several MMP and MMP regulating proteins were found to be significantly differentially expressed in L-ORD iPSC-RPE (Table 3.1 and Fig. S3). MMPs play an important role in ECM remodelling (see Chapter 1). *TIMP3* and *MMP17* were significantly upregulated and *ADAMTS18* and *MMP11* were significantly downregulated in expression in L-ORD iPSC-RPE (Table 3.1). Mutations in *TIMP3* can cause SFD, a disease rather similar to L-ORD (see Chapter 1), whilst a mutation in *ADAMTS18* can cause autosomal recessive early onset severe retinal dystrophy[92]. ADAMTS18 is an MMP like MMP11 and MMP17, and TIMP3 is an MMP inhibitor. ADAMTS16 was also found to be significantly downregulated like ADAMTS18 (Table 3.1b). ADAMTS16 is not well characterised yet but is structurally very similar to ADAMTS18[240]. ADAMTS-like (ADAMTSL) proteins are thought to regulate ADAMTS function[240]. ADAMTSL1 was also found to be significantly upregulated in L-ORD iPSC-RPE (Table 3.1a). It is thought that dysregulated MMP pathways are the cause of deposit formation in AMD[241]. MMP9, when mutated, was found to have an important role in the development of AMD[242]. It is therefore possible that the different expression of MMPs and MMP regulators found in L-ORD iPSC-RPE contribute to the L-ORD phenotype in a similar manner as in AMD.

A recent genome-wide association study identified several loci associated with macular thickness[243]. Of the genes most significantly associated with macular thickness, *LINC00461* was found to be significantly downregulated and *SLC6A20* significantly upregulated in expression in L-ORD iPSC-RPE (Table 3.1). However, the mechanism of how these genes affect

macular thickness is not yet known. Nonetheless, these genes could possibly explain the changes in macular thickness found in L-ORD.

The genes *PLIN2* and *PLIN4* were both found to be significantly upregulated in L-ORD iPSC-RPE in the RNA-seq data (Table 3.1a). *PLIN2* encodes for adipose differentiation-related protein (ADRP). ADRP is a structural component of retinyl ester storage structures, specialised lipid droplets (LDs) in RPE that are also called retinosomes[244]. *PLIN2* expression is upregulated in RPE fed with PUFAs, including DHA[245]. PLIN4 is thought to be important for the stabilisation of LDs[246]. LDs function as neutral lipid stores. LDs are also mobilised during autophagy to support autophagic membrane formation[247]. Mice with *Plin2* exon 2 and 3 deleted were found to have aberrant trafficking of all-*trans*-retinyl esters in RPE caused by abnormal maintenance of retinosomes in the dark-adapted state[248]. Moreover, the mice were found to have delayed dark adaptation. Patients with L-ORD also have a delayed dark adaptation. It is possible that the increased expression of *PLIN2* results in abnormal retinosomes, followed by aberrant trafficking of all-*trans*-retinyl esters in L-ORD RPE, and resulting in delayed dark adaptation in L-ORD patients. Increased formation of LDs caused by overexpression of *PLIN4* can result in lipotoxicity and subsequent neurodegeneration in Parkinson's disease[249]. Increased *PLIN4* expression in L-ORD RPE could possibly also contribute to RPE degeneration through lipotoxicity. Altered expression of PLINs, increased phagocytosis, and dysregulated lipid metabolism (see below) could all contribute to altered delay adaptation in patients with L-ORD.

GO gene set enrichment analysis of the RNA-seq data revealed lipid metabolism changes and changes to the AMPK signalling pathway in L-ORD iPSC-RPE compared to its isogenic gene-corrected control (Table 3.2a). Furthermore, IPA of the RNA-seq data revealed metabolic changes between L-ORD iPSC-RPE compared to its isogenic gene-corrected control (Fig. 3.9a) and that AMPK is an important upstream regulator of some of the significantly differentially expressed genes (Table S11). The expression of *C1QTNF1* and *HMGCS2* were significantly upregulated in L-ORD iPSC-RPE (Table 3.1a). Both genes are involved in lipid metabolism. C1QTNF1 increases β-oxidation of fatty acids through AMPK pathway activation[176]. RPE can catabolise saturated fatty acids through β-oxidation[250]. In addition, RPE were found to be able to use fatty acids to produce ketone bodies, like the liver[251]. β-oxidation generates acetyl-CoA which subsequently enters the tricarboxylic acid (TCA) cycle, but a fraction is used in the ketogenic pathway which ultimately produces β-hydroxybutyrate (β-HB). β-HB is a

ketone body that effectively functions as an energy storage unit that can be metabolised at a later time point. RPE were found to produce and secrete β-HB apically through ketogenesis of palmitate[251]. β-HB could therefore possibly be used by the retina as a substrate for oxidative metabolism. The rate of β-HB production is dependent on HMGCS2 expression and activity. It is therefore possible that L-ORD iPSC-RPE increase lipid metabolism as well as ketogenesis to deal with cellular stress.

Catalase was significantly upregulated in L-ORD iPSC-RPE (Table 3.1a and Fig. 3.9). Catalase is an important anti-oxidant to protect the RPE from oxidative stress[252] (see Chapter 4). This could indicate that L-ORD iPSC-RPE are oxidatively stressed and therefore increase the expression of catalase.

Complement system regulator proteins were also found to be significantly differentially expressed in L-ORD iPSC-RPE. *CFI* was significantly downregulated and *CD55* was significantly upregulated (Table 3.1). CFI and CD55 both interact with C3b and inactivate it (see Chapter 5). CD55 can also work in concert with CFH to protect self from complement system-mediated attack. Mutations in CFI, CD55, and CFH are associated with AMD. Dysregulation of complement regulator proteins therefore could possibly also contribute to the L-ORD phenotype that is similar to AMD.

CCL2 was found to be significantly downregulated in expression in L-ORD iPSC-RPE in the RNA-seq data (Table 3.1b). C-C Motif Chemokine Ligand 2 (CCL2), also known as monocyte chemoattractant protein-1 (MCP-1), is a chemokine that has chemotactic activity for monocytes and basophils. CCL2 is thought to play a role in AMD CNV formation together with VEGF[253]. It is thought that ocular-infiltrating macrophages attracted by CCL2 play an important role in CNV formation. Depletion of macrophages was found to reduce CNV formation[254,255]. Additionally, deficiency of CCR2, the receptor for CCL2, reduces CNV in mice[256]. DHA was also found to reduce CCL2 expression via a PPAR-γ and NF-κB-dependent pathway in RPE[257]. DHA may therefore also potentially reduce CNV formation. CCL2 can also attract microglia in the retina. Microglia are also known to phagocytose debris in the retina. Patients with L-ORD are found to develop CNV only at a late stage in the disease[81]. It is possible that CNV formation is inhibited at the earlier stages of L-ORD through the downregulation of CCL2 expression and subsequent reduced macrophage infiltration in the retina. Furthermore, macrophages are also thought to play a role in the clearance of sub-RPE

debris. Downregulation of CCL2 in L-ORD RPE could therefore possibly contribute to drusen formation.

Calcium regulation is important for normal RPE functioning. Ca^{2+} is known to be important for POS phagocytosis and for VEGF secretion by RPE[17]. Several genes involved in Ca^{2+} regulation were significantly differentially expressed (Fig. S3). Pathways involved in Ca^{2+} binding and the response to Ca^{2+} were downregulated in L-ORD iPSC-RPE (Table 3.2b). Notably, *ANO4* expression was significantly downregulated in L-ORD iPSC-RPE compared to its isogenic gene-corrected control (Table 3.1b). *ANO4* encodes for anoctamin-4 which is a Ca^{2+}-dependent non-selective cation channel in RPE[258]. Anoctamins are known to be involved in Ca^{2+} regulation in RPE[259]. Dysregulation of Ca^{2+} signalling through mutations in *BEST1* is known to cause macular dystrophy[42,43]. Therefore, it is possible that aberrant expression of several genes involved in Ca^{2+} regulation could contribute to the macular degenerative phenotype of L-ORD.

These results show that iPSC-RPE can be generated and resemble native RPE in morphology and functionality. L-ORD iPSC-RPE differed from their isogenic gene-corrected control in phagocytosis capability, C1QTNF5 protein structure, gene expression, and possibly in cellular adherence function. Many of the transcriptomic changes found fit the clinical presentation of L-ORD and AMD.

Chapter 4 Oxidative Stress in RPE Cell Lines and L-ORD iPSC-RPE

4.1 Introduction

4.1.1 Oxidative stress

The mitochondria are the major source of cellular ROS generation[260]. The principal function of mitochondria is to produce ATP for cellular energy through oxidative phosphorylation, in addition to the oxidation of metabolites by the Krebs cycle and β-oxidation of fatty acids. Oxidative phosphorylation occurs in protein complexes in the inner mitochondrial membrane, via a process known as the electron transport chain (ETC). The ETC is a cascade of redox reactions that produce ATP. However, about 1-2% of electrons from the ETC can leak and react with oxygen to generate superoxide ($O_2^{\cdot-}$) radical, which also serves as the precursor to most ROS.

Mitochondria are an important target for ROS because of the generation of ROS in the ETC[260]. Mitochondria therefore have an elaborate antioxidative defence. Within mitochondria, superoxide dismutase (SOD) can convert $O_2^{\cdot-}$ into hydrogen peroxide (H_2O_2). The most important mitochondrial antioxidant is glutathione (GSH). In addition, the two GSH-linked antioxidant enzymes glutathione peroxidase 1 (GPX1) and glutathione peroxidase 4 (GPX4) are also essential to the mitochondrial antioxidative defence[260]. GPX1 and GPX4 catalyse the reduction of H_2O_2 and lipid hydroperoxide (LOOH) respectively, with GSH as the electron donor.

The cell is said to be oxidatively stressed when the levels of ROS are high enough to damage the cell. In this case, the levels of ROS are higher than the antioxidant defence can cope with. Depending on the impact of the high levels of ROS, the cell could either repair the damage or trigger pathways leading to cell death. ROS can cause damage to DNA, lipids, and proteins. However, low levels of mitochondrial ROS act as important signalling molecules in cellular differentiation, tissue regeneration, and prevention of ageing[261]. Numerous factors can significantly increase cellular ROS generation, including ultraviolet (UV) radiation, air pollutants, and heavy metals.

4.1.2 ROS

ROS encompass partially reduced oxygen-containing molecules, including $O_2^{\cdot-}$, free radicals such as hydroxyl radical ($HO^{\cdot}$), and peroxides such as H_2O_2. Free iron (Fe^{2+}) can react with H_2O_2 to form $HO^{\cdot}$, H_2O, and ferric iron (Fe^{3+}) through the Fenton reaction. $O_2^{\cdot-}$ can react with Fe^{3+} through the Haber-Weiss reaction, forming O_2 and Fe^{2+}. Fe^{2+} can subsequently be used again for the Fenton reaction, thus forming a redox cycle. However, $O_2^{\cdot-}$ can also be protonated, forming hydroperoxyl ($HO^{\cdot}_2$). Subsequent protonation of $HO^{\cdot}_2$ forms H_2O_2 for the Fenton reaction.

Lipid peroxidation is caused by ROS attacking double carbon-carbon bonds in lipids, causing the breakdown of the double bond. Polyunsaturated fatty acids (PUFAs) are especially susceptible to this due to their multiple double bonds. Lipid peroxidation leads to the abstraction of a hydrogen from a carbon and insertion of an oxygen, resulting in lipid peroxyl radicals ($LOO^{\cdot}$) and LOOH[262]. There are three steps of the lipid peroxidation process: initiation, propagation, and termination[262]. Oxidants like $HO^{\cdot}$ and $HO^{\cdot}_2$ can abstract the allylic hydrogen from a lipid, forming the lipid radical ($L^{\cdot}$) in the initiation phase[263]. In the propagation phase, $L^{\cdot}$ subsequently reacts with oxygen forming $LOO^{\cdot}$ which can again subtract a hydrogen from a lipid forming another $L^{\cdot}$, thus forming a chain reaction. LOOH is also formed in this reaction. Antioxidants like vitamin E can donate a hydrogen to $LOO^{\cdot}$ in the termination phase. This results in a vitamin E radical that reacts with another $LOO^{\cdot}$, forming non-radical products.

Lipid peroxidation can produce a wide variety of oxidation products in addition to the primary product LOOH[263]. Many different aldehydes can be formed as secondary products during lipid peroxidation, including propanal, hexanal, 4-hydroxynonenal (4-HNE), and malondialdehyde (MDA). Of these secondary products, MDA is the most mutagenic and 4-HNE the most toxic[264,265]. 4-HNE rapidly reacts with thiols and amino groups, explaining its high toxicity[266]. MDA has specific epitopes that can trigger an immune response[267]. 4-HNE and MDA are also found to reduce lysosomal degradation of phagocytosed POS in RPE[268]. Moreover, impaired lysosomal degradation caused by these lipid peroxidation products lead to transcytosis of POS, possibly contributing to sub-RPE deposit formation[269].

4.1.3 Oxidative stress in RPE and AMD

Oxidative stress is commonly attributed to age-associated pathology in many diseases with damage from oxidative stress accumulating during ageing[270]. In addition, the antioxidant capacity diminishes and the efficiency of repair systems is compromised with age[271,272]. Oxidative stress also has an important role in the initiation and progression of AMD[273,274]. Smoking, causing oxidative stress, also increases the risk of developing AMD[274-277]. Antioxidants, such as vitamin C, vitamin E, β-carotene, and zinc, have been found to ameliorate AMD[273].

Various stimuli can induce different forms of oxidative stress in the eye[278]. Proportionally compared to the rest of the body, the retina consumes the most oxygen and therefore has several adaptations to deal with oxidative stress[279]. In the retina, the RPE are continuously exposed to oxidative stress. RPE metabolise and recycle POS[17,280], have large oxygen fluxes near the plasma membrane[16,17], and are exposed to light[17,279]. Therefore, RPE need to be well adapted to handle oxidative stress.

RPE have several specific adaptations to deal with oxidative stress. There are several antioxidant enzymes including SOD, catalase, GPX, and antioxidative vitamins, such as vitamin C and vitamin E, all of which protect the RPE from oxidative stress[252]. The enzyme catalase is important for RPE protection from ROS produced during phagocytosis[280,281]. RPE also produce melanin in their melanosomes to absorb scattered light and thereby prevent excessive photo-oxidation in the retina and subsequent oxidative stress. Therefore, the RPE also provides protection from oxidative stress for the rest of the retina.

An important function of RPE is to phagocytose POS[22,23]. POS are enriched with PUFAs, to the point that POS possess the highest relative concentration of PUFAs compared to all other body tissues[282]. The high amount of double bonds in PUFAs make them susceptible to oxidation, also called lipid peroxidation. POS phagocytosed by RPE also contain complex aggregates termed lipofuscin[283].

Lipofuscin are formed by autofluorescent lipid-protein complexes and accumulate in lysosomes of RPE with age[284,285]. The autofluorescent nature of lipofuscin is also the cause of the autofluorescence of the fundus[286], making confocal laser scanning ophthalmoscopy and fundus photography possible. Lipofuscin accumulation has been associated with cellular senescence and high levels in RPE lead ultimately to photoreceptor degeneration[287].

Lipofuscin contain lipid peroxidation products, including 4-HNE and MDA[288]. 2-[2,6-dimethyl-8-(2,6,6-trimethyl-1-cyclohexen-1-yl)-1E,3E,5E,7E-octatetraenyl]-1-(2-hydroxyethyl)-4-[4-methyl-6-(2,6,6-trimethyl-1-cyclohexen-1-yl)-1E,3E,5E-hexatrienyl]-pyridinium (A2E), also known as *N*-retinylidene-*N*-retinylethanolamine, is a blue light-excitable fluorophore that is an important component of lipofuscin. Photoinduction of lipofuscin can lead to the generation of singlet O_2, $O_2^{\cdot-}$, H_2O_2, and LOOH[289]. Blue light radiation of A2E leads to photooxidation in RPE[290] and it is thought that blue light radiation of A2E in lipofuscin causes the production of the secondary lipid peroxidation products 4-HNE and MDA in RPE[291].

Docosahexaenoic acid (DHA; 22:6) is an omega-3 PUFA that is relatively rare in human tissue. However, DHA accounts for 60% of the PUFAs in the retina, with its highest concentration in POS[282]. DHA is an essential structural component of the cell membrane in POS[292]. However, DHA is the most oxidizable fatty acid in humans[282]. RPE are constantly exposed to high concentrations of DHA through phagocytosis of POS and through transport of DHA from the choriocapillaris to the photoreceptors for photoreceptor membrane biogenesis[293]. Oxidative stress can therefore potentially cause lipid peroxidation of DHA in RPE, leading to RPE damage and possibly cell death. In addition, oxidation of DHA can result in a very reactive product, 4-hydroxy-7-oxohept-5-enoic acid (HOHA).

Carboxyethylpyrrole (CEP) protein adducts are formed by HOHA, an oxidation product unique to DHA[294]. CEP forms when the aldehyde group on HOHA binds to an ε-lysyl amino group of a protein. CEP adducts are found to be more abundant in AMD retinal tissue, specifically in the RPE, Bruch's membrane, and choroid[73]. In addition, CEP adducts are also found in AMD drusen[73] and in lipofuscin[283]. These adducts have been shown to stimulate angiogenesis[295,296]. Moreover, mice immunised with CEP adducts develop a gaAMD-like phenotype, indicating a role for CEP adducts in the aetiology of AMD[297]. CEP adducts were also found to be elevated in the plasma of patients with AMD[294]. CEP adducts could therefore play a role in AMD pathology and possibly function as a biomarker for AMD.

Increased iron accumulation is found within the retina of AMD patients[298,299], which is thought to promote oxidative stress through the Fenton reaction. Iron was also recently found to promote oxidative cell death caused by bisretinoids in the retina[300], the precursor of lipofuscin. Therefore, iron accumulation could play an important role in the pathology of AMD.

Although the lens in the eye blocks most of UV radiation, some UV can still penetrate the eye and reach the retina to potentially cause photo-oxidation. UV is associated with various ocular diseases[301]. UV light comprises light with a wavelength between 100-400 nm and can be categorised into UVA (315-400 nm), UVB (280-315 nm), and UVC (100-280 nm). Light with a longer wavelength carries less energy and therefore has less potential to do damage but can penetrate deeper into tissue. About 1% of UV below 340 nm and 2% of UV between 340-360 nm reaches the retina[302]. It is, however, still uncertain if UV radiation can contribute to the onset and progression of AMD[301].

Oxidative stress can also lead to induced cellular senescence in RPE[79]. Oxidative stress-induced cellular senescence was shown to increase the expression of VEGF and reduce the expression of CFH[303]. However, prolonged severe oxidative stress can lead to cell death. In addition, oxidative stress makes the RPE more susceptible to complement system-mediated cell death[304].

4.1.4 Oxidative stress-mediated cell death in RPE

Oxidative stress generally leads to two different forms of cell death: apoptosis and necrosis[305]. Apoptosis is a regulated form of cell death and necrosis is considered to be a non-regulated form of cell death. Oxidative stress by H_2O_2 in RPE has been shown to lead to necroptosis, rather than apoptosis[306]. Necroptosis is a regulated form of necrosis[307]. This cell death pathway is activated by TNFα and regulated by receptor-interacting protein kinases (RIPKs)[307-309].

TNFα can activate different signalling pathways through its receptor TNFR1, including cell survival, apoptosis, and necroptosis[309]. RIPK1 is recruited to activated TNFR1 and regulates the decision between the three different downstream pathways. Normally, necroptosis is inhibited by caspase-8, which cleaves both RIPK1 and RIPK3. When not cleaved, RIPK1 and RIPK3 are autophosphorylated and together form a complex termed the necrosome. The necrosome functions as a signalling platform that binds to and activates regulators of different cellular pathways, including mitochondrial fragmentation, metabolism, autophagy, and growth factor signalling. An important downstream effector of the necrosome is mixed lineage kinase domain-like protein (MLKL)[310]. RIPK3 phosphorylates MLKL and thereby causes its oligomerisation and subsequent translocation to cellular membranes[311-313]. MLKL

activation by RIPK3 has been found to be both necessary and sufficient to cause necroptosis through membrane permeabilization.

Ferroptosis is another form of regulated necrotic cell death that can be caused by oxidative stress. Ferroptosis is an iron- and PUFA-dependent form of cell death caused by lipid peroxidation in plasma membranes[314]. Human cells were found to undergo ferroptosis when oxidatively stressed with *tert*-butyl hydroperoxide (tBHP)[315]. tBHP was also recently shown to induce ferroptosis in RPE[316].

Ferroptosis can be induced by changes in signalling and membrane transport processes. Central in the regulation of ferroptosis is the glutathione peroxidase GPX4. GPX4 is the only known enzyme that can reduce LOOH in cellular membranes[317]. Inactivation or inhibition of GPX4 induces ferroptosis[318]. GPX4 inhibition has been shown to induce PUFA peroxidation and the generation of fatty acid radicals. An important regulator of cell membrane lipid composition is acyl-CoA synthetase long-chain family member 4 (ACSL4). ACSL4 catalyses the activation of PUFAs by esterification, producing acyl-CoA. Acyl-CoA is an intermediate in various metabolic pathways, including phospholipid production for membrane biogenesis. ACSL4 has been shown to create the right membrane lipid composition for the induction of ferroptosis[319]. It was subsequently found that specifically phosphatidylethanolamine (PE) phospholipids produced by ACSL4 cause ferroptosis[320]. PE produced by ACSL4 is inserted into membrane phospholipids by lysophosphatidylcholine acyltransferase 3 (LPCAT3). LPCAT3 has been therefore also found to be important for the induction of ferroptosis[320,321].

Still much is unknown about RPE cell death in response to oxidative stress and how this could be prevented for possible therapy development.

4.1.5 Aims and objectives

In order to study the response of RPE in general and L-ORD iPSC-RPE to oxidative stress, the following was carried out in this chapter:

1. The mode of cell death in RPE cell lines in response to different types of oxidative stress was investigated by cell viability assays, immunostaining, qPCR, and western blotting
2. The response of L-ORD iPSC-RPE to different types of oxidative stress was investigated by cell viability assays and immunostaining

4.2 Materials and methods

4.2.1 Cell culture

ARPE-19 (ATCC, Manassas, VA) and hTERT RPE-1 (ATCC) immortalised cell lines were cultured and maintained in DMEM/F12 (Gibco) supplemented with 10% foetal calf serum (FCS; Gibco) and L-glutamine (Gibco) at 37 °C and 5% CO_2. For experiments, cells were split and seeded in DMEM/F12 supplemented with 1% FCS and L-glutamine unless otherwise stated.

iPSCs were cultured as described in Chapter 2 (2.2.1) and differentiated to RPE as described in Chapter 3 (3.2.2).

4.2.2 Fatty acid-BSA conjugation

Palmitic acid (PA; Sigma-Aldrich) and DHA (Sigma-Aldrich) were conjugated to fatty acid-free bovine serum albumin (BSA; Sigma-Aldrich) as previously described[322], but with some modifications. Briefly, PA and DHA were dissolved in 50% ethanol to 150 mM at 90 °C and 70 °C respectively. The dissolved fatty acids were then immediately diluted, using prewarmed tips, in prewarmed 10% fatty acid-free BSA solution to 7.5 mM whilst stirring. This was incubated at 37 °C for 1 hour to achieve BSA-fatty acid conjugation. The conjugated BSA-fatty acids were 0.22 µm filter-sterilised, aliquoted, and stored at -20 °C. Conjugated BSA-fatty acids were used in medium at a final concentration of 500 µM fatty acid and 0.67% BSA unless otherwise stated.

4.2.3 Cell viability and toxicity assays

RPE cell lines were seeded at $7.5*10^3$ cells/well in a 96-well plate. The following day the cells were pre-treated for 24 hours with 40 µM Z-VAD-FMK (Merck Millipore), 40 µM Necrostatin-1 (Nec-1; Cayman Chemical, Ann Arbor, MI), 1 µM GSK2791840B (GSK'840B; GlaxoSmithKline, Brentford, UK), 1 µM Necrosulfonamide (NSA; Merck Millipore), or 5 µM Ferrostatin-1 (Fer-1; Sigma-Aldrich). Pre-treatment with 500 µM deferoxamine (DFO; Sigma-Aldrich) was 1 hour before injury. The cells were then treated with a final concentration of 500 µM H_2O_2 (Sigma-Aldrich) for 6 hours or 500 µM DHA for 18 hours at 37 °C and 5% CO_2.

After treatment, the cells were incubated with PrestoBlue (Invitrogen) in medium with 1% FCS and L-glutamine for 1 hour at 37 °C and 5% CO_2. The medium with PrestoBlue was then transferred to a black 96-well assay plate and read with a GloMAX plate reader (Promega).

iPSC-RPE were seeded at $7.5*10^3$ cells/well in a 96-well plate and cultured for four weeks until mature and confluent. The medium was replaced with DMEM without additions two days before H_2O_2, DHA or tBHP treatment. The cells were treated with different concentrations of H_2O_2, DHA or tBHP for 24 hours at 37 °C and 5% CO_2. The medium was subsequently replaced with DMEM without additions and the cells were incubated for another 24 hours at 37 °C and 5% CO2. The cells were stained with 3 µg/ml Hoechst and 6 µg/ml propidium iodide (PI) for 20 minutes at 37 °C and 5% CO_2, and subsequently fixed with pre-warmed 4% PFA for 10 minutes. After three washes with PBS the cells were imaged with a Zeiss Axio Observer Z1 motorised inverted microscope with an automatic stage (Carl Zeiss Ltd.).

iPSC-RPE were seeded at $7.5*10^3$ cells/well in a 96-well plate and cultured for four weeks until mature and confluent. The medium was replaced with DMEM without phenol red (Gibco) and without additions one day before UV exposure. The cells were exposed to UV light (290 nm) for 24 hours at 37 °C and 5% CO_2. The medium was subsequently replaced with DMEM without additions and the cells were incubated for another 24 hours at 37 °C and 5% CO2. The cells were then stained with 0.2 µM DRAQ7 and trypsinised. The samples were kept on ice until analysis with a NovoCyte flowcytometer (Acea Biosciences Inc, San Diego, CA). UV light exposure and flowcytometric analysis were carried out by Graham Anderson (The University of Edinburgh) and Dr Bagnaninchi (The University of Edinburgh).

4.2.4 Immunocytochemistry

4,4-difluoro-5-(4-phenyl-1,3-butadienyl)-4-bora-3a,4a-diaza-s-indacene-3-undecanoic acid (C11-BODIPY$^{581/591}$; Invitrogen) was used to assess lipid peroxidation in RPE cell line membranes. C11-BODIPY$^{581/591}$ incorporates into membranes and the excitation and emission fluorescence spectra of this lipid analogue both shift to shorter wavelengths when oxidised[323].

Cells were treated with inhibitors as described above (see section 4.2.3) in 96-well plates. The cells were stained with 3 µM C11-BODIPY$^{581/591}$ before H_2O_2, DHA or POS treatment. H_2O_2

or DHA treatment was done as described above (see section 4.2.3). POS-FITC were prepared as described before (see section 3.2.6). After treatment, the cells were washed with PBS and subsequently stained with 6 µg/ml Hoechst 33342 (Sigma-Aldrich). The cells were then fixed with prewarmed 4% PFA for 10 minutes at 21 °C and washed with PBS. For pMLKL and PI staining, the cells were washed with PBS after H_2O_2 treatment and subsequently stained with 3 µg/ml PI (Sigma-Aldrich) for 20 minutes at 21 °C. The cells were then fixed with prewarmed 4% PFA for 10 minutes and permeabilised with 0.1% Triton™ X-100 (Sigma-Aldrich) for 15 minutes at 21 °C. The cells were then incubated with 1:100 phospho S358 MLKL antibody (Abcam) in 3% goat serum for 1 hour at 4 °C. After two washes with PBS, the cells were incubated with 1:250 Alexa Fluor 647 antibody (Molecular Probes, Eugene, OR) for 30 minutes at 21 °C covered from light. After another two washes with PBS, the nuclei were counterstained with 300 nM DAPI (Biotium) for 10 minutes at 21 °C covered from light, followed by another three washes with PBS. Stained cells were imaged with a Leica DMi8 inverted microscope (Leica Microsystems). The antibodies and concentrations used are listed in Table S8.

iPSC-RPE were seeded at $7.5*10^3$ cells/well in a 96-well plate and cultured for four weeks until mature and confluent. Pre-treatment with inhibitors was done as described above (see section 4.2.3). The iPSC-RPE were treated with 1 mM H_2O_2 for 18 hours. The cells were then fixed, permeabilised, stained with phospho S358 MLKL antibody and DAPI, and imaged as described above.

4.2.5 Flow cytometry for lipid peroxidation

RPE cell lines were seeded and treated with inhibitors in 96-well plates as described above (see section 4.2.3). Medium with inhibitors was transferred to a new plate and kept at 37 °C and 5% CO_2. The cells were then incubated for 1 hour at 37 °C and 5% CO_2 with a final concentration of 3 µM C11-BODIPY$^{581/591}$ in DMEM/F12 without phenol red (Gibco) and no FCS. The cells were washed once with PBS and the medium with inhibitors was transferred back to the cells. The cells were then treated with a final concentration of 500 µM H_2O_2 for 3 hours at 37 °C and 5% CO_2. After H_2O_2 treatment, the cells were washed once with PBS, trypsinised, and transferred to Eppendorf's containing medium with 10% FCS to inactivate the trypsin. The cells were then washed once with flow buffer, resuspended in 250 µl of flow buffer containing a final concentration of 2.4 µM DRAQ7 (Biostatus, Shepshed, UK). The

samples were kept on ice until analysis with a BD Accuri C6 flowcytometer (BD Biosciences, Franklin Lakes, NJ).

4.2.6 Flow cytometry for Annexin V, PI, MLKL, and pMLKL

RPE cell lines were seeded and when needed treated with inhibitors in 96-well plates as described above (see section 4.2.3). The cells were then treated with a final concentration of 500 µM H_2O_2 for 3 hours at 37 °C and 5% CO_2. After H_2O_2 treatment, the cells were washed once with PBS, trypsinised, and transferred to Eppendorf's containing medium with 10% FCS to inactivate the trypsin.

For Annexin V and PI staining, the cells were stained using the Annexin V-FITC Apoptosis Detection Kit (Affymetrix, Santa Clara, CA) according to the manufacturer's instructions.

For MLKL and pMLKL staining, the cells were fixed in prewarmed 4% paraformaldehyde for 10 minutes at room temperature. After washing with flow buffer, consisting of PBS with 1% BSA and 0.05% NaN_3, the cells were permeabilised with 0.2% Triton X-100 for 5 minutes at room temperature. After washing with flow buffer the cells were incubated with 1:100 MLKL antibody (Abcam) or 1:100 phospho S358 MLKL antibody (Abcam)[313] in 10% normal goat serum in flow buffer for 1 hour on ice. After washing the cells were incubated with 1:250 Alexa Fluor 488 antibody (Cell Signaling Technology, Danvers, MA) or 1:250 Alexa Fluor 647 antibody (Molecular Probes) for 30 minutes on ice. The cells were then washed once with flow buffer, resuspended in 250 µl of flow buffer. The samples were kept on ice until analysis with a BD Accuri C6 flowcytometer. The antibodies and concentrations used are listed in Table S8.

4.2.7 qPCR

RPE cell lines were seeded at $3*10^5$ cells/well in a 6-well plate. The following day the cells were treated with 300 µM H_2O_2 and 300 µM BSA-DHA for 24 hours. RNA was extracted using TRIzol® Reagent (Ambion) according to manufacturer's instructions. cDNA was made using the High Capacity cDNA Reverse Transcription Kit (Applied Biosystems) according to manufacturer's instructions and primers were designed by Primerdesign Ltd., see Table S7

for sequences. Power SYBR® Green PCR Master Mix (Applied Biosystems) was used in combination with a StepOnePlus™ Real-Time PCR System (Applied Biosystems).

4.2.8 Western blotting

RPE cell lines were seeded at $2.5*10^5$ cells/well in a 6-well plate. The following day the cells were treated with 500 µM H_2O_2, 500 µM BSA-PA, and 500 µM BSA-DHA for 6 hours. The cells were then lysed in RIPA buffer supplemented with Complete Mini protease inhibitor cocktail (Sigma-Aldrich) and PhosSTOP phosphatase inhibitor (Roche) and passed through a 21-gauge needle (Sterican) to shear the DNA. 20 µg of cell lysate in Laemmli sample buffer (Bio-Rad) supplemented with β-mercaptoethanol was heated to 98 °C for 5 minutes and subsequently loaded and ran on a 12% SDS-PAGE gel. The gel was then blotted onto a nitrocellulose membrane (Bio-Rad), blocked with TBS +5% Marvel for 30 minutes at room temperature, and incubated with 1:500 ACSL4 antibody (Santa Cruz, Santa Cruz, CA) overnight at 4 °C. The following day the membrane was incubated with 1:4,000 HRP-conjugated secondary antibody (Merck Millipore) for 30 minutes at room temperature. After incubation with Amersham ECL reagent (GE Healthcare), an Amersham Hyperfilm (GE Healthcare) was exposed to the membrane. The same membrane was reprobed with 1:5,000 β-actin antibody (Abcam) for 1 hour at room temperature followed by 1:4,000 HRP-conjugated secondary antibody (Merck Millipore) for 30 minutes at room temperature to check for loading control. Exposed films were developed in a Mi-5 X-ray developer machine (Jet Xray). The antibodies and concentrations used are listed in Table S9.

4.2.9 UV exposure and ECIS

UV light (340 nm) exposure was performed as described above (4.2.3) and ECIS was performed as described in Chapter 3 (3.2.4). UV light exposure and ECIS recording were both performed by Graham Anderson (The University of Edinburgh) and Dr Bagnaninchi (The University of Edinburgh).

4.2.10 Statistics

Experiments were repeated at least three times. Statistical analysis was performed using Microsoft Excel version 1905 and GraphPad Prism 6 software. Student's *t*-tests were used to determine statistical significance between groups. *P*-values of less than 0.05 were considered to be statistically significant.

4.3 Results

4.3.1 RPE undergo necrosis and not apoptosis after H_2O_2 exposure

RPE were exposed to 500 µM H_2O_2 for 3 hours to investigate the mode of cell death RPE undergo when oxidatively stressed. PI, which stains necrotic cells, was found to stain RPE treated with H_2O_2 (Fig. 4.1). In contrast, H_2O_2-treated RPE did not stain for Annexin V, which stains apoptotic cells. Therefore, exposure to H_2O_2 caused necrosis rather than apoptosis in RPE. In contrast, staurosporine, a known inducer of apoptosis, caused apoptosis but no necrosis in RPE (Fig. 4.1).

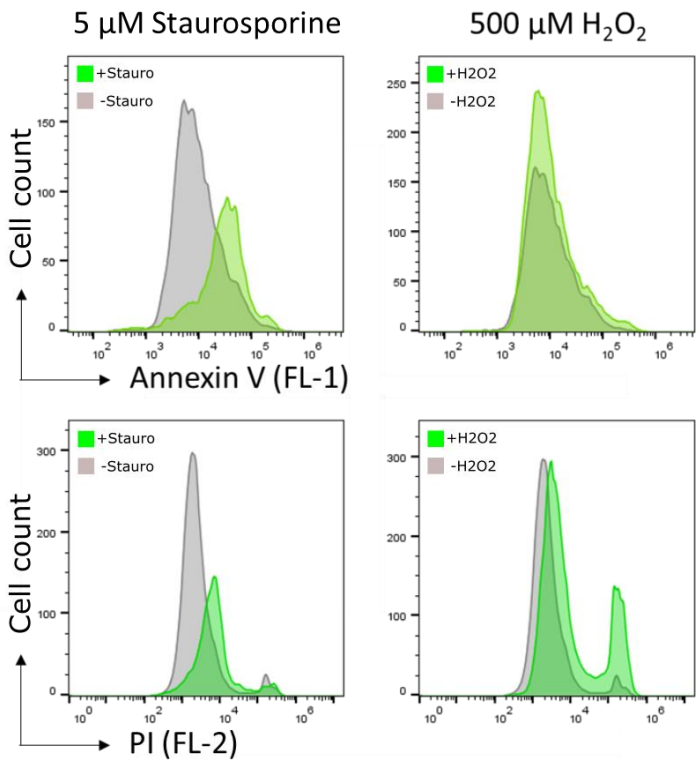

Figure 4.1 | H_2O_2 exposure leads to necrotic and not apoptotic cell death in RPE. ARPE-19 cells were treated with 5 µM staurosporine or 500 µM H_2O_2 for 3 hours. Staurosporine but not H_2O_2 exposure leads to increased Annexin V staining. H_2O_2 but not staurosporine exposure leads to increased PI staining.

4.3.2 Increased RPE cell viability by necroptosis and ferroptosis inhibitors after H_2O_2 or DHA exposure

PUFAs, like oxidative stress, could possibly also induce RPE cell death at high concentrations. RPE cell death in response to oxidative stress or PUFA injury was further investigated. RPE

were therefore pre-treated with specific cell death inhibitors, followed by H_2O_2 or DHA injury. The necroptosis inhibitor NSA and the ferroptosis inhibitor Fer-1 were able to significantly alleviate H_2O_2 injury in RPE (Fig. 4.2a). Both NSA and Fer-1 combined did not increase cell viability even further. The necroptosis inhibitor Nec-1 and Fer-1 were able to significantly alleviate DHA injury in RPE (Fig. 4.2b). However, the apoptosis inhibitor Z-VAD did not alleviate H_2O_2 or DHA injury. This suggests that necroptosis and ferroptosis, but not apoptosis, play a role in H_2O_2- and DHA-mediated cell death.

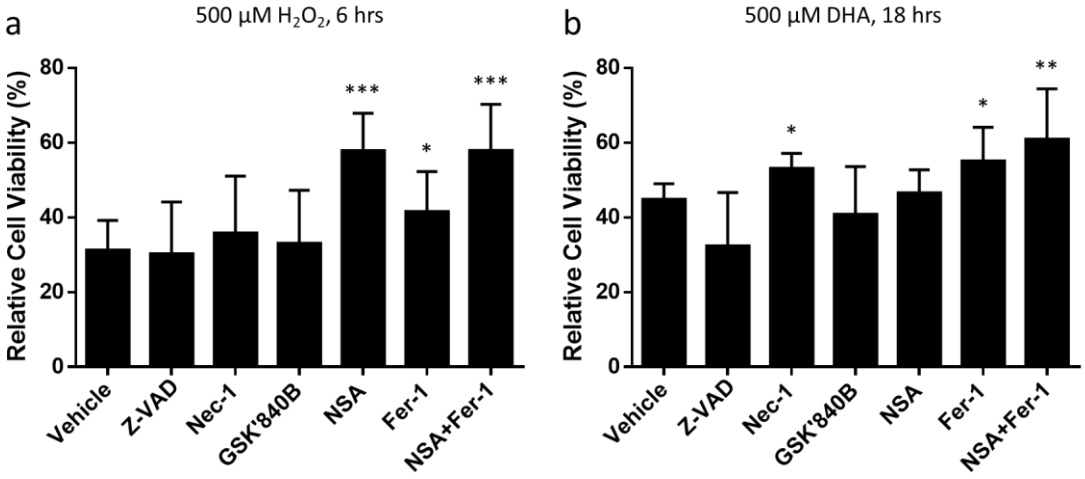

Figure 4.2 | H_2O_2- and DHA-induced RPE cell death is ameliorated by necroptosis and ferroptosis inhibitors. ARPE-19 and hTERT RPE-1 cells were treated with 40 µM Z-VAD, 40 µM Nec-1, 1 µM GSK'840B, 1 µM NSA, 5 µM Fer-1, or 1 µM NSA and 5 µM Fer-1 24 hours before 6-hour treatment with 500 µM H_2O_2 (**a**) or 18-hour treatment with 500 µM DHA (**b**). Cell viability was measured with PrestoBlue after treatment. Error bars represent SD of at least three independent experiments. **P*<0.05, ***P*<0.01, and ****P*<0.0001, determined by *t*-test compared to vehicle.

4.3.3 Increased lipid ROS in RPE after H_2O_2, DHA, or POS exposure and is inhibited by Fer-1 and DFO

Next, the role of ferroptosis was investigated in RPE stressed with H_2O_2, DHA, or POS. Ferroptosis is an iron- and PUFA-dependent form of cell death and is characterised by peroxidation of PUFAs. The iron chelator DFO should therefore reduce the amount of PUFA peroxidation and thereby reduce cell death through ferroptosis. Pre-treatment with DFO or

the ferroptosis inhibitor Fer-1 reduced the amount of lipid ROS caused by H_2O_2, DHA, or POS injury (Fig. 4.3a and b). The apoptosis inhibitor Z-VAD did not reduce lipid ROS (Fig. 4.3a) and neither did the necroptosis inhibitor Nec-1 (Fig. 4.3b). This indicates that iron chelation or Fer-1 are more effective to reduce lipid ROS common to ferroptosis that is caused by H_2O_2, DHA, or POS injury.

Addition of DHA or POS to H_2O_2-injured RPE could possibly increase lipid peroxidation. Injury of RPE with both H_2O_2 and DHA or H_2O_2 and POS increased the amount of lipid ROS more than H_2O_2 injury alone (Fig. 4.3c). This shows that oxidative stress-induced lipid peroxidation can be increased with the addition of DHA or POS.

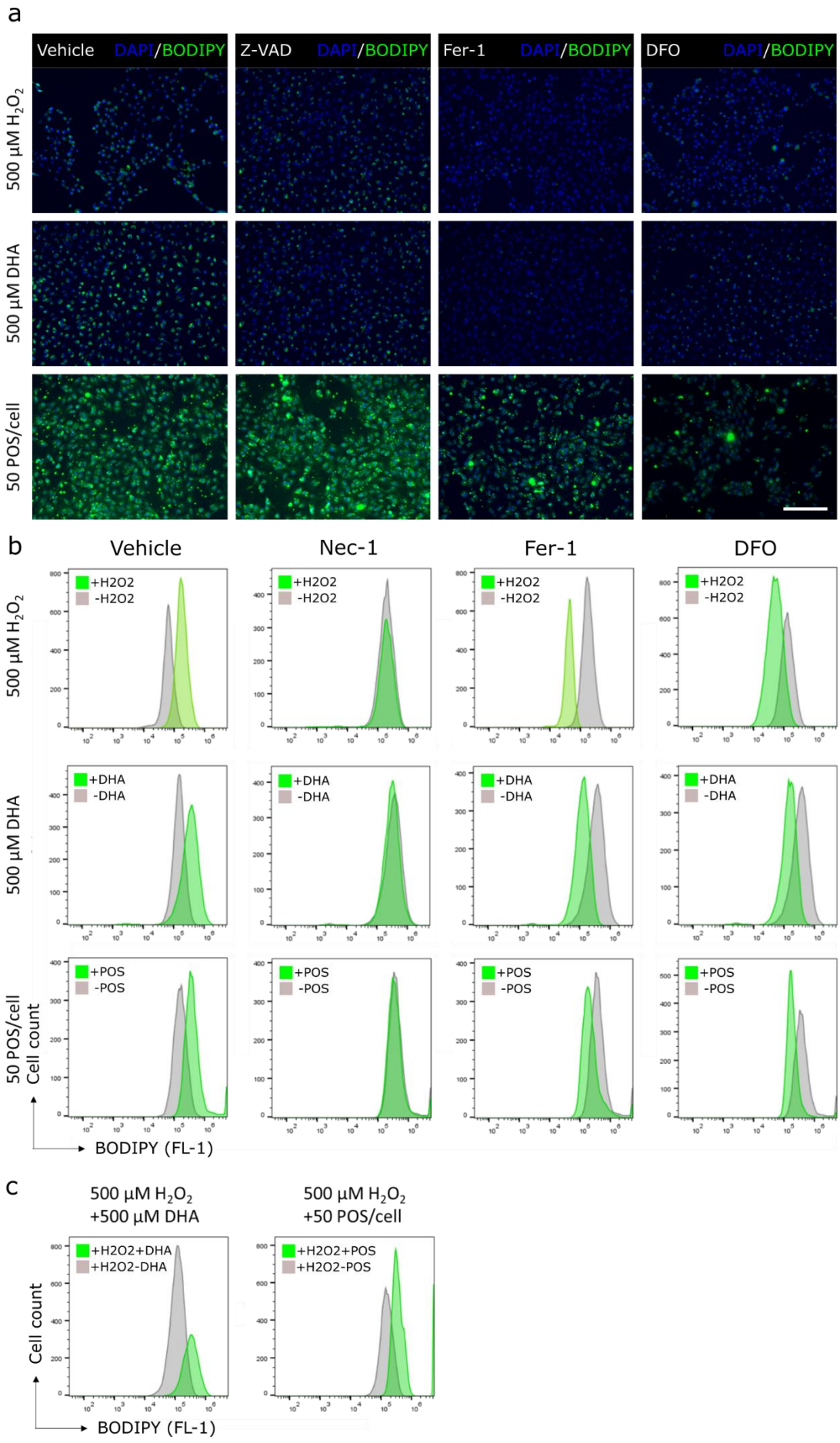
a
Vehicle DAPI/BODIPY
Z-VAD DAPI/BODIPY
Fer-1 DAPI/BODIPY
DFO DAPI/BODIPY
500 µM H2O2
500 µM DHA
50 POS/cell
b
Vehicle
Nec-1
Fer-1
DFO
+H2O2
-H2O2
+DHA
-DHA
+POS
-POS
Cell count
BODIPY (FL-1)
c
500 µM H2O2
+500 µM DHA
500 µM H2O2
+50 POS/cell
+H2O2+DHA
+H2O2-DHA
+H2O2+POS
+H2O2-POS
Cell count
BODIPY (FL-1)

Figure 4.3 | H_2O_2-, DHA-, and POS-induced lipid ROS in RPE are reduced by Fer-1 and DFO. ARPE-19 cells were treated with 40 µM Z-VAD, 40 µM Nec-1, or 5 µM Fer-1 24 hours or 500 µM DFO 1 hour before injury. Subsequent 3-hour treatment with 500 µM H_2O_2, 500 µM DHA, or 50 POS/cell shows increase of lipid ROS (BODIPY) (**a** and **b**). Pre-treatment with Fer-1 and DFO reduces the amount of lipid ROS after injury. Injury with DHA or POS in addition to H_2O_2 increases the amount of lipid ROS compared to H_2O_2 alone (**c**). Scale bar equals 200 µm.

4.3.4 MLKL is phosphorylated after H_2O_2 or POS exposure in RPE

Next, the role of necroptosis was investigated in RPE stressed with H_2O_2, DHA, or POS. MLKL is the effector protein of necroptosis when activated through phosphorylation. RPE were found to express MLKL (Fig. 4.4a). Treatment with H_2O_2 increases the amount of pMLKL (Fig. 4.4b) and therefore causes necroptosis. DHA or POS treatment did not increase the amount of pMLKL in RPE and therefore likely do not cause necroptosis.

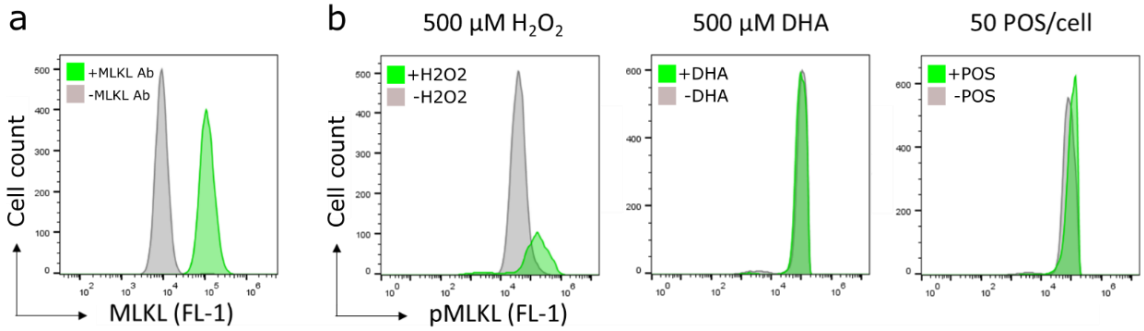

Figure 4.4 | Increase of pMLKL in RPE after H_2O_2 or POS exposure. ARPE-19 cells express MLKL (**a**). Treatment of ARPE-19 cells with 500 µM H_2O_2, but not 500 µM DHA or 50 POS/cell, for 3 hours increases phosphorylation of MLKL (**b**).

4.3.5 Expression changes after H_2O_2 or DHA exposure in RPE

Prolonged exposure to H_2O_2 or DHA can cause cellular stress in RPE. However, the cellular response to either injury may vary. SQSTM1, also known as p62, is a multifunctional protein involved in cellular processes including autophagy and stress. H_2O_2 causes a significant downregulation of *SQSTM1* expression (Fig. 4.5a). In contrast, DHA causes a significant upregulation of *SQSTM1* expression. HSPA1B, also known as Hsp70, is involved in a wide

range of cellular processes, including protection of the proteome to stress. *HSPA1B* expression is significantly upregulated by both H_2O_2 and DHA exposure (Fig. 4.5a). *CDKN2A*, which expresses the protein $p16^{INK4a}$, is involved in regulating the cell cycle and is regarded as a marker of cellular senescence. *CDKN2A* expression was significantly downregulated by DHA exposure, but not H_2O_2 exposure (Fig. 4.5a).

Cellular stress can lead to cell death. To investigate the role of apoptosis in H_2O_2- or DHA-mediated cell death in RPE, expression of certain apoptosis markers was measured after H_2O_2 or DHA exposure. BCL2 is an important regulator of apoptosis and blocks apoptotic cell death. BAX and BAK1 are both BCL2 antagonists and therefore have a proapoptotic function. *BCL2* expression was significantly downregulated in RPE exposed to H_2O_2 (Fig. 4.5b), indicating that apoptosis could play a role in H_2O_2-mediated cell death. However, *BAX* expression did not significantly change and moreover *BAK1* expression was significantly downregulated (Fig. 4.5b). *BCL2*, *BAX* and *BAK1* expression did not significantly change in RPE exposed to DHA (Fig. 4.5b).

Expression differences of ferroptosis-related genes was also assessed in H_2O_2- or DHA-mediated cell death in RPE. The expression of *ACSL4* and *LPCAT3* were significantly downregulated in RPE treated with H_2O_2 (Fig. 4.5c). In contrast, in DHA treated RPE only *LPCAT3* expression was significantly downregulated (Fig. 4.5c).

Prolonged cellular stress can also affect cellular metabolism. PPARG plays a role in regulating lipid metabolism and its expression was significantly downregulated in H_2O_2-treated RPE but upregulated in DHA-treated RPE (Fig. 4.5d).

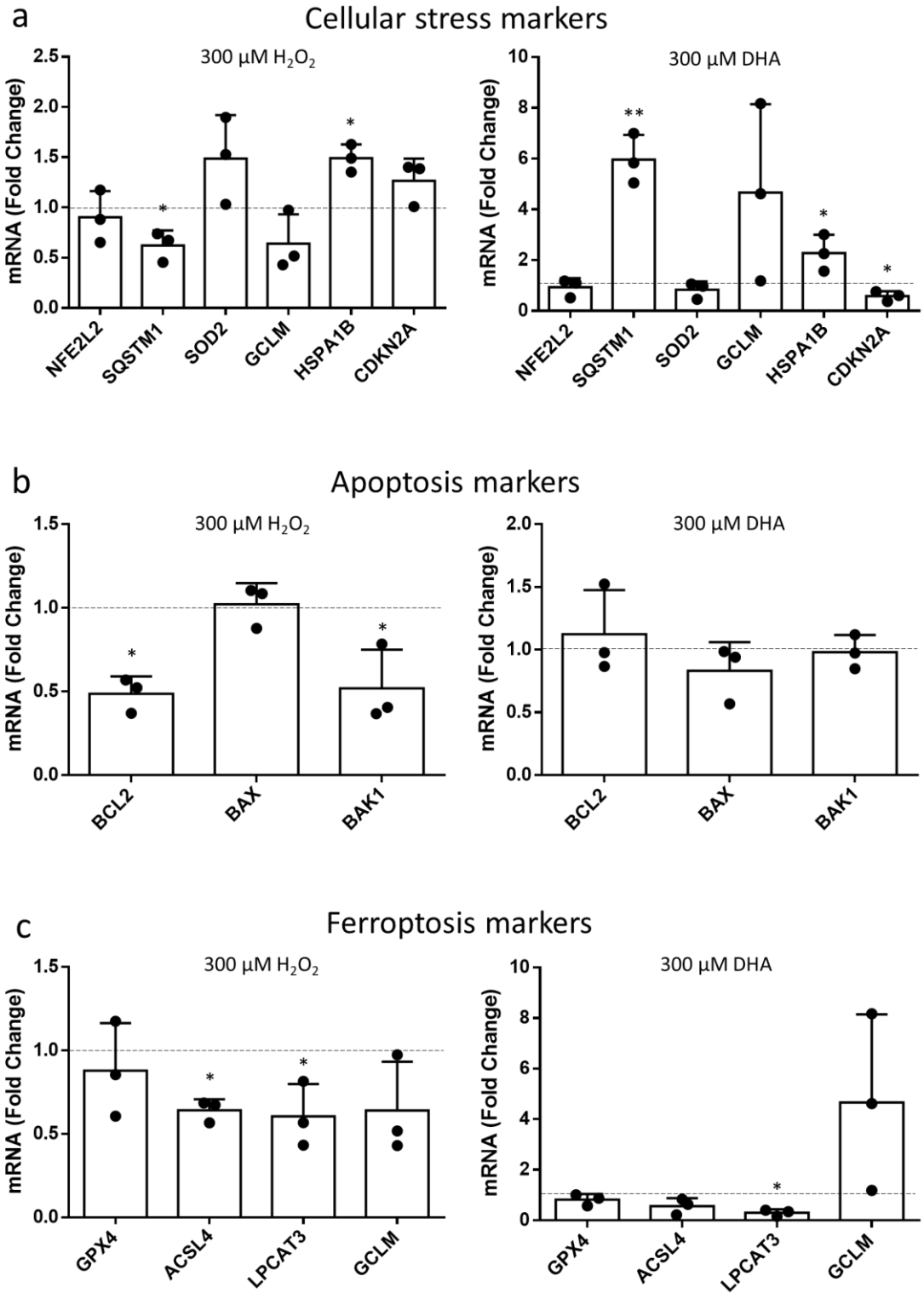
a
Cellular stress markers
300 µM H_2O_2
300 µM DHA
mRNA (Fold Change)
NFE2L2
SQSTM1
SOD2
GCLM
HSPA1B
CDKN2A
b
Apoptosis markers
BCL2
BAX
BAK1
c
Ferroptosis markers
GPX4
ACSL4
LPCAT3
GCLM

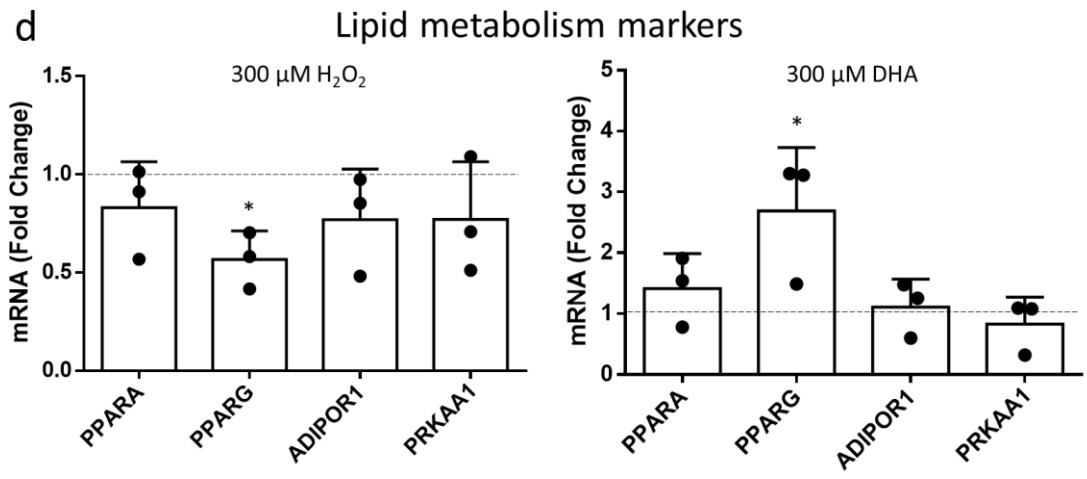

Figure 4.5 | Differential gene expression in RPE exposed to H_2O_2 or DHA. ARPE-19 cells were to 300 µM H_2O_2 or 300 µM DHA for 24 hours. The fold change in mRNA expression was determined of genes related to cellular stress (**a**), apoptosis (**b**), ferroptosis (**c**), and lipid metabolism (**d**). Error bars represent SD of three independent experiments. **P*<0.05 and ***P*<0.001, determined by *t*-test on ΔCT values.

4.3.6 Decreased expression of ACSL4 after H_2O_2 and DHA exposure in RPE

RPE were exposed to H_2O_2 and PA or H_2O_2 and DHA to further investigate the downregulation of ACSL4 caused by H_2O_2 and the possible role that fatty acids could have in this. H_2O_2 significantly reduced the ACSL4 protein levels and addition of DHA but not PA exacerbated this effect (Fig. 4.6a and b).

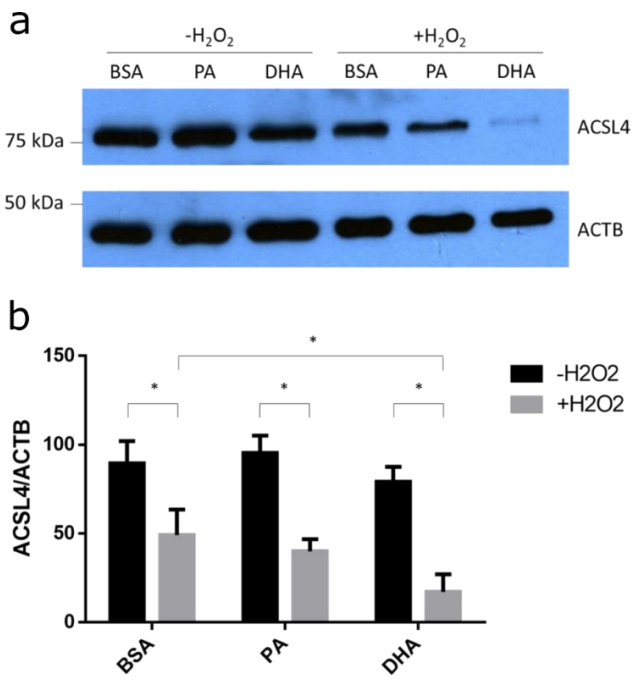

Figure 4.6 | ACSL4 is downregulated in RPE after H_2O_2 and DHA exposure. ARPE-19 cells were exposed to 500 µM H_2O_2, 500 µM PA, and 500 µM DHA for 6 hours. Representative blot out of three depicting ACSL4 expression changes to H_2O_2 and fatty acids (**a**). Densitometric analysis (**b**). Error bars represent SD of three independent experiments. **P*<0.05, determined by *t*-test. BSA = bovine serum albumin; PA = palmitic acid; DHA = docosahexaenoic acid.

4.3.7 H_2O_2 and DHA exposure of iPSC-RPE

The effect of oxidative stress induced by H_2O_2 and DHA were also tested on iPSC-RPE. iPSC-RPE were exposed for 24 hours to different concentrations of H_2O_2 with and without DHA (Fig. 4.7a) and to different concentrations of DHA with and without H_2O_2 (Fig. 4.7b). DHA was not found to increase oxidative stress caused by H_2O_2. C1QTNF5 KO did not affect the susceptibility of iPSC-RPE to oxidative stress. Only the L-ORD iPSC-RPE line LORD4 showed a higher susceptibility to oxidative stress-mediated cell death compared to its isogenic gene-corrected control line (Fig. 4.7a and b). However, LORD3 did not show the same behaviour. iPSC-RPE were also exposed to different concentrations of tBHP, but none of the concentrations used were able to cause oxidative stress-induced cell death (Fig. 4.7c).

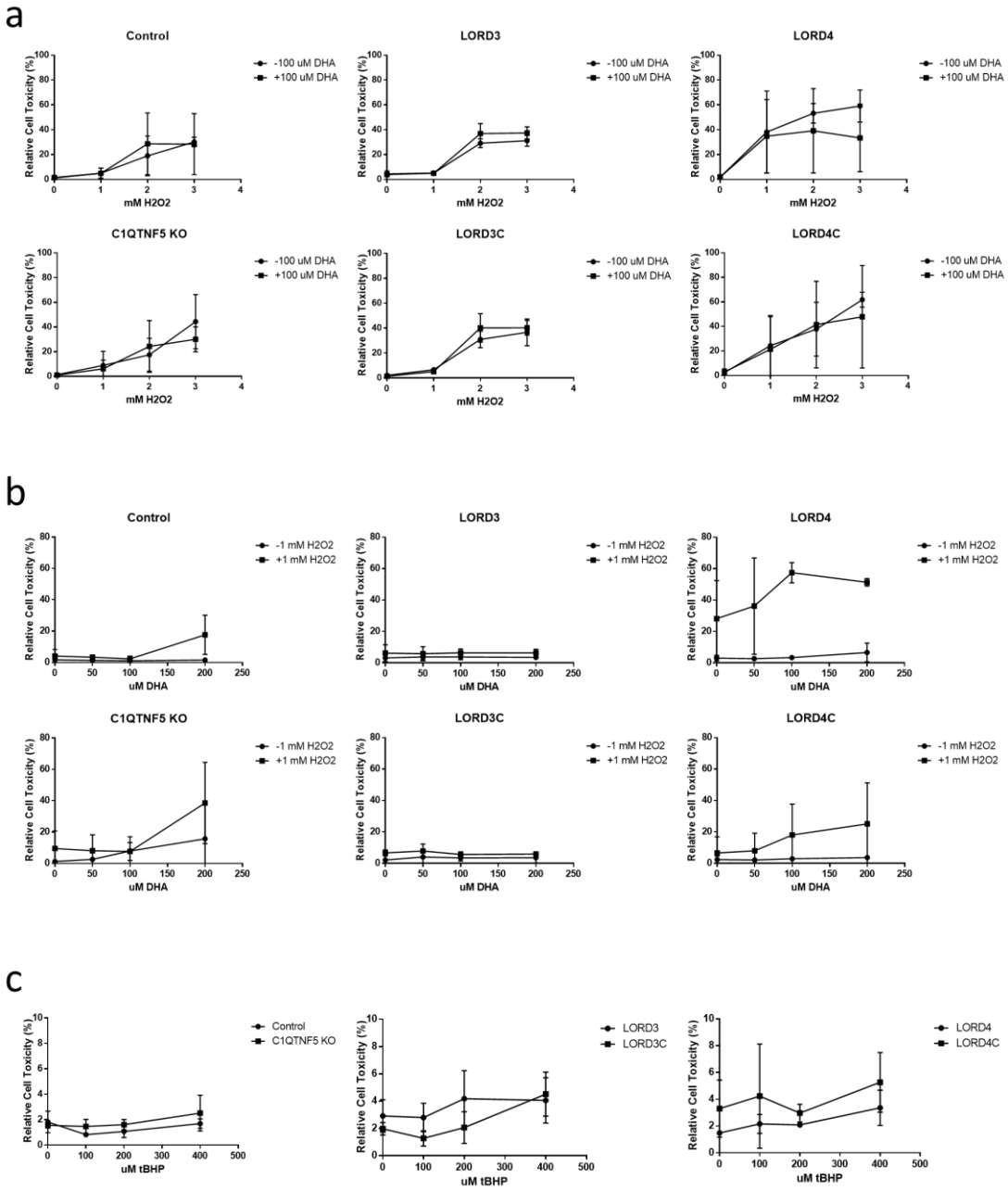

Figure 4.7 | iPSC-RPE cell toxicity after H_2O_2 and DHA exposure. iPSC-RPE lines were exposed for 24 hours to different concentrations of H_2O_2 with and without DHA (**a**), to different concentrations of DHA with and without H_2O_2 (**b**), or to different concentrations of tBHP (**c**) and relative cell toxicity was measured. Error bars represent SD of three independent experiments.

4.3.8 Increased membrane pMLKL in L-ORD iPSC-RPE after H_2O_2 exposure

Even though the iPSC-RPE did not show increased toxicity when stressed with H_2O_2, it is still possible to investigate early signs of cell death. Therefore, iPSC-RPE were stained for pMLKL, a marker of necroptosis, after H_2O_2 treatment. pMLKL was found to be increased and located in the plasma membrane of L-ORD iPSC-RPE compared to its isogenic gene-corrected control when oxidatively stressed with H_2O_2, especially in areas where there was cell death (Fig. 4.8a and b). The amount of pMLKL was reduced with Nec-1, GSK'840B, and Fer-1. Although this experiment was performed only once, the result does fit with the RPE cell line data, and possibly confirms a trend where H_2O_2-treated RPE have the proclivity to undergo necroptotic cell death.

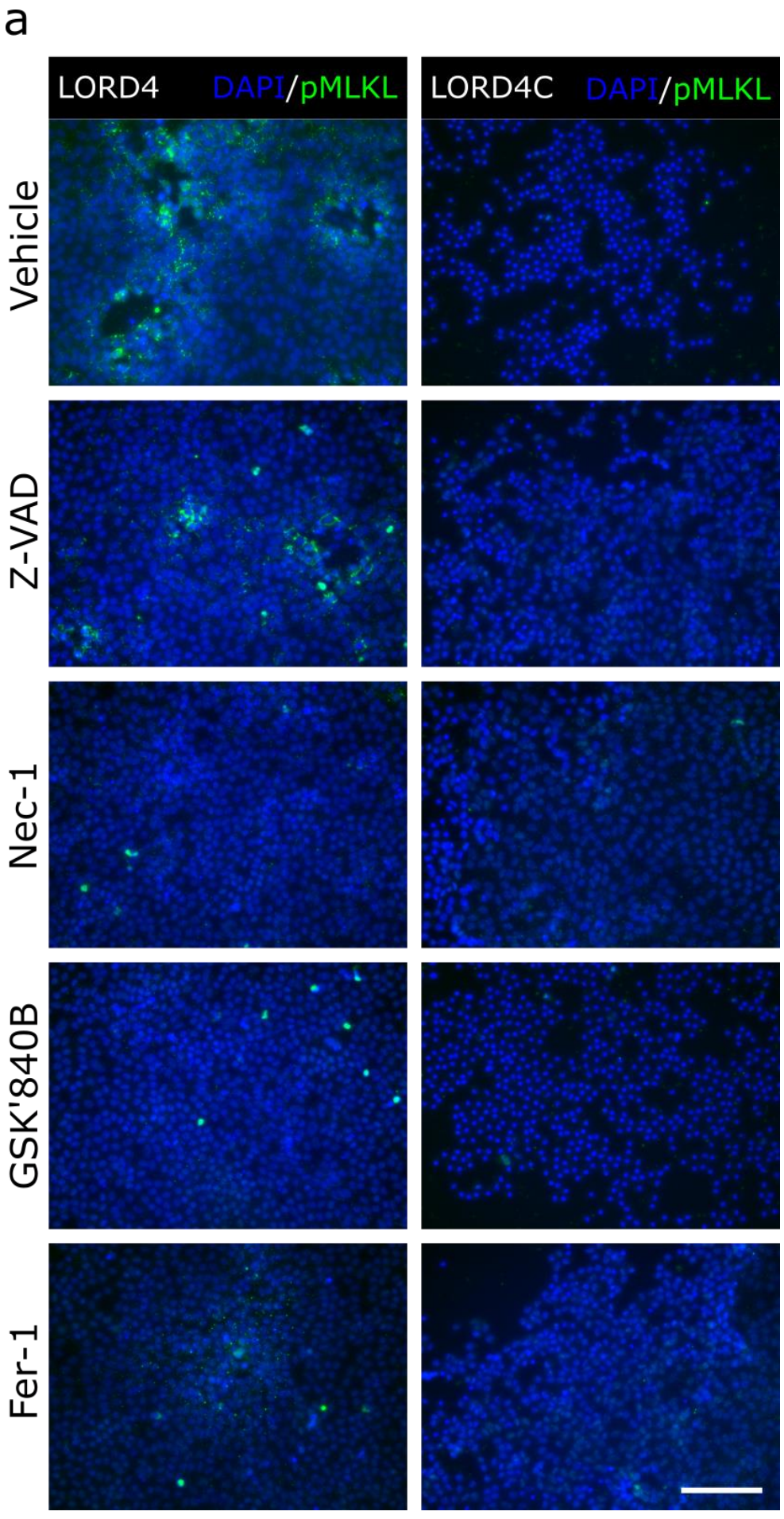
a
LORD4
DAPI/pMLKL
LORD4C
DAPI/pMLKL
Vehicle
Z-VAD
Nec-1
GSK'840B
Fer-1

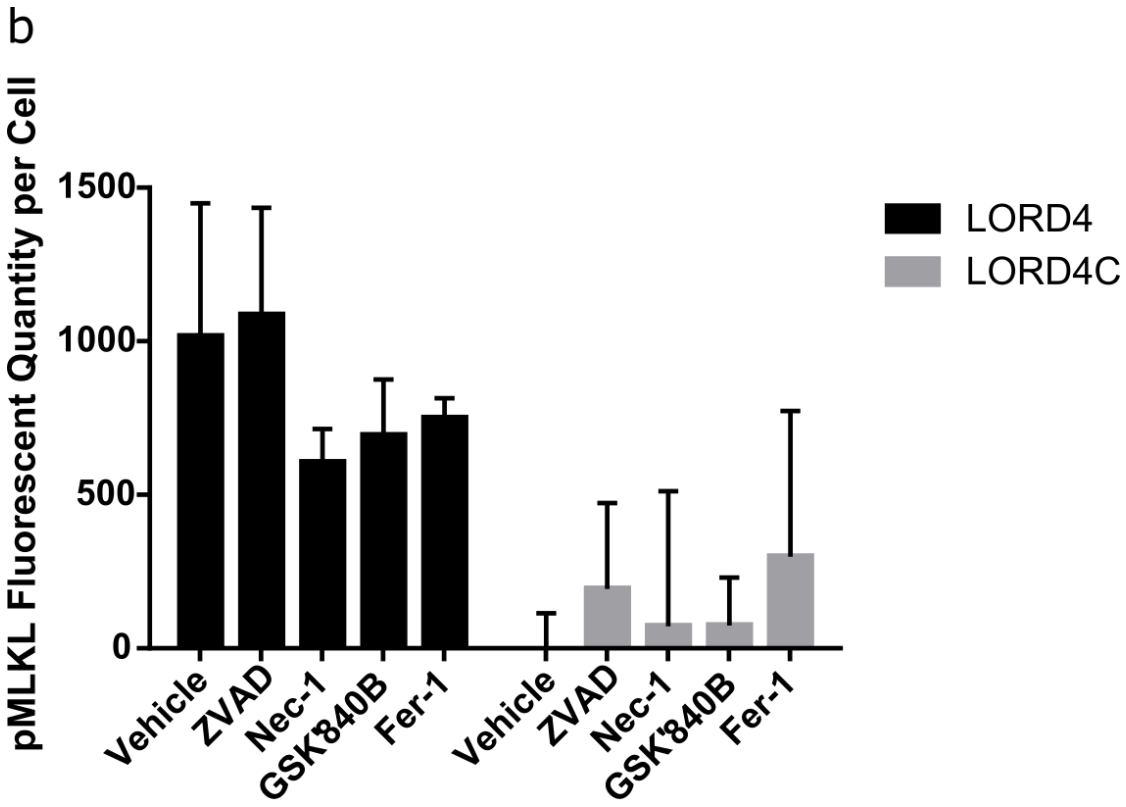

Figure 4.8 | pMLKL is increased in L-ORD iPSC-RPE after H_2O_2 exposure. iPSC-RPE cells were treated with 40 µM Z-VAD, 40 µM Nec-1, 1 µM GSK'840B or 5 µM Fer-1 24 hours before injury. Subsequent 18-hour treatment with 1 mM H_2O_2 shows increase of pMLKL staining in L-ORD iPSC-RPE (**a** and **b**). Pre-treatment with Nec-1, GSK'840B, and Fer-1 reduces the amount of pMLKL after injury. Scale bar equals 100 µm. Error bars represent SD of three technical repeats.

4.3.9 UV exposure of iPSC-RPE

RPE can also be photo-oxidatively stressed with UV radiation. Exposure of L-ORD iPSC-RPE to UVA light (340 nm) resulted in a relative more rapid decline in cellular impedance measured by ECIS (Fig. 4.9a). This could signify increased cell death caused by the UV irradiation and a subsequent detachment of the cells form the ECIS arrays. Furthermore, the cell viability of L-ORD iPSC-RPE was lower compared to its isogenic gene-corrected control when exposed to UVB light (290 nm; Fig. 4.9b). Although these experiments were performed only once, together they suggest that L-ORD iPSC-RPE are more sensitive to UV-mediated photo-oxidative stress.

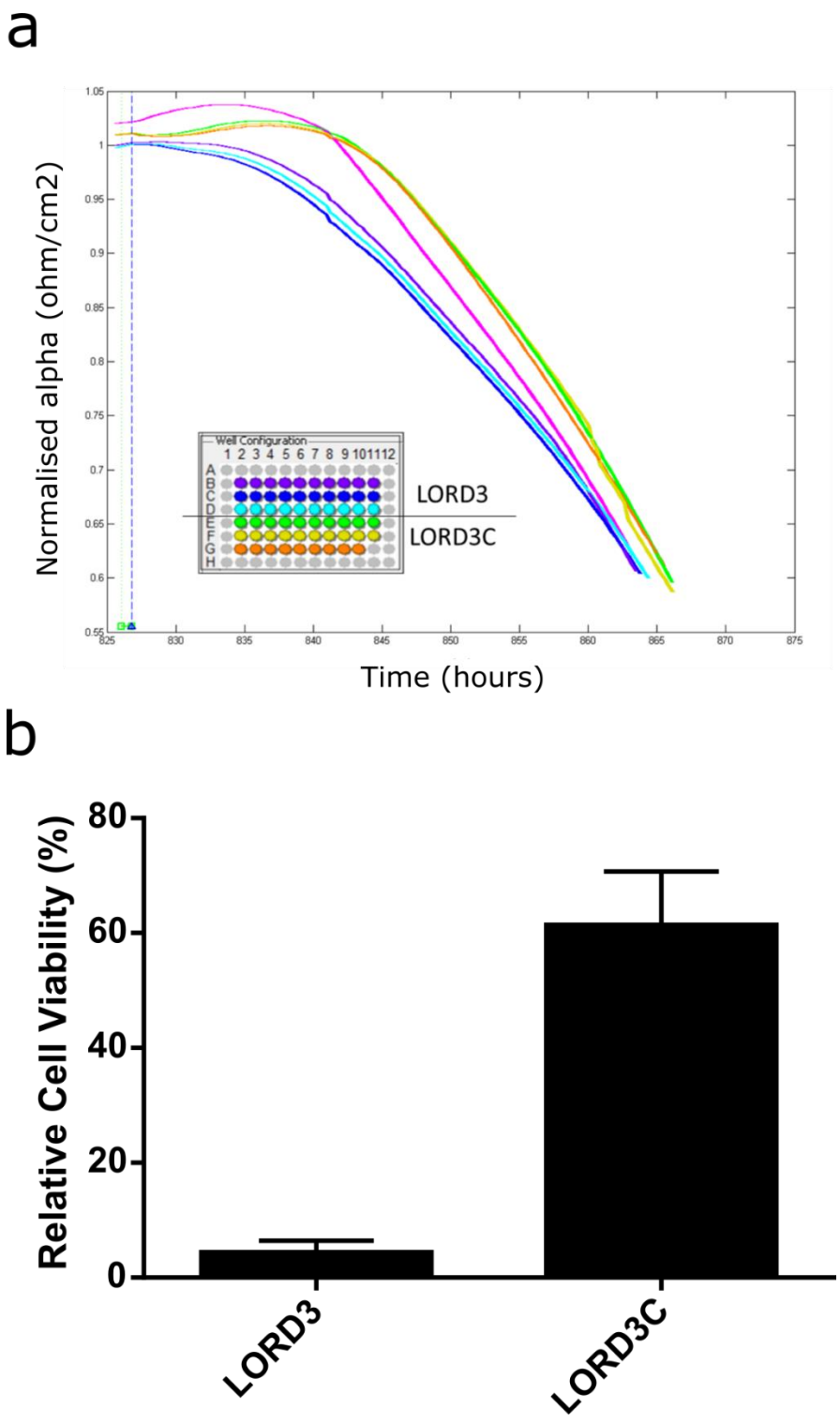

Figure 4.9 | Adherence and cell viability differences in L-ORD iPSC-RPE when exposed to UV light. LORD3 (purple, blue, and cyan) and LORD3C (green, yellow, and orange) iPSC-RPE were exposed to 340 nm UV for 24 hours and ECIS was recorded after exposure (**a**). LORD3 and LORD3C iPSC-RPE were also exposed to 290 nm UV for 24 hours, incubated for another 24 hours, stained with DRAQ7, and analysed and quantified with flow cytometry (**b**). Error bars represent SD of three technical repeats.

4.4 Discussion

Oxidative stress is important in the pathology of AMD. Especially RPE endure high levels of oxidative stress in the retina. RPE can cope with high levels of oxidative stress but dysfunction of RPE or an excess of oxidative stress could cause RPE cell death as part of the AMD pathology. Investigating the cause of oxidative stress and the subsequent effects it has on RPE could lead to a better understanding of how RPE die in AMD and could potentially lead to the development of new therapies for AMD. Here, I have shown that oxidative stress in RPE leads to necrotic cell death and that this could be alleviated with necroptosis and ferroptosis inhibitors. Furthermore, I showed that oxidative stress leads to gene expression changes and that the expression of important ferroptosis regulators are affected.

RPE were found to undergo necrosis rather than apoptosis (Fig. 4.1), similar as what has been found before[306]. Consistent with previous findings, necroptosis inhibitors reduced RPE cell death caused by H_2O_2-induced oxidative stress (Fig. 4.2). The PUFA DHA also caused oxidative stress-mediated cell death that could be alleviated with a necroptosis inhibitor. Furthermore, both H_2O_2- and DHA-mediated cell death could be alleviated with a ferroptosis inhibitor, suggesting that ferroptosis also plays a role in oxidative stress-induced cell death. Together these data show that two forms of regulated necrosis play a role in oxidatively stressed RPE.

H_2O_2, DHA, and POS were found to increase the amount of lipid ROS in RPE (Fig. 4.3), a hallmark of ferroptosis. The ferroptosis inhibitor Fer-1 reduced the amount of lipid ROS. Furthermore, the iron chelator DFO also reduced the amount of lipid ROS, indicating that this process is iron-dependent, like ferroptosis. The amount of lipid ROS could be further increased when RPE were exposed to both H_2O_2 and DHA or H_2O_2 and POS (Fig. 4.3c). This could indicate that the high turnover of DHA that RPE naturally have leave them susceptible to exogenous oxidative stress leading to increased lipid ROS generation and subsequent ferroptotic cell death.

DHA, although able to induce ferroptosis, is essential for normal functioning of the retina. Omega-3 long-chain PUFAs (LC-PUFAs; C20-C22), like DHA, are thought to be protective of the retina[274,292]. It is also thought that omega-3 PUFAs reduce the progression of AMD[324,325]. Approximately 50% of the phospholipids in the vertebrate rod photoreceptors contain DHA[326]. DHA-containing phospholipids are reservoirs for docosanoids, potent bioactive

mediators. The docosanoid neuroprotection D1 (NPD1) forms after oxidative stress and promotes RPE survival[327,328]. Furthermore, another function of DHA is that it serves as a ligand for nuclear hormone receptors such as PPAR-α. However, increasing dietary DHA uptake has shown to improve intermediate AMD, but not advanced AMD[329]. Phospholipids in photoreceptor membranes consist mostly of dipolyunsaturated molecular species. Phosphatidylcholine (PC) phospholipids especially in rod photoreceptors consist of very-long-chain PUFAs (VLC-PUFAs; C≥28) and LC-PUFAs[330]. DHA is the predominant partner of VLC-PUFAs in dipolyunsaturated PC[331,332]. Phospholipids containing VLC-PUFA and DHA are important for proper photoreceptor functioning because a deficit in VLC-PUFA production caused by a mutation in the enzyme ELOVL4 causes Stargardt-like macular dystrophy (STGD3), an autosomal dominant juvenile macular degeneration[332]. Nonetheless, too much DHA in combination with oxidative stress could be detrimental to RPE.

The reduction of lipid ROS by DFO shows that lipid ROS caused by H_2O_2, DHA, and POS is iron-dependent in RPE, consistent with a ferroptotic phenotype. Moreover, patients with AMD have increased accumulation of iron in the retina[298,299]. Iron was also recently found to promote oxidative cell death in the retina[300]. DFO is also commonly used to treat patients with hemosiderosis caused by blood transfusions. However, DFO treatment has been found to be toxic to RPE and to cause retinopathy[333-335]. If ferroptosis is an important form of cell death in AMD it is possible that DFO could be beneficial to RPE instead of toxic.

Oxidative stress of RPE caused by H_2O_2 or DHA resulted in different gene expression changes (Fig. 4.5). SQSTM1, also known as p62, was upregulated in RPE exposed to DHA (Fig. 4.5a). This is consistent with previous findings where DHA induces *SQSTM1* expression and thereby increases autophagy[336]. H_2O_2 and DHA did not cause gene expression changes necessary for apoptosis, suggesting that RPE use an alternate mode of cell death when oxidatively stressed (Fig. 4.5b). However, the ferroptosis inducers ACSL4 and LPCAT3 were both found to be downregulated in RPE exposed to H_2O_2, suggesting that ferroptosis is actively inhibited in RPE (Fig. 4.5c). LPCAT3 was also downregulated in RPE when exposed to DHA. However, it is not yet known if LPCAT3 can incorporate DHA into membranes and thereby can cause ferroptosis. DHA is known to be incorporated in phospholipids by lysophosphatidic acid acyltransferases (LPAATs)[337,338]. *PPARG* expression, important for regulating lipid metabolism, was downregulated in RPE exposed to H_2O_2, but upregulated when exposed to DHA (Fig. 4.5d). This suggests that lipid metabolism regulation is important during oxidative

stress in RPE. This data is also consistent with previous finding where phagocytosis of POS, rich in DHA content, leads to increased *PPARG* expression[339].

The important regulator of ferroptosis ACSL4 was found to be downregulated in RPE exposed to H_2O_2 but not DHA (Fig. 4.5c and 4.6). However, exposure of RPE to both H_2O_2 and DHA even further lowered the expression of ACSL4 (Fig. 4.6). This shows that when DHA is peroxidised by H_2O_2 ACSL4 is even further downregulated. ACSL4 is known to be able to target DHA for conversion to acyl-CoA and subsequent incorporation into phospholipids[340,341]. DHA in cellular membranes is known to efficiently cause ferroptosis[319]. Downregulation of ACSL4 would therefore result in less DHA incorporation into RPE membrane phospholipids, leading to less ferroptosis. A pathway to protect from ferroptosis is possibly activated in RPE when PUFAs are peroxidised to lower ACSL4 expression.

It is thought that necroptosis and ferroptosis can compensate each other when either one is inhibited[342]. Inhibition of ACSL4 is known to promote necroptosis[342]. H_2O_2 was found to downregulate ACSL4 expression (Fig. 4.5 and 4.6) and was also found to increase phosphorylation of MLKL (Fig. 4.4). Phosphorylated MLKL is a hallmark of necroptosis[313]. It is possible that H_2O_2-induced cell death in RPE also inhibits ferroptosis and thereby promotes necroptosis. Neither DHA nor POS alone increased the phosphorylation of MLKL (Fig. 4.4). This suggests that the importance of necroptosis in oxidative stress-induced cell death depends on the cause of oxidative stress in RPE.

H_2O_2-induced oxidative stress was also found to increase phosphorylated MLKL in the plasma membrane of L-ORD iPSC-RPE, especially around areas with cell death (Fig. 4.8). This was found to be less in the isogenic gene-corrected control iPSC-RPE. Moreover, phosphorylated MLKL was found to be reduced with necroptosis inhibitors. Even though this experiment was performed only once, these results suggest that L-ORD iPSC-RPE undergo necroptotic cell death in response to H_2O_2-induced oxidative stress.

The proclivity of RPE to undergo cell death through necroptosis and ferroptosis after oxidative injury have both been found before[306,315]. Ferroptosis in particular seems a logical form of cell death in RPE. RPE accumulate PUFAs through the phagocytosis of DHA-rich POS. DHA when incorporated into cellular membranes is known to efficiently cause ferroptosis[319]. Moreover, CEP adducts generated by an oxidation product unique to DHA are abundant in AMD retinal tissue[73]. This indicates that DHA peroxidation is increased and that ferroptosis could be a common form of cell death in AMD. Furthermore, the levels of the antioxidant

GSH decreases with age and this has been linked to AMD[272]. The important ferroptosis inhibitor GPX4 is GSH-dependent. However, oxidative stress caused by H_2O_2 or DHA did not change the expression of GPX4 or GSH in RPE (Fig. 4.5c).

Control, L-ORD, and C1QTNF5 KO iPSC-RPE seemed to react similarly to H_2O_2-induced oxidative stress (Fig. 4.7). Except LORD4 seemed to be more sensitive at 1 mM H_2O_2. Additional exposure to DHA did not seem to cause more cell death in iPSC-RPE and relatively high concentrations of tBHP did not seem to affect iPSC-RPE. This shows that iPSC-RPE are more robust in handling oxidative stress than RPE cell lines like ARPE-19 and hTERT RPE-1. One explanation for this could be that iPSC-RPE are more similar to primary RPE than RPE cell lines by expressing all the mature RPE markers, pigmenting, and only have a limited capacity to proliferate. It is also possible that iPSC-RPE have a more developed antioxidant defence similar to primary RPE than RPE cell lines.

UV light-induced oxidative stress was found to have a differential response on L-ORD iPSC-RPE compared to its isogenic gene-corrected control. The electrical resistance of L-ORD iPSC-RPE declined faster than compared to its control (Fig. 4.9a), as opposed to the increased resistance of L-ORD iPSC-RPE during proliferation (see Chapter 3). This could indicate that L-ORD iPSC-RPE are more sensitive to UV light-induced oxidative stress and this causes them to detach faster. Moreover, L-ORD iPSC-RPE seemed to be more sensitive to UV light-induced cell death (Fig. 4.9b). Both of these experiments have been performed only once, but together suggest that L-ORD iPSC-RPE are more sensitive to UV-mediated photo-oxidative stress.

DHA and light exposure are known to induce cell toxicity through CEP-adduct formation in RPE[343]. Furthermore, constant illumination causes reduction of DHA through lipid peroxidation and subsequent photoreceptor degeneration in rats[344]. Increased DHA levels are known to increase stress-induced photoreceptor cell death[345]. Conversely, low levels of DHA protect the photoreceptors from light-induced cell death[346]. Although DHA did not show increased cell toxicity in combination with H_2O_2 in RPE, it is possible that DHA levels can influence photo-oxidative stress in a similar way in RPE as in photoreceptors.

The results in this chapter show that RPE undergo regulated necrotic cell death when oxidatively stressed. Importantly, the mode of regulated necrotic cell death seems to depend on how oxidative stress was induced. H_2O_2 seems to induce mostly necroptosis, whereas DHA seems to induce ferroptosis. H_2O_2 also seems to induce more necroptosis in at least one L-

ORD iPSC-RPE line, but there was no difference found between L-ORD and control iPSC-RPE in sensitivity towards H_2O_2- and DHA-induced oxidative stress. However, L-ORD iPSC-RPE were found to be more sensitive to UV light-induced oxidative stress. Together, this shows that RPE have a differential response to different types of oxidative stress and that L-ORD iPSC-RPE are particularly more sensitive to at least one type of oxidative stress.

Chapter 5 Complement System Dysregulation in L-ORD iPSC-RPE

5.1 Introduction

5.1.1 The complement system

The complement system is part of the innate immune system and functions to clear bacteria and damaged cells[347-350]. It complements the antibacterial activity of antibodies, but it can also be activated in the absence of antibodies. The complement system consists of over 30 proteins that react with each other to opsonise pathogens and to induce a series of inflammatory responses. Several complement proteins are zymogens, proteases that are themselves activated by proteolytic cleavage.

The complement system has three functions in immune surveillance[349]. One function is probing of healthy cells by a constant low level of complement activation. The presence of membrane-bound regulators prevents a strong complement system response. Bacteria, however, activate a stronger response induced by various pattern recognition proteins and is strongly amplified in the absence of regulators. This leads to opsonisation of the bacteria by complement proteins and pro-inflammatory signalling. Subsequently, macrophages are recruited for phagocytosis, the membrane attack complex (MAC) is formed for cell lysis, and further downstream immune responses are activated. Pattern recognition proteins also recognise apoptotic cells. Recruited regulator proteins, however, prevent amplification of the complement response and formation of the MAC. Nevertheless, opsonisation still facilitates clearance of the apoptotic cell without a further immune response. When dysregulated, the complement system can also attack healthy cells, leading to immune and inflammatory diseases[348].

The complement system consists of three independent but interacting pathways[349,350]. These are the classical, alternative, and lectin pathways, whose independent activation leads to the formation of the MAC (Fig. 5.1).

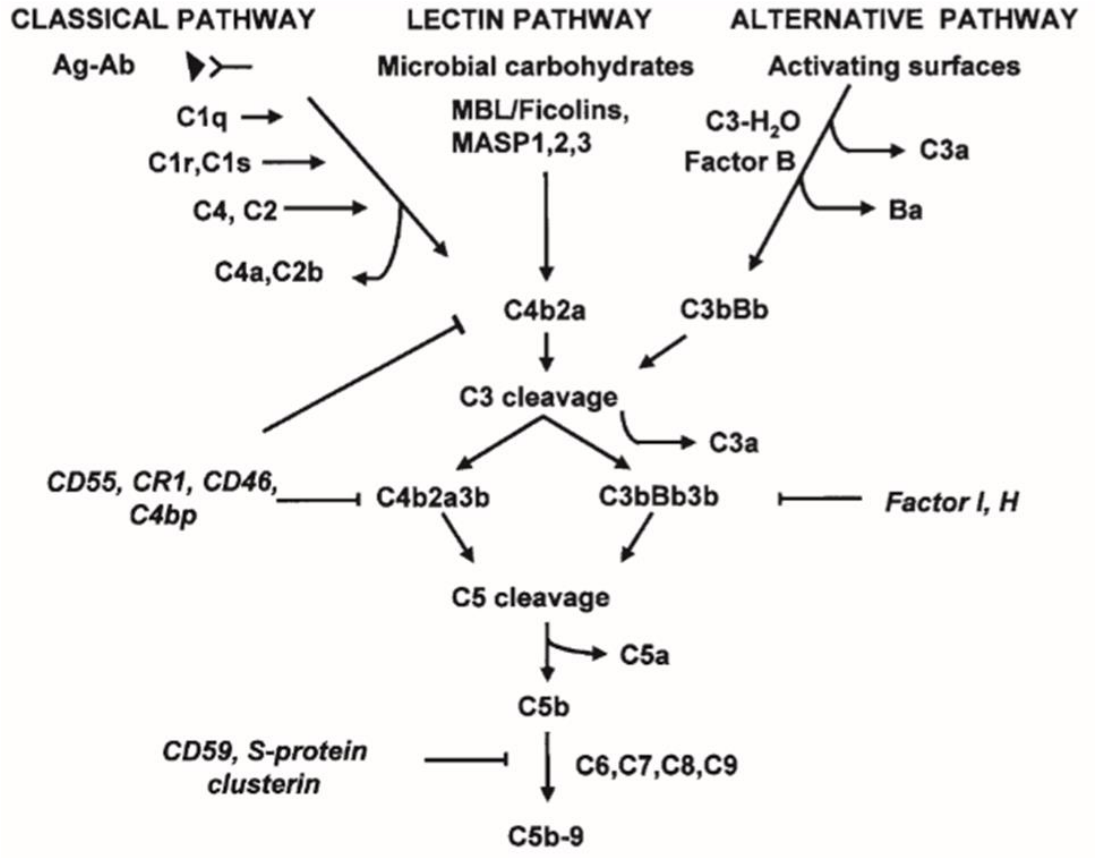

Figure 5.1 | The complement system pathways. The complement system comprises the classical pathway, the lectin pathway, and the alternative pathway, which are initiated by antigen-antibody (Ag-Ab) recognition, microbial carbohydrates, and activating surfaces respectively. The three pathways converge into the terminal complement pathway, which leads to the formation of the C5b-9 complex. Reproduced from Rus et al. (2005)[351].

The classical pathway is activated when IgM or IgG antibodies complexed with antigens bind C1q or when C1q binds the surface of a pathogen (Fig. 5.1). C1q then forms the C1 complex together with two molecules of C1r and two molecules of C1s. C1q bound to an antibody or a pathogen causes conformational changes in C1q. This leads to activation of C1r in the C1 complex and subsequent cleavage of C1s. The active C1 complex cleaves C4 and subsequently C2 into C4a and C4b, and C2a and C2b respectively. C4b then binds C2a to form the C3 convertase (C4b2a complex) and this promotes the cleavage of C3 into C3a and C3b. C3b binds to the C3 convertase to from the C5 convertase (C4b2a3b complex). C3b acts also as an opsonin and binds covalently to a pathogen to mark it for phagocytosis. When bound to a pathogen, C3b can also bind the C5 convertase.

The alternative pathway is continuously activated at a low level. In this pathway, C3 is spontaneously hydrolysed to C3a and C3b (Fig. 5.1). C3b can be further spontaneously hydrolysed into iC3b and C3dg. Complement factor B (CFB) can bind iC3b, which allows complement factor D (CFD) to cleave CFB into Ba and Bb. This results in the formation of a C3 convertase different from the classical pathway (C3bBb complex). This complex is unstable until it binds the serum protein properdin. An additional C3b binds this complex forming the C5 convertase of the alternative pathway (C3bBbC3bP complex).

In the lectin pathway, mannose-binding lectin (MBL) or ficolin bind certain saccharides, as found on carbohydrate or glycoprotein components of pathogen membranes[352] (Fig. 5.1). Multimers of MBL form a complex with MBL-associated serine protease 1 (MASP1), MASP2, and MASP3. MASPs cleave and activate C4 and C2, similar to the C1 complex of the classical pathway. However, unlike the classical pathway, C4b then binds C2b instead of C2a to form the C3 convertase (C4b2b complex). This results therefore also in a different C5 convertase (C4b2b3b complex).

The different C5 convertases generated by the three complement pathways have the same function and lead to the same terminal complement pathway[349,350] (Fig. 5.1). C5 convertase promotes the cleavage of C5 into C5a and C5b. C5b, C6, C7, C8, and C9 assemble a protein complex known as the MAC (C5b-9 complex) which is capable of forming pores in the membranes of pathogens and inducing subsequent cell lysis.

The fragments C3a, C4a, and C5a are anaphylatoxins, small proteins that mediate a number of important effects. These effects include vasodilation and enhanced vascular permeability, release of histamine from mast cells, smooth muscle contraction, chemotaxis, inflammation, and oxygen radical formation[353].

The complement system has the potential to do a lot of damage to host tissue and is therefore tightly regulated[349,350]. There are several regulators of the complement system termed complement control proteins (CCPs). CCPs comprise a range of membrane-associated and soluble, fluid phase, proteins. CCPs contain CCP domains. Two important non-CCP complement regulators are C1 inhibitor and complement factor I (CFI). An important regulator of the classical and lectin pathways is the C1 inhibitor[354,355]. CFI cleaves, as a cofactor of CFH, C3b and C4b and thereby modulates C3 convertase activity of all three complement pathways[356]. Vitronectin and clusterin inhibit the terminal pathway.

5.1.2 Regulation of the alternative pathway

C3b in the alternative pathway is continuously generated and opsonises membrane surfaces in an indiscriminate manner. C3b therefore needs tight regulation to prevent host plasma membranes being targeted by the alternative pathway. Cells of the host express integral membrane proteins that control complement activation. These CCP membrane proteins include CD35 (complement receptor type 1; CR1), CD46 (membrane cofactor protein; MCP), CD55 (decay accelerating factor; DAF), and CD59. CD35, CD46, and CD55 promote C3b inactivation, whilst CD59 prevents MAC formation.

The main regulator of the alternative pathway is CFH[357-359]. CFH is a soluble 150 kDa glycoprotein and contains 20 CCP domains and the N-terminus is responsible for complement regulation[360,361]. CFH has multiple binding sites for C3b[362] and is therefore thought to compete with CFB for C3b to prevent the formation of the C3 convertase of the alternative pathway. RPE expresses CFH[363], and its expression can be downregulated with the pro-inflammatory cytokines TNF-α and IL-6[364], as well as oxidative stress[303,304,365]. In contrast, the pro-inflammatory cytokine IFN-γ can increase CFH expression in RPE[365,366]. The *CFH* gene is located in a cluster with five paralogs on chromosome 1 (1q31.3)[367]. The five *CFH*-related (*CFHR*) gene paralogs are *CFHR1*, *CFHR2*, *CFHR3*, *CFHR4*, and *CFHR5*. It is not yet clear what the function is of the CFHRs. Complete deletion of CFHR1 and CFHR3 is common and confers protection against AMD[368,369].

CFH can also attach to the cell surface with its C-terminus[370-372]. The C-terminus is important for the membrane-associated protective function of host cells by CFH[373]. Host cells can display polyanionic molecules to allow discrimination of self from non-self by binding CFH and thereby providing host protection from C3b[374]. CFH works in concert with CD46, CD55, and CD59 to provide host cell protection from the complement system[373].

RPE is known to express the membrane CCPs CD46, CD55, and CD59[375]. These membrane CCPs were found to be increased in expression in response to inflammatory cytokines[375] and in the presence of activated T-cells[376]. Moreover, CD55 was found to protect RPE from human complement[377]. Oxidative stress reduces the expression of membrane CCPs in RPE, making RPE more susceptible to complement-mediated cell death[304]. This is most likely also due to the oxidative stress-mediated downregulation of CFH. Moreover, RPE were also found to

release microparticles with CD46, CD55, and CD59 after oxidative stress[378]. Therefore, RPE can regulate the alternative pathway of the complement system, but this ability can be modulated by inflammation as well as oxidative stress.

5.1.3 The complement system and AMD

Components of the complement system are small proteins primarily synthesised by liver hepatocytes and released into the bloodstream. Most tissues are therefore dependent on circulating complement system components. Some tissues can however produce complement system components locally. Tissues with limited access to blood such as the brain and the retina mainly produce these components locally[379].

Many genes that confer risk of AMD are involved in the complement system and, in particular, the alternative pathway. Furthermore, complement system proteins are often found in drusen. Dysregulation of the complement system is therefore thought to play an important role in the progression of AMD[380].

A common p.Y402H mutation in *CFH* was found to be strongly associated with AMD[381-385]. The CFH^{Y402H} mutation changes the seventh CCP domain and therefore affects CFH binding to a number of ligands[386]. Notably, CFH was found to bind less to glycosaminoglycan (GAG) chains of proteoglycans. CFH uses GAGs to anchor itself to cell surfaces and the ECM[387]. Less localisation of CFH on cell surfaces and in the Bruch's membrane could lead to local inflammation. Moreover, more C5b-9 was found in the choroid and the Bruch's membrane of individuals with the homozygous CFH^{Y402H} mutation than aged-matched controls[388]. The amount of C5b-9 also increases in the choroid and Bruch's membrane with age[389]. Both *CFH* and *ARMS2*, another gene strongly associated with AMD, are associated with systemic complement system activation when mutated[59].

More complement system gene mutations have been associated with AMD. Mutations in C3 have been associated with increased risk of AMD[390,391]. A p.R102G mutation in *C3* causes reduced binding of C3 to CFH, leading to reduced CFI cofactor activity and subsequent increased C3 convertase lifetime[392]. This results in alternative pathway amplification. In contrast, mutations in *CFB* and *C2* can have a protective effect against AMD[393,394]. A common SNP near *CFI* and a rare mutation in *CFI* have also been associated with an increased risk of AMD[395,396]. However, the precise effects of these mutations are not yet known.

One of the early hallmarks of AMD is deposit-formation between the RPE and the Bruch's membrane, termed drusen[68]. Drusen consist of various proteins and lipid components. It is thought that lipoproteins in drusen could stimulate complement activation[397]. Modified proteins and lipids from damaged RPE also accumulate in drusen and are thought to trigger complement activation[398,399]. Moreover, various components of the complement system as well as activators of this system have been found in drusen[379], including CFH, C3, C5, C6, C7, C8, C9, and C5b-9[73,400,401]. Complement regulatory proteins such as vitronectin and clusterin are also found in drusen[73].

C1QTNF5 is also thought to be involved in complement regulation. C1QTNF5 has been found to bind to CFH (PhD thesis, Dr Slingsby, The University of Edinburgh and PhD thesis, Dr Borooah, The University of Edinburgh). By binding CFH on the cell membrane C1QTNF5 could possibly protect the host cells from complement-mediated inflammation and lysis. In addition, family member C1QTNF6 is found to suppress the alternative complement pathway by competing with CFB for C3 binding[184]. It is possible that C1QTNF5 has a similar function in the retina which could be affected when mutated in L-ORD.

5.1.4 APOE

Apolipoprotein E (APOE) is one of the most common proteins found in AMD drusen[73,77]. APOE is a transport protein for lipids, fat-soluble vitamins, and cholesterol. It is thought that APOE also plays a role in innate immunity[402]. *APOE* is highly expressed in RPE and is a polymorphic gene, with three major alleles: *APOE-ε2* (cys112, cys158), *APOE-ε3* (cys112, arg158), and *APOE-ε4* (arg112, arg158). The allelic different forms alter APOE structure and function and can therefore result in different physiological phenotypes. *APOE-ε4* is known to be a strong genetic risk factor for Alzheimer's disease, whilst *APOE-ε2* is protective. In AMD the reverse is true, *APOE-ε2* is associated with increased risk of AMD and *APOE-ε4* is protective[403]. *APOE-ε2* is associated with increased mononuclear phagocyte infiltration and inflammation in the subretinal space in AMD[404]. However, *APOE-ε2* is a rare variant.

RPE exposed to serum containing the complement system should form deposits on the basal side resembling drusen[405,406]. APOE should also be found in these deposits if it can function as a marker for drusen. In addition, C5b-9 and C1QTNF5 can also be localised to reveal which components are contained in the deposits and if there is a difference between L-ORD iPSC-

RPE and its isogenic gene-corrected control, as well as if there is a difference between C1QTNF5 KO iPSC-RPE and its isogenic control. Localisation of possible drusen components could lead to a better understanding of how drusen are formed.

5.1.5 Aims and objectives

In order to study the response of L-ORD iPSC-RPE to human complement serum, the following was carried out in this chapter:

1. C5b-9 deposition on L-ORD iPSC-RPE after human complement serum exposure was investigated by immunostaining and confocal microscopy
2. iPSC-RPE cytotoxicity after human complement serum exposure was investigated by cell toxicity assays
3. Localisation of C5b-9 with C1QTNF5 on iPSC-RPE after human complement serum exposure was investigated by immunostaining and confocal microscopy
4. Localisation of C5b-9 with APOE on iPSC-RPE after human complement serum exposure was investigated by immunostaining and confocal microscopy

5.2 Materials and methods

5.2.1 Cell culture

iPSCs were cultured as described in Chapter 2 (2.2.1) and were differentiated to RPE as described in Chapter 3 (3.2.2).

5.2.2 Human complement serum treatment and immunocytochemistry

For C5b-9 imaging experiments iPSC-RPE were seeded onto 0.4 µm pore membrane transwell inserts coated with 1 µg/cm^2 of Laminin-521 in a 12-well plate and allowed to mature for four weeks. iPSC-RPE were grown on porous filter supports which allows nutrient supply to the basolateral side and therefore promotes epithelial differentiation closer to native epithelium[227,228]. RPE grown on a porous membrane generate drusen-like deposits in the pores[405].

iPSC-RPE were treated with 40% human complement serum for 12 hours at 37 °C and 5% CO_2. The cells were then washed with PBS and fixed with 4% PFA for 10 min. After another two washes with PBS the cells were permeabilised with 0.1% TritonX-100 for 15 min and subsequently blocked with 3% normal goat serum for 1 hour. Staining with the primary antibody was at 4 °C overnight. The cells were washed twice with PBS and subsequently stained with a secondary Alexa Fluor®-conjugated antibody for 30 minutes and counterstained with 300 nM DAPI for 10 minutes. After another three washes with PBS, the cells were mounted in Fluorsave mounting medium and imaged with a Leica DMi8 inverted microscope (Leica Microsystems). The antibodies and concentrations used are listed in Table S8.

Z-stack images were made with a Zeiss LSM 710 Confocal Laser Scanning Microscope.

5.2.3 Cell toxicity assay

iPSC-RPE were seeded at 7.5*10^3 cells/well in a 96-well plate and cultured for four weeks until mature and confluent. The medium was replaced with DMEM without additions two days before human complement serum treatment. The cells were treated with different

concentrations of human complement serum for 12 hours at 37 °C and 5% CO_2. The medium was subsequently replaced with DMEM without additions and the cells were incubated for another 24 hours at 37 °C and 5% CO_2. The cells were stained with 3 µg/ml Hoechst and 6 µg/ml PI for 20 min at 37 °C and 5% CO_2, and subsequently fixed with pre-warmed 4% PFA for 10 minutes. After three washes with PBS the cells were imaged with a Zeiss Axio Observer Z1 motorised inverted microscope with an automatic stage.

5.2.4 Statistics

Experiments were repeated at least three times. Statistical analysis was performed using Microsoft Excel version 1905 and GraphPad Prism 6 software. Student's *t*-tests were used to determine statistical significance between groups. *P*-values of less than 0.05 were considered to be statistically significant.

5.3 Results

5.3.1 C5b-9 binds more to L-ORD iPSC-RPE after human serum exposure

iPSC-RPE were exposed to human serum containing active complement system pathways. If complement system regulation is compromised, more terminal complement system complex C5b-9 should bind to the iPSC-RPE. Exposure to human complement serum resulted in higher levels of C5b-9 deposits on L-ORD iPSC-RPE compared to its isogenic gene-corrected control (Fig. 5.2a and b). No difference in C5b-9 binding was found between C1QTNF5 KO iPSC-RPE and its isogenic control.

Confocal microscopy can be used to image the iPSC-RPE monolayer in multiple layers on the Z-axis. These layers can be stacked to construct a Z-stack, which provides positional information on the Z-axis. The constructed Z-stack image essentially provides a side view of the iPSC-RPE monolayer allowing to discriminate between the apical and basal side of the cells. Using this method, the binding of C5b-9 to iPSC-RPE was found to occur mostly at the basal side and less frequent at the apical side as protein aggregates (Fig. 5.2c).

a

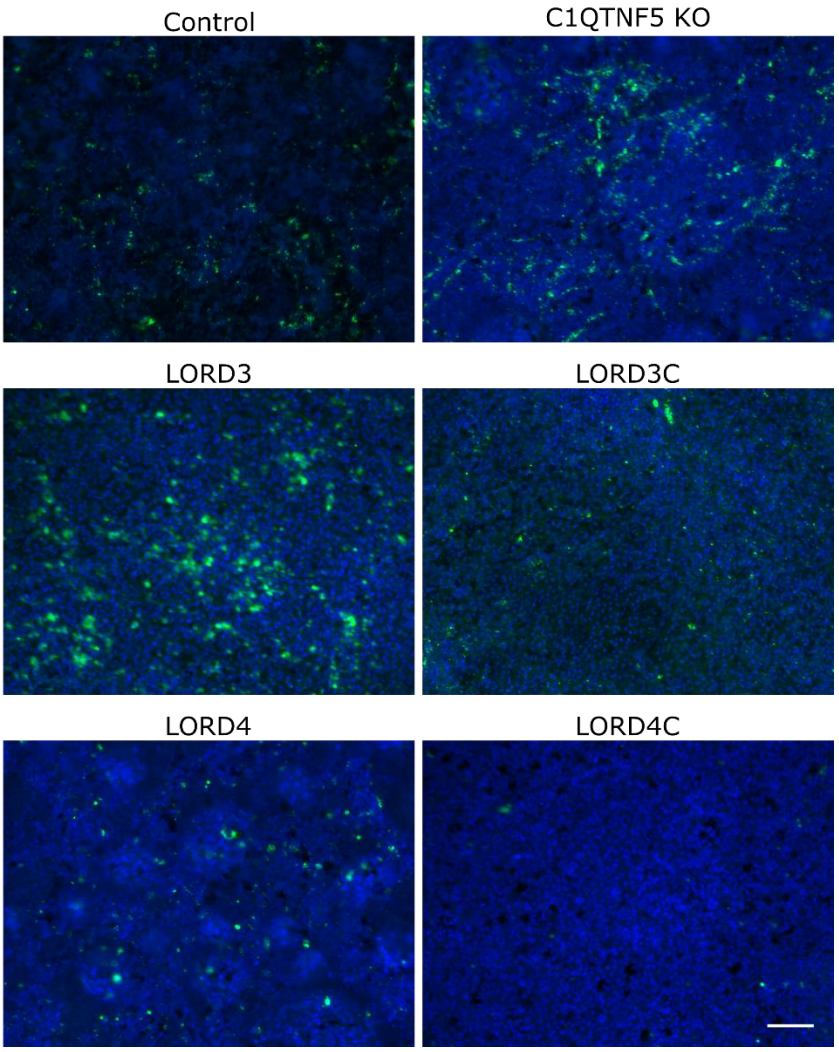

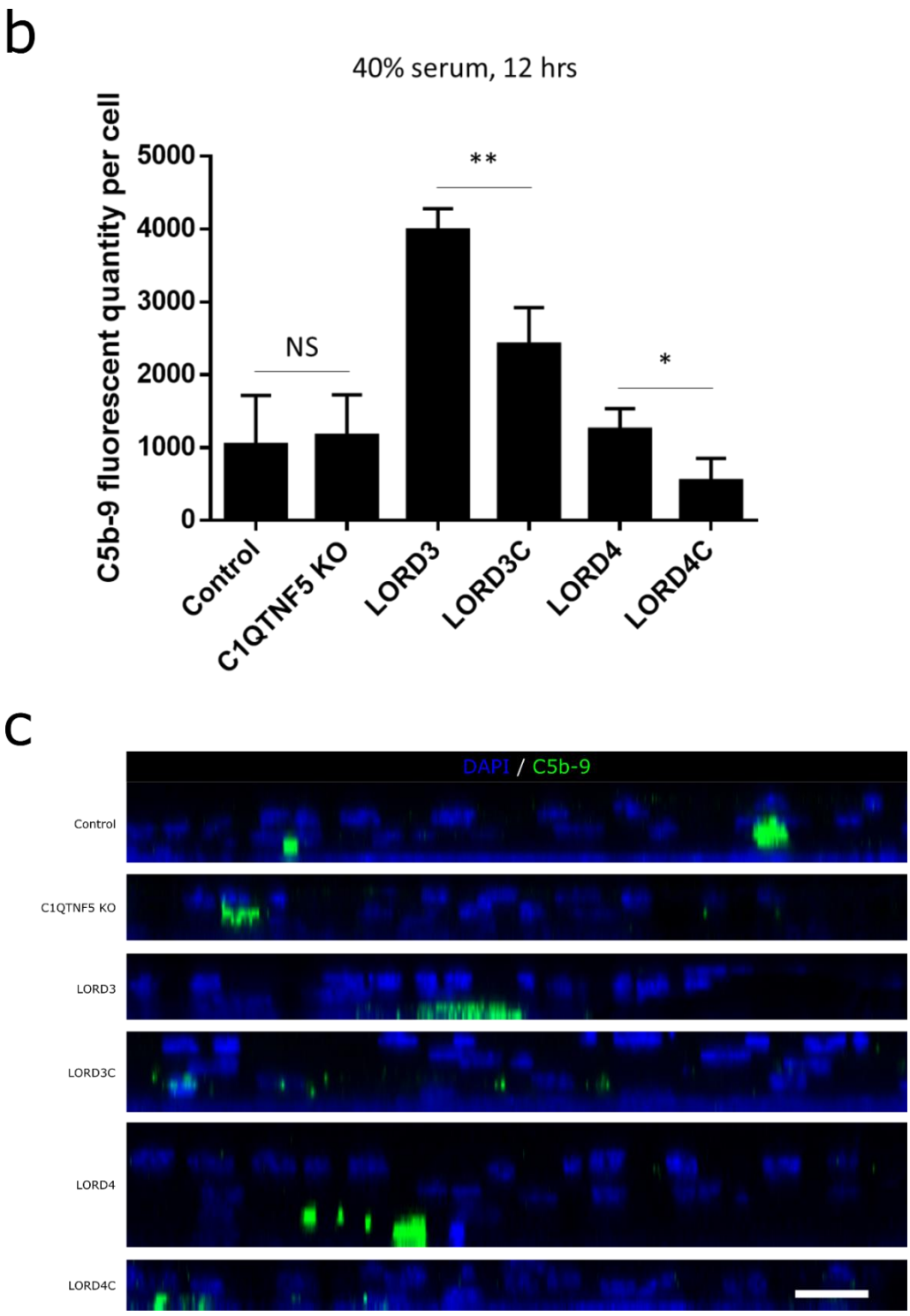

Figure 5.2 | L-ORD iPSC-RPE bind more C5b-9 after human complement serum exposure. Control, C1QTNF5 KO, LORD3, and LORD3C iPSC-RPE were exposed for 12 hours to 40% human complement serum. L-ORD iPSC-RPE bind more C5b-9 than control and C1QTNF KO iPSC-RPE lines (**a** and **b**). C5b-9 binds mostly to the basal side of iPSC-RPE as shown in a Z-stack image (**c**). Scale bar **a** equals 100 µm. Scale bar **c** equals 20 µm. Error bars represent SD of at least three independent experiments. **P*<0.05, ***P*<0.01, NS = non-significant, determined by *t*-test compared to respective isogenic control line.

5.3.2 iPSC-RPE are resistant to human serum exposure

Increased binding of C5b-9 could lead to more complement-mediated cell death. To investigate if increased C5b-9 binding results in more iPSC-RPE cell death, iPSC-RPE were exposed to different concentrations of human complement serum and cell toxicity was measured 24 hours after exposure. No increased cell toxicity was found for any of the concentrations used of human complement serum for this length of exposure (Fig. 5.3).

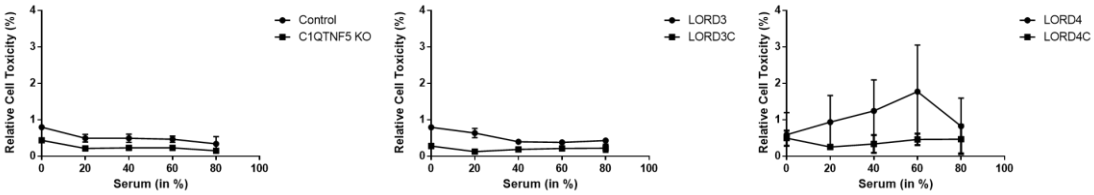

Figure 5.3 | iPSC-RPE cell toxicity after human complement serum exposure. iPSC-RPE lines were exposed for 12 hours to different concentrations of human complement serum and relative cell toxicity was measured with PI staining 24 hours after exposure. Error bars represent SD of three independent experiments.

5.3.3 C5b-9 colocalises only apically with C1QTNF5 after human serum exposure

To investigate the role of C1QTNF5 in regulating the binding of C5b-9 to iPSC-RPE, both C5b-9 and C1QTNF5 were localised on iPSC-RPE through immunostaining. C1QTNF5 did not seem to colocalise with all C5b-9 deposits (Fig. 5.4a). Using confocal microscopy, multiple cross sections of the iPSC-RPE monolayer were imaged and a Z-stack was constructed to determine protein localisation on the apical/basal axis. The Z-stack image showed colocalisation of C1QTNF5 with C5b-9 only at the apical side of the iPSC-RPE in deposits (Fig. 5.4b). No difference in colocalisation was seen between wt and L-ORD iPSC-RPE.

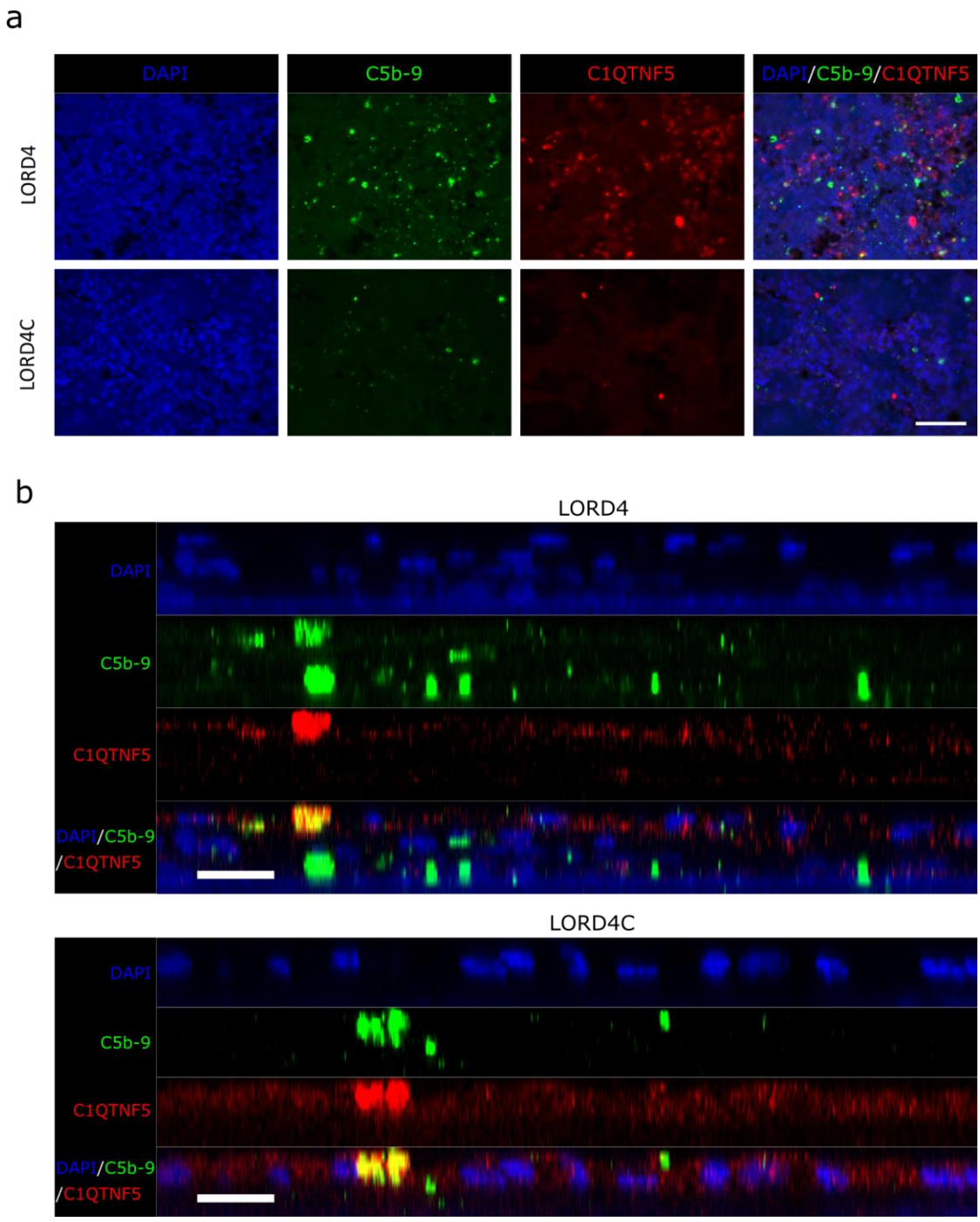

Figure 5.4 | C5b-9 and C1QTNF5 colocalise in aggregates on the apical side of iPSC-RPE. LORD4 and LORD4C iPSC-RPE were exposed for 12 hours to 40% human complement serum. C5b-9 did not appear to colocalise often with C1QTNF5 (**a**). C5b-9 did colocalise with C1QTNF5 in aggregates on de apical side of iPSC-RPE as shown in a Z-stack image (**b**). Scale bar **a** equals 100 µm. Scale bar **b** equals 20 µm.

5.3.4 C5b-9 colocalises with APOE after human serum exposure

APOE is highly expressed by RPE and is often found in AMD drusen[73,77]. L-ORD sub-RPE drusen-like deposits could likely also contain APOE. C5b-9 and APOE were found to colocalise together, typically in deposits (Fig. 5.5a). The colocalisation of C5b-9 and APOE in aggregates was found to be on both the apical as well as basal side of the iPSC-RPE (Fig. 5.5b). No difference was seen in colocalisation between wt and L-ORD iPSC-RPE.

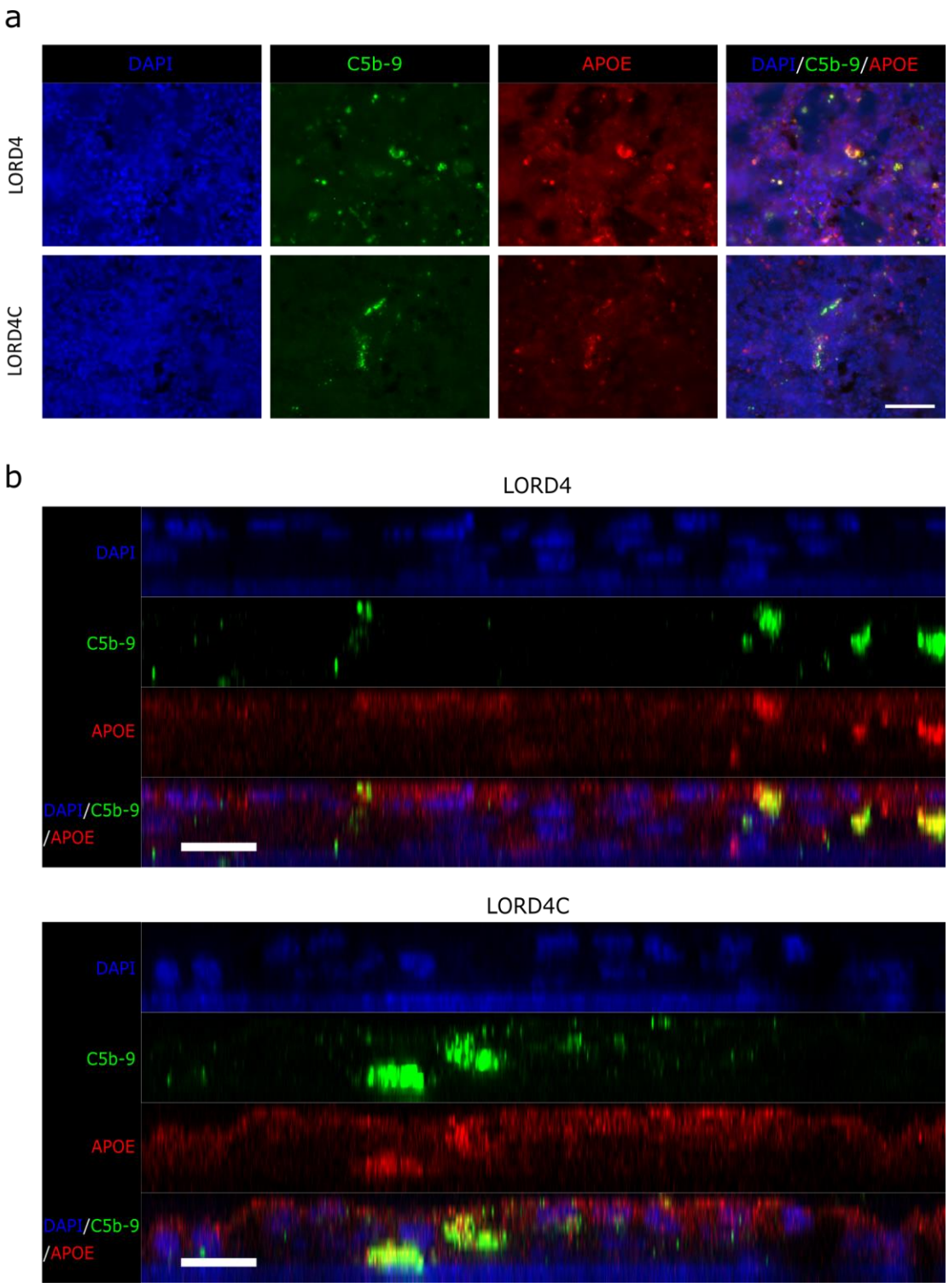

Figure 5.5 | C5b-9 and APOE colocalise in aggregates on iPSC-RPE. LORD4 and LORD4C iPSC-RPE were exposed for 12 hours to 40% human complement serum. C5b-9 colocalises with APOE (**a**). C5b-9 colocalises with APOE in aggregates on iPSC-RPE (**b**). Scale bar **a** equals 100 µm. Scale bar **b** equals 20 µm.

5.4 Discussion

Complement system activation is important in the onset and progression of AMD. Several genes that confer a high risk of AMD when mutated encode for complement system proteins. Furthermore, complement system proteins are found in abundance in drusen, the hallmark of AMD. Here, I showed that C5b-9 binds relatively more to L-ORD iPSC-RPE, that C5b-9 colocalises apically with C1QTNF5, and that C5b-9 colocalises with APOE in deposit-like aggregates. These results indicate a role for complement system dysregulation in L-ORD that is similar in AMD.

iPSC-RPE treated with human complement serum resulted in more C5b-9 binding to L-ORD iPSC-RPE compared to its isogenic gene-corrected control (Fig. 5.2). Binding of C5b-9 to iPSC-RPE was found to be predominantly to the basal side (Fig. 5.2c). Increased binding of C5b-9 could potentially lead to more complement-mediated cell death. However, more binding of C5b-9 to L-ORD iPSC-RPE did not seem to affect cell toxicity (Fig. 5.3) and KO of C1QTNF5 did not seem to cause any difference in C5b-9 binding (Fig. 5.2). This indicates that the C1QTNF5^{S163R} has a specific negative effect on iPSC-RPE, leading to more C5b-9 binding.

C1QTNF5 exogenously expressed in RPE cell lines is known to be able to bind to CFH (PhD thesis, Dr Slingsby, The University of Edinburgh and PhD thesis, Dr Borooah, The University of Edinburgh). It is therefore possible that C1QTNF5 has a role in regulating CFH and that this role is compromised by the L-ORD mutation. This could explain why there is more C5b-9 binding to L-ORD iPSC-RPE.

Treatment of iPSC-RPE with human complement serum resulted in mostly basal C5b-9 aggregates resembling drusen-like deposits (Fig. 5.2c). Some apical pseudodrusen-like deposits were observed as well. Pseudodrusen are drusen-like deposits in the subretinal space between the photoreceptors and the RPE[407,408]. Only the apical pseudodrusen-like deposits contained both C5b-9 and C1QTNF5 (Fig. 5.4b). It is possible that C1QTNF5 only facilitates CFH binding to the cell surface and subsequent complement system protection at the apical side of RPE. Since C1QTNF5 is secreted on both sides of iPSC-RPE (Fig. 3.7b), it is possible that C1QTNF5 binds differently to CFH when not bound to a cell surface.

All C5b-9 deposits contained accumulation of APOE (Fig. 5.5). APOE is a common component found in drusen[73,77]. APOE could therefore possibly function as a marker of drusen. Exposure

of human fRPE or iPSC-RPE to exogenous serum is known to produce sub-RPE deposits containing both C5b-9 and APOE[405,406]. Importantly, in iPSC-RPE models of SFD and ML/DHRD, also C5b-9 and APOE-containing deposits were formed after serum exposure but did not affect the number of deposits[406]. L-ORD iPSC-RPE were also found to have similar amounts of APOE-containing deposits compared to control. The thickness of sub-RPE deposits between L-ORD and control was also previously found to be not significantly different (PhD thesis, Dr Borooah, The University of Edinburgh).

RNA-seq data analysis revealed that *CFI* was significantly downregulated and *CD55* was significantly upregulated in L-ORD iPSC-RPE (see Chapter 3). Downregulation of CFI would lead to less cleavage of C3b and C4b, increased lifespan of the C3 convertase, and subsequent amplification of the alternative complement pathway. However, *CD55* expression was upregulated in L-ORD iPSC-RPE and CD55 also promotes C3b and C4b inactivation. It is possible that L-ORD iPSC-RPE react to the increased amount of C5b-9 binding by increasing cell-surface bound CD55 expression for protection at the expense of soluble CFI expression.

These results show that dysregulation of the complement system is a pathological feature of L-ORD, similar to AMD. C1QTNF5 possibly has a direct role in the regulation of the complement system by binding CFH. The *C1QTNF5*^{S163R} mutation caused more binding of C5b-9 to the cell surface, likely due to aberrant regulation of the complement system. C1QTNF5 was also found to localise with C5b-9 at the apical surface of iPSC-RPE. C5b-9 was also found to localise with APOE in deposits. Together, these results show that L-ORD iPSC-RPE respond differently to complement system attack and C1QTNF5 could have a direct role in regulating this.

Chapter 6 Discussion

6.1 AMD and L-ORD

AMD is one of the leading causes of vision loss, affecting nearly 200 million people worldwide in 2020[48]. With an ageing global population, this is expected to increase. An increase in AMD prevalence will inevitably increase the burden on health care systems worldwide. AMD is a complex disease with both environmental and genetic risk factors. Unfortunately, there is still a lack of understanding about the molecular mechanisms affected in AMD. Hereditary macular degenerations are relatively rare but often have a very similar clinical presentation to AMD. Hereditary macular degenerations therefore are likely to have similar molecular pathways affected and studying these diseases could therefore contribute to the understanding of macular degeneration onset and progression. One of these diseases is L-ORD. L-ORD is caused by a single mutation in *C1QTNF5* but it is not yet clear what the function is of C1QTNF5. C1QTNF5 likely plays a role in molecular pathways that can lead to macular degeneration when dysregulated. Studying C1QTNF5 could reveal its function and could uncover currently unknown molecular mechanisms that lead to macular degeneration. To this end, L-ORD patient-derived iPSCs were gene corrected using CRISPR/Cas9, differentiated into RPE, and these iPSC-RPE were used to study the C1QTNF5 protein, transcriptomics, and cellular pathways typically affected in macular degeneration (Fig. 6.1).

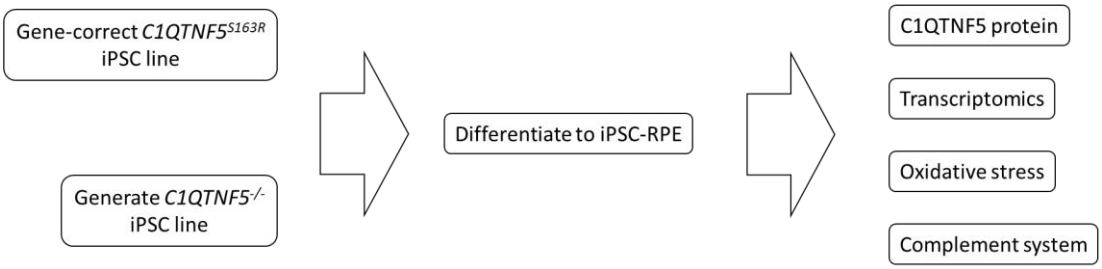

Figure 6.1 | Experimental overview. L-ORD patient-derived iPSCs were gene edited by using CRISPR/Cas9 to correct the L-ORD mutation. In addition, a C1QTNF5 null line was generated by using CRISPR/Cas9. These iPSC lines were then differentiated to RPE. These iPSC-RPE were used to study the C1QTNF5 protein function, to analyse and compare using RNA-seq, and to study macular degeneration-specific affected cellular processes such as oxidative stress and the complement system.

6.2 The main findings of this study

Gene editing allows for the study of the effect of a single mutation causing a disease. L-ORD patient-derived iPSC lines were therefore *C1QTNF5* gene-corrected to generate isogenic pairs with an efficiency of 7.8%. In addition, *C1QTNF5* was knocked out in a wt iPSC line in both alleles with an efficiency of 4.3%. Absence of C1QTNF5 could contribute to the understanding of the function of the protein. No evidence was found for off-target editing for any of the gRNAs used.

L-ORD, gene-corrected, wt, and C1QTNF5 KO iPSC lines were differentiated to RPE. iPSC-RPE generated had RPE-like morphology and functionality. However, L-ORD iPSC-RPE were found to possibly adhere differently to the substrate compared to their isogenic gene-corrected control, indicating a possible function of C1QTNF5 in cellular adhesion. L-ORD and C1QTNF5 KO iPSC-RPE were found to phagocytose more, indicating a possible function of C1QTNF5 in regulating phagocytosis.

The C1QTNF5^{S163R} mutation that causes L-ORD was found to have a destabilising effect on the octadecamer quaternary structure of C1QTNF5. C1QTNF5 was also found to be expressed in cortical astrocytes and oligodendrocytes. Transcriptomic comparison of L-ORD iPSC-RPE and its isogenic gene-corrected control revealed differences in MMPs expression which are responsible for ECM remodelling, PLINs expression which are involved in dark adaptation, lipid metabolism, oxidative stress management, complement system regulation, macrophage recruitment, and calcium regulation. These transcriptomic differences are in line with the symptoms that L-ORD patients present.

One of the main environmental risk factors for AMD is oxidative stress. RPE cell lines were found to undergo necroptosis and ferroptosis in response to oxidative stress. However, iPSC-RPE were found to be very resistant to oxidative stress. LORD4, but not LORD3, iPSC-RPE were found to be more sensitive to H_2O_2-induced oxidative stress at high concentrations. LORD3 iPSC-RPE did seem to be more affected by UV light-induced photo-oxidative stress in preliminary experiments.

Dysregulation of the complement system has often been implicated in AMD. The terminal complement system complex C5b-9 was found to bind more often to L-ORD iPSC-RPE compared to its isogenic gene-corrected control when exposed to human serum containing active complement system pathways. C5b-9 was found to bind mostly to the basal side of

iPSC-RPE and typically in aggregates resembling drusen-like deposits. Moreover, APOE, commonly found in drusen, colocalised in these drusen-like deposits with C5b-9. C5b-9 was occasionally found in apical pseudodrusen-like deposits, where it colocalised with C1QTNF5.

6.3 Effects of the p.S163R mutation on C1QTNF5 function in L-ORD iPSC-RPE

Structurally, it is known that C1QTNF5^{S163R} assembles into multimers with wt C1QTNF, and C1QTNF5^{S163R}-containing multimers are unable to assemble HMW multimers[165] (Fig. 3.7c). The *C1QTNF5^{S163R}* mutation causing L-ORD is thought to be a dominant negative mutation, based on the ability of C1QTNF5^{S163R} to retain wt C1QTNF5 inside the cell[165]. This was not observed in this study, as wt and L-ORD iPSC-RPE secreted equal amounts of C1QTNF5 (Fig. 3.7a). L-ORD iPSC-RPE and C1QTNF5 KO iPSC-RPE both showed increased phagocytosis of POS compared to their isogenic controls (Fig. 3.5). This could indicate that C1QTNF5^{S163R} is a loss-of-function mutation. However, serum treatment of L-ORD iPSC-RPE showed increased binding of C5b-9 which was not observed in C1QTNF5 KO iPSC-RPE (Fig. 5.2). This could indicate that the C1QTNF5^{S163R} mutation is a gain-of-function mutation instead. The C1QTNF5^{S163R} mutation leads to a loss of function if the C1QTNF5 octadecamer is the functional unit for phagocytosis regulation. Therefore, depending on the cellular process C1QTNF5 is involved in, the C1QTNF5^{S163R} mutation could lead to either a loss of function or a gain of function.

6.4 Altered lipid metabolism and oxidative stress response in L-ORD iPSC-RPE

RNA-seq data revealed that catalase was significantly upregulated in L-ORD iPSC-RPE (Table 3.1a) and is part of a metabolic network affected in L-ORD (Fig. 3.9a). Catalase is an important antioxidant in RPE and protects the RPE from ROS produced during phagocytosis[280,281] (see section 4.1.3). Increased phagocytic capability found in L-ORD iPSC-RPE (Fig. 3.5) could explain why the L-ORD iPSC-RPE would need to upregulate catalase expression. However, L-ORD iPSC-RPE still showed increased pMLKL staining when treated with H_2O_2 (Fig. 4.8) and were more sensitive to photo-oxidative stress (Fig. 4.9).

Increased phagocytosis found in L-ORD iPSC-RPE and C1QTNF5 KO iPSC-RPE (Fig. 3.5) could lead to more accumulation of DHA in the RPE. This provides an increased pool of PUFAs that

can be peroxidised, leading to increased sensitivity to oxidative stress. In addition, RNA-seq data revealed that L-ORD iPSC-RPE have an altered (lipid) metabolism (Table 3.2a and Fig. 3.9a). If DHA is more incorporated in RPE cell membranes because of the increased DHA pool, it is possible that RPE are more susceptible to oxidative stress-mediated cell death through ferroptosis. However, the combination of H_2O_2 and DHA did not show any increased cell death of L-ORD or C1QTNF5 KO iPSC-RPE (Fig. 4.7). Nonetheless, this could be dependent on the concentrations used and the length of the treatment. In addition, a cellular pathway involved in both cell death and survival was significantly changed in L-ORD iPSC-RPE (Fig. 3.9b), indicating that iPSC-RPE cell death and survival is tightly regulated.

6.5 Protection from oxidative stress by CFH is possibly affected in L-ORD

CFH can bind the lipid peroxidation product MDA (see section 4.1.2) and thereby protects from oxidative stress[409]. CFH also interacts with oxidised phospholipids[410]. The AMD risk mutation *CFH*^{Y402H} leads to less binding of CFH to MDA[409]. MDA is known to have oxidation-specific epitopes that can trigger both innate and adaptive immune responses[267]. CFH therefore appears to have an important function in regulating oxidative stress. However, it is known that oxidative stress can downregulate the expression of CFH in RPE[303,304,365]. In addition, oxidative stress makes the RPE more susceptible to complement system-mediated cell death[304,411]. C1QTNF5 has been shown to be able to bind to CFH (PhD thesis, Dr Slingsby, The University of Edinburgh and PhD thesis, Dr Borooah, The University of Edinburgh) and could therefore have a function in oxidative stress regulation together with CFH.

6.6 Changes in ECM remodelling in L-ORD iPSC-RPE

RNA-seq data revealed changes in ECM remodelling in L-ORD iPSC-RPE (Table 3.2). Several proteins have been identified that when mutated cause an increased risk to AMD or directly cause macular degeneration, such as EFEMP1 and TIMP3 (see section 1.5). The hallmark of AMD, the formation of drusen, is also located in the ECM on the basal side of the RPE.

Changes in the ECM caused by the *EFEMP1*^{R345W} mutation are known to cause RPE to produce deposits and to activate the alternative complement pathway[412]. It is possible that ECM changes caused by *C1QTNF5*^{S163R} mutation could have a similar effect. Moreover, it was found that L-ORD iPSC-RPE treated with human complement serum developed more C5b-9-

containing deposits (Fig. 5.2c). These drusen-like deposits also contained APOE, a protein commonly found in drusen (Fig. 5.5).

6.7 Dysregulated complement regulation in L-ORD iPSC-RPE

CFI expression was found to be significantly downregulated in L-ORD iPSC-RPE (see Chapter 3). CFI is an important regulator of the complement system (see sections 5.1.1 and 5.1.2). CFI functions as an important cofactor for CFH to cleave C3b and C4b[356]. Downregulation of CFI would therefore cause more generation of the C3 convertase and amplify the alternative complement pathway. This could explain the increased amount of C5b-9 binding to L-ORD iPSC-RPE (Fig. 5.2). Mutations in and near *CFI* have been associated with AMD[395,396] (see section 5.1.3). CD55 was, however, found to be significantly upregulated in L-ORD iPSC-RPE (see Chapter 3). CD55 is also an important regulator of the complement system (see section 5.1.2) and is known to protect RPE from human complement[377].

6.8 Macular degeneration and dementia

AMD has in the recent years often been linked to dementia, and in particular Alzheimer's disease[413-418]. Multiple studies have shown that patients with Alzheimer's disease have an increased risk of AMD. Similarly, patients with AMD have increased risk of cognitive impairment, such as Alzheimer's disease[419].

Alzheimer's disease and AMD also share phenotypical similarities. Both diseases can be characterised by deposit formation. Plaques in Alzheimer's disease and drusen in AMD contain Aβ. Aβ modulates CFI activity in both AMD and Alzheimer's[420]. HTRA1, a risk protein in AMD, is known to participate in APP processing[60]. Furthermore, both diseases are influenced by APOE variants (see section 5.1.4).

C1QTNF5 was found to be expressed in cortical astrocytes and oligodendrocytes (Fig. 3.7d), which was confirmed in cortical astrocytes RNA-seq data (unpublished data, Tuula Ritakari, The University of Edinburgh). In addition, iPSC-derived microglia also showed expression of *C1QTNF5* in RNA-seq data (unpublished data, Dr Banerjee, The University of Edinburgh). It is therefore possible that C1QTNF5 has a similar function in these cell types in regulation of phagocytosis, cellular adhesion, and complement regulation. The *C1QTNF5*^{S163R} mutation

could therefore also affect the function of these cell types in the brain. However, it is not known if patients with L-ORD have an increased risk of cognitive impairment. Nonetheless, it was found that APP is predicted to be involved in cellular networks affected in L-ORD based on IPA of RNA-seq data (Fig. 3.9b). In addition, the third most significant predicted upstream regulator of genes significantly differentially expressed in L-ORD was found to be C9orf72 (Table S11), a protein when mutated can cause familial frontotemporal dementia as well as amyotrophic lateral sclerosis[421,422]. Together, this could indicate that a possible link could be found between L-ORD patients and an increased risk of cognitive impairment.

6.9 L-ORD therapy development

The eyes are one of the most easily accessible organs of the human body, which makes them an ideal target for regenerative medicine. Current approaches for therapy in the retina are transplantation of RPE, exogenous expression of protein, or *in vivo* gene editing.

Of the cell types in the retina, RPE are relatively easy to transplant into the eye. RPE can be transplanted as single cells or monolayer patches and do not require synaptic integration like retinal neural cells. RPE transplantation does come with some difficulties but different methods are being tested for delivery as a cell suspension or as a monolayer graft[423]. Transplantation of allogenic ESC-derived RPE can rescue visual function long-term in RCS rats[424]. Transplantation of ESC-derived cells does require immunosuppression for several months to prevent rejection of the transplanted cells. ESC-RPE have already been used in clinical trials on patients to treat Stargardt's macular dystrophy, gaAMD, and nvAMD[425-427]. One study did not find significant improvements in visual acuity and the other found some improvement in visual acuity in some patients. The first trial was followed up and was found to be safe for medium to long-term[428].

iPSC-derived RPE have an important advantage over ESC-derived RPE for transplantation. An iPSC-based approach allows for autologous transplantation: iPSCs are derived from a patient, converted to RPE *ex vivo*, and transplanted back to the same patient. The transplanted cells are therefore genetically identical and should not evoke an immune response and the patients therefore do not require immunosuppression. However, an important concern with transplantation of iPSC-derived cells is the risk of tumorigenicity[429], because iPSCs are reprogrammed with transcription factors of which some have been implicated with inducing

tumorigenicity. Furthermore, iPSC-derived cells used for transplantation can still evoke an immune response, even when genetically identical[430]. Additionally, iPSC-RPE have been found to inhibit T-cell activation[431]. Nonetheless, iPSC-RPE have been recently transplanted to a patient with nvAMD for the first time[432]. One year after transplantation visual acuity was not improved, but no signs of tumorigenicity were found either.

An ESC- or iPSC-RPE-based treatment could also be an option for patients with L-ORD. Patient-derived iPSCs could be gene-corrected, as shown in this work, before differentiation to RPE and subsequent transplantation. However, the efficacy and long-term safety of iPSC-RPE will need to be assessed first. Nonetheless, development of cell replacement therapy is necessary to replace lost RPE in late-stage L-ORD.

In early stage hereditary macular degeneration, before the loss of RPE and photoreceptors, gene therapy would be the preferred treatment. The mutated gene could be replaced or repaired *in vivo*. Different viral vectors have been developed for precise targeting of the different cell types in the retina[433]. In particular, adeno-associated viruses (AAVs) are well-suited for gene delivery[434]. AAVs can be used for transient exogenous expression of the gene of interest or used in combination with CRISPR/Cas9 for permanent correction of the mutated gene.

AAV vectors targeted at RPE for exogenous expression of protein have been tested in clinical trials. Patients with choroideremia have been treated in this way[435,436] and were found to have improved visual acuity[437]. AAV vectors have also been used for exogenous expression of RPE65 in RPE from patients with a form of Leber's congenital amaurosis (LCA), an early on-set autosomal recessive retinal dystrophy, which was found to only have a small temporary improvement of visual acuity[438,439]. Exogenous expression of C1QTNF5 via AAV vectors in L-ORD patients may only have a limited effect, since the *C1QTNF5*^{S163R} mutation is thought to cause both a gain of function and a loss of function (see section 6.3).

CRISPR/Cas9 deliver by AAVs would lead to a more permanent solution and has been extensively tested on mouse models[440]. CRISPR/Cas9 deliver by AAVs need to be well optimised, because of their relatively small packaging capacity[441]. Nonetheless, CRISPR/Cas9 constructs have been delivered by an AAV targeted to photoreceptors to effectively treat a form of retinal degeneration[442], autosomal dominant forms of retinitis pigmentosa[443,444], and a form of LCA[445] in mice. Furthermore, AAV-delivered CRISPR/Cas9 has been used to target *Vegfa* and *Hif1a* in RPE of a mouse model of nvAMD and was found to reduce CNV[446] and to

have a long-lasting effect[447]. CRISPR/Cas9 deliver by AAVs are currently not yet used in clinical trials. The *C1QTNF5*^{S163R} allele could potentially be repaired or knocked out in patients using the gRNA Correction for targeting used in this work, packaged in an AAV vector together with Cas9 or a base editor.

6.10 Future directions

The generation of the C1QTNF5 KO iPSC line could be supplemented with the generation of C1QTNF5 KO in one of the patient-derived LORD iPSC lines. This could provide a unique insight in the function of the protein and the effect of the mutation in an identical genetic background.

Comparison of L-ORD with other hereditary macular degenerations would greatly contribute to the understanding of the common molecular mechanisms affected in macular degenerations. ML/DHRD and SFD patient-derived iPSC could be generated. Alternatively, the *EFEMP*^{R345W} and *TIMP3*^{S181C} mutations, responsible for ML/DHRD and SFD respectively, could be introduced in a wt iPSC line with gene editing to generate isogenic pairs. These CRISPR/Cas9 constructs have already been made (data not shown) but still need to be tested.

The degree to which necroptosis and ferroptosis contribute to oxidative stress-mediated cell death could be further investigated in iPSC-RPE. iPSC-RPE showed a similar proclivity to undergo necroptotic cell death as the RPE cell lines but this will need to be repeated. Although UV light-induced photo-oxidative stress showed a trend where L-ORD iPSC-RPE appeared to be more sensitive than their isogenic gene-corrected controls, these experiments will need to be repeated. In addition, blue light could be more relevant since blue light strongly reacts with lipofuscin that accumulate in the RPE with age. The UV light experiments could therefore be replicated with blue light instead and in combination with POS phagocytosis.

A potential role for C1QTNF5 in regulating autophagy should be investigated. Dysregulated autophagy in RPE is a contributing factor to AMD pathology[448]. It is thought that cell death in AMD is regulated by autophagy[449]. Moreover, dysregulated autophagy is associated with increased susceptibility to oxidative stress in RPE[450]. The expression of *SQSTM1* was found to be downregulated in RPE exposed to H_2O_2 but upregulated when exposed to DHA (Fig. 4.5a). It is thought that one of the functions of C1QTNF5 is to block ADIPOR1. Adiponectin is known

to induce the AMPK pathway through ADIPOR1, at least in myocytes[451]. The AMPK/mTOR pathway plays are role in autophagy regulation[452]. C1QTNF5^{S163R} could therefore potentially differentially regulate ADIPOR1 activation, leading to altered AMPK pathway signalling, followed by dysregulated autophagy and subsequent increased susceptibility to oxidative stress.

The role of complement system dysregulation in L-ORD should be further investigated. In particular, the importance of C1QTNF5 binding to CFH and the subsequent effect on complement system regulation could be further investigated. Furthermore, inhibitors that prevent C5b-9 formation could be tested on the iPSC-RPE and may form the basis of a macular degeneration therapy.

C1QTNF5 has been shown to play a role in regulating cellular lipid metabolism in other cell types. It is likely that C1QTNF5 has a similar function in RPE as is revealed by the RNA-seq data analysis (Table 3.2a and Fig. 3.9a). L-ORD and wt iPSC-RPE can be compared in the amount of AMPK and ACC phosphorylation via western blotting or ELISA. In addition, a Seahorse XF analyser could be used to measure possible fatty acid oxidation differences between L-ORD and wt iPSC-RPE.

The expression of C1QTNF5 in astrocytes and microglia could have implications for a role of these glia in L-ORD pathology. The C1QTNF5^{S163R} mutation could also affect the function of these cell types in a similar fashion as in RPE. Astrocytes and microglia also phagocytose and therefore C1QTNF5 could also affect this function in these cells. Microglia also play an important role in the complement system, which could also be regulated by C1QTNF5. In addition, studying C1QTNF5 KO astrocytes and microglia should give an indication of the importance of C1QTNF5 in normal astrocyte and microglia functioning. Moreover, C1QTNF5 KO astrocytes and microglia could confirm possible functions of C1QTNF5. Similarly, the role of C1QTNF5 in cortical astrocytes, oligodendrocytes, and microglia in brain could also be studied. A follow up of patients with L-ORD to assess their cognitive ability should be an initial indication of the importance of the C1QTNF5^{S163R} mutation in the brain.

The relative ease of accessibility of the retina and the apparent ease of gene-correcting the L-ORD mutation could make L-ORD an ideal candidate disease for the first AAV-delivered CRISPR/Cas9-mediated gene correction therapy in humans. For this, AAV vectors will need to be designed and tested on L-ORD iPSC-RPE and possibly L-ORD mouse models before a phase 1 clinical trial can be initiated.

References

1 Hoon, M., Okawa, H., Della Santina, L. & Wong, R. Functional architecture of the retina: Development and disease. *Progress In Retinal And Eye Research* **42**, 44-84, doi:10.1016/j.preteyeres.2014.06.003 (2014).

2 Nguyen-Ba-Charvet, K. T. & Chedotal, A. Development of retinal layers. *C R Biol* **337**, 153-159, doi:10.1016/j.crvi.2013.11.010 (2014).

3 Rathnasamy, G., Foulds, W. S., Ling, E. A. & Kaur, C. Retinal microglia - A key player in healthy and diseased retina. *Prog Neurobiol* **173**, 18-40, doi:10.1016/j.pneurobio.2018.05.006 (2019).

4 Masland, R. H. The neuronal organization of the retina. *Neuron* **76**, 266-280, doi:10.1016/j.neuron.2012.10.002 (2012).

5 Besharse, J. C., Hollyfield, J. G. & Rayborn, M. E. Photoreceptor outer segments: accelerated membrane renewal in rods after exposure to light. *Science* **196**, 536-538, doi:10.1126/science.300504 (1977).

6 Wassle, H., Puller, C., Muller, F. & Haverkamp, S. Cone contacts, mosaics, and territories of bipolar cells in the mouse retina. *J Neurosci* **29**, 106-117, doi:10.1523/jneurosci.4442-08.2009 (2009).

7 Van Essen, D. C. Organization of visual areas in macaque and human cerebral cortex. *The visual neurosciences* **1**, 507-521 (2003).

8 de Hoz, R. *et al.* Retinal Macroglial Responses in Health and Disease. *Biomed Res Int* **2016**, 2954721, doi:10.1155/2016/2954721 (2016).

9 Bringmann, A. *et al.* Cellular signaling and factors involved in Muller cell gliosis: neuroprotective and detrimental effects. *Prog Retin Eye Res* **28**, 423-451, doi:10.1016/j.preteyeres.2009.07.001 (2009).

10 Ramirez, J. M., Trivino, A., Ramirez, A. I., Salazar, J. J. & Garcia-Sanchez, J. Immunohistochemical study of human retinal astroglia. *Vision Res* **34**, 1935-1946 (1994).

11 Li, L., Eter, N. & Heiduschka, P. The microglia in healthy and diseased retina. *Exp Eye Res* **136**, 116-130, doi:10.1016/j.exer.2015.04.020 (2015).

12 Silverman, S. M. & Wong, W. T. Microglia in the Retina: Roles in Development, Maturity, and Disease. *Annu Rev Vis Sci* **4**, 45-77, doi:10.1146/annurev-vision-091517-034425 (2018).

13 Streit, W. J. Microglia as neuroprotective, immunocompetent cells of the CNS. *Glia* **40**, 133-139, doi:10.1002/glia.10154 (2002).

14 Eter, N. *et al.* In vivo visualization of dendritic cells, macrophages, and microglial cells responding to laser-induced damage in the fundus of the eye. *Invest Ophthalmol Vis Sci* **49**, 3649-3658, doi:10.1167/iovs.07-1322 (2008).

15 Saijo, K. & Glass, C. K. Microglial cell origin and phenotypes in health and disease. *Nat Rev Immunol* **11**, 775-787, doi:10.1038/nri3086 (2011).

16 Wangsa-Wirawan, N. D. & Linsenmeier, R. A. Retinal oxygen: fundamental and clinical aspects. *Arch Ophthalmol* **121**, 547-557, doi:10.1001/archopht.121.4.547 (2003).

17 Strauss, O. The retinal pigment epithelium in visual function. *Physiol Rev* **85**, 845-881, doi:10.1152/physrev.00021.2004 (2005).

18 Campbell, M. & Humphries, P. The blood-retina barrier: tight junctions and barrier modulation. *Adv Exp Med Biol* **763**, 70-84 (2012).

19 Marks, M. S. & Seabra, M. C. The melanosome: membrane dynamics in black and white. *Nat Rev Mol Cell Biol* **2**, 738-748, doi:10.1038/35096009 (2001).
20 Thompson, D. A. & Gal, A. Vitamin A metabolism in the retinal pigment epithelium: genes, mutations, and diseases. *Prog Retin Eye Res* **22**, 683-703 (2003).
21 Sheedlo, H. J. *et al.* RPE secreted proteins and antibody influence photoreceptor cell survival and maturation. *Brain Res Dev Brain Res* **107**, 57-69 (1998).
22 Kevany, B. M. & Palczewski, K. Phagocytosis of retinal rod and cone photoreceptors. *Physiology (Bethesda)* **25**, 8-15, doi:10.1152/physiol.00038.2009 (2010).
23 Mazzoni, F., Safa, H. & Finnemann, S. C. Understanding photoreceptor outer segment phagocytosis: use and utility of RPE cells in culture. *Exp Eye Res* **126**, 51-60, doi:10.1016/j.exer.2014.01.010 (2014).
24 Finnemann, S. C. & Silverstein, R. L. Differential roles of CD36 and alphavbeta5 integrin in photoreceptor phagocytosis by the retinal pigment epithelium. *J Exp Med* **194**, 1289-1298, doi:10.1084/jem.194.9.1289 (2001).
25 Feng, W., Yasumura, D., Matthes, M. T., LaVail, M. M. & Vollrath, D. Mertk triggers uptake of photoreceptor outer segments during phagocytosis by cultured retinal pigment epithelial cells. *J Biol Chem* **277**, 17016-17022, doi:10.1074/jbc.M107876200 (2002).
26 Strick, D. J., Feng, W. & Vollrath, D. Mertk drives myosin II redistribution during retinal pigment epithelial phagocytosis. *Invest Ophthalmol Vis Sci* **50**, 2427-2435, doi:10.1167/iovs.08-3058 (2009).
27 Gal, A. *et al.* Mutations in MERTK, the human orthologue of the RCS rat retinal dystrophy gene, cause retinitis pigmentosa. *Nat Genet* **26**, 270-271, doi:10.1038/81555 (2000).
28 Jinda, W. *et al.* A novel start codon mutation of the MERTK gene in a patient with retinitis pigmentosa. *Mol Vis* **22**, 342-351 (2016).
29 Sun, M. *et al.* Light-induced oxidation of photoreceptor outer segment phospholipids generates ligands for CD36-mediated phagocytosis by retinal pigment epithelium: a potential mechanism for modulating outer segment phagocytosis under oxidant stress conditions. *J Biol Chem* **281**, 4222-4230, doi:10.1074/jbc.M509769200 (2006).
30 Tanihara, H., Inatani, M. & Honda, Y. Growth factors and their receptors in the retina and pigment epithelium. *Progress in Retinal and Eye Research* **16**, 271-301, doi:http://dx.doi.org/10.1016/S1350-9462(96)00028-6 (1997).
31 Fernandez-Godino, R., Garland, D. L. & Pierce, E. A. A local complement response by RPE causes early-stage macular degeneration. *Hum Mol Genet* **24**, 5555-5569, doi:10.1093/hmg/ddv287 (2015).
32 Detrick, B. & Hooks, J. J. Immune regulation in the retina. *Immunol Res* **47**, 153-161, doi:10.1007/s12026-009-8146-1 (2010).
33 Rosenthal, R. & Strauss, O. Ca2+-channels in the RPE. *Adv Exp Med Biol* **514**, 225-235 (2002).
34 Reichhart, N. & Strauss, O. Ion channels and transporters of the retinal pigment epithelium. *Exp Eye Res* **126**, 27-37, doi:10.1016/j.exer.2014.05.005 (2014).
35 Marmorstein, A. D. *et al.* Bestrophin-1 influences transepithelial electrical properties and Ca2+ signaling in human retinal pigment epithelium. *Mol Vis* **21**, 347-359 (2015).
36 Neussert, R., Muller, C., Milenkovic, V. M. & Strauss, O. The presence of bestrophin-1 modulates the Ca2+ recruitment from Ca2+ stores in the ER. *Pflugers Arch* **460**, 163-175, doi:10.1007/s00424-010-0840-2 (2010).

37 Marmorstein, A. D. *et al.* Bestrophin, the product of the Best vitelliform macular dystrophy gene (VMD2), localizes to the basolateral plasma membrane of the retinal pigment epithelium. *Proc Natl Acad Sci U S A* **97**, 12758-12763, doi:10.1073/pnas.220402097 (2000).
38 Barro-Soria, R. *et al.* ER-localized bestrophin 1 activates Ca2+-dependent ion channels TMEM16A and SK4 possibly by acting as a counterion channel. *Pflugers Arch* **459**, 485-497, doi:10.1007/s00424-009-0745-0 (2010).
39 Rosenthal, R. *et al.* Expression of bestrophin-1, the product of the VMD2 gene, modulates voltage-dependent Ca2+ channels in retinal pigment epithelial cells. *Faseb j* **20**, 178-180, doi:10.1096/fj.05-4495fje (2006).
40 Muller, C., Mas Gomez, N., Ruth, P. & Strauss, O. CaV1.3 L-type channels, maxiK Ca(2+)-dependent K(+) channels and bestrophin-1 regulate rhythmic photoreceptor outer segment phagocytosis by retinal pigment epithelial cells. *Cell Signal* **26**, 968-978, doi:10.1016/j.cellsig.2013.12.021 (2014).
41 Rosenthal, R. *et al.* Ca2+ channels in retinal pigment epithelial cells regulate vascular endothelial growth factor secretion rates in health and disease. *Mol Vis* **13**, 443-456 (2007).
42 Petrukhin, K. *et al.* Identification of the gene responsible for Best macular dystrophy. *Nat Genet* **19**, 241-247, doi:10.1038/915 (1998).
43 Marquardt, A. *et al.* Mutations in a novel gene, VMD2, encoding a protein of unknown properties cause juvenile-onset vitelliform macular dystrophy (Best's disease). *Hum Mol Genet* **7**, 1517-1525 (1998).
44 Steinberg, R. H., Linsenmeier, R. A. & Griff, E. R. Three light-evoked responses of the retinal pigment epithelium. *Vision Res* **23**, 1315-1323 (1983).
45 Klein, R., Klein, B. E. & Linton, K. L. Prevalence of age-related maculopathy. The Beaver Dam Eye Study. *Ophthalmology* **99**, 933-943 (1992).
46 Klaver, C. C., Wolfs, R. C., Vingerling, J. R., Hofman, A. & de Jong, P. T. Age-specific prevalence and causes of blindness and visual impairment in an older population: the Rotterdam Study. *Arch Ophthalmol* **116**, 653-658 (1998).
47 Hawkins, B. S., Bird, A., Klein, R. & West, S. K. Epidemiology of age-related macular degeneration. *Mol Vis* **5**, 26 (1999).
48 Wong, W. L. *et al.* Global prevalence of age-related macular degeneration and disease burden projection for 2020 and 2040: a systematic review and meta-analysis. *Lancet Glob Health* **2**, e106-116, doi:10.1016/s2214-109x(13)70145-1 (2014).
49 Brown, G. C. *et al.* The burden of age-related macular degeneration: a value-based medicine analysis. *Trans Am Ophthalmol Soc* **103**, 173-184; discussion 184-176 (2005).
50 Wysong, A., Lee, P. P. & Sloan, F. A. Longitudinal incidence of adverse outcomes of age-related macular degeneration. *Arch Ophthalmol* **127**, 320-327, doi:10.1001/archophthalmol.2008.613 (2009).
51 Brody, B. L. *et al.* Depression, visual acuity, comorbidity, and disability associated with age-related macular degeneration. *Ophthalmology* **108**, 1893-1900; discussion 1900-1891 (2001).
52 Augustin, A. *et al.* Anxiety and depression prevalence rates in age-related macular degeneration. *Invest Ophthalmol Vis Sci* **48**, 1498-1503, doi:10.1167/iovs.06-0761 (2007).
53 Mitchell, P., Liew, G., Gopinath, B. & Wong, T. Y. Age-related macular degeneration. *Lancet* **392**, 1147-1159, doi:10.1016/s0140-6736(18)31550-2 (2018).

54 Tezel, T. H., Bora, N. S. & Kaplan, H. J. Pathogenesis of age-related macular degeneration. *Trends Mol Med* **10**, 417-420, doi:10.1016/j.molmed.2004.07.004 (2004).
55 Katta, S., Kaur, I. & Chakrabarti, S. The molecular genetic basis of age-related macular degeneration: an overview. *J Genet* **88**, 425-449 (2009).
56 Swaroop, A., Branham, K. E., Chen, W. & Abecasis, G. Genetic susceptibility to age-related macular degeneration: a paradigm for dissecting complex disease traits. *Hum Mol Genet* **16 Spec No. 2**, R174-182, doi:10.1093/hmg/ddm212 (2007).
57 Fritsche, L. G. *et al.* A large genome-wide association study of age-related macular degeneration highlights contributions of rare and common variants. *Nat Genet* **48**, 134-143, doi:10.1038/ng.3448 (2016).
58 Fritsche, L. G. *et al.* Seven new loci associated with age-related macular degeneration. *Nat Genet* **45**, 433-439, 439e431-432, doi:10.1038/ng.2578 (2013).
59 Smailhodzic, D. *et al.* Risk alleles in CFH and ARMS2 are independently associated with systemic complement activation in age-related macular degeneration. *Ophthalmology* **119**, 339-346, doi:10.1016/j.ophtha.2011.07.056 (2012).
60 Grau, S. *et al.* Implications of the serine protease HtrA1 in amyloid precursor protein processing. *Proc Natl Acad Sci U S A* **102**, 6021-6026, doi:10.1073/pnas.0501823102 (2005).
61 Johnson, L. V. *et al.* The Alzheimer's A beta -peptide is deposited at sites of complement activation in pathologic deposits associated with aging and age-related macular degeneration. *Proc Natl Acad Sci U S A* **99**, 11830-11835, doi:10.1073/pnas.192203399 (2002).
62 Anderson, D. H. *et al.* Characterization of beta amyloid assemblies in drusen: the deposits associated with aging and age-related macular degeneration. *Exp Eye Res* **78**, 243-256 (2004).
63 Hageman, G. S. *et al.* An integrated hypothesis that considers drusen as biomarkers of immune-mediated processes at the RPE-Bruch's membrane interface in aging and age-related macular degeneration. *Prog Retin Eye Res* **20**, 705-732 (2001).
64 Kozlowski, M. R. RPE cell senescence: a key contributor to age-related macular degeneration. *Med Hypotheses* **78**, 505-510, doi:10.1016/j.mehy.2012.01.018 (2012).
65 Sparrow, J. R., Hicks, D. & Hamel, C. P. The retinal pigment epithelium in health and disease. *Curr Mol Med* **10**, 802-823 (2010).
66 Newman, A. M. *et al.* Systems-level analysis of age-related macular degeneration reveals global biomarkers and phenotype-specific functional networks. *Genome Med* **4**, 16, doi:10.1186/gm315 (2012).
67 Ferris, F. L., 3rd *et al.* Clinical classification of age-related macular degeneration. *Ophthalmology* **120**, 844-851, doi:10.1016/j.ophtha.2012.10.036 (2013).
68 Bird, A. C. *et al.* An international classification and grading system for age-related maculopathy and age-related macular degeneration. The International ARM Epidemiological Study Group. *Surv Ophthalmol* **39**, 367-374 (1995).
69 Ferris, F. L. *et al.* A simplified severity scale for age-related macular degeneration: AREDS Report No. 18. *Arch Ophthalmol* **123**, 1570-1574, doi:10.1001/archopht.123.11.1570 (2005).
70 Ferris, F. L., 3rd, Fine, S. L. & Hyman, L. Age-related macular degeneration and blindness due to neovascular maculopathy. *Arch Ophthalmol* **102**, 1640-1642 (1984).
71 Maguire, M. G. *et al.* Five-Year Outcomes with Anti-Vascular Endothelial Growth Factor Treatment of Neovascular Age-Related Macular Degeneration: The

Comparison of Age-Related Macular Degeneration Treatments Trials. *Ophthalmology* **123**, 1751-1761, doi:10.1016/j.ophtha.2016.03.045 (2016).
72 Grunwald, J. E. *et al.* Risk of geographic atrophy in the comparison of age-related macular degeneration treatments trials. *Ophthalmology* **121**, 150-161, doi:10.1016/j.ophtha.2013.08.015 (2014).
73 Crabb, J. W. *et al.* Drusen proteome analysis: an approach to the etiology of age-related macular degeneration. *Proc Natl Acad Sci U S A* **99**, 14682-14687, doi:10.1073/pnas.222551899 (2002).
74 Curcio, C. A. *et al.* Esterified and unesterified cholesterol in drusen and basal deposits of eyes with age-related maculopathy. *Exp Eye Res* **81**, 731-741, doi:10.1016/j.exer.2005.04.012 (2005).
75 Kamei, M. & Hollyfield, J. G. TIMP-3 in Bruch's membrane: changes during aging and in age-related macular degeneration. *Invest Ophthalmol Vis Sci* **40**, 2367-2375 (1999).
76 Hageman, G. S., Mullins, R. F., Russell, S. R., Johnson, L. V. & Anderson, D. H. Vitronectin is a constituent of ocular drusen and the vitronectin gene is expressed in human retinal pigmented epithelial cells. *Faseb j* **13**, 477-484 (1999).
77 Anderson, D. H. *et al.* Local cellular sources of apolipoprotein E in the human retina and retinal pigmented epithelium: implications for the process of drusen formation. *Am J Ophthalmol* **131**, 767-781 (2001).
78 Childs, B. G., Durik, M., Baker, D. J. & van Deursen, J. M. Cellular senescence in aging and age-related disease: from mechanisms to therapy. *Nat Med* **21**, 1424-1435, doi:10.1038/nm.4000 (2015).
79 Honda, S., Hjelmeland, L. M. & Handa, J. T. Senescence associated beta galactosidase activity in human retinal pigment epithelial cells exposed to mild hyperoxia in vitro. *Br J Ophthalmol* **86**, 159-162 (2002).
80 Hayward, C. *et al.* Mutation in a short-chain collagen gene, CTRP5, results in extracellular deposit formation in late-onset retinal degeneration: a genetic model for age-related macular degeneration. *Hum Mol Genet* **12**, 2657-2667, doi:10.1093/hmg/ddg289 (2003).
81 Borooah, S., Collins, C., Wright, A. & Dhillon, B. Late-onset retinal macular degeneration: clinical insights into an inherited retinal degeneration. *Br J Ophthalmol* **93**, 284-289, doi:10.1136/bjo.2008.150151 (2009).
82 Subrayan, V., Morris, B., Armbrecht, A. M., Wright, A. F. & Dhillon, B. Long anterior lens zonules in late-onset retinal degeneration (L-ORD). *Am J Ophthalmol* **140**, 1127-1129, doi:10.1016/j.ajo.2005.06.023 (2005).
83 Ayyagari, R. *et al.* Late-onset macular degeneration and long anterior lens zonules result from a CTRP5 gene mutation. *Invest Ophthalmol Vis Sci* **46**, 3363-3371, doi:10.1167/iovs.05-0159 (2005).
84 Jacobson, S. G., Cideciyan, A. V., Wright, E. & Wright, A. F. Phenotypic marker for early disease detection in dominant late-onset retinal degeneration. *Invest Ophthalmol Vis Sci* **42**, 1882-1890 (2001).
85 Stone, E. M. *et al.* A single EFEMP1 mutation associated with both Malattia Leventinese and Doyne honeycomb retinal dystrophy. *Nat Genet* **22**, 199-202, doi:10.1038/9722 (1999).
86 Blackburn, J., Tarttelin, E. E., Gregory-Evans, C. Y., Moosajee, M. & Gregory-Evans, K. Transcriptional regulation and expression of the dominant drusen gene FBLN3 (EFEMP1) in mammalian retina. *Invest Ophthalmol Vis Sci* **44**, 4613-4621 (2003).

87 Hulleman, J. D. Malattia Leventinese/Doyne Honeycomb Retinal Dystrophy: Similarities to Age-Related Macular Degeneration and Potential Therapies. *Adv Exp Med Biol* **854**, 153-158, doi:10.1007/978-3-319-17121-0_21 (2016).
88 Kobayashi, N. *et al.* A comparative analysis of the fibulin protein family. Biochemical characterization, binding interactions, and tissue localization. *J Biol Chem* **282**, 11805-11816, doi:10.1074/jbc.M611029200 (2007).
89 Djokic, J., Fagotto-Kaufmann, C., Bartels, R., Nelea, V. & Reinhardt, D. P. Fibulin-3, -4, and -5 are highly susceptible to proteolysis, interact with cells and heparin, and form multimers. *J Biol Chem* **288**, 22821-22835, doi:10.1074/jbc.M112.439158 (2013).
90 Klenotic, P. A., Munier, F. L., Marmorstein, L. Y. & Anand-Apte, B. Tissue inhibitor of metalloproteinases-3 (TIMP-3) is a binding partner of epithelial growth factor-containing fibulin-like extracellular matrix protein 1 (EFEMP1). Implications for macular degenerations. *J Biol Chem* **279**, 30469-30473, doi:10.1074/jbc.M403026200 (2004).
91 Wyatt, M. K. *et al.* Interaction of complement factor h and fibulin3 in age-related macular degeneration. *PLoS One* **8**, e68088, doi:10.1371/journal.pone.0068088 (2013).
92 Peluso, I. *et al.* The ADAMTS18 gene is responsible for autosomal recessive early onset severe retinal dystrophy. *Orphanet J Rare Dis* **8**, 16, doi:10.1186/1750-1172-8-16 (2013).
93 Marmorstein, L. Y. *et al.* Aberrant accumulation of EFEMP1 underlies drusen formation in Malattia Leventinese and age-related macular degeneration. *Proc Natl Acad Sci U S A* **99**, 13067-13072, doi:10.1073/pnas.202491599 (2002).
94 Fu, L. *et al.* The R345W mutation in EFEMP1 is pathogenic and causes AMD-like deposits in mice. *Hum Mol Genet* **16**, 2411-2422, doi:10.1093/hmg/ddm198 (2007).
95 Marmorstein, L. Y., McLaughlin, P. J., Peachey, N. S., Sasaki, T. & Marmorstein, A. D. Formation and progression of sub-retinal pigment epithelium deposits in Efemp1 mutation knock-in mice: a model for the early pathogenic course of macular degeneration. *Hum Mol Genet* **16**, 2423-2432, doi:10.1093/hmg/ddm199 (2007).
96 Sohn, E. H. *et al.* Comparison of drusen and modifying genes in autosomal dominant radial drusen and age-related macular degeneration. *Retina* **35**, 48-57, doi:10.1097/iae.0000000000000263 (2015).
97 Stone, E. M. *et al.* Missense variations in the fibulin 5 gene and age-related macular degeneration. *N Engl J Med* **351**, 346-353, doi:10.1056/NEJMoa040833 (2004).
98 Mullins, R. F., Olvera, M. A., Clark, A. F. & Stone, E. M. in *Exp Eye Res* Vol. 84 378-380 (2007).
99 Thompson, C. L. *et al.* Complement factor H and hemicentin-1 in age-related macular degeneration and renal phenotypes. *Hum Mol Genet* **16**, 2135-2148, doi:10.1093/hmg/ddm164 (2007).
100 Klein, M. L. *et al.* Age-related macular degeneration. Clinical features in a large family and linkage to chromosome 1q. *Arch Ophthalmol* **116**, 1082-1088 (1998).
101 Schultz, D. W. *et al.* Analysis of the ARMD1 locus: evidence that a mutation in HEMICENTIN-1 is associated with age-related macular degeneration in a large family. *Hum Mol Genet* **12**, 3315-3323, doi:10.1093/hmg/ddg348 (2003).
102 Sorsby, A. & Mason, M. E. A fundus dystrophy with unusual features. *Br J Ophthalmol* **33**, 67-97 (1949).
103 Weber, B. H., Vogt, G., Pruett, R. C., Stohr, H. & Felbor, U. Mutations in the tissue inhibitor of metalloproteinases-3 (TIMP3) in patients with Sorsby's fundus dystrophy. *Nat Genet* **8**, 352-356, doi:10.1038/ng1294-352 (1994).

104 Tabata, Y., Isashiki, Y., Kamimura, K., Nakao, K. & Ohba, N. A novel splice site mutation in the tissue inhibitor of the metalloproteinases-3 gene in Sorsby's fundus dystrophy with unusual clinical features. *Hum Genet* **103**, 179-182 (1998).
105 Langton, K. P. *et al.* A novel tissue inhibitor of metalloproteinases-3 mutation reveals a common molecular phenotype in Sorsby's fundus dystrophy. *J Biol Chem* **275**, 27027-27031, doi:10.1074/jbc.M909677199 (2000).
106 Della, N. G., Campochiaro, P. A. & Zack, D. J. Localization of TIMP-3 mRNA expression to the retinal pigment epithelium. *Invest Ophthalmol Vis Sci* **37**, 1921-1924 (1996).
107 Fariss, R. N., Apte, S. S., Olsen, B. R., Iwata, K. & Milam, A. H. Tissue inhibitor of metalloproteinases-3 is a component of Bruch's membrane of the eye. *Am J Pathol* **150**, 323-328 (1997).
108 Matrisian, L. M. The matrix-degrading metalloproteinases. *Bioessays* **14**, 455-463, doi:10.1002/bies.950140705 (1992).
109 Jackson, H. W., Defamie, V., Waterhouse, P. & Khokha, R. TIMPs: versatile extracellular regulators in cancer. *Nat Rev Cancer* **17**, 38-53, doi:10.1038/nrc.2016.115 (2017).
110 Felbor, U., Stohr, H., Amann, T., Schonherr, U. & Weber, B. H. A novel Ser156Cys mutation in the tissue inhibitor of metalloproteinases-3 (TIMP3) in Sorsby's fundus dystrophy with unusual clinical features. *Hum Mol Genet* **4**, 2415-2416 (1995).
111 Felbor, U., Suvanto, E. A., Forsius, H. R., Eriksson, A. W. & Weber, B. H. Autosomal recessive Sorsby fundus dystrophy revisited: molecular evidence for dominant inheritance. *Am J Hum Genet* **60**, 57-62 (1997).
112 Jacobson, S. G. *et al.* Night blindness in Sorsby's fundus dystrophy reversed by vitamin A. *Nat Genet* **11**, 27-32, doi:10.1038/ng0995-27 (1995).
113 Barbazetto, I. A., Hayashi, M., Klais, C. M., Yannuzzi, L. A. & Allikmets, R. A novel TIMP3 mutation associated with Sorsby fundus dystrophy. *Arch Ophthalmol* **123**, 542-543, doi:10.1001/archopht.123.4.542 (2005).
114 Jacobson, S. G. *et al.* Novel mutation in the TIMP3 gene causes Sorsby fundus dystrophy. *Arch Ophthalmol* **120**, 376-379 (2002).
115 Meunier, I. *et al.* A new autosomal dominant eye and lung syndrome linked to mutations in TIMP3 gene. *Sci Rep* **6**, 32544, doi:10.1038/srep32544 (2016).
116 Langton, K. P., Barker, M. D. & McKie, N. Localization of the functional domains of human tissue inhibitor of metalloproteinases-3 and the effects of a Sorsby's fundus dystrophy mutation. *J Biol Chem* **273**, 16778-16781 (1998).
117 Anand-Apte, B. *et al.* Inhibition of angiogenesis by tissue inhibitor of metalloproteinase-3. *Invest Ophthalmol Vis Sci* **38**, 817-823 (1997).
118 Ebrahem, Q. *et al.* Increased neovascularization in mice lacking tissue inhibitor of metalloproteinases-3. *Invest Ophthalmol Vis Sci* **52**, 6117-6123, doi:10.1167/iovs.10-5899 (2011).
119 Qi, J. H. *et al.* Tissue inhibitor of metalloproteinases-3 peptides inhibit angiogenesis and choroidal neovascularization in mice. *PLoS One* **8**, e55667, doi:10.1371/journal.pone.0055667 (2013).
120 Qi, J. H. *et al.* A novel function for tissue inhibitor of metalloproteinases-3 (TIMP3): inhibition of angiogenesis by blockage of VEGF binding to VEGF receptor-2. *Nat Med* **9**, 407-415, doi:10.1038/nm846 (2003).
121 Sivaprasad, S., Webster, A. R., Egan, C. A., Bird, A. C. & Tufail, A. Clinical course and treatment outcomes of Sorsby fundus dystrophy. *Am J Ophthalmol* **146**, 228-234, doi:10.1016/j.ajo.2008.03.024 (2008).

122 Thomson, J. A. *et al.* Embryonic stem cell lines derived from human blastocysts. *Science* **282**, 1145-1147 (1998).
123 Takahashi, K. *et al.* Induction of Pluripotent Stem Cells from Adult Human Fibroblasts by Defined Factors. *Cell* **131**, 861-872, doi:10.1016/j.cell.2007.11.019 (2007).
124 Yu, J. *et al.* Induced pluripotent stem cell lines derived from human somatic cells. *Science* **318**, 1917-1920, doi:10.1126/science.1151526 (2007).
125 Wright, A. V., Nunez, J. K. & Doudna, J. A. Biology and Applications of CRISPR Systems: Harnessing Nature's Toolbox for Genome Engineering. *Cell* **164**, 29-44, doi:10.1016/j.cell.2015.12.035 (2016).
126 Barrangou, R. & Horvath, P. A decade of discovery: CRISPR functions and applications. *Nat Microbiol* **2**, 17092, doi:10.1038/nmicrobiol.2017.92 (2017).
127 Ran, F. A. *et al.* Genome engineering using the CRISPR-Cas9 system. *Nat Protoc* **8**, 2281-2308, doi:10.1038/nprot.2013.143 (2013).
128 Makarova, K. S. *et al.* An updated evolutionary classification of CRISPR-Cas systems. *Nat Rev Microbiol* **13**, 722-736, doi:10.1038/nrmicro3569 (2015).
129 Mohanraju, P. *et al.* Diverse evolutionary roots and mechanistic variations of the CRISPR-Cas systems. *Science* **353**, aad5147, doi:10.1126/science.aad5147 (2016).
130 Faure, G. *et al.* CRISPR-Cas in mobile genetic elements: counter-defence and beyond. *Nat Rev Microbiol*, doi:10.1038/s41579-019-0204-7 (2019).
131 Jackson, S. A. *et al.* CRISPR-Cas: Adapting to change. *Science* **356**, doi:10.1126/science.aal5056 (2017).
132 Jinek, M. *et al.* A programmable dual-RNA-guided DNA endonuclease in adaptive bacterial immunity. *Science (New York, N.Y.)* **337**, 816-821, doi:10.1126/science.1225829 (2012).
133 Ran, F. A. *et al.* Double nicking by RNA-guided CRISPR Cas9 for enhanced genome editing specificity. *Cell* **154**, 1380-1389, doi:10.1016/j.cell.2013.08.021 (2013).
134 Koressaar, T. & Remm, M. Enhancements and modifications of primer design program Primer3. *Bioinformatics* **23**, 1289-1291, doi:10.1093/bioinformatics/btm091 (2007).
135 Untergasser, A. *et al.* Primer3--new capabilities and interfaces. *Nucleic Acids Res* **40**, e115, doi:10.1093/nar/gks596 (2012).
136 Koressaar, T. *et al.* Primer3_masker: integrating masking of template sequence with primer design software. *Bioinformatics* **34**, 1937-1938, doi:10.1093/bioinformatics/bty036 (2018).
137 Guschin, D. Y. *et al.* A rapid and general assay for monitoring endogenous gene modification. *Methods Mol Biol* **649**, 247-256, doi:10.1007/978-1-60761-753-2_15 (2010).
138 Hodgkins, A. *et al.* WGE: a CRISPR database for genome engineering. *Bioinformatics* **31**, 3078-3080, doi:10.1093/bioinformatics/btv308 (2015).
139 McLaren, W. *et al.* The Ensembl Variant Effect Predictor. *Genome Biol* **17**, 122, doi:10.1186/s13059-016-0974-4 (2016).
140 Komor, A. C., Kim, Y. B., Packer, M. S., Zuris, J. A. & Liu, D. R. Programmable editing of a target base in genomic DNA without double-stranded DNA cleavage. *Nature* **533**, 420-424, doi:10.1038/nature17946 (2016).
141 Gaudelli, N. M. *et al.* Programmable base editing of A*T to G*C in genomic DNA without DNA cleavage. *Nature* **551**, 464-471, doi:10.1038/nature24644 (2017).
142 Rees, H. A. & Liu, D. R. Base editing: precision chemistry on the genome and transcriptome of living cells. *Nat Rev Genet* **19**, 770-788, doi:10.1038/s41576-018-0059-1 (2018).

143 Gajula, K. S. Designing an Elusive C*G-->G*C CRISPR Base Editor. *Trends Biochem Sci* **44**, 91-94, doi:10.1016/j.tibs.2018.10.004 (2019).
144 Zhou, C. *et al.* Off-target RNA mutation induced by DNA base editing and its elimination by mutagenesis. *Nature*, doi:10.1038/s41586-019-1314-0 (2019).
145 Martinez-Morales, J. R., Rodrigo, I. & Bovolenta, P. Eye development: a view from the retina pigmented epithelium. *Bioessays* **26**, 766-777, doi:10.1002/bies.20064 (2004).
146 Horsford, D. J. *et al.* Chx10 repression of Mitf is required for the maintenance of mammalian neuroretinal identity. *Development* **132**, 177-187, doi:10.1242/dev.01571 (2005).
147 Meyer, J. S. *et al.* Modeling early retinal development with human embryonic and induced pluripotent stem cells. *Proc Natl Acad Sci U S A* **106**, 16698-16703, doi:10.1073/pnas.0905245106 (2009).
148 Xu, C. *et al.* Basic fibroblast growth factor supports undifferentiated human embryonic stem cell growth without conditioned medium. *Stem Cells* **23**, 315-323, doi:10.1634/stemcells.2004-0211 (2005).
149 Levenstein, M. E. *et al.* Basic fibroblast growth factor support of human embryonic stem cell self-renewal. *Stem Cells* **24**, 568-574, doi:10.1634/stemcells.2005-0247 (2006).
150 Chen, G. *et al.* Chemically defined conditions for human iPSC derivation and culture. *Nat Methods* **8**, 424-429, doi:10.1038/nmeth.1593 (2011).
151 Kawasaki, H. *et al.* Generation of dopaminergic neurons and pigmented epithelia from primate ES cells by stromal cell-derived inducing activity. *Proc Natl Acad Sci U S A* **99**, 1580-1585, doi:10.1073/pnas.032662199 (2002).
152 Haruta, M. *et al.* In vitro and in vivo characterization of pigment epithelial cells differentiated from primate embryonic stem cells. *Invest Ophthalmol Vis Sci* **45**, 1020-1025 (2004).
153 Klimanskaya, I. *et al.* Derivation and comparative assessment of retinal pigment epithelium from human embryonic stem cells using transcriptomics. *Cloning Stem Cells* **6**, 217-245, doi:10.1089/clo.2004.6.217 (2004).
154 Lund, R. D. *et al.* Human embryonic stem cell-derived cells rescue visual function in dystrophic RCS rats. *Cloning Stem Cells* **8**, 189-199, doi:10.1089/clo.2006.8.189 (2006).
155 Vugler, A. *et al.* Elucidating the phenomenon of HESC-derived RPE: anatomy of cell genesis, expansion and retinal transplantation. *Exp Neurol* **214**, 347-361, doi:10.1016/j.expneurol.2008.09.007 (2008).
156 Buchholz, D. E. *et al.* Derivation of functional retinal pigmented epithelium from induced pluripotent stem cells. *Stem Cells* **27**, 2427-2434, doi:10.1002/stem.189 (2009).
157 Meyer, J. S. *et al.* Optic vesicle-like structures derived from human pluripotent stem cells facilitate a customized approach to retinal disease treatment. *Stem Cells* **29**, 1206-1218, doi:10.1002/stem.674 (2011).
158 Mellough, C. B., Sernagor, E., Moreno-Gimeno, I., Steel, D. H. & Lako, M. Efficient stage-specific differentiation of human pluripotent stem cells toward retinal photoreceptor cells. *Stem Cells* **30**, 673-686, doi:10.1002/stem.1037 (2012).
159 Elkabetz, Y. *et al.* Human ES cell-derived neural rosettes reveal a functionally distinct early neural stem cell stage. *Genes Dev* **22**, 152-165, doi:10.1101/gad.1616208 (2008).

160 Idelson, M. *et al.* Directed differentiation of human embryonic stem cells into functional retinal pigment epithelium cells. *Cell Stem Cell* **5**, 396-408, doi:10.1016/j.stem.2009.07.002 (2009).
161 Nakano, T. *et al.* Self-formation of optic cups and storable stratified neural retina from human ESCs. *Cell Stem Cell* **10**, 771-785, doi:10.1016/j.stem.2012.05.009 (2012).
162 Khalili, S. *et al.* Induction of rod versus cone photoreceptor-specific progenitors from retinal precursor cells. *Stem Cell Res* **33**, 215-227, doi:10.1016/j.scr.2018.11.005 (2018).
163 Janssen, J. J. *et al.* Retinoic acid delays transcription of human retinal pigment neuroepithelium marker genes in ARPE-19 cells. *Neuroreport* **11**, 1571-1579 (2000).
164 Singh, R. *et al.* Functional analysis of serially expanded human iPS cell-derived RPE cultures. *Invest Ophthalmol Vis Sci* **54**, 6767-6778, doi:10.1167/iovs.13-11943 (2013).
165 Stanton, C. M. *et al.* Novel pathogenic mutations in C1QTNF5 support a dominant negative disease mechanism in late-onset retinal degeneration. *Sci Rep* **7**, 12147, doi:10.1038/s41598-017-11898-3 (2017).
166 Shapiro, L. & Scherer, P. E. The crystal structure of a complement-1q family protein suggests an evolutionary link to tumor necrosis factor. *Curr Biol* **8**, 335-338 (1998).
167 Kishore, U. *et al.* C1q and tumor necrosis factor superfamily: modularity and versatility. *Trends Immunol* **25**, 551-561, doi:10.1016/j.it.2004.08.006 (2004).
168 Schaffler, A. & Buechler, C. CTRP family: linking immunity to metabolism. *Trends Endocrinol Metab* **23**, 194-204, doi:10.1016/j.tem.2011.12.003 (2012).
169 Seldin, M. M., Tan, S. Y. & Wong, G. W. Metabolic function of the CTRP family of hormones. *Rev Endocr Metab Disord* **15**, 111-123, doi:10.1007/s11154-013-9255-7 (2014).
170 Yamauchi, T. *et al.* Adiponectin stimulates glucose utilization and fatty-acid oxidation by activating AMP-activated protein kinase. *Nat Med* **8**, 1288-1295, doi:10.1038/nm788 (2002).
171 Hardie, D. G., Hawley, S. A. & Scott, J. W. AMP-activated protein kinase--development of the energy sensor concept. *J Physiol* **574**, 7-15, doi:10.1113/jphysiol.2006.108944 (2006).
172 Yokota, T. *et al.* Adiponectin, a new member of the family of soluble defense collagens, negatively regulates the growth of myelomonocytic progenitors and the functions of macrophages. *Blood* **96**, 1723-1732 (2000).
173 Cacicedo, J. M. *et al.* Activation of AMP-activated protein kinase prevents lipotoxicity in retinal pericytes. *Invest Ophthalmol Vis Sci* **52**, 3630-3639, doi:10.1167/iovs.10-5784 (2011).
174 Kim, J. E. *et al.* AMP-activated protein kinase activation by 5-aminoimidazole-4-carboxamide-1-beta-D-ribofuranoside (AICAR) inhibits palmitate-induced endothelial cell apoptosis through reactive oxygen species suppression. *J Pharmacol Sci* **106**, 394-403 (2008).
175 Kim, J., Park, Y. J., Jang, Y. & Kwon, Y. H. AMPK activation inhibits apoptosis and tau hyperphosphorylation mediated by palmitate in SH-SY5Y cells. *Brain Res* **1418**, 42-51, doi:10.1016/j.brainres.2011.08.059 (2011).
176 Peterson, J. M., Aja, S., Wei, Z. & Wong, G. W. CTRP1 protein enhances fatty acid oxidation via AMP-activated protein kinase (AMPK) activation and acetyl-CoA carboxylase (ACC) inhibition. *J Biol Chem* **287**, 1576-1587, doi:10.1074/jbc.M111.278333 (2012).

177 Wong, G. W., Wang, J., Hug, C., Tsao, T. S. & Lodish, H. F. A family of Acrp30/adiponectin structural and functional paralogs. *Proc Natl Acad Sci U S A* **101**, 10302-10307, doi:10.1073/pnas.0403760101 (2004).
178 Wong, G. W. *et al.* Identification and characterization of CTRP9, a novel secreted glycoprotein, from adipose tissue that reduces serum glucose in mice and forms heterotrimers with adiponectin. *Faseb j* **23**, 241-258, doi:10.1096/fj.08-114991 (2009).
179 Wei, Z., Peterson, J. M. & Wong, G. W. Metabolic regulation by C1q/TNF-related protein-13 (CTRP13): activation OF AMP-activated protein kinase and suppression of fatty acid-induced JNK signaling. *J Biol Chem* **286**, 15652-15665, doi:10.1074/jbc.M110.201087 (2011).
180 Weigert, J. *et al.* The adiponectin paralog CORS-26 has anti-inflammatory properties and is produced by human monocytic cells. *FEBS Lett* **579**, 5565-5570, doi:10.1016/j.febslet.2005.09.022 (2005).
181 Enomoto, T. *et al.* Adipolin/C1qdc2/CTRP12 protein functions as an adipokine that improves glucose metabolism. *J Biol Chem* **286**, 34552-34558, doi:10.1074/jbc.M111.277319 (2011).
182 Biswas, P. *et al.* Whole-Exome Sequencing Identifies Novel Variants that Co-segregates with Autosomal Recessive Retinal Degeneration in a Pakistani Pedigree. *Adv Exp Med Biol* **1074**, 219-228, doi:10.1007/978-3-319-75402-4_27 (2018).
183 Kim, M. J., Lee, W., Park, E. J. & Park, S. Y. C1qTNF-related protein-6 increases the expression of interleukin-10 in macrophages. *Mol Cells* **30**, 59-64, doi:10.1007/s10059-010-0088-x (2010).
184 Murayama, M. A. *et al.* CTRP6 is an endogenous complement regulator that can effectively treat induced arthritis. *Nat Commun* **6**, 8483, doi:10.1038/ncomms9483 (2015).
185 Dick, D. M. *et al.* Genome-wide association study of conduct disorder symptomatology. *Mol Psychiatry* **16**, 800-808, doi:10.1038/mp.2010.73 (2011).
186 Liu, F. *et al.* C1ql1/Ctrp14 and C1ql4/Ctrp11 promote angiogenesis of endothelial cells through activation of ERK1/2 signal pathway. *Mol Cell Biochem* **424**, 57-67, doi:10.1007/s11010-016-2842-7 (2017).
187 Wei, Z. *et al.* C1q/tumor necrosis factor-related protein 11 (CTRP11), a novel adipose stroma-derived regulator of adipogenesis. *J Biol Chem* **288**, 10214-10229, doi:10.1074/jbc.M113.458711 (2013).
188 Kautz, L. *et al.* Identification of erythroferrone as an erythroid regulator of iron metabolism. *Nat Genet* **46**, 678-684, doi:10.1038/ng.2996 (2014).
189 Seldin, M. M., Peterson, J. M., Byerly, M. S., Wei, Z. & Wong, G. W. Myonectin (CTRP15), a novel myokine that links skeletal muscle to systemic lipid homeostasis. *J Biol Chem* **287**, 11968-11980, doi:10.1074/jbc.M111.336834 (2012).
190 Zhao, X., Yang, H., Yamoah, E. N. & Lundberg, Y. W. Gene targeting reveals the role of Oc90 as the essential organizer of the otoconial organic matrix. *Dev Biol* **304**, 508-524, doi:10.1016/j.ydbio.2007.01.013 (2007).
191 Schmid, A. *et al.* Regulation and function of C1Q/TNF-related protein-5 (CTRP-5) in the context of adipocyte biology. *Exp Clin Endocrinol Diabetes* **121**, 310-317, doi:10.1055/s-0032-1333299 (2013).
192 Jiang, F. *et al.* C1q/TNF-Related Protein5 (CTRP5) as a Biomarker to Predict Metabolic Syndrome and Each of Its Components. *Int J Endocrinol* **2018**, 7201473, doi:10.1155/2018/7201473 (2018).

193 Mandal, M. N. *et al.* CTRP5 is a membrane-associated and secretory protein in the RPE and ciliary body and the S163R mutation of CTRP5 impairs its secretion. *Invest Ophthalmol Vis Sci* **47**, 5505-5513, doi:10.1167/iovs.06-0312 (2006).
194 Tu, X. & Palczewski, K. Crystal structure of the globular domain of C1QTNF5: Implications for late-onset retinal macular degeneration. *J Struct Biol* **180**, 439-446, doi:10.1016/j.jsb.2012.07.011 (2012).
195 Tu, X. & Palczewski, K. The macular degeneration-linked C1QTNF5 (S163) mutation causes higher-order structural rearrangements. *J Struct Biol* **186**, 86-94, doi:10.1016/j.jsb.2014.02.001 (2014).
196 Park, S. Y. *et al.* C1q tumor necrosis factor alpha-related protein isoform 5 is increased in mitochondrial DNA-depleted myocytes and activates AMP-activated protein kinase. *J Biol Chem* **284**, 27780-27789, doi:10.1074/jbc.M109.005611 (2009).
197 Yang, W. M. & Lee, W. CTRP5 ameliorates palmitate-induced apoptosis and insulin resistance through activation of AMPK and fatty acid oxidation. *Biochem Biophys Res Commun* **452**, 715-721, doi:10.1016/j.bbrc.2014.08.145 (2014).
198 Lei, X. *et al.* Loss of CTRP5 improves insulin action and hepatic steatosis. *Am J Physiol Endocrinol Metab* **310**, E1036-1052, doi:10.1152/ajpendo.00010.2016 (2016).
199 Shu, X. *et al.* Disease mechanisms in late-onset retinal macular degeneration associated with mutation in C1QTNF5. *Hum Mol Genet* **15**, 1680-1689, doi:10.1093/hmg/ddl091 (2006).
200 Kuntz, C. A. *et al.* Sub-retinal pigment epithelial deposits in a dominant late-onset retinal degeneration. *Invest Ophthalmol Vis Sci* **37**, 1772-1782 (1996).
201 Jacobson, S. G., Cideciyan, A. V., Sumaroka, A., Roman, A. J. & Wright, A. F. Late-onset retinal degeneration caused by C1QTNF5 mutation: sub-retinal pigment epithelium deposits and visual consequences. *JAMA Ophthalmol* **132**, 1252-1255, doi:10.1001/jamaophthalmol.2014.2059 (2014).
202 Chavali, V. R. *et al.* A CTRP5 gene S163R mutation knock-in mouse model for late-onset retinal degeneration. *Hum Mol Genet* **20**, 2000-2014, doi:10.1093/hmg/ddr080 (2011).
203 Shu, X. *et al.* Characterisation of a C1qtnf5 Ser163Arg knock-in mouse model of late-onset retinal macular degeneration. *PLoS One* **6**, e27433, doi:10.1371/journal.pone.0027433 (2011).
204 Kameya, S. *et al.* Mfrp, a gene encoding a frizzled related protein, is mutated in the mouse retinal degeneration 6. *Hum Mol Genet* **11**, 1879-1886 (2002).
205 Blumenthal, T. Gene clusters and polycistronic transcription in eukaryotes. *Bioessays* **20**, 480-487, doi:10.1002/(sici)1521-1878(199806)20:6<480::aid-bies6>3.0.co;2-q (1998).
206 Lopez-Lastra, M., Rivas, A. & Barria, M. I. Protein synthesis in eukaryotes: the growing biological relevance of cap-independent translation initiation. *Biol Res* **38**, 121-146 (2005).
207 Chavali, V. R., Sommer, J. R., Petters, R. M. & Ayyagari, R. Identification of a promoter for the human C1Q-tumor necrosis factor-related protein-5 gene associated with late-onset retinal degeneration. *Invest Ophthalmol Vis Sci* **51**, 5499-5507, doi:10.1167/iovs.10-5543 (2010).
208 Mandal, M. N. *et al.* Spatial and temporal expression of MFRP and its interaction with CTRP5. *Invest Ophthalmol Vis Sci* **47**, 5514-5521, doi:10.1167/iovs.06-0449 (2006).

209 Katoh, M. Molecular cloning and characterization of MFRP, a novel gene encoding a membrane-type Frizzled-related protein. *Biochem Biophys Res Commun* **282**, 116-123, doi:10.1006/bbrc.2001.4551 (2001).
210 Sundin, O. H. *et al.* Extreme hyperopia is the result of null mutations in MFRP, which encodes a Frizzled-related protein. *Proc Natl Acad Sci U S A* **102**, 9553-9558, doi:10.1073/pnas.0501451102 (2005).
211 Yamauchi, T. *et al.* Cloning of adiponectin receptors that mediate antidiabetic metabolic effects. *Nature* **423**, 762-769, doi:10.1038/nature01705 (2003).
212 Yamauchi, T. *et al.* Targeted disruption of AdipoR1 and AdipoR2 causes abrogation of adiponectin binding and metabolic actions. *Nat Med* **13**, 332-339, doi:10.1038/nm1557 (2007).
213 Rice, D. S. *et al.* Adiponectin receptor 1 conserves docosahexaenoic acid and promotes photoreceptor cell survival. *Nat Commun* **6**, 6228, doi:10.1038/ncomms7228 (2015).
214 Sluch, V. M. *et al.* ADIPOR1 is essential for vision and its RPE expression is lost in the Mfrp(rd6) mouse. *Sci Rep* **8**, 14339, doi:10.1038/s41598-018-32579-9 (2018).
215 Gamal, W. *et al.* Real-time quantitative monitoring of hiPSC-based model of macular degeneration on Electric Cell-substrate Impedance Sensing microelectrodes. *Biosens Bioelectron* **71**, 445-455, doi:10.1016/j.bios.2015.04.079 (2015).
216 Sonoda, S. *et al.* A protocol for the culture and differentiation of highly polarized human retinal pigment epithelial cells. *Nat Protoc* **4**, 662-673, doi:10.1038/nprot.2009.33 (2009).
217 Mao, Y. & Finnemann, S. C. Analysis of photoreceptor outer segment phagocytosis by RPE cells in culture. *Methods Mol Biol* **935**, 285-295, doi:10.1007/978-1-62703-080-9_20 (2013).
218 Zerbino, D. R. *et al.* Ensembl 2018. *Nucleic Acids Res* **46**, D754-d761, doi:10.1093/nar/gkx1098 (2018).
219 Dobin, A. *et al.* STAR: ultrafast universal RNA-seq aligner. *Bioinformatics* **29**, 15-21, doi:10.1093/bioinformatics/bts635 (2013).
220 Liao, Y., Smyth, G. K. & Shi, W. featureCounts: an efficient general purpose program for assigning sequence reads to genomic features. *Bioinformatics* **30**, 923-930, doi:10.1093/bioinformatics/btt656 (2014).
221 Love, M. I., Huber, W. & Anders, S. Moderated estimation of fold change and dispersion for RNA-seq data with DESeq2. *Genome Biol* **15**, 550, doi:10.1186/s13059-014-0550-8 (2014).
222 Alexa, A., Rahnenfuhrer, J. & Lengauer, T. Improved scoring of functional groups from gene expression data by decorrelating GO graph structure. *Bioinformatics* **22**, 1600-1607, doi:10.1093/bioinformatics/btl140 (2006).
223 Wu, D. & Smyth, G. K. Camera: a competitive gene set test accounting for inter-gene correlation. *Nucleic Acids Res* **40**, e133, doi:10.1093/nar/gks461 (2012).
224 Kramer, A., Green, J., Pollard, J., Jr. & Tugendreich, S. Causal analysis approaches in Ingenuity Pathway Analysis. *Bioinformatics* **30**, 523-530, doi:10.1093/bioinformatics/btt703 (2014).
225 Giaever, I. & Keese, C. R. Monitoring fibroblast behavior in tissue culture with an applied electric field. *Proc Natl Acad Sci U S A* **81**, 3761-3764, doi:10.1073/pnas.81.12.3761 (1984).
226 Giaever, I. & Keese, C. R. Micromotion of mammalian cells measured electrically. *Proc Natl Acad Sci U S A* **88**, 7896-7900, doi:10.1073/pnas.88.17.7896 (1991).

227 Simons, K. & Fuller, S. D. Cell surface polarity in epithelia. *Annu Rev Cell Biol* **1**, 243-288, doi:10.1146/annurev.cb.01.110185.001331 (1985).
228 Zegers, M. M., O'Brien, L. E., Yu, W., Datta, A. & Mostov, K. E. Epithelial polarity and tubulogenesis in vitro. *Trends Cell Biol* **13**, 169-176 (2003).
229 Powell, D. W. Barrier function of epithelia. *Am J Physiol* **241**, G275-288, doi:10.1152/ajpgi.1981.241.4.G275 (1981).
230 Singh, R. *et al.* iPS cell modeling of Best disease: insights into the pathophysiology of an inherited macular degeneration. *Hum Mol Genet* **22**, 593-607, doi:10.1093/hmg/dds469 (2013).
231 Dinculescu, A. *et al.* Pathological Effects of Mutant C1QTNF5 (S163R) Expression in Murine Retinal Pigment Epithelium. *Invest Ophthalmol Vis Sci* **56**, 6971-6980, doi:10.1167/iovs.15-17166 (2015).
232 Tao, C. & Zhang, X. Development of astrocytes in the vertebrate eye. *Dev Dyn* **243**, 1501-1510, doi:10.1002/dvdy.24190 (2014).
233 Fruttiger, M. Development of the retinal vasculature. *Angiogenesis* **10**, 77-88, doi:10.1007/s10456-007-9065-1 (2007).
234 Glabinski, A. R. & Ransohoff, R. M. Sentries at the gate: chemokines and the blood-brain barrier. *J Neurovirol* **5**, 623-634 (1999).
235 Ramirez, J. M., Ramirez, A. I., Salazar, J. J., de Hoz, R. & Trivino, A. Changes of astrocytes in retinal ageing and age-related macular degeneration. *Exp Eye Res* **73**, 601-615, doi:10.1006/exer.2001.1061 (2001).
236 Penn, J. S. *et al.* Vascular endothelial growth factor in eye disease. *Prog Retin Eye Res* **27**, 331-371, doi:10.1016/j.preteyeres.2008.05.001 (2008).
237 Gasque, P., Fontaine, M. & Morgan, B. P. Complement expression in human brain. Biosynthesis of terminal pathway components and regulators in human glial cells and cell lines. *J Immunol* **154**, 4726-4733 (1995).
238 Gasque, P., Singhrao, S. K., Neal, J. W., Gotze, O. & Morgan, B. P. Expression of the receptor for complement C5a (CD88) is up-regulated on reactive astrocytes, microglia, and endothelial cells in the inflamed human central nervous system. *Am J Pathol* **150**, 31-41 (1997).
239 Strunnikova, N. V. *et al.* Transcriptome analysis and molecular signature of human retinal pigment epithelium. *Hum Mol Genet* **19**, 2468-2486, doi:10.1093/hmg/ddq129 (2010).
240 Kelwick, R., Desanlis, I., Wheeler, G. N. & Edwards, D. R. The ADAMTS (A Disintegrin and Metalloproteinase with Thrombospondin motifs) family. *Genome Biol* **16**, 113, doi:10.1186/s13059-015-0676-3 (2015).
241 Hussain, A. A., Lee, Y., Zhang, J. J., Francis, P. T. & Marshall, J. Disturbed Matrix Metalloproteinase Pathway in Both Age-Related Macular Degeneration and Alzheimer's Disease. *J Neurodegener Dis* **2017**, 4810232, doi:10.1155/2017/4810232 (2017).
242 Liutkeviciene, R. *et al.* The Role of Matrix Metalloproteinases Polymorphisms in Age-Related Macular Degeneration. *Ophthalmic Genet* **36**, 149-155, doi:10.3109/13816810.2013.838274 (2015).
243 Gao, X. R., Huang, H. & Kim, H. Genome-wide association analyses identify 139 loci associated with macular thickness in the UK Biobank cohort. *Hum Mol Genet* **28**, 1162-1172, doi:10.1093/hmg/ddy422 (2019).
244 Imanishi, Y., Batten, M. L., Piston, D. W., Baehr, W. & Palczewski, K. Noninvasive two-photon imaging reveals retinyl ester storage structures in the eye. *J Cell Biol* **164**, 373-383, doi:10.1083/jcb.200311079 (2004).

245 Malek, G., Hu, P., Wielgus, A., Dwyer, M. & Cousins, S. PPAR nuclear receptors and altered RPE lipid metabolism in age-related macular degeneration. *Adv Exp Med Biol* **664**, 429-436, doi:10.1007/978-1-4419-1399-9_49 (2010).
246 Copic, A. *et al.* A giant amphipathic helix from a perilipin that is adapted for coating lipid droplets. *Nat Commun* **9**, 1332, doi:10.1038/s41467-018-03717-8 (2018).
247 Dupont, N. *et al.* Neutral lipid stores and lipase PNPLA5 contribute to autophagosome biogenesis. *Curr Biol* **24**, 609-620, doi:10.1016/j.cub.2014.02.008 (2014).
248 Imanishi, Y., Sun, W., Maeda, T., Maeda, A. & Palczewski, K. Retinyl ester homeostasis in the adipose differentiation-related protein-deficient retina. *J Biol Chem* **283**, 25091-25102, doi:10.1074/jbc.M802981200 (2008).
249 Han, X. *et al.* Plin4-Dependent Lipid Droplets Hamper Neuronal Mitophagy in the MPTP/p-Induced Mouse Model of Parkinson's Disease. *Front Neurosci* **12**, 397, doi:10.3389/fnins.2018.00397 (2018).
250 Tyni, T. *et al.* Mitochondrial fatty acid beta-oxidation in the retinal pigment epithelium. *Pediatr Res* **52**, 595-600, doi:10.1203/00006450-200210000-00021 (2002).
251 Adijanto, J. *et al.* The retinal pigment epithelium utilizes fatty acids for ketogenesis. *J Biol Chem* **289**, 20570-20582, doi:10.1074/jbc.M114.565457 (2014).
252 Beatty, S., Koh, H., Phil, M., Henson, D. & Boulton, M. The role of oxidative stress in the pathogenesis of age-related macular degeneration. *Surv Ophthalmol* **45**, 115-134 (2000).
253 Yamada, K., Sakurai, E., Itaya, M., Yamasaki, S. & Ogura, Y. Inhibition of laser-induced choroidal neovascularization by atorvastatin by downregulation of monocyte chemotactic protein-1 synthesis in mice. *Invest Ophthalmol Vis Sci* **48**, 1839-1843, doi:10.1167/iovs.06-1085 (2007).
254 Espinosa-Heidmann, D. G. *et al.* Macrophage depletion diminishes lesion size and severity in experimental choroidal neovascularization. *Invest Ophthalmol Vis Sci* **44**, 3586-3592 (2003).
255 Sakurai, E., Anand, A., Ambati, B. K., van Rooijen, N. & Ambati, J. Macrophage depletion inhibits experimental choroidal neovascularization. *Invest Ophthalmol Vis Sci* **44**, 3578-3585 (2003).
256 Tsutsumi, C. *et al.* The critical role of ocular-infiltrating macrophages in the development of choroidal neovascularization. *J Leukoc Biol* **74**, 25-32 (2003).
257 Fang, I. M., Yang, C. H. & Yang, C. M. Docosahexaenoic acid reduces linoleic acid induced monocyte chemoattractant protein-1 expression via PPARgamma and nuclear factor-kappaB pathway in retinal pigment epithelial cells. *Mol Nutr Food Res* **58**, 2053-2065, doi:10.1002/mnfr.201400196 (2014).
258 Reichhart, N. *et al.* Anoctamin-4 is a bona fide Ca(2+)-dependent non-selective cation channel. *Sci Rep* **9**, 2257, doi:10.1038/s41598-018-37287-y (2019).
259 Schreiber, R. & Kunzelmann, K. Expression of anoctamins in retinal pigment epithelium (RPE). *Pflugers Arch* **468**, 1921-1929, doi:10.1007/s00424-016-1898-2 (2016).
260 Ott, M., Gogvadze, V., Orrenius, S. & Zhivotovsky, B. Mitochondria, oxidative stress and cell death. *Apoptosis* **12**, 913-922, doi:10.1007/s10495-007-0756-2 (2007).
261 Sena, L. A. & Chandel, N. S. Physiological roles of mitochondrial reactive oxygen species. *Mol Cell* **48**, 158-167, doi:10.1016/j.molcel.2012.09.025 (2012).
262 Yin, H., Xu, L. & Porter, N. A. Free radical lipid peroxidation: mechanisms and analysis. *Chem Rev* **111**, 5944-5972, doi:10.1021/cr200084z (2011).

263 Ayala, A., Munoz, M. F. & Arguelles, S. Lipid peroxidation: production, metabolism, and signaling mechanisms of malondialdehyde and 4-hydroxy-2-nonenal. *Oxid Med Cell Longev* **2014**, 360438, doi:10.1155/2014/360438 (2014).
264 Esterbauer, H., Eckl, P. & Ortner, A. Possible mutagens derived from lipids and lipid precursors. *Mutat Res* **238**, 223-233 (1990).
265 Esterbauer, H., Schaur, R. J. & Zollner, H. Chemistry and biochemistry of 4-hydroxynonenal, malonaldehyde and related aldehydes. *Free Radic Biol Med* **11**, 81-128 (1991).
266 Schaur, R. J. Basic aspects of the biochemical reactivity of 4-hydroxynonenal. *Mol Aspects Med* **24**, 149-159 (2003).
267 Papac-Milicevic, N., Busch, C. J. & Binder, C. J. Malondialdehyde Epitopes as Targets of Immunity and the Implications for Atherosclerosis. *Adv Immunol* **131**, 1-59, doi:10.1016/bs.ai.2016.02.001 (2016).
268 Kaemmerer, E., Schutt, F., Krohne, T. U., Holz, F. G. & Kopitz, J. Effects of lipid peroxidation-related protein modifications on RPE lysosomal functions and POS phagocytosis. *Invest Ophthalmol Vis Sci* **48**, 1342-1347, doi:10.1167/iovs.06-0549 (2007).
269 Krohne, T. U., Holz, F. G. & Kopitz, J. Apical-to-basolateral transcytosis of photoreceptor outer segments induced by lipid peroxidation products in human retinal pigment epithelial cells. *Invest Ophthalmol Vis Sci* **51**, 553-560, doi:10.1167/iovs.09-3755 (2010).
270 Balaban, R. S., Nemoto, S. & Finkel, T. Mitochondria, oxidants, and aging. *Cell* **120**, 483-495, doi:10.1016/j.cell.2005.02.001 (2005).
271 Zhang, H., Davies, K. J. A. & Forman, H. J. Oxidative stress response and Nrf2 signaling in aging. *Free Radic Biol Med* **88**, 314-336, doi:10.1016/j.freeradbiomed.2015.05.036 (2015).
272 Samiec, P. S. *et al.* Glutathione in human plasma: decline in association with aging, age-related macular degeneration, and diabetes. *Free Radic Biol Med* **24**, 699-704 (1998).
273 A randomized, placebo-controlled, clinical trial of high-dose supplementation with vitamins C and E, beta carotene, and zinc for age-related macular degeneration and vision loss: AREDS report no. 8. *Arch Ophthalmol* **119**, 1417-1436 (2001).
274 Seddon, J. M., George, S. & Rosner, B. Cigarette smoking, fish consumption, omega-3 fatty acid intake, and associations with age-related macular degeneration: the US Twin Study of Age-Related Macular Degeneration. *Arch Ophthalmol* **124**, 995-1001, doi:10.1001/archopht.124.7.995 (2006).
275 Christen, W. G., Glynn, R. J., Manson, J. E., Ajani, U. A. & Buring, J. E. A prospective study of cigarette smoking and risk of age-related macular degeneration in men. *Jama* **276**, 1147-1151 (1996).
276 Seddon, J. M., Willett, W. C., Speizer, F. E. & Hankinson, S. E. A prospective study of cigarette smoking and age-related macular degeneration in women. *Jama* **276**, 1141-1146 (1996).
277 Woodell, A. & Rohrer, B. A mechanistic review of cigarette smoke and age-related macular degeneration. *Adv Exp Med Biol* **801**, 301-307, doi:10.1007/978-1-4614-3209-8_38 (2014).
278 Shen, J. K. *et al.* Oxidative damage in age-related macular degeneration. *Histol Histopathol* **22**, 1301-1308, doi:10.14670/hh-22.1301 (2007).
279 Sacca, S. C., Roszkowska, A. M. & Izzotti, A. Environmental light and endogenous antioxidants as the main determinants of non-cancer ocular diseases. *Mutat Res* **752**, 153-171, doi:10.1016/j.mrrev.2013.01.001 (2013).

280 Miceli, M. V., Liles, M. R. & Newsome, D. A. Evaluation of oxidative processes in human pigment epithelial cells associated with retinal outer segment phagocytosis. *Exp Cell Res* **214**, 242-249, doi:10.1006/excr.1994.1254 (1994).
281 Tate, D. J., Jr., Miceli, M. V. & Newsome, D. A. Phagocytosis and H2O2 induce catalase and metallothionein gene expression in human retinal pigment epithelial cells. *Invest Ophthalmol Vis Sci* **36**, 1271-1279 (1995).
282 Fliesler, S. J. & Anderson, R. E. Chemistry and metabolism of lipids in the vertebrate retina. *Prog Lipid Res* **22**, 79-131 (1983).
283 Sparrow, J. R. & Boulton, M. RPE lipofuscin and its role in retinal pathobiology. *Exp Eye Res* **80**, 595-606, doi:10.1016/j.exer.2005.01.007 (2005).
284 Eldred, G. E., Miller, G. V., Stark, W. S. & Feeney-Burns, L. Lipofuscin: resolution of discrepant fluorescence data. *Science* **216**, 757-759 (1982).
285 Feeney-Burns, L. & Eldred, G. E. The fate of the phagosome: conversion to 'age pigment' and impact in human retinal pigment epithelium. *Trans Ophthalmol Soc U K* **103 (Pt 4)**, 416-421 (1983).
286 Delori, F. C. *et al.* In vivo fluorescence of the ocular fundus exhibits retinal pigment epithelium lipofuscin characteristics. *Invest Ophthalmol Vis Sci* **36**, 718-729 (1995).
287 Dorey, C. K., Wu, G., Ebenstein, D., Garsd, A. & Weiter, J. J. Cell loss in the aging retina. Relationship to lipofuscin accumulation and macular degeneration. *Invest Ophthalmol Vis Sci* **30**, 1691-1699 (1989).
288 Schutt, F., Bergmann, M., Holz, F. G. & Kopitz, J. Proteins modified by malondialdehyde, 4-hydroxynonenal, or advanced glycation end products in lipofuscin of human retinal pigment epithelium. *Invest Ophthalmol Vis Sci* **44**, 3663-3668 (2003).
289 Boulton, M., Rozanowska, M. & Rozanowski, B. Retinal photodamage. *J Photochem Photobiol B* **64**, 144-161 (2001).
290 Sparrow, J. R. *et al.* Involvement of oxidative mechanisms in blue-light-induced damage to A2E-laden RPE. *Invest Ophthalmol Vis Sci* **43**, 1222-1227 (2002).
291 Zhou, J. *et al.* Mechanisms for the induction of HNE- MDA- and AGE-adducts, RAGE and VEGF in retinal pigment epithelial cells. *Exp Eye Res* **80**, 567-580, doi:10.1016/j.exer.2004.11.009 (2005).
292 SanGiovanni, J. P. & Chew, E. Y. The role of omega-3 long-chain polyunsaturated fatty acids in health and disease of the retina. *Prog Retin Eye Res* **24**, 87-138, doi:10.1016/j.preteyeres.2004.06.002 (2005).
293 Bazan, N. G., Molina, M. F. & Gordon, W. C. Docosahexaenoic acid signalolipidomics in nutrition: significance in aging, neuroinflammation, macular degeneration, Alzheimer's, and other neurodegenerative diseases. *Annu Rev Nutr* **31**, 321-351, doi:10.1146/annurev.nutr.012809.104635 (2011).
294 Gu, X. *et al.* Carboxyethylpyrrole protein adducts and autoantibodies, biomarkers for age-related macular degeneration. *J Biol Chem* **278**, 42027-42035, doi:10.1074/jbc.M305460200 (2003).
295 Ebrahem, Q. *et al.* Carboxyethylpyrrole oxidative protein modifications stimulate neovascularization: Implications for age-related macular degeneration. *Proc Natl Acad Sci U S A* **103**, 13480-13484, doi:10.1073/pnas.0601552103 (2006).
296 West, X. Z. *et al.* Oxidative stress induces angiogenesis by activating TLR2 with novel endogenous ligands. *Nature* **467**, 972-976, doi:10.1038/nature09421 (2010).
297 Hollyfield, J. G. *et al.* Oxidative damage-induced inflammation initiates age-related macular degeneration. *Nat Med* **14**, 194-198, doi:10.1038/nm1709 (2008).

298 Wong, R. W., Richa, D. C., Hahn, P., Green, W. R. & Dunaief, J. L. Iron toxicity as a potential factor in AMD. *Retina* **27**, 997-1003, doi:10.1097/IAE.0b013e318074c290 (2007).
299 He, X. *et al.* Iron homeostasis and toxicity in retinal degeneration. *Prog Retin Eye Res* **26**, 649-673, doi:10.1016/j.preteyeres.2007.07.004 (2007).
300 Ueda, K. *et al.* Iron promotes oxidative cell death caused by bisretinoids of retina. *Proc Natl Acad Sci U S A* **115**, 4963-4968, doi:10.1073/pnas.1722601115 (2018).
301 Yam, J. C. & Kwok, A. K. Ultraviolet light and ocular diseases. *Int Ophthalmol* **34**, 383-400, doi:10.1007/s10792-013-9791-x (2014).
302 Voke, J. Radiation effects on the eye. *Part 3b-Ocular effects of ultraviolet radiation. OT*, 37-40 (1999).
303 Marazita, M. C., Dugour, A., Marquioni-Ramella, M. D., Figueroa, J. M. & Suburo, A. M. Oxidative stress-induced premature senescence dysregulates VEGF and CFH expression in retinal pigment epithelial cells: Implications for Age-related Macular Degeneration. *Redox Biol* **7**, 78-87, doi:10.1016/j.redox.2015.11.011 (2016).
304 Thurman, J. M. *et al.* Oxidative stress renders retinal pigment epithelial cells susceptible to complement-mediated injury. *J Biol Chem* **284**, 16939-16947, doi:10.1074/jbc.M808166200 (2009).
305 Ryter, S. W. *et al.* Mechanisms of cell death in oxidative stress. *Antioxid Redox Signal* **9**, 49-89, doi:10.1089/ars.2007.9.49 (2007).
306 Hanus, J. *et al.* Induction of necrotic cell death by oxidative stress in retinal pigment epithelial cells. *Cell Death Dis* **4**, e965, doi:10.1038/cddis.2013.478 (2013).
307 Christofferson, D. E. & Yuan, J. Necroptosis as an alternative form of programmed cell death. *Curr Opin Cell Biol* **22**, 263-268, doi:10.1016/j.ceb.2009.12.003 (2010).
308 Vanden Berghe, T., Linkermann, A., Jouan-Lanhouet, S., Walczak, H. & Vandenabeele, P. Regulated necrosis: the expanding network of non-apoptotic cell death pathways. *Nat Rev Mol Cell Biol* **15**, 135-147, doi:10.1038/nrm3737 (2014).
309 Christofferson, D. E., Li, Y. & Yuan, J. Control of life-or-death decisions by RIP1 kinase. *Annu Rev Physiol* **76**, 129-150, doi:10.1146/annurev-physiol-021113-170259 (2014).
310 Sun, L. *et al.* Mixed lineage kinase domain-like protein mediates necrosis signaling downstream of RIP3 kinase. *Cell* **148**, 213-227, doi:10.1016/j.cell.2011.11.031 (2012).
311 Cai, Z. *et al.* Plasma membrane translocation of trimerized MLKL protein is required for TNF-induced necroptosis. *Nat Cell Biol* **16**, 55-65, doi:10.1038/ncb2883 (2014).
312 Chen, X. *et al.* Translocation of mixed lineage kinase domain-like protein to plasma membrane leads to necrotic cell death. *Cell Res* **24**, 105-121, doi:10.1038/cr.2013.171 (2014).
313 Wang, H. *et al.* Mixed lineage kinase domain-like protein MLKL causes necrotic membrane disruption upon phosphorylation by RIP3. *Mol Cell* **54**, 133-146, doi:10.1016/j.molcel.2014.03.003 (2014).
314 Dixon, S. J. *et al.* Ferroptosis: an iron-dependent form of nonapoptotic cell death. *Cell* **149**, 1060-1072, doi:10.1016/j.cell.2012.03.042 (2012).
315 Wenz, C. *et al.* t-BuOOH induces ferroptosis in human and murine cell lines. *Arch Toxicol*, doi:10.1007/s00204-017-2066-y (2017).
316 Totsuka, K. *et al.* Oxidative stress induces ferroptotic cell death in retinal pigment epithelial cells. *Exp Eye Res*, doi:10.1016/j.exer.2018.08.019 (2018).
317 Brigelius-Flohe, R. & Maiorino, M. Glutathione peroxidases. *Biochim Biophys Acta* **1830**, 3289-3303, doi:10.1016/j.bbagen.2012.11.020 (2013).

318 Yang, W. S. *et al.* Regulation of ferroptotic cancer cell death by GPX4. *Cell* **156**, 317-331, doi:10.1016/j.cell.2013.12.010 (2014).
319 Doll, S. *et al.* ACSL4 dictates ferroptosis sensitivity by shaping cellular lipid composition. *Nat Chem Biol* **13**, 91-98, doi:10.1038/nchembio.2239 (2017).
320 Kagan, V. E. *et al.* Oxidized arachidonic and adrenic PEs navigate cells to ferroptosis. *Nat Chem Biol* **13**, 81-90, doi:10.1038/nchembio.2238 (2017).
321 Dixon, S. J. *et al.* Human Haploid Cell Genetics Reveals Roles for Lipid Metabolism Genes in Nonapoptotic Cell Death. *ACS Chem Biol* **10**, 1604-1609, doi:10.1021/acschembio.5b00245 (2015).
322 Oliveira, A. F. *et al.* In vitro use of free fatty acids bound to albumin: A comparison of protocols. *Biotechniques* **58**, 228-233, doi:10.2144/000114285 (2015).
323 Drummen, G. P., van Liebergen, L. C., Op den Kamp, J. A. & Post, J. A. C11-BODIPY(581/591), an oxidation-sensitive fluorescent lipid peroxidation probe: (micro)spectroscopic characterization and validation of methodology. *Free Radic Biol Med* **33**, 473-490 (2002).
324 SanGiovanni, J. P. *et al.* The relationship of dietary lipid intake and age-related macular degeneration in a case-control study: AREDS Report No. 20. *Arch Ophthalmol* **125**, 671-679, doi:10.1001/archopht.125.5.671 (2007).
325 SanGiovanni, J. P. *et al.* The relationship of dietary omega-3 long-chain polyunsaturated fatty acid intake with incident age-related macular degeneration: AREDS report no. 23. *Arch Ophthalmol* **126**, 1274-1279, doi:10.1001/archopht.126.9.1274 (2008).
326 Stone, W. L., Farnsworth, C. C. & Dratz, E. A. A reinvestigation of the fatty acid content of bovine, rat and frog retinal rod outer segments. *Exp Eye Res* **28**, 387-397 (1979).
327 Mukherjee, P. K. *et al.* Neurotrophins enhance retinal pigment epithelial cell survival through neuroprotectin D1 signaling. *Proc Natl Acad Sci U S A* **104**, 13152-13157, doi:10.1073/pnas.0705949104 (2007).
328 Bazan, N. G. Neuroprotectin D1 (NPD1): a DHA-derived mediator that protects brain and retina against cell injury-induced oxidative stress. *Brain Pathol* **15**, 159-166 (2005).
329 Wu, J. *et al.* Dietary Intakes of Eicosapentaenoic Acid and Docosahexaenoic Acid and Risk of Age-Related Macular Degeneration. *Ophthalmology* **124**, 634-643, doi:10.1016/j.ophtha.2016.12.033 (2017).
330 Agbaga, M. P. *et al.* Differential composition of DHA and very-long-chain PUFAs in rod and cone photoreceptors. *J Lipid Res* **59**, 1586-1596, doi:10.1194/jlr.M082495 (2018).
331 Berdeaux, O. *et al.* Identification and quantification of phosphatidylcholines containing very-long-chain polyunsaturated fatty acid in bovine and human retina using liquid chromatography/tandem mass spectrometry. *J Chromatogr A* **1217**, 7738-7748, doi:10.1016/j.chroma.2010.10.039 (2010).
332 Logan, S. & Anderson, R. E. Dominant Stargardt Macular Dystrophy (STGD3) and ELOVL4. *Adv Exp Med Biol* **801**, 447-453, doi:10.1007/978-1-4614-3209-8_57 (2014).
333 Haimovici, R., D'Amico, D. J., Gragoudas, E. S. & Sokol, S. The expanded clinical spectrum of deferoxamine retinopathy. *Ophthalmology* **109**, 164-171 (2002).
334 Klettner, A., Koinzer, S., Waetzig, V., Herdegen, T. & Roider, J. Deferoxamine mesylate is toxic for retinal pigment epithelium cells in vitro, and its toxicity is mediated by p38. *Cutan Ocul Toxicol* **29**, 122-129, doi:10.3109/15569521003745685 (2010).

335 Di Nicola, M., Barteselli, G., Dell'Arti, L., Ratiglia, R. & Viola, F. Functional and Structural Abnormalities in Deferoxamine Retinopathy: A Review of the Literature. *Biomed Res Int* **2015**, 249617, doi:10.1155/2015/249617 (2015).
336 Johansson, I. *et al.* The marine n-3 PUFA DHA evokes cytoprotection against oxidative stress and protein misfolding by inducing autophagy and NFE2L2 in human retinal pigment epithelial cells. *Autophagy* **11**, 1636-1651, doi:10.1080/15548627.2015.1061170 (2015).
337 Eto, M., Shindou, H. & Shimizu, T. A novel lysophosphatidic acid acyltransferase enzyme (LPAAT4) with a possible role for incorporating docosahexaenoic acid into brain glycerophospholipids. *Biochem Biophys Res Commun* **443**, 718-724, doi:10.1016/j.bbrc.2013.12.043 (2014).
338 Valentine, W. J. *et al.* LPAAT3 incorporates docosahexaenoic acid into skeletal muscle cell membranes and is upregulated by PPARdelta activation. *J Lipid Res* **59**, 184-194, doi:10.1194/jlr.M077321 (2018).
339 Ershov, A. V. & Bazan, N. G. Photoreceptor phagocytosis selectively activates PPARgamma expression in retinal pigment epithelial cells. *J Neurosci Res* **60**, 328-337, doi:10.1002/(sici)1097-4547(20000501)60:3<328::aid-jnr7>3.0.co;2-5 (2000).
340 Van Horn, C. G. *et al.* Characterization of recombinant long-chain rat acyl-CoA synthetase isoforms 3 and 6: identification of a novel variant of isoform 6. *Biochemistry* **44**, 1635-1642, doi:10.1021/bi047721l (2005).
341 Shimshoni, J. A. *et al.* Valproate uncompetitively inhibits arachidonic acid acylation by rat acyl-CoA synthetase 4: relevance to valproate's efficacy against bipolar disorder. *Biochim Biophys Acta* **1811**, 163-169, doi:10.1016/j.bbalip.2010.12.006 (2011).
342 Muller, T. *et al.* Necroptosis and ferroptosis are alternative cell death pathways that operate in acute kidney failure. *Cell Mol Life Sci*, doi:10.1007/s00018-017-2547-4 (2017).
343 Cheng, Y. S. *et al.* Light-induced generation and toxicity of docosahexaenoate-derived oxidation products in retinal pigmented epithelial cells. *Exp Eye Res*, doi:10.1016/j.exer.2018.09.012 (2018).
344 Wiegand, R. D., Giusto, N. M., Rapp, L. M. & Anderson, R. E. Evidence for rod outer segment lipid peroxidation following constant illumination of the rat retina. *Invest Ophthalmol Vis Sci* **24**, 1433-1435 (1983).
345 Tanito, M. *et al.* High levels of retinal membrane docosahexaenoic acid increase susceptibility to stress-induced degeneration. *J Lipid Res* **50**, 807-819, doi:10.1194/jlr.M800170-JLR200 (2009).
346 Organisciak, D. T., Darrow, R. M., Jiang, Y. L. & Blanks, J. C. Retinal light damage in rats with altered levels of rod outer segment docosahexaenoate. *Invest Ophthalmol Vis Sci* **37**, 2243-2257 (1996).
347 Janeway, C. *Immunobiology : the immune system in health and disease*. Sixth edition.. edn, (New York ; London : Garland Science/Churchill Livingstone, 2005).
348 Walport, M. J. Complement. First of two parts. *N Engl J Med* **344**, 1058-1066, doi:10.1056/nejm200104053441406 (2001).
349 Ricklin, D., Hajishengallis, G., Yang, K. & Lambris, J. D. Complement: a key system for immune surveillance and homeostasis. *Nat Immunol* **11**, 785-797, doi:10.1038/ni.1923 (2010).
350 Dunkelberger, J. R. & Song, W. C. Complement and its role in innate and adaptive immune responses. *Cell Res* **20**, 34-50, doi:10.1038/cr.2009.139 (2010).
351 Rus, H., Cudrici, C. & Niculescu, F. The role of the complement system in innate immunity. *Immunol Res* **33**, 103-112, doi:10.1385/ir:33:2:103 (2005).

352 Fujita, T., Endo, Y. & Nonaka, M. Primitive complement system--recognition and activation. *Mol Immunol* **41**, 103-111, doi:10.1016/j.molimm.2004.03.026 (2004).
353 Klos, A., Wende, E., Wareham, K. J. & Monk, P. N. International Union of Basic and Clinical Pharmacology. [corrected]. LXXXVII. Complement peptide C5a, C4a, and C3a receptors. *Pharmacol Rev* **65**, 500-543 (2013).
354 Davis, A. E., 3rd. Biological effects of C1 inhibitor. *Drug News Perspect* **17**, 439-446 (2004).
355 Cicardi, M., Zingale, L., Zanichelli, A., Pappalardo, E. & Cicardi, B. C1 inhibitor: molecular and clinical aspects. *Springer Semin Immunopathol* **27**, 286-298, doi:10.1007/s00281-005-0001-4 (2005).
356 Goldberger, G., Bruns, G. A., Rits, M., Edge, M. D. & Kwiatkowski, D. J. Human complement factor I: analysis of cDNA-derived primary structure and assignment of its gene to chromosome 4. *J Biol Chem* **262**, 10065-10071 (1987).
357 Weiler, J. M., Daha, M. R., Austen, K. F. & Fearon, D. T. Control of the amplification convertase of complement by the plasma protein beta1H. *Proc Natl Acad Sci U S A* **73**, 3268-3272 (1976).
358 Whaley, K. & Ruddy, S. Modulation of the alternative complement pathways by beta 1 H globulin. *J Exp Med* **144**, 1147-1163 (1976).
359 Pangburn, M. K., Schreiber, R. D. & Muller-Eberhard, H. J. Human complement C3b inactivator: isolation, characterization, and demonstration of an absolute requirement for the serum protein beta1H for cleavage of C3b and C4b in solution. *J Exp Med* **146**, 257-270 (1977).
360 Alsenz, J., Lambris, J. D., Schulz, T. F. & Dierich, M. P. Localization of the complement-component-C3b-binding site and the cofactor activity for factor I in the 38kDa tryptic fragment of factor H. *Biochem J* **224**, 389-398 (1984).
361 Kuhn, S., Skerka, C. & Zipfel, P. F. Mapping of the complement regulatory domains in the human factor H-like protein 1 and in factor H1. *J Immunol* **155**, 5663-5670 (1995).
362 Sharma, A. K. & Pangburn, M. K. Identification of three physically and functionally distinct binding sites for C3b in human complement factor H by deletion mutagenesis. *Proc Natl Acad Sci U S A* **93**, 10996-11001 (1996).
363 Mandal, M. N. & Ayyagari, R. Complement factor H: spatial and temporal expression and localization in the eye. *Invest Ophthalmol Vis Sci* **47**, 4091-4097, doi:10.1167/iovs.05-1655 (2006).
364 Chen, M., Forrester, J. V. & Xu, H. Synthesis of complement factor H by retinal pigment epithelial cells is down-regulated by oxidized photoreceptor outer segments. *Exp Eye Res* **84**, 635-645, doi:10.1016/j.exer.2006.11.015 (2007).
365 Wu, Z., Lauer, T. W., Sick, A., Hackett, S. F. & Campochiaro, P. A. Oxidative stress modulates complement factor H expression in retinal pigmented epithelial cells by acetylation of FOXO3. *J Biol Chem* **282**, 22414-22425, doi:10.1074/jbc.M702321200 (2007).
366 Ward, H. M., Higgs, N. H., Blackmore, T. K., Sadlon, T. A. & Gordon, D. L. Cloning and analysis of the human complement factor H gene promoter. *Immunol Cell Biol* **75**, 508-510, doi:10.1038/icb.1997.79 (1997).
367 Cantsilieris, S. *et al.* Recurrent structural variation, clustered sites of selection, and disease risk for the complement factor H (CFH) gene family. *Proc Natl Acad Sci U S A* **115**, E4433-e4442, doi:10.1073/pnas.1717600115 (2018).
368 Sudmant, P. H. *et al.* Diversity of human copy number variation and multicopy genes. *Science* **330**, 641-646, doi:10.1126/science.1197005 (2010).

369 Hughes, A. E. *et al.* A common CFH haplotype, with deletion of CFHR1 and CFHR3, is associated with lower risk of age-related macular degeneration. *Nat Genet* **38**, 1173-1177, doi:10.1038/ng1890 (2006).
370 Hellwage, J. *et al.* Complement C3b/C3d and cell surface polyanions are recognized by overlapping binding sites on the most carboxyl-terminal domain of complement factor H. *J Immunol* **169**, 6935-6944 (2002).
371 Ferreira, V. P., Herbert, A. P., Hocking, H. G., Barlow, P. N. & Pangburn, M. K. Critical role of the C-terminal domains of factor H in regulating complement activation at cell surfaces. *J Immunol* **177**, 6308-6316 (2006).
372 Jozsi, M., Manuelian, T., Heinen, S., Oppermann, M. & Zipfel, P. F. Attachment of the soluble complement regulator factor H to cell and tissue surfaces: relevance for pathology. *Histol Histopathol* **19**, 251-258, doi:10.14670/hh-19.251 (2004).
373 Jozsi, M., Oppermann, M., Lambris, J. D. & Zipfel, P. F. The C-terminus of complement factor H is essential for host cell protection. *Mol Immunol* **44**, 2697-2706, doi:10.1016/j.molimm.2006.12.001 (2007).
374 Meri, S. & Pangburn, M. K. Discrimination between activators and nonactivators of the alternative pathway of complement: regulation via a sialic acid/polyanion binding site on factor H. *Proc Natl Acad Sci U S A* **87**, 3982-3986 (1990).
375 Yang, P., Tyrrell, J., Han, I. & Jaffe, G. J. Expression and modulation of RPE cell membrane complement regulatory proteins. *Invest Ophthalmol Vis Sci* **50**, 3473-3481, doi:10.1167/iovs.08-3202 (2009).
376 Juel, H. B. *et al.* Retinal pigment epithelial cells upregulate expression of complement factors after co-culture with activated T cells. *Exp Eye Res* **92**, 180-188, doi:10.1016/j.exer.2011.01.003 (2011).
377 Ma, K. N., Cashman, S. M., Sweigard, J. H. & Kumar-Singh, R. Decay accelerating factor (CD55)-mediated attenuation of complement: therapeutic implications for age-related macular degeneration. *Invest Ophthalmol Vis Sci* **51**, 6776-6783, doi:10.1167/iovs.10-5887 (2010).
378 Carver, K. A. & Yang, D. N-Acetylcysteine Amide Protects Against Oxidative Stress-Induced Microparticle Release From Human Retinal Pigment Epithelial Cells. *Invest Ophthalmol Vis Sci* **57**, 360-371, doi:10.1167/iovs.15-17117 (2016).
379 Anderson, D. H. *et al.* The pivotal role of the complement system in aging and age-related macular degeneration: hypothesis re-visited. *Prog Retin Eye Res* **29**, 95-112, doi:10.1016/j.preteyeres.2009.11.003 (2010).
380 Gehrs, K. M., Jackson, J. R., Brown, E. N., Allikmets, R. & Hageman, G. S. Complement, age-related macular degeneration and a vision of the future. *Arch Ophthalmol* **128**, 349-358, doi:10.1001/archophthalmol.2010.18 (2010).
381 Edwards, A. O. *et al.* Complement factor H polymorphism and age-related macular degeneration. *Science* **308**, 421-424, doi:10.1126/science.1110189 (2005).
382 Haines, J. L. *et al.* Complement factor H variant increases the risk of age-related macular degeneration. *Science* **308**, 419-421, doi:10.1126/science.1110359 (2005).
383 Klein, R. J. *et al.* Complement factor H polymorphism in age-related macular degeneration. *Science* **308**, 385-389, doi:10.1126/science.1109557 (2005).
384 Hageman, G. S. *et al.* A common haplotype in the complement regulatory gene factor H (HF1/CFH) predisposes individuals to age-related macular degeneration. *Proc Natl Acad Sci U S A* **102**, 7227-7232, doi:10.1073/pnas.0501536102 (2005).
385 Zareparsi, S. *et al.* Strong association of the Y402H variant in complement factor H at 1q32 with susceptibility to age-related macular degeneration. *Am J Hum Genet* **77**, 149-153, doi:10.1086/431426 (2005).

386 Clark, S. J., Bishop, P. N. & Day, A. J. Complement factor H and age-related macular degeneration: the role of glycosaminoglycan recognition in disease pathology. *Biochem Soc Trans* **38**, 1342-1348, doi:10.1042/bst0381342 (2010).
387 Clark, S. J. *et al.* Impaired binding of the age-related macular degeneration-associated complement factor H 402H allotype to Bruch's membrane in human retina. *J Biol Chem* **285**, 30192-30202, doi:10.1074/jbc.M110.103986 (2010).
388 Mullins, R. F. *et al.* Elevated membrane attack complex in human choroid with high risk complement factor H genotypes. *Exp Eye Res* **93**, 565-567, doi:10.1016/j.exer.2011.06.015 (2011).
389 Mullins, R. F. *et al.* The membrane attack complex in aging human choriocapillaris: relationship to macular degeneration and choroidal thinning. *Am J Pathol* **184**, 3142-3153, doi:10.1016/j.ajpath.2014.07.017 (2014).
390 Yates, J. R. *et al.* Complement C3 variant and the risk of age-related macular degeneration. *N Engl J Med* **357**, 553-561, doi:10.1056/NEJMoa072618 (2007).
391 Maller, J. B. *et al.* Variation in complement factor 3 is associated with risk of age-related macular degeneration. *Nat Genet* **39**, 1200-1201, doi:10.1038/ng2131 (2007).
392 Heurich, M. *et al.* Common polymorphisms in C3, factor B, and factor H collaborate to determine systemic complement activity and disease risk. *Proc Natl Acad Sci U S A* **108**, 8761-8766, doi:10.1073/pnas.1019338108 (2011).
393 Gold, B. *et al.* Variation in factor B (BF) and complement component 2 (C2) genes is associated with age-related macular degeneration. *Nat Genet* **38**, 458-462, doi:10.1038/ng1750 (2006).
394 Spencer, K. L. *et al.* Protective effect of complement factor B and complement component 2 variants in age-related macular degeneration. *Hum Mol Genet* **16**, 1986-1992, doi:10.1093/hmg/ddm146 (2007).
395 Fagerness, J. A. *et al.* Variation near complement factor I is associated with risk of advanced AMD. *Eur J Hum Genet* **17**, 100-104, doi:10.1038/ejhg.2008.140 (2009).
396 van de Ven, J. P. *et al.* A functional variant in the CFI gene confers a high risk of age-related macular degeneration. *Nat Genet* **45**, 813-817, doi:10.1038/ng.2640 (2013).
397 Wang, L. *et al.* Abundant lipid and protein components of drusen. *PLoS One* **5**, e10329, doi:10.1371/journal.pone.0010329 (2010).
398 Anderson, D. H., Mullins, R. F., Hageman, G. S. & Johnson, L. V. A role for local inflammation in the formation of drusen in the aging eye. *Am J Ophthalmol* **134**, 411-431 (2002).
399 Johnson, L. V., Leitner, W. P., Staples, M. K. & Anderson, D. H. Complement activation and inflammatory processes in Drusen formation and age related macular degeneration. *Exp Eye Res* **73**, 887-896, doi:10.1006/exer.2001.1094 (2001).
400 Johnson, L. V., Ozaki, S., Staples, M. K., Erickson, P. A. & Anderson, D. H. A potential role for immune complex pathogenesis in drusen formation. *Exp Eye Res* **70**, 441-449, doi:10.1006/exer.1999.0798 (2000).
401 Mullins, R. F., Russell, S. R., Anderson, D. H. & Hageman, G. S. Drusen associated with aging and age-related macular degeneration contain proteins common to extracellular deposits associated with atherosclerosis, elastosis, amyloidosis, and dense deposit disease. *Faseb j* **14**, 835-846 (2000).
402 Vitek, M. P., Brown, C. M. & Colton, C. A. APOE genotype-specific differences in the innate immune response. *Neurobiol Aging* **30**, 1350-1360, doi:10.1016/j.neurobiolaging.2007.11.014 (2009).

403 Cezario, S. M. *et al.* Association of high-density lipoprotein and apolipoprotein E genetic variants with age-related macular degeneration. *Arq Bras Oftalmol* **78**, 85-88, doi:10.5935/0004-2749.20150023 (2015).
404 Levy, O. *et al.* Apolipoprotein E promotes subretinal mononuclear phagocyte survival and chronic inflammation in age-related macular degeneration. *EMBO Mol Med* **7**, 211-226, doi:10.15252/emmm.201404524 (2015).
405 Johnson, L. V. *et al.* Cell culture model that mimics drusen formation and triggers complement activation associated with age-related macular degeneration. *Proc Natl Acad Sci U S A* **108**, 18277-18282, doi:10.1073/pnas.1109703108 (2011).
406 Galloway, C. A. *et al.* Drusen in patient-derived hiPSC-RPE models of macular dystrophies. *Proc Natl Acad Sci U S A* **114**, E8214-e8223, doi:10.1073/pnas.1710430114 (2017).
407 Rabiolo, A. *et al.* Spotlight on reticular pseudodrusen. *Clin Ophthalmol* **11**, 1707-1718, doi:10.2147/opth.s130165 (2017).
408 Spaide, R. F., Ooto, S. & Curcio, C. A. Subretinal drusenoid deposits AKA pseudodrusen. *Surv Ophthalmol* **63**, 782-815, doi:10.1016/j.survophthal.2018.05.005 (2018).
409 Weismann, D. *et al.* Complement factor H binds malondialdehyde epitopes and protects from oxidative stress. *Nature* **478**, 76-81, doi:10.1038/nature10449 (2011).
410 Shaw, P. X. *et al.* Complement factor H genotypes impact risk of age-related macular degeneration by interaction with oxidized phospholipids. *Proc Natl Acad Sci U S A* **109**, 13757-13762, doi:10.1073/pnas.1121309109 (2012).
411 Yang, P. *et al.* Retinal pigment epithelial cell death by the alternative complement cascade: role of membrane regulatory proteins, calcium, PKC, and oxidative stress. *Invest Ophthalmol Vis Sci* **55**, 3012-3021, doi:10.1167/iovs.13-13554 (2014).
412 Fernandez-Godino, R., Bujakowska, K. M. & Pierce, E. A. Changes in extracellular matrix cause RPE cells to make basal deposits and activate the alternative complement pathway. *Hum Mol Genet* **27**, 147-159, doi:10.1093/hmg/ddx392 (2018).
413 Keenan, T. D., Goldacre, R. & Goldacre, M. J. Associations between age-related macular degeneration, Alzheimer disease, and dementia: record linkage study of hospital admissions. *JAMA Ophthalmol* **132**, 63-68, doi:10.1001/jamaophthalmol.2013.5696 (2014).
414 Ratnayaka, J. A., Serpell, L. C. & Lotery, A. J. Dementia of the eye: the role of amyloid beta in retinal degeneration. *Eye (Lond)* **29**, 1013-1026, doi:10.1038/eye.2015.100 (2015).
415 Chung, S. D. *et al.* Association between neovascular age-related macular degeneration and dementia: a population-based case-control study in Taiwan. *PLoS One* **10**, e0120003, doi:10.1371/journal.pone.0120003 (2015).
416 Frost, S. *et al.* Alzheimer's Disease and the Early Signs of Age-Related Macular Degeneration. *Curr Alzheimer Res* **13**, 1259-1266 (2016).
417 Shah, T. M., Gupta, S. M., Chatterjee, P., Campbell, M. & Martins, R. N. Beta-amyloid sequelae in the eye: a critical review on its diagnostic significance and clinical relevance in Alzheimer's disease. *Mol Psychiatry* **22**, 353-363, doi:10.1038/mp.2016.251 (2017).
418 Biscetti, L. *et al.* Associations of Alzheimer's disease with macular degeneration. *Front Biosci (Elite Ed)* **9**, 174-191 (2017).
419 Woo, S. J. *et al.* Cognitive impairment in age-related macular degeneration and geographic atrophy. *Ophthalmology* **119**, 2094-2101, doi:10.1016/j.ophtha.2012.04.026 (2012).

420 Lashkari, K. *et al.* A monoclonal antibody targeting amyloid beta (Abeta) restores complement factor I bioactivity: Potential implications in age-related macular degeneration and Alzheimer's disease. *PLoS One* **13**, e0195751, doi:10.1371/journal.pone.0195751 (2018).
421 DeJesus-Hernandez, M. *et al.* Expanded GGGGCC hexanucleotide repeat in noncoding region of C9ORF72 causes chromosome 9p-linked FTD and ALS. *Neuron* **72**, 245-256, doi:10.1016/j.neuron.2011.09.011 (2011).
422 Renton, A. E. *et al.* A hexanucleotide repeat expansion in C9ORF72 is the cause of chromosome 9p21-linked ALS-FTD. *Neuron* **72**, 257-268, doi:10.1016/j.neuron.2011.09.010 (2011).
423 Alexander, P., Thomson, H. A., Luff, A. J. & Lotery, A. J. Retinal pigment epithelium transplantation: concepts, challenges, and future prospects. *Eye (Lond)* **29**, 992-1002, doi:10.1038/eye.2015.89 (2015).
424 McGill, T. J. *et al.* Long-Term Efficacy of GMP Grade Xeno-Free hESC-Derived RPE Cells Following Transplantation. *Transl Vis Sci Technol* **6**, 17, doi:10.1167/tvst.6.3.17 (2017).
425 Schwartz, S. D. *et al.* Embryonic stem cell trials for macular degeneration: a preliminary report. *Lancet* **379**, 713-720, doi:10.1016/s0140-6736(12)60028-2 (2012).
426 Song, W. K. *et al.* Treatment of macular degeneration using embryonic stem cell-derived retinal pigment epithelium: preliminary results in Asian patients. *Stem Cell Reports* **4**, 860-872, doi:10.1016/j.stemcr.2015.04.005 (2015).
427 da Cruz, L. *et al.* Phase 1 clinical study of an embryonic stem cell-derived retinal pigment epithelium patch in age-related macular degeneration. *Nat Biotechnol* **36**, 328-337, doi:10.1038/nbt.4114 (2018).
428 Schwartz, S. D. *et al.* Human embryonic stem cell-derived retinal pigment epithelium in patients with age-related macular degeneration and Stargardt's macular dystrophy: follow-up of two open-label phase 1/2 studies. *Lancet* **385**, 509-516, doi:10.1016/s0140-6736(14)61376-3 (2015).
429 Kanemura, H. *et al.* Tumorigenicity studies of induced pluripotent stem cell (iPSC)-derived retinal pigment epithelium (RPE) for the treatment of age-related macular degeneration. *PLoS One* **9**, e85336, doi:10.1371/journal.pone.0085336 (2014).
430 Zhao, T., Zhang, Z. N., Rong, Z. & Xu, Y. Immunogenicity of induced pluripotent stem cells. *Nature* **474**, 212-215, doi:10.1038/nature10135 (2011).
431 Sugita, S. *et al.* Inhibition of T-cell activation by retinal pigment epithelial cells derived from induced pluripotent stem cells. *Invest Ophthalmol Vis Sci* **56**, 1051-1062, doi:10.1167/iovs.14-15619 (2015).
432 Mandai, M. *et al.* Autologous Induced Stem-Cell-Derived Retinal Cells for Macular Degeneration. *N Engl J Med* **376**, 1038-1046, doi:10.1056/NEJMoa1608368 (2017).
433 Planul, A. & Dalkara, D. Vectors and Gene Delivery to the Retina. *Annu Rev Vis Sci* **3**, 121-140, doi:10.1146/annurev-vision-102016-061413 (2017).
434 Day, T. P., Byrne, L. C., Schaffer, D. V. & Flannery, J. G. Advances in AAV vector development for gene therapy in the retina. *Adv Exp Med Biol* **801**, 687-693, doi:10.1007/978-1-4614-3209-8_86 (2014).
435 MacLaren, R. E. *et al.* Retinal gene therapy in patients with choroideremia: initial findings from a phase 1/2 clinical trial. *Lancet* **383**, 1129-1137, doi:10.1016/s0140-6736(13)62117-0 (2014).
436 Edwards, T. L. *et al.* Visual Acuity after Retinal Gene Therapy for Choroideremia. *N Engl J Med* **374**, 1996-1998, doi:10.1056/NEJMc1509501 (2016).

437 Xue, K. *et al.* Beneficial effects on vision in patients undergoing retinal gene therapy for choroideremia. *Nat Med* **24**, 1507-1512, doi:10.1038/s41591-018-0185-5 (2018).
438 Jacobson, S. G. *et al.* Improvement and decline in vision with gene therapy in childhood blindness. *N Engl J Med* **372**, 1920-1926, doi:10.1056/NEJMoa1412965 (2015).
439 Bainbridge, J. W. *et al.* Long-term effect of gene therapy on Leber's congenital amaurosis. *N Engl J Med* **372**, 1887-1897, doi:10.1056/NEJMoa1414221 (2015).
440 Lau, C. H. & Suh, Y. In vivo genome editing in animals using AAV-CRISPR system: applications to translational research of human disease. *F1000Res* **6**, 2153, doi:10.12688/f1000research.11243.1 (2017).
441 Recchia, A. AAV-CRISPR Persistence in the Eye of the Beholder. *Mol Ther* **27**, 12-14, doi:10.1016/j.ymthe.2018.12.007 (2019).
442 Yu, W. *et al.* Nrl knockdown by AAV-delivered CRISPR/Cas9 prevents retinal degeneration in mice. *Nat Commun* **8**, 14716, doi:10.1038/ncomms14716 (2017).
443 Tsai, Y. T. *et al.* Clustered Regularly Interspaced Short Palindromic Repeats-Based Genome Surgery for the Treatment of Autosomal Dominant Retinitis Pigmentosa. *Ophthalmology* **125**, 1421-1430, doi:10.1016/j.ophtha.2018.04.001 (2018).
444 Giannelli, S. G. *et al.* Cas9/sgRNA selective targeting of the P23H Rhodopsin mutant allele for treating retinitis pigmentosa by intravitreal AAV9.PHP.B-based delivery. *Hum Mol Genet* **27**, 761-779, doi:10.1093/hmg/ddx438 (2018).
445 Ruan, G. X. *et al.* CRISPR/Cas9-Mediated Genome Editing as a Therapeutic Approach for Leber Congenital Amaurosis 10. *Mol Ther* **25**, 331-341, doi:10.1016/j.ymthe.2016.12.006 (2017).
446 Kim, E. *et al.* In vivo genome editing with a small Cas9 orthologue derived from Campylobacter jejuni. *Nat Commun* **8**, 14500, doi:10.1038/ncomms14500 (2017).
447 Jo, D. H., Koo, T., Cho, C. S., Kim, J. H. & Kim, J. S. Long-Term Effects of In Vivo Genome Editing in the Mouse Retina Using Campylobacter jejuni Cas9 Expressed via Adeno-Associated Virus. *Mol Ther* **27**, 130-136, doi:10.1016/j.ymthe.2018.10.009 (2019).
448 Golestaneh, N., Chu, Y., Xiao, Y. Y., Stoleru, G. L. & Theos, A. C. Dysfunctional autophagy in RPE, a contributing factor in age-related macular degeneration. *Cell Death Dis* **8**, e2537, doi:10.1038/cddis.2016.453 (2017).
449 Kaarniranta, K., Tokarz, P., Koskela, A., Paterno, J. & Blasiak, J. Autophagy regulates death of retinal pigment epithelium cells in age-related macular degeneration. *Cell Biol Toxicol* **33**, 113-128, doi:10.1007/s10565-016-9371-8 (2017).
450 Mitter, S. K. *et al.* Dysregulated autophagy in the RPE is associated with increased susceptibility to oxidative stress and AMD. *Autophagy* **10**, 1989-2005, doi:10.4161/auto.36184 (2014).
451 Iwabu, M. *et al.* Adiponectin and AdipoR1 regulate PGC-1alpha and mitochondria by Ca(2+) and AMPK/SIRT1. *Nature* **464**, 1313-1319, doi:10.1038/nature08991 (2010).
452 Ha, J., Guan, K. L. & Kim, J. AMPK and autophagy in glucose/glycogen metabolism. *Mol Aspects Med* **46**, 46-62, doi:10.1016/j.mam.2015.08.002 (2015).

Appendix

Table S1 | crRNA ssODN sequences for annealing and pSpCas9n ligation.

Name	Sequence (5`-3`)
C1QTNF5 crRNA-1 Top	CACCGACGGCGAAGTAGTAGACCCC
C1QTNF5 crRNA-1 Bottom	AAACGGGGTCTACTACTTCGCCGTC
C1QTNF5 crRNA-2 Top	CACCGGGCCAGCCTGCAGTTTGATC
C1QTNF5 crRNA-2 Bottom	AAACGATCAAACTGCAGGCTGGCCC
C1QTNF5 crRNA-3 Top	CACCGCCGGTAGACGGTGGCATGGA
C1QTNF5 crRNA-3 Bottom	AAACTCCATGCCACCGTCTACCGGC
C1QTNF5 crRNA-4 Top	CACCGCAGTTTGATCTGGTGAAGAA
C1QTNF5 crRNA-4 Bottom	AAACTTCTTCACCAGATCAAACTGC
C1QTNF5 crRNA-5 Top	CACCGAGTAGTAGACCCCAGGCACC
C1QTNF5 crRNA-5 Bottom	AAACGGTGCCTGGGGTCTACTACTC
C1QTNF5 crRNA-6 Top	CACCGCGTCCATGCCACCGTCTACC
C1QTNF5 crRNA-6 Bottom	AAACGGTAGACGGTGGCATGGACGC

Table S2 | crRNA sequences for pSpCas9 ligation.

Name	Sequence (5`-3`)
C1QTNF5 crRNA Correction	ATGCCACCGTCTACCGGGCCAGG
C1QTNF5 crRNA KO Forward	CAAGATCCCCAGCCTCTGCCCGG
C1QTNF5 crRNA KO Reverse	CCGCCCTCGCCTTTCTCTCCCGG

Table S3 | RNA sequences for RNP complex formation.

Name	Sequence (5`-3`)
C1QTNF5 crRNA Correction	ATGCCACCGTCTACCGGGCC
tracrRNA	GTTTTAGAGCTAGAAATAGCAAGTTAAAATAAGGCTAGTCCGTT
	ATCAACTTGAAAAAGTGGCACCGAGTCGGTGC

Table S4 | HDR template ssODN sequences.

Name	Sequence (5`-3`)
C1QTNF5 HDR Template 1	GGGACATTACGACGCCGTCACCGGCAAGTTCACCTGTCAGGTGC CTGGGGTCTACTACTTCGCCGTCCATGCCACCGTCTACCGAGCC AGGCTGCAGTTTGATCTAGTGAAGAATGGCGAATCCATTGCCTC TTTCTTCCAGTTTTTCGGGGGGGTGGCCCAAGCCAGCCTCGCTCTC GGGGGGGGCCATGGTGAGG
C1QTNF5 HDR Template 2	CTTCGACCGCGTGCTGGTGAACGAGCAGGGACATTACGACGCC GTCACCGGCAAGTTCACCTGCCAGGTGCCTGGGGTCTACTACTT CGCAGTCCATGCCACCGTCTACCGGGCCAGGCTGCAGTTTGATC TGGTGAAGAATGGCGAATCCATTGCCTCTTTCTTCCAGTTTTTCG GGGGGTGGCCCAAGCCAGCCTCGCTCTCGGGG
C1QTNF5 HDR Template 3	GCCTCCGCCGTCTGACGCACCCTTGCCCTTCGACCGCGTGCTGG TGAACGAGCAGGGACATTACGACGCCGTCACCGGCAAGTTCAC CTGTCAGGTGCCTGGGGTCTACTACTTCGCCGTCCATGCCACCG TCTACCGAGCCAGGCTGCAGTTTGATCTGGTGAAGAATGGCGA ATCCATTGCCTCTTTCTTCCAGTTTTTCGGGGGGTGGCCCAAGCC AGCCTCGCTCTCGGGG
C1QTNF5 HDR wt Template (191 bp)	GAGCAGGGACATTACGACGCCGTCACCGGCAAGTTCACCTGCC AGGTGCCTGGGGTCTACTACTTCGCCGTCCATGCCACCGTCTAC CGGGCCAGCCTGCAGTTTGATCTGGTGAAGAATGGCGAATCCA TTGCCTCTTTCTTCCAGTTTTTCGGGGGGTGGCCCAAGCCAGCCT CGCTCTCGGGGGGGGC
C1QTNF5 HDR wt Template (181 bp)	GGGACATTACGACGCCGTCACCGGCAAGTTCACCTGCCAGGTG CCTGGGGTCTACTACTTCGCCGTCCATGCCACCGTCTACCGGGC CAGCCTGCAGTTTGATCTGGTGAAGAATGGCGAATCCATTGCCT CTTTCTTCCAGTTTTTCGGGGGGTGGCCCAAGCCAGCCTCGCTCT CGGGG

Table S5 | Top possible gene editing off-target sites.

Name	Sequence (5`-3`)	Locus	Strand	Type
Correction 1	AGGCCACTGTCTCCTGGGCCCGG	1:10625252-10625274	-	Intronic
Correction 2	ATGCCACTGTCCAGCAGGCCAGG	1:18387308-18387330	+	Intergenic
Correction 3	TTTCCACCGTCTCCCGGGCAGGG	1:21933559-21933581	+	Intronic
Correction 4	ATCCCACCCTCAGCCGGGCCCGG	1:22955453-22955475	-	Intronic
Correction 5	CTGCCACCATCGACTGGGCCAGG	1:160360396-160360418	+	Intergenic
KO Forward 1	CAAGATCCCCAGTCCCTGCCCGG	12:125255642-125255664	-	Intronic
KO Forward 2	CTTCATCCCCAGCCTCTGCCAGG	7:43991301-43991323	+	Intergenic
KO Forward 3	CACCACCCCCAGCCTCTGCCTGG	16:10566025-10566047	+	Intronic
KO Forward 4	CAGAATGCCCAGCCTCTGCCAGG	7:72239723-72239745	+	Intronic
KO Forward 5	CCACATCCTCAGCCTCTGCCTGG	7:271883-271905	-	Intergenic
KO Reverse 1	CAGACCTCGCCTTTCTCTCCTGG	22:43244109-43244131	+	Intronic
KO Reverse 2	CCGACCTCCCCTTTCTCTCCCGG	19:9974187-9974209	+	Exonic
KO Reverse 3	GAGCCCTGGCCTTTCTCTCCAGG	9:133726626-133726648	+	Intronic
KO Reverse 4	CCCTCCTCTCCTTTCTCTCCTGG	18:45594527-45594549	+	Intronic
KO Reverse 5	CCCGCCTCTCCTTTCTCTCCGGG	21:45992188-45992210	-	Exonic

Table S6 | PCR primer sequences.

Name	Forward (5`-3`)	Reverse (5`-3`)
C1QTNF5	ACGAGCAGGGACATTACGAC	AGAAATCCGGAGAAGGTGCT
C1QTNF5 KO	CAGCGCTATGAGGCCACT	ACTCTAAGGTCACCGTACCC
pSpCas9n-C1QTNF5-gRNA-1	GACGGCGAAGTAGTAGACCC	TTTGTCTGCAGAATTGGCGC
pSpCas9n-C1QTNF5-gRNA-2	GCAGTTTGATCGTTTTAGAGC	TTTGTCTGCAGAATTGGCGC
Correction Off-Target 1	CTGTGTAGACATGGGACGGT	AGTGGGTGTTCTGGAGCTAC
Correction Off-Target 2	CACGCCTGTAATCCCAACAC	GCTCATCTGCAGGGTATGGA
Correction Off-Target 3	AGGTGTAGAGGAGGGTGTCT	TGAGCGCAGACAAGTTAGGA
Correction Off-Target 4	TGAGGTGATGTGGGCTCTTT	GCAGTTAGTATGTGCCAGGC
Correction Off-Target 5	GGGTCTCAAGCACTCCTCTT	GGATGGCTGTGCTCCTTCTA
KO Forward Off-Target 1	CTTTCTCTGTATGTGGGCGC	AACATGTCCTTCCAGAGCCA
KO Forward Off-Target 2	CCAGGCTCAAGGTTCTCAGA	CACCTCGGCCTCTCAAAATG
KO Forward Off-Target 3	CCCCTTTGGTTTCTCTGCAG	TTCTGAAGCTTAGGGTCCGG
KO Forward Off-Target 4	GATTCTGTGACGCTCTGCTG	TTGGCTTGTGTTGTCTCTGC
KO Forward Off-Target 5	TGGCGGATTTAGGAGCTGAA	GAAATCTGGGATGCAGGCAC
KO Reverse Off-Target 1	TGGAAGCTCTGCCTATGGAG	ACTCATTAGACACCTCCGCC
KO Reverse Off-Target 2	CCAAAAGGCCACATTGACCA	TGACTTCATTCCCAAGCCCT
KO Reverse Off-Target 3	CATGCCTGTAGTCCCAGCTA	ATCAGGCAGGGATCAGATGG
KO Reverse Off-Target 4	GGAGTCTGGGGAAAGCAGAA	TGAAGTCTCACAGGGGTTGG
KO Reverse Off-Target 5	GAGTTTGCCAATTTGCCAGC	TCTCAGGGACGTGGAGTAGA

a

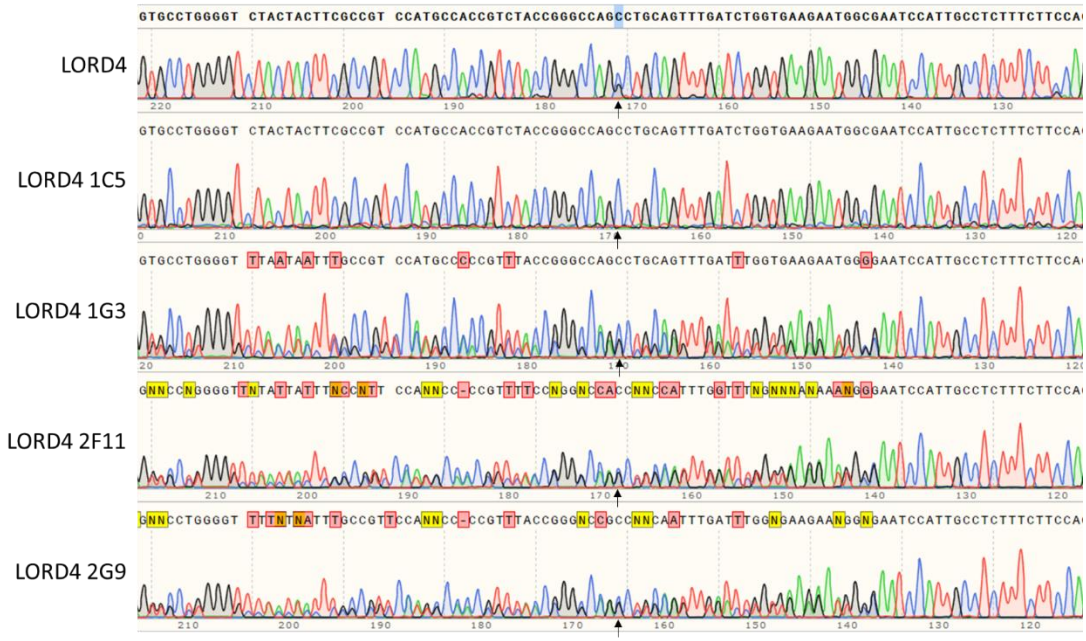
LORD4
LORD4 1C5
LORD4 1G3
LORD4 2F11
LORD4 2G9

b

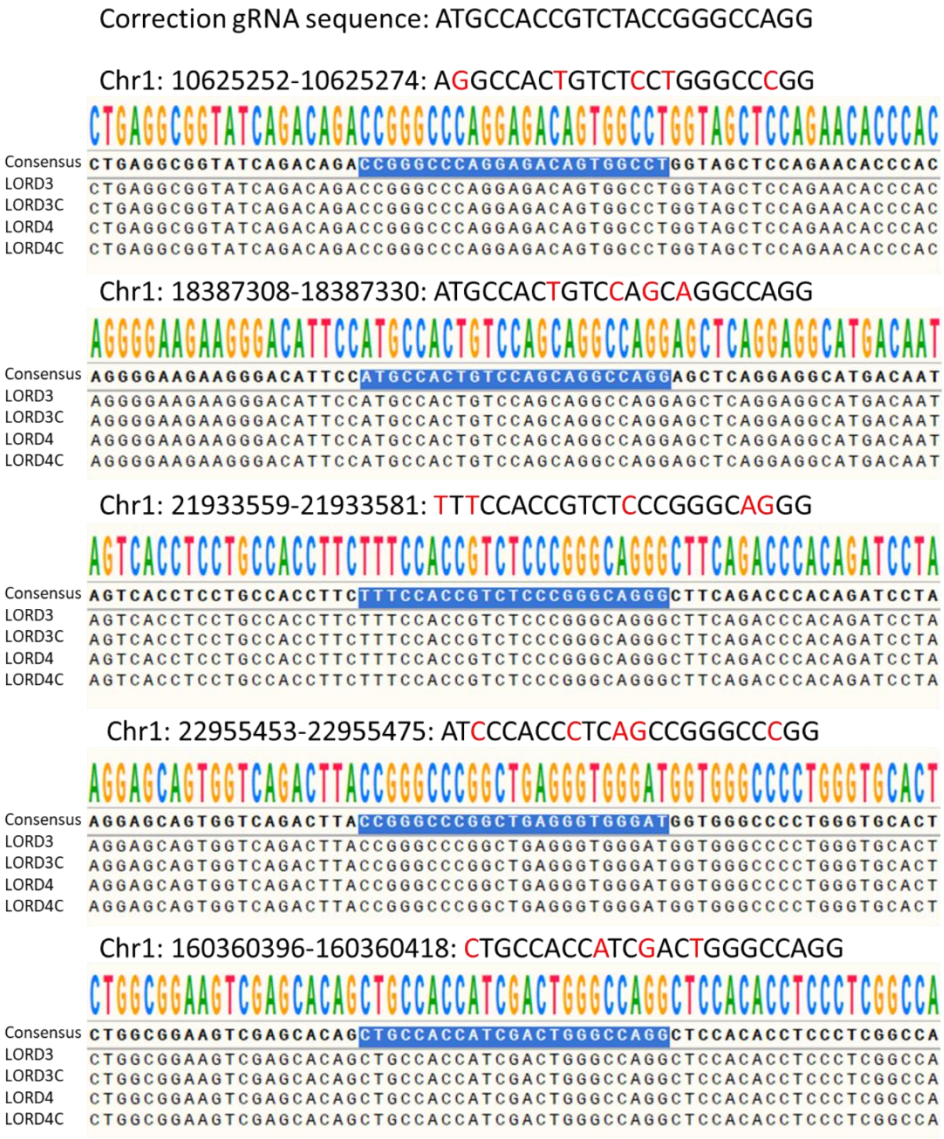
Correction gRNA sequence: ATGCCACCGTCTACCGGGCCAGG
Chr1: 10625252-10625274: AGGCCACTGTCTCCTGGGCCCGG
Consensus CTGAGGCGGTATCAGACAGACCGGGCCCAGGAGACAGTGGCCTGGTAGCTCCAGAACACCCAC
LORD3 CTGAGGCGGTATCAGACAGACCGGGCCCAGGAGACAGTGGCCTGGTAGCTCCAGAACACCCAC
LORD3C CTGAGGCGGTATCAGACAGACCGGGCCCAGGAGACAGTGGCCTGGTAGCTCCAGAACACCCAC
LORD4 CTGAGGCGGTATCAGACAGACCGGGCCCAGGAGACAGTGGCCTGGTAGCTCCAGAACACCCAC
LORD4C CTGAGGCGGTATCAGACAGACCGGGCCCAGGAGACAGTGGCCTGGTAGCTCCAGAACACCCAC
Chr1: 18387308-18387330: ATGCCACTGTCCAGCAGGCCAGG
Consensus AGGGGAAGAAGGGACATTCCATGCCACTGTCCAGCAGGCCAGGAGCTCAGGAGGCATGACAAT
LORD3 AGGGGAAGAAGGGACATTCCATGCCACTGTCCAGCAGGCCAGGAGCTCAGGAGGCATGACAAT
LORD3C AGGGGAAGAAGGGACATTCCATGCCACTGTCCAGCAGGCCAGGAGCTCAGGAGGCATGACAAT
LORD4 AGGGGAAGAAGGGACATTCCATGCCACTGTCCAGCAGGCCAGGAGCTCAGGAGGCATGACAAT
LORD4C AGGGGAAGAAGGGACATTCCATGCCACTGTCCAGCAGGCCAGGAGCTCAGGAGGCATGACAAT
Chr1: 21933559-21933581: TTTCCACCGTCTCCCGGGCAGGG
Consensus AGTCACCTCCTGCCACCTTCTTTCCACCGTCTCCCGGGCAGGGCTTCAGACCCACAGATCCTA
LORD3 AGTCACCTCCTGCCACCTTCTTTCCACCGTCTCCCGGGCAGGGCTTCAGACCCACAGATCCTA
LORD3C AGTCACCTCCTGCCACCTTCTTTCCACCGTCTCCCGGGCAGGGCTTCAGACCCACAGATCCTA
LORD4 AGTCACCTCCTGCCACCTTCTTTCCACCGTCTCCCGGGCAGGGCTTCAGACCCACAGATCCTA
LORD4C AGTCACCTCCTGCCACCTTCTTTCCACCGTCTCCCGGGCAGGGCTTCAGACCCACAGATCCTA
Chr1: 22955453-22955475: ATCCCACCCTCAGCCGGGCCCGG
Consensus AGGAGCAGTGGTCAGACTTACCGGGCCCGGCTGAGGGTGGGATGGTGGGCCCCTGGGTGCACT
LORD3 AGGAGCAGTGGTCAGACTTACCGGGCCCGGCTGAGGGTGGGATGGTGGGCCCCTGGGTGCACT
LORD3C AGGAGCAGTGGTCAGACTTACCGGGCCCGGCTGAGGGTGGGATGGTGGGCCCCTGGGTGCACT
LORD4 AGGAGCAGTGGTCAGACTTACCGGGCCCGGCTGAGGGTGGGATGGTGGGCCCCTGGGTGCACT
LORD4C AGGAGCAGTGGTCAGACTTACCGGGCCCGGCTGAGGGTGGGATGGTGGGCCCCTGGGTGCACT
Chr1: 160360396-160360418: CTGCCACCATCGACTGGGCCAGG
Consensus CTGGCGGAAGTCGAGCACAGCTGCCACCATCGACTGGGCCAGGCTCCACACCTCCCTCGGCCA
LORD3 CTGGCGGAAGTCGAGCACAGCTGCCACCATCGACTGGGCCAGGCTCCACACCTCCCTCGGCCA
LORD3C CTGGCGGAAGTCGAGCACAGCTGCCACCATCGACTGGGCCAGGCTCCACACCTCCCTCGGCCA
LORD4 CTGGCGGAAGTCGAGCACAGCTGCCACCATCGACTGGGCCAGGCTCCACACCTCCCTCGGCCA
LORD4C CTGGCGGAAGTCGAGCACAGCTGCCACCATCGACTGGGCCAGGCTCCACACCTCCCTCGGCCA

Figure S1 | Sanger sequencing of potential off-target gene editing sites for gRNA Correction. All 34 edited clones of LORD4 were sequenced and aligned. All edits, gene correction or NHEJ, were found to be in the L-ORD allele, as the wt trace is always in the background and the wt C is always visible (arrows; not all clones shown) (**a**). Top five predicted off-target sites for gRNA Correction were sequenced in the corrected LORD clones and the LORD parent line (**b**). Predicted off-target sequences shown with mismatches compared to gRNA Correction highlighted in red. Predicted off-target sequences highlighted in blue in the alignment. Alignment shows no off-target edits.

gRNA KO Fw sequence: CAAGATCCCCAGCCTCTGCCCGG

Chr12: 125255642-125255664: CAAGATCCCCAGTCCCTGCCCGG

Chr7: 43991301-43991323: CTTCATCCCCAGCCTCTGCCAGG

Chr16: 10566025-10566047: CACCACCCCCAGCCTCTGCCTGG

Chr7: 72239723-72239745: CAGAATGCCCAGCCTCTGCCAGG

gRNA KO Rev sequence: CCGCCCTCGCCTTTCTCTCCCGG

Chr22: 43244109-43244131: CAGACCTCGCCTTTCTCTCCTGG

Chr19: 9974187-9974209: CCGACCTCCCCTTTCTCTCCCGG

Chr18: 45594527-45594549: CCCTCCTCTCCTTTCTCTCCTGG

Chr21: 45992188-45992210: CCCGCCTCTCCTTTCTCTCCGGG

Figure S2 | Sanger sequencing of potential off-target gene editing sites for gRNA KO Forward and Reverse. Top four predicted off-target sites for both gRNA KO Forward and gRNA KO Reverse were sequenced in the C1QTNF5 KO clone 36 and the wt parent line. Predicted off-target sequences shown with mismatches compared to gRNA KO Fw and gRNA KO Rev highlighted in red. Predicted off-target sequences are highlighted in blue in the alignment. Alignment shows no off-target edits.

Table S7 | qPCR primer sequences.

Name	Accession	Forward (5`-3`)	Reverse (5`-3`)
18S	M10098	*	*
ACSL4	NM_004458	ATTCTTCTCCGCTTACACTCTCT	CTCTTGGACTTTGCTCATAACATTC
ADIPOR1	NM_00129055	CTTCAAGAGCATCTTCCGCATT	GGTCTGAGCATGGTCAAGATTC
BAK1	NM_001188	GCCAAGGTCCTGCTCAACT	CACCCCAAGCCCAGAATCC
BAX	NM_138761	ATGGAGCTGCAGAGGATGAT	CAGTTGAAGTTGCCGTCAGA
BCL2	NM_000633	GAGGTCACGGGGGCTAATT	GAGGCTGGGCACATTTACTG
C1QTNF5	NM_015645.4	GGCAAGTTCACCTGCCAGG	TCGCCATTCTTCACCAGATCAA
CDKN2A	NM_000077	ATGTCCTGCCTTTTAACGTAGATA	CTCACTCCAGAAAACTCCAACA
GCLM	NM_002061.3	GGAATTATCAAATCAAAAGGCTACATT	TTTTTACACATCTCAATTTTCTCTCAT
GPX4	NM_002085	AGTAACGAAGAGATCAAAGAGTTC	CCTTGCCCTTGGGTTGG
HSPA1B	NM_005346.4	GCGTGATGACTGCCCTGAT	GTTGTCGGAGTAGGTGGTGAA
LPCAT3	NM_005768.5	CAGAGCTGATTGACATACCAGGA	AGGAGATAGTCTTCTGTGATGTGG
NFE2L2	NM_006164.4	CCCAGCACATCCAGTCAGA	CAGTCATCAAAGTACAAAGCATCT
PPARA	NM_00100192	TCATCACGGACACGCTTTCA	TCCCCGCAGATTCTACATTCG

PPARG	NM_138711	GAATAAAGATGGGGTTCTCATATCC	AACTTCACAGCAAACTCAAACTT
PRKAA1	NM_006251	GCATCCTCATATAATTAAACTGTACCA	TTCATCCAGCCTTCCATTCTTAC
SOD2	NM_000636.3	CGACCTGCCCTACGACTAC	AACGCCTCCTGGTACTTCTC
SQSTM1	NM_003900.4	ACCATCCAGTATTCAAAGCATCC	AAGAGGGGCACGCAGAAG

*Primerdesign proprietary sequence

Table S8 | Antibodies used for immunocytochemistry and FACS.

Name	Dilution	Company	Cat. No.
APOE	1:100	Abcam	ab7620
BEST1	1:100	Merck Millipore	MAB5466
C1QTNF5	1:800	R&D Systems	AF3167
C5b-9	1:100	Dako	M077701
CRALBP	1:250	Abcam	ab15051
MITF	1:500	Abcam	ab80651
pMLKL (phospho Ser358)	1:100	Abcam	ab187091
NANOG	1:800	Cell Signaling Technology	3580
Nestin	1:100	Merck Millipore	MAB5326
Oct-3/4	1:250	Santa Cruz	SC5279
PAX6	1:250	Proteintech	12323-1-AP
TRA-1-60	1:100	Santa Cruz	sc-21705
ZO-1	1:100	Abcam	ab59720
Donkey anti-goat, Alexa Fluor 488 conjugate	1:250	Thermo Scientific	A11055
Donkey anti-goat, Alexa Fluor 647 conjugate	1:250	Thermo Scientific	A32849
Donkey anti-mouse, Alexa Fluor 488 conjugate	1:250	Thermo Scientific	A21202
Donkey anti-mouse, Alexa Fluor 594 conjugate	1:250	Thermo Scientific	A21203
Goat anti-mouse, Alexa Fluor 488 conjugate	1:250	Thermo Scientific	A11017

Goat anti-mouse, Alexa Fluor 594 conjugate	1:250	Thermo Scientific	A11020
Goat anti-mouse, Alexa Fluor 647 conjugate	1:500	Abcam	Ab150123
Goat anti-rabbit, Alexa Fluor 488 conjugate	1:250	Cell Signaling Technology	4412S
Goat anti-rabbit, Alexa Fluor 594 conjugate	1:250	Thermo Scientific	A11037
Goat anti-rabbit, Alexa Fluor 647 conjugate	1:250	Thermo Scientific	A21244

Table S9 | Antibodies used for western blot.

Name	Dilution	Company	Cat. No.
ACSL4	1:500	Santa Cruz	sc-271800
AMPKα	1:1000	Cell Signaling Technology	2603
pAMPKα (phospho Thr172)	1:1000	Cell Signaling Technology	2535
pAMPKα 1 (phospho Ser487)	1:1000	Abcam	ab131357
C1QTNF5	1:1000	R&D Systems	AF3167
MLKL	1:1000	Abcam	ab184718
RIPK3	1:1000	Abcam	ab56164
TBP	1:1000	Cell Signaling Technology	8515
β-actin	1:5000	Abcam	ab6276
Anti-rabbit, HRP conjugate	1:2000	Cell Signaling Technology	7074
Goat anti-mouse, HRP conjugate	1:2000	Upstate	12-349
Rabbit anti-goat, HRP conjugate	1:2000	Merck Millipore	AP106P

Table S10 | RNA-seq significantly differentially expressed genes between LORD4 and LORD4C.

Gene	Average FPKM LORD4	Average FPKM LORD4C	Log2 Fold Change	*p*-value
NCAN	0.351711	39.09155	4.959128	1.26E-61
FABP7	1.858688	20.24663	2.957222	8.77E-39
GFAP	6.386901	155.627	3.572968	6.19E-34
NEUROD2	0.009434	0.705084	3.407816	3.41E-22

PI15	0.83122	4.814303	2.158834	6.31E-19
PEX5L	1.064751	3.996574	1.694427	2.71E-14
A2M	2.193618	28.6967	2.540108	1.07E-13
MYH14	0.832318	0.027981	-2.70842	4.19E-13
KRT17	6.958446	35.28958	1.991943	1.67E-11
FXYD6	8.796219	26.42434	1.387183	3.28E-11
PMP2	0.1452	3.244355	2.518652	3.72E-11
NF1P8	0.046664	3.214651	2.575884	5.42E-11
KCNJ10	0.041434	0.750729	2.468895	6.07E-11
LIX1	2.901954	8.042419	1.29036	3.61E-10
SLC38A11	1.276815	0.128636	-2.25345	8.27E-10
HEY1	0.670907	2.829073	1.731384	1.09E-09
GABRG3	0.57645	1.623173	1.333956	1.09E-09
PCDHB5	1.653035	0.140253	-2.29779	1.11E-09
WFIKKN2	59.37098	9.807661	-2.01348	1.28E-09
CNTN6	2.751911	12.40976	1.730998	2.84E-09
HEPHL1	0.154845	1.000389	1.961815	3.92E-09
PLP1	1.768414	5.691758	1.430034	3.92E-09
FOXG1	0.573012	2.377033	1.71463	6.00E-09
TCEA3	7.127021	1.913379	-1.65247	8.84E-09
TMEM176A	8.950373	24.99288	1.297048	8.91E-09
B3GALT2	2.835654	9.129678	1.414959	2.33E-08
BCL11A	0.464199	1.556001	1.460813	4.53E-08
DSC3	6.300826	13.53714	0.988484	6.74E-08
RAMP2	5.838449	16.62644	1.305167	9.70E-08
SIM1	0.291972	0.012868	-2.17468	9.70E-08
GALNT14	12.34868	49.81081	1.622615	9.70E-08
SOX2	1.87372	6.592339	1.581792	9.74E-08
TMEM176B	23.26508	66.01043	1.294012	1.10E-07
APC2	0.412364	1.511352	1.508002	1.50E-07
PRELP	12.0015	2.526136	-1.71386	1.78E-07
ADAMTS16	27.99358	67.59305	1.092365	2.82E-07
CD109	1.854881	0.477473	-1.6104	2.82E-07
GLIPR2	14.95094	34.6606	1.060985	4.09E-07
BHMT	0.100381	1.19332	2.015839	5.89E-07
CITED1	0.703256	3.183296	1.669625	6.09E-07
COL26A1	7.631402	22.3782	1.306915	6.27E-07
PRPH	9.585109	26.77121	1.258272	7.14E-07
EDN1	0.788645	2.882947	1.516809	7.94E-07
LINC00461	0.599685	1.895855	1.426772	9.45E-07
CEBPZOS	13.21205	5.766974	-1.14379	9.45E-07
LPCAT2	8.294364	2.924539	-1.37559	9.45E-07

SPOCK2	0.56644	2.614646	1.646248	1.18E-06
LTBR	8.7125	4.262616	-1.02925	1.49E-06
HHATL	1.082598	0.075697	-1.99192	1.54E-06
PDGFB	0.255953	1.194958	1.669525	2.04E-06
FAM69C	0.259793	1.549753	1.824421	2.20E-06
TUBB2B	11.1484	40.59888	1.454002	2.36E-06
LTF	0.007842	1.241859	1.927756	3.84E-06
EFHD1	3.83879	11.50907	1.297043	4.47E-06
ZNF667	0.359374	0.003504	-1.91503	4.78E-06
LRRC17	30.20186	86.89149	1.246112	5.33E-06
AL391650.1	4.151594	17.40048	1.573608	6.75E-06
CHRDL1	8.276747	21.73588	1.146052	6.75E-06
MME	3.849118	0.536053	-1.79644	6.75E-06
ADGRG1	6.493311	20.16526	1.320479	7.18E-06
EGLN3	3.505399	8.297092	1.056952	7.37E-06
R3HDML	2.221798	13.73306	1.730951	7.83E-06
CNN1	1.147883	4.96319	1.566028	8.99E-06
LGR6	0.711747	3.225721	1.553695	9.15E-06
MYCN	1.963107	5.033458	1.156265	9.86E-06
TNFRSF19	4.698116	10.65713	1.016487	1.00E-05
SHISA9	0.325108	1.306355	1.49984	1.01E-05
SALL1	0.845075	3.449676	1.520222	1.14E-05
CRMP1	11.44185	28.36865	1.133759	1.46E-05
SUSD4	0.915239	2.6703	1.260961	1.75E-05
GDF6	1.175103	4.441005	1.464597	1.81E-05
XAF1	0.48973	0.009527	-1.81605	2.01E-05
ANKRD1	3.85967	16.79221	1.56466	2.25E-05
DMRTA2	0.020361	0.384196	1.818952	2.38E-05
AC120042.3	0.078238	0.549806	1.727307	2.40E-05
ABCC3	0.353728	2.597419	1.721424	2.80E-05
RBFOX1	0.096538	0.578468	1.681949	2.80E-05
SEZ6	0.391266	1.827133	1.560069	2.82E-05
ADAMTS18	0.628661	2.241709	1.333639	3.02E-05
SELENBP1	20.67617	9.748562	-1.04233	3.02E-05
CACNG8	0.154994	0.529811	1.388272	3.43E-05
LY6H	2.652626	9.048783	1.423221	3.52E-05
PLA2G2A	1.85207	0.087947	-1.7826	3.66E-05
JPH4	0.139695	0.983782	1.709036	3.73E-05
POU3F2	0.070604	0.500636	1.703887	3.94E-05
JCAD	5.836781	3.081388	-0.90211	3.94E-05
HSPA2	0.989575	0.204224	-1.61777	4.25E-05
ABCC9	1.977251	0.960131	-1.03265	4.41E-05

MLC1	0.675424	5.50358	1.71939	4.81E-05
KIF5C	11.23707	30.14822	1.173776	4.98E-05
GFRA2	1.291776	3.637876	1.232596	5.11E-05
CACNG4	3.303094	6.7694	0.911915	5.11E-05
SYT1	8.751664	18.03568	0.900096	5.52E-05
PLIN4	3.275269	1.056122	-1.39868	5.86E-05
CDH4	0.125862	0.607535	1.556713	5.95E-05
RTN1	1.2693	3.923519	1.287576	5.95E-05
LINC01630	0.609002	1.778531	1.250543	6.09E-05
RGS8	0.368217	1.573276	1.469551	6.20E-05
PDE3A	1.331159	0.478417	-1.31822	6.20E-05
MEGF11	0.342594	1.01863	1.300588	6.23E-05
CLDN23	0.995714	0.187765	-1.63396	7.17E-05
AC009271.1	0.727132	3.855373	1.596695	7.39E-05
AC092490.1	1.116618	0.23282	-1.57988	8.26E-05
TRIM38	1.312588	0.655447	-0.98367	8.48E-05
SLPI	9.519877	0.965494	-1.70849	8.48E-05
CLDN1	22.8755	74.66089	1.28746	9.63E-05
EYA1	1.78257	0.824605	-1.06751	9.63E-05
IGFL3	0.095924	3.814542	1.6809	9.92E-05
CHCHD2	52.17219	173.0574	1.378166	1.04E-04
ZNF662	0.980089	0.322118	-1.32819	1.19E-04
PITX3	0.731813	2.610552	1.378114	1.21E-04
GREM2	0.415138	0.024457	-1.68345	1.28E-04
FAM109B	1.69111	0.554692	-1.3278	1.42E-04
HFE	3.394978	1.725283	-0.9625	1.43E-04
RDH10	34.11247	15.92008	-1.03937	1.46E-04
SERPINE3	455.484	203.7129	-1.11233	1.46E-04
ATCAY	0.277968	0.908474	1.339884	1.47E-04
SLCO1A2	0.816421	0.270944	-1.35189	1.57E-04
CACNG7	0.137417	1.035937	1.628151	1.68E-04
IGFBP3	113.5208	327.1978	1.223447	1.75E-04
LRFN2	0.350941	1.256095	1.368601	1.79E-04
CXCL14	8.459074	20.01815	1.029167	2.16E-04
CAT	27.58707	11.83021	-1.12293	2.22E-04
SOCS2	1.649981	5.591685	1.334436	2.76E-04
THUMPD3	9.79677	5.492265	-0.83759	2.78E-04
FIBCD1	4.750792	23.71655	1.503263	3.03E-04
MLIP	3.851365	12.41174	1.312129	3.05E-04
APLNR	0.020272	1.302029	1.57204	3.10E-04
C2orf80	0.47763	2.105205	1.455978	3.35E-04
LAMA2	10.95936	6.523727	-0.75464	3.38E-04

SNED1	2.734914	0.786731	-1.40422	3.70E-04
CHD5	0.341663	1.019571	1.227126	3.77E-04
ARX	0.075858	0.771314	1.58516	4.46E-04
ALPK2	1.007161	6.040642	1.530565	4.46E-04
BEX1	17.27324	42.37619	1.100573	4.46E-04
EBF2	0.388357	0.004069	-1.52982	4.52E-04
AC021504.1	2.886711	7.042254	1.071513	4.61E-04
ENPP2	42.24926	18.19891	-1.12398	4.61E-04
MISP	0.510643	1.77785	1.328458	4.68E-04
PI16	2.757728	0.141542	-1.56357	4.70E-04
AGAP2	0.165022	0.581645	1.334109	4.74E-04
HLA-DRA	0.350329	3.037733	1.569036	4.96E-04
PPP1R14C	0.85566	2.842558	1.296076	4.96E-04
ZNF471	0.146431	0.011071	-1.57207	4.96E-04
NRCAM	1.403533	3.794152	1.217247	5.17E-04
OPN3	10.46509	25.50158	1.042733	5.17E-04
PAPPA2	1.252011	5.176303	1.399715	5.33E-04
GYPC	4.047407	1.781547	-1.08603	5.39E-04
JPH2	3.357661	9.524408	1.168147	5.43E-04
NKX6-1	0.05847	0.469728	1.554402	5.44E-04
BFSP2	2.384788	6.71239	1.180655	5.44E-04
CBFA2T3	0.872146	2.157552	1.082285	5.51E-04
TOX	11.86688	29.65707	1.064674	5.89E-04
TFAP2C	0.066304	0.784996	1.548167	6.80E-04
COLGALT2	10.63803	31.3822	1.199704	7.06E-04
NLGN1	1.694656	3.233039	0.802807	7.28E-04
PCDHGB7	2.85617	0.532929	-1.48744	7.44E-04
SIAH3	0.523353	1.250856	1.032882	7.71E-04
ABCA2	43.82226	18.6783	-1.09407	7.71E-04
COL8A1	175.0595	86.07025	-1.00403	7.88E-04
HNMT	3.142927	1.164984	-1.21156	7.91E-04
LFNG	2.878806	7.016738	1.035048	8.01E-04
MEIS3	13.1533	24.36134	0.765875	8.07E-04
PLN	0.007801	0.445353	1.486047	8.42E-04
SLC2A10	12.33835	7.422419	-0.75323	8.66E-04
GPD1	6.71373	18.84305	1.171813	8.96E-04
DPP10	5.204859	9.133357	0.714104	9.01E-04
BBOX1-AS1	1.994285	6.650903	1.266157	9.16E-04
TBX5	0.203059	0.013425	-1.50995	9.16E-04
GNG4	1.747424	4.065871	1.012345	9.72E-04
NCALD	10.67611	20.29239	0.785068	9.92E-04
COL13A1	1.504038	0.600126	-1.14103	9.94E-04

SULF1	177.2071	72.82885	-1.14075	0.001016
NANOS1	61.45329	17.94749	-1.35609	0.001017
OR51E2	10.85608	4.082407	-1.21646	0.001086
AC103770.1	7.044894	1.383414	-1.44035	0.001195
PRKAG2	3.783159	7.746967	0.86463	0.001309
RORC	1.744124	0.404831	-1.4206	0.001352
TMEM178A	2.656013	6.317702	1.026451	0.001353
HACD4	0.520378	0.224587	-1.09352	0.001411
CYP4V2	8.866884	4.61616	-0.92274	0.001515
NRXN2	0.786139	1.848706	1.027331	0.001522
AJ009632.2	0.176949	1.022862	1.441418	0.001535
GREM1	5.269527	14.7182	1.133202	0.001575
SCN2A	0.497947	1.011444	0.864485	0.001593
STXBP6	4.607873	9.511727	0.880746	0.001601
ERC2	3.04359	5.802396	0.807221	0.001601
NECAB1	6.490323	3.419795	-0.93679	0.001601
LMO2	0.262806	1.457631	1.425364	0.001669
HAPLN3	9.563245	28.44675	1.174526	0.001669
FBN3	0.7832	1.621798	0.910197	0.001754
ITIH5	18.47779	10.14867	-0.84546	0.001754
CHST2	5.631105	14.28557	1.010073	0.001765
SLC16A14	43.60143	13.20966	-1.32576	0.001767
CRYBG1	2.606571	0.747031	-1.36087	0.001773
AC022424.1	1.488557	4.392112	1.190763	0.001779
ACTA2	127.7662	405.0608	1.21383	0.001814
SALL3	0.010748	0.196733	1.43815	0.001833
WNT10A	0.347562	1.204463	1.266508	0.001838
ADARB2	0.040976	0.235278	1.423526	0.001896
CPXM1	8.829	25.26135	1.172539	0.001896
PLEKHG1	1.15532	2.690523	1.026652	0.001943
DYSF	0.419489	0.956059	0.982082	0.001943
CHCHD2P9	1.712678	7.307371	1.362374	0.001945
SIPA1L2	4.878551	8.698055	0.720176	0.001963
LBX1-AS1	0.108412	0.710307	1.434799	0.00198
SLC5A12	0.346213	1.185226	1.247944	0.002125
ASPA	0.56894	0.221405	-1.15256	0.002148
CDH20	5.423603	16.71998	1.219541	0.002203
TMEFF2	5.15671	20.86116	1.318264	0.00222
ADCY1	0.85314	1.619748	0.784341	0.002245
DGAT2	2.206464	4.028374	0.753613	0.002276
RARRES2	39.16267	14.98395	-1.15921	0.002319
FLRT2	3.885719	2.398248	-0.71276	0.002333

TMEM200C	0.527864	1.260164	1.01324	0.00253
KMO	4.262386	11.849	1.111367	0.002549
NTN1	1.34719	3.280296	1.003488	0.002556
ANK1	0.091282	0.355605	1.321023	0.002642
PDXK	45.15398	83.12267	0.748731	0.002735
VWA1	2.588889	5.63553	0.916633	0.002855
LINC00862	0.298975	1.415787	1.372066	0.003027
GRIN2B	0.018037	0.065648	1.284463	0.003027
TMEM30B	1.025952	0.2022	-1.36873	0.00311
STMN3	17.65255	32.5247	0.744199	0.003242
TMEM163	0.229996	0.876654	1.276756	0.003407
HLA-DRB1	0.17717	1.128296	1.385646	0.003495
ACKR3	8.965796	20.98408	0.956587	0.003954
EMID1	6.36054	11.32491	0.727975	0.003954
NDP	0.43728	1.35552	1.192697	0.004105
SMPD5	0.801237	2.225384	1.120976	0.004317
ECE1	6.680625	14.02013	0.865421	0.004345
NALCN	5.126381	1.942898	-1.16487	0.004345
NEAT1	2.647717	1.731408	-0.6433	0.00438
LAMC3	0.207158	0.765612	1.243369	0.004473
RHOU	5.349324	2.699705	-0.93142	0.004495
KL	4.299751	2.195228	-0.95803	0.004495
AC004947.2	0.420479	1.210717	1.133452	0.004686
CRYBB2	6.103567	34.53898	1.330622	0.004717
PTHLH	6.727362	15.09334	0.978008	0.004763
NES	2.008197	7.57003	1.250061	0.004909
ANO4	0.941726	2.842843	1.12192	0.004994
NPNT	5.336293	10.30965	0.77982	0.005009
MT1E	10.89793	2.696095	-1.29433	0.005125
PSG4	0.287264	0.011161	-1.30908	0.005141
C14orf180	0.938151	0.191198	-1.33601	0.005449
GJA3	0.283187	0.728507	1.077862	0.00551
SLC6A15	27.33461	47.8335	0.697834	0.00551
NFIL3	9.764172	17.44126	0.711448	0.005607
MEGF6	2.705413	6.192241	0.952071	0.005612
HCN4	0.165093	0.459538	1.104211	0.005757
CPED1	0.417477	0.134954	-1.20649	0.005757
AC015522.1	8.393674	27.5848	1.181706	0.006056
RIPK4	2.857324	5.383602	0.765279	0.006056
LINC01551	0.170571	1.394733	1.340103	0.00609
USH2A	0.360422	0.093626	-1.28749	0.006136
CD55	9.974705	6.360052	-0.66831	0.006343

CGREF1	2.941204	1.07278	-1.13327	0.006389
LMNB1	2.590117	5.199112	0.838108	0.006494
L1CAM	2.170502	4.361408	0.829773	0.006712
PCDHA4	0.93883	1.776351	0.76921	0.006904
FBP2	1.794463	0.293396	-1.33004	0.006904
CLIC6	75.85745	31.4988	-1.08393	0.00702
NDRG1	16.16913	10.17478	-0.67623	0.007085
SLC1A3	1.051997	4.320158	1.252608	0.007184
MAN2A1	40.97327	19.91283	-0.96535	0.007202
CCND1	66.68193	46.02734	-0.57867	0.007242
FAR2P4	0.016121	0.498759	1.261611	0.007266
PAX6	18.62451	38.42171	0.844312	0.007266
SLC2A12	70.48869	28.74859	-1.10666	0.007266
PAK3	1.771286	3.058714	0.670925	0.007291
ERICH5	33.35037	60.511	0.720117	0.007312
SOCS2-AS1	0.70563	2.325378	1.186242	0.007352
CHGA	0.027152	0.497222	1.282848	0.007758
HOXB2	0.05921	0.838545	1.290003	0.008043
CADM3	9.25381	21.48556	0.951203	0.008043
NCAM1	3.023272	9.231307	1.124461	0.008293
NOTCH3	9.514927	16.17455	0.659021	0.008428
ENPEP	0.279819	0.06082	-1.28308	0.008428
LRRC3B	0.207021	0.919373	1.27152	0.00846
CSRNP1	7.942957	14.46387	0.722855	0.008493
CD38	0.008515	0.129825	1.278175	0.0085
EDN2	8.162437	21.59656	1.06756	0.0085
ZNF558	1.84471	4.685276	1.052476	0.0085
JUP	24.76212	44.55463	0.706991	0.0085
NTNG1	7.452195	3.341732	-1.00635	0.0085
CLEC3B	3.418851	0.120918	-1.23491	0.008507
LINC01139	0.444171	0.010488	-1.22525	0.008612
LHX1	0.024044	0.24601	1.292128	0.008768
LINC02009	0.9571	0.243156	-1.25416	0.008834
PLEKHG4	0.770346	0.369776	-0.9365	0.008863
GALNT8	0.161001	1.256231	1.299513	0.008973
ROBO2	2.93862	1.362972	-0.9725	0.009206
MYRIP	38.60031	18.77586	-0.95159	0.009209
PPP1R1A	0.515518	1.34037	1.052107	0.009248
ZXDA	0.176144	0.67636	1.226307	0.009403
TOX2	1.33337	2.803434	0.897445	0.009496
CLVS1	0.172653	0.643239	1.219666	0.009515
MCAM	7.109842	17.45069	0.971995	0.009645

OLFM2	28.20953	48.43134	0.684332	0.009758
LBX1	0.096193	0.578629	1.285039	0.009885
DRAXIN	0.119862	0.793519	1.285167	0.009915
MAMDC2	18.23339	53.10391	1.094366	0.009915
AP000892.3	2.082873	5.751682	1.080626	0.009915
RAMP2-AS1	0.887941	1.854884	0.877097	0.009915
TSPAN12	16.23866	31.32936	0.782313	0.009915
ADD2	2.261461	3.986018	0.699731	0.009915
ANKH	4.772498	3.09013	-0.65437	0.009915
NID2	41.87008	22.1325	-0.87564	0.009915
SPRY1	7.070796	2.928354	-1.07952	0.009989
ADPRH	2.017884	0.915272	-0.99535	0.010044
ADAMTSL1	2.705108	1.1107	-1.00039	0.010045
KCNJ5	0.536637	2.088576	1.197477	0.010068
KIFC3	7.73318	16.06885	0.831461	0.010125
CSDC2	5.740875	12.38024	0.900907	0.010195
SSX1	0.093013	1.149498	1.252304	0.010902
GPC2	1.477085	2.920454	0.814641	0.010902
PPP1R3D	1.966414	1.02684	-0.86832	0.011011
HUNK	0.943663	1.708615	0.731414	0.01129
AJAP1	0.008657	0.086322	1.260249	0.011302
TRIM55	0.166808	0.625761	1.201302	0.011302
GPR153	5.706489	10.97215	0.76987	0.011302
NTRK3	0.242109	0.885625	1.180653	0.011516
FADS3	18.11564	9.058898	-0.89938	0.011763
CHCHD2P6	1.648078	5.186994	1.139348	0.012025
ENC1	5.792835	13.15441	0.917371	0.012025
LGI2	0.120477	0.462448	1.197162	0.012047
SCRG1	9.426024	30.60447	1.141767	0.012047
PDE1C	1.330988	3.681184	1.073833	0.012047
BANCR	2.161818	6.099455	1.085858	0.012079
EBF1	0.576644	0.06456	-1.25644	0.012115
GHR	6.826249	4.071213	-0.77648	0.012179
CRYAB	794.8187	1572.041	0.807383	0.012316
CCDC68	2.743942	0.508534	-1.25929	0.012316
SRGAP1	1.095857	1.773787	0.593407	0.012529
PLPPR3	12.25072	23.13652	0.820785	0.013442
LRRN3	2.240987	5.759691	1.020917	0.013564
CDH2	50.98751	85.88191	0.62788	0.0137
ITGA10	0.797389	0.044442	-1.20167	0.013755
AC113137.1	0.07517	1.18049	1.208235	0.013891
SNAP91	4.265208	7.367713	0.667617	0.013891

LINC02302	2.070354	0.720865	-1.11362	0.014388
CRABP2	28.8192	14.16891	-0.90884	0.015251
PCOLCE2	1.849924	0.880085	-0.968	0.015251
GRB14	0.872685	2.368151	1.038328	0.01552
GNG3	0.451356	2.094392	1.218111	0.015673
SLC30A8	3.919738	2.163079	-0.82935	0.016243
PTGDS	122.3596	47.11283	-1.08438	0.01625
MARCHF11	0.472541	1.745793	1.17066	0.016463
DMXL2	8.100777	5.242511	-0.65591	0.017174
JAKMIP2	0.765284	1.748051	0.934657	0.017312
HEG1	13.14896	8.455954	-0.64349	0.017312
MGAM2	0.534435	0.204347	-1.09385	0.017312
AC145212.1	0.260528	0.003699	-1.12581	0.017312
ABL2	14.80557	8.943586	-0.74035	0.017518
SLC16A12	4.393971	2.457419	-0.85084	0.017518
PREX2	0.19463	0.526559	1.026798	0.017703
GPM6B	9.880538	18.61397	0.738342	0.017703
CNTN4	1.666319	2.896883	0.672768	0.017703
DNAJC15	6.29453	4.278373	-0.59196	0.017703
LAMA1	1.554283	3.988059	0.994291	0.017852
SLC6A17	7.675304	20.52341	1.030684	0.017856
TIMP3	903.7854	583.512	-0.64585	0.017856
B3GNT8	0.968792	2.334744	0.963149	0.018167
LINC01133	1.738433	0.131913	-1.18036	0.018167
CBLN2	0.145454	0.680321	1.197997	0.018241
CRABP1	14.68031	44.89269	1.096494	0.018535
PCDH8	0.826474	1.737195	0.861205	0.018623
ICAM5	0.506795	1.175689	0.950112	0.018769
F3	13.34273	8.540333	-0.65931	0.019378
C9orf64	2.34569	1.06363	-0.9856	0.019378
PLAG1	2.117448	1.303471	-0.71515	0.019986
PCDH18	22.65418	13.32161	-0.76276	0.019986
SLC15A3	0.570423	0.221975	-1.06293	0.019986
LCN9	0.070063	1.348786	1.152855	0.020236
SLC6A20	94.50356	49.29904	-0.8831	0.020657
PSMB9	0.925159	1.958303	0.861111	0.020725
AL355916.1	0.305926	1.170629	1.160303	0.020767
TAGLN	60.33831	170.584	1.04971	0.020988
RASSF2	8.128666	13.92591	0.654486	0.021093
GRIN2A	0.037533	0.140119	1.15105	0.02112
KALRN	1.582242	2.875846	0.707526	0.021185
AHNAK2	12.38944	22.17633	0.704964	0.021185

CHADL	4.877	1.560058	-1.13788	0.021185
MED15P8	0.042673	1.914789	1.105668	0.021196
LRRC32	13.39921	39.38392	1.074682	0.021196
BCAS1	0.463888	1.125126	0.976515	0.021535
CNGB3	8.395277	3.44404	-1.04419	0.021535
FZD5	4.753588	2.573411	-0.83362	0.022103
AC013451.2	0.301534	1.663119	1.193399	0.022332
ZNF667-AS1	1.5096	0.053122	-1.10628	0.022362
KRT81	0.147033	0.626338	1.176523	0.022428
AC131571.1	0.686141	3.850977	1.192372	0.02248
LINC01122	0.369502	0.850273	0.939299	0.022599
GEN1	3.178045	1.775946	-0.8185	0.02285
RASGRP1	0.440972	1.44126	1.10655	0.022862
CASC10	1.096048	2.274411	0.852907	0.023205
LPAR5	0.071395	0.440621	1.188122	0.023527
AC098864.1	1.65669	5.930678	1.11958	0.023811
ATP10B	0.632767	0.302258	-0.92274	0.023811
RNF152	2.003947	1.165075	-0.77013	0.024306
RASGRF1	0.69031	2.400968	1.108228	0.024591
CYP27A1	110.6218	46.53698	-1.01918	0.024678
SMIM24	1.072162	2.460019	0.924827	0.024717
MMP11	9.898381	18.56788	0.738786	0.025094
GLDN	0.14445	0.467165	1.096933	0.025214
NEK2P4	0.043585	0.478609	1.151344	0.025501
WIPF1	14.37785	9.4564	-0.62907	0.025594
RBM24	11.60248	24.89456	0.863407	0.02562
SLC4A5	4.380466	1.324626	-1.14092	0.02562
ACKR1	0.522332	1.474328	1.047896	0.025883
EPPK1	0.33783	0.609736	0.715412	0.026831
CFI	0.100605	0.489829	1.166799	0.027054
GRIA4	3.06663	8.367085	1.026788	0.027054
LRRK2	0.434605	0.201651	-0.96334	0.027726
HMX1	3.887326	13.21412	1.106917	0.02801
MRO	2.332524	1.285026	-0.81745	0.02801
PRKCG	0.27607	0.825986	1.075317	0.028163
PLA1A	6.57165	2.610381	-1.05683	0.028163
CPA2	3.108882	0.913583	-1.1378	0.028272
ADGRD1	0.271435	0.077424	-1.13881	0.028272
ARSI	2.717855	7.287069	0.982435	0.028463
KRT23	0.143841	0.566435	1.143174	0.028886
FYB2	22.33292	12.49619	-0.82675	0.029064
IGSF10	0.319735	0.115857	-1.08773	0.029064

ENOX1	2.662463	1.362299	-0.85527	0.029267
PMEPA1	17.84535	36.13797	0.805899	0.029325
GRASP	5.13448	9.628551	0.729129	0.029384
CCL2	16.37548	46.33865	1.01686	0.029773
ITPR1	8.325793	5.338162	-0.65535	0.029773
GABRQ	0.083951	0.285604	1.10037	0.029838
CAPN6	6.656705	12.63695	0.753747	0.029856
GEM	69.1456	32.33381	-0.95362	0.030146
CHRM4	5.859824	16.18971	1.027076	0.030166
ZIC3	0.092263	0.362894	1.129569	0.030529
OR10J3	0.246542	1.06176	1.146369	0.030753
IL17RB	6.00833	1.984978	-1.09438	0.030753
MARCHF1	2.694182	6.318632	0.909521	0.031438
CACNA1C	2.946595	1.814096	-0.69301	0.031438
MGST1	36.46606	21.50817	-0.73429	0.031438
TMEM56	4.973333	2.805052	-0.77874	0.031729
SMC6	30.1715	16.2122	-0.84858	0.03227
PDCD1	0.124274	0.553502	1.142019	0.03244
CA10	1.409737	5.389413	1.108649	0.032852
LRP8	7.73131	3.29275	-0.95015	0.033092
CHGB	0.232141	0.859596	1.115883	0.033326
KCNMB4	1.511414	2.618722	0.659159	0.033635
SULT1A1	2.627207	1.356297	-0.85765	0.033635
CST3	885.3399	374.332	-0.98966	0.033635
AMPD3	1.885394	0.820888	-0.9895	0.033652
DNAJA4	0.601619	0.204221	-1.08679	0.033652
CACNB3	9.027352	14.29709	0.580422	0.033858
NR2E1	5.708187	2.21891	-1.0229	0.033897
PCSK1N	91.39807	138.0201	0.505693	0.033948
C1QTNF1	8.582561	5.637892	-0.62609	0.034163
CPQ	36.12607	25.54798	-0.53335	0.034269
SLC46A1	15.5716	7.616223	-0.89763	0.034491
MX1	1.448329	0.808215	-0.78129	0.034596
PLD5	31.9427	13.28825	-1.01341	0.034596
TACC1	50.33945	31.86349	-0.67233	0.0346
SPINK5	0.288925	0.942258	1.071035	0.034648
SST	3.610237	10.76443	1.031192	0.034648
LAYN	31.3236	20.90921	-0.58379	0.034648
UMODL1	0.244903	0.069702	-1.11764	0.034737
SLC25A18	0.194636	0.666928	1.096828	0.034929
FRMPD4	0.127806	0.034509	-1.12169	0.03505
CHDH	6.649692	2.748223	-1.00404	0.035075

SCG5	382.3171	156.6115	-1.01521	0.035245
GABRA5	0.52868	1.215788	0.911551	0.035537
SORL1	3.278723	1.665301	-0.88092	0.035627
MMP17	3.562602	1.697067	-0.90694	0.035627
AC025263.1	0.727799	0.254232	-1.06089	0.03572
SERPINB1	2.645578	1.176419	-0.9542	0.035916
PTN	137.0249	85.19698	-0.67283	0.036042
CYP2W1	16.8503	7.704391	-0.93831	0.036195
ACP6	17.05622	9.76243	-0.78088	0.036324
ACTC1	1.377804	2.972658	0.862894	0.036636
IGDCC3	0.32051	0.787975	0.943152	0.03665
PLAU	3.21765	8.139613	0.949048	0.037235
ITGB8	8.124477	3.731999	-0.93402	0.037235
SLC39A12	58.2968	21.72415	-1.04484	0.037235
AL451048.1	1.30366	5.569376	1.117742	0.038158
SGK3	11.38454	6.481526	-0.78745	0.038158
PADI3	0.652314	1.439556	0.865931	0.038312
HOXB4	0.006218	0.127551	1.052214	0.038325
KIRREL3	0.385572	1.579598	1.095473	0.039167
PTGER4	1.250438	3.085278	0.933944	0.039332
NAV3	7.354966	4.075473	-0.81221	0.039591
SLC16A3	37.68725	19.00596	-0.87037	0.039591
AMIGO1	7.122306	4.696758	-0.61881	0.039819
DSP	36.85902	17.91474	-0.90807	0.040247
POPDC3	3.99386	1.58119	-1.02568	0.040247
KCNE3	0.526327	0.148017	-1.10407	0.040247
CKB	44.73071	67.82438	0.532432	0.040743
TBC1D30	3.391251	1.766063	-0.8271	0.040743
LYPD6B	0.901783	2.819284	1.016288	0.040966
NPW	12.74968	21.06025	0.636682	0.040988
WNT2	0.112672	0.418502	1.089011	0.041224
AP000280.1	0.817416	2.396849	1.025926	0.041224
CPEB2	6.188542	4.289493	-0.56347	0.041756
ROBO4	0.1521	0.029677	-1.11213	0.041814
NRIP3	1.18844	2.745064	0.897532	0.041833
ZFYVE16	16.73191	9.491923	-0.76441	0.041833
SPHKAP	0.223951	0.581151	0.979249	0.042479
ME3	10.5699	5.339776	-0.85691	0.042479
ARHGEF37	24.15753	11.41884	-0.91907	0.042479
TSPAN13	32.22851	14.90658	-0.94687	0.042479
SP140	0.365418	0.089204	-1.10757	0.042479
NKAIN3	0.059769	0.489077	1.089618	0.042599

AMPH	5.828826	10.68743	0.700421	0.042599
ITGB6	0.137911	0.498536	1.080617	0.042651
MIR503HG	1.519562	5.265762	1.067998	0.042861
TRIM71	0.027699	0.119941	1.100984	0.042876
COL24A1	0.407148	0.154442	-1.02892	0.042876
AGTR1	0.234149	0.023506	-1.06544	0.044072
MAPK4	11.997	5.607216	-0.91034	0.044131
FBXO27	2.887902	1.68286	-0.73829	0.044184
TRIM4	4.619858	8.289172	0.688854	0.04439
TEAD3	10.0987	17.53703	0.650186	0.044818
BCAN	8.825931	18.09492	0.821449	0.045039
FSTL3	26.70418	53.28903	0.802347	0.045039
GADD45B	16.15501	25.3136	0.555329	0.045059
DDR2	36.39646	26.07857	-0.51578	0.045059
PIP4P2	9.207809	6.020449	-0.62882	0.045059
SEMA4A	13.48697	6.213251	-0.91241	0.045059
IL16	0.797647	0.307857	-1.02494	0.045059
NTF3	1.381221	4.265771	1.031011	0.046275
PLIN2	35.72114	16.8457	-0.90269	0.04699
JPT1	12.98186	21.68676	0.611103	0.04734
DDR1	54.6464	82.48943	0.500245	0.04734
C2CD4C	1.352368	2.978355	0.901708	0.047459
FICD	5.938805	4.142017	-0.55359	0.047459
TANC2	6.369184	2.896855	-0.91223	0.047459
AIFM3	4.823406	1.960527	-0.97853	0.047459
AL139384.2	0.534659	1.171379	0.864081	0.047501
DLK1	0.072848	0.325543	1.090427	0.047528
SLC1A2	0.058205	0.22699	1.075983	0.047528
HBEGF	0.987761	2.386771	0.927445	0.047617
MALT1	3.624718	7.565516	0.807217	0.047793
HMGCS2	4.642353	1.153068	-1.08593	0.04807
PARD6G	4.125095	6.388233	0.535934	0.048648
STRIP2	206.0972	92.89444	-0.95904	0.049514
CD248	3.860373	0.903112	-1.08403	0.049514
BEND4	0.210284	0.583556	0.996158	0.049799
MGARP	6.132964	15.9295	0.948454	0.049949
PCDHA13	0.083849	0.00823	-1.04004	0.049949

Table S11 | RNA-seq Ingenuity Pathway Analysis predicted upstream transcriptional regulators and other regulators of the differentially expressed genes between LORD4 and LORD4C.

Upstream Regulator	Expr Log Ratio	Molecule Type	*p*-value of overlap
ZNF217	-0.214	transcription regulator	3.19E-06
PDLIM2	-0.012	other	3.29E-06
C9orf72	0.108	other	4.77E-06
BMP4	-0.396	growth factor	7.86E-06
AMBP	-0.003	transporter	1.76E-05
SMARCA4	0.047	transcription regulator	0.000038
PKNOX1	0.227	transcription regulator	6.89E-05
RUNX2	-0.197	transcription regulator	9.56E-05
NRXN1	0.404	transporter	0.000106
EPAS1	-0.692	transcription regulator	0.000117
HIC1	0.417	transcription regulator	0.000156
ACTG1	0.187	other	0.000169
SBDS	-0.014	other	0.000366
TREM1	-0.218	transmembrane receptor	0.000471
KDM3A	-0.052	transcription regulator	0.000492
PPP1R13L	0.342	transcription regulator	0.000494
CEACAM1	0.112	transporter	0.000494
TGFB1	-0.183	growth factor	0.000598
Growth hormone		group	0.0006
estrogen receptor		group	0.000829
PDGF BB		complex	0.000874
MGAT3	0.277	enzyme	0.000892
TAZ	-0.238	enzyme	0.000892
NEUROG1	0.041	transcription regulator	0.000914
TNF	0.083	cytokine	0.00106
Notch		group	0.00114
TEAD4	0.479	transcription regulator	0.00117
TEAD1	0.178	transcription regulator	0.00132
CTCF	0.023	transcription regulator	0.00175
MUC1	0.146	other	0.00175
SNAI2	-0.33	transcription regulator	0.00191
PELP1	0.068	other	0.00193
PRDM5	-0.248	transcription regulator	0.00194
Beta Secretase		group	0.002
CYP2E1	0.335	enzyme	0.002
HOXB1		transcription regulator	0.002
EPHA2	0.59	kinase	0.002
PRKAA1	-0.132	kinase	0.00202
MYOCD	0.104	transcription regulator	0.00224
ETV5	0.11	transcription regulator	0.00228
CD44	0.305	other	0.00246
RORA	-0.255	ligand-dependent nuclear receptor	0.00248
TEAD2	0.353	transcription regulator	0.0029

SP3	0.1	transcription regulator	0.00295
SNCA	0.215	enzyme	0.00315
SFN	0.444	other	0.0032
let-7a-5p (and other miRNAs w/seed GAGGUAG)		mature microRNA	0.00324
PTTG1	0.486	transcription regulator	0.00324
TEAD3	0.65	transcription regulator	0.00326
Hdac		group	0.00358
IGF1	0.354	growth factor	0.00358
HNRNPA2B1	0.05	other	0.0037
ZXDC	-0.048	transcription regulator	0.00392
NOTCH4	-0.134	transcription regulator	0.00392
SLPI	-1.708	other	0.00392
RGCC	0.232	other	0.00392
TNFAIP6	-0.797	other	0.00392
Ap1		complex	0.00407
MUC4		other	0.00414
MRTFB	-0.174	transcription regulator	0.00425
LIN28B	0.106	other	0.00516
NOTCH1	0.053	transcription regulator	0.00543
SMAD2	0.14	transcription regulator	0.00567
EZH2	0.195	transcription regulator	0.00602
EGR1	-0.666	transcription regulator	0.00609
AR	-0.477	ligand-dependent nuclear receptor	0.00611
PCA3	0.181	other	0.00643
PDGFA	0.114	growth factor	0.00643
NFIC	-0.09	transcription regulator	0.00643
ST8SIA1	0.271	enzyme	0.00643
miR-145-5p (and other miRNAs w/seed UCCAGUU)		mature microRNA	0.00645
SMAD3	-0.176	transcription regulator	0.00684
UPF2	-0.046	other	0.00729
RAD21	-0.032	transcription regulator	0.00729
SUZ12	-0.094	enzyme	0.0076
Akt		group	0.00808
IL1B	0.075	cytokine	0.00861
ITGB1	0.216	transmembrane receptor	0.00918
NCF1	-0.008	enzyme	0.00948
COL1A1	-0.207	other	0.00948
PLSCR1	-0.299	enzyme	0.00948
CBR3-AS1	-0.228	other	0.00948
TNFRSF11A	-0.846	transmembrane receptor	0.00948
SF1	-0.04	transcription regulator	0.00948
Hif		complex	0.00948
STAT3	0.228	transcription regulator	0.00972
KMT2D	-0.185	transcription regulator	0.0103
HOTAIR	0.045	other	0.0107
FN1	0.127	enzyme	0.0107

TWIST2	-0.275	transcription regulator	0.0107
CXCR4	0.256	G-protein coupled receptor	0.0107
SOX2	1.582	transcription regulator	0.0121
YAP1	-0.154	transcription regulator	0.0121
SENP7	-0.106	peptidase	0.013
CIITA	-0.424	transcription regulator	0.013
TFDP1	0.074	transcription regulator	0.013
PRKG1	0.281	kinase	0.013
CD4	-0.102	transmembrane receptor	0.013
TIMP1	0.028	cytokine	0.013
XPO1	0.032	transporter	0.013
DSP	-0.908	other	0.013
NAB2	0.229	transcription regulator	0.013
TRKC-miR2		microRNA	0.013
SPI1	-0.182	transcription regulator	0.0141
SMAD4	0.018	transcription regulator	0.0149
NORAD	-0.053	other	0.0152
SNAI1	-0.009	transcription regulator	0.0152
ERG	-0.444	transcription regulator	0.0156
CTNNB1	-0.019	transcription regulator	0.016
POU2F1	-0.039	transcription regulator	0.0165
PIN1	0.072	enzyme	0.0165
CCN2	0.303	growth factor	0.0165
TCF4	0.389	transcription regulator	0.0167
Nuclear factor 1		group	0.0171
CSNK2B	-0.048	kinase	0.0171
RETN		other	0.0171
PITX2	-0.244	transcription regulator	0.0171
RIPK1	0.024	kinase	0.0171
LRP1	-0.441	transmembrane receptor	0.0171
BTG2	-0.342	transcription regulator	0.0171
IFNA1/IFNA13		cytokine	0.0171
TLR7	-0.057	transmembrane receptor	0.018
FGF2	-0.375	growth factor	0.0182
PDX1		transcription regulator	0.0182
H2AFY	0.181	other	0.0186
RNF31	-0.03	enzyme	0.0187
KLF5	0.318	transcription regulator	0.0187
DICER1	-0.333	enzyme	0.019
EGFR	-0.273	kinase	0.0199
BMP7	-0.678	growth factor	0.0211
WWC1	-0.08	transcription regulator	0.0216
TUG1	-0.055	other	0.0216
GLI1	-0.323	transcription regulator	0.0219
FSH		complex	0.0221
JAK1	-0.262	kinase	0.0237
SP1	0.05	transcription regulator	0.0239
GPER1	-0.08	G-protein coupled receptor	0.0252
CIP2A	0.274	other	0.0255
FKHR		group	0.026

DNAJ		group	0.026
ASB9	0.098	transcription regulator	0.026
MYCNOS	0.663	other	0.026
IFNA10		cytokine	0.026
TET3	0.227	enzyme	0.026
IFNA21		cytokine	0.026
TFAP2E	0.098	transcription regulator	0.026
CALCOCO1	0.109	transcription regulator	0.026
REM2	0.015	enzyme	0.026
SDR9C7		enzyme	0.026
IFNA5		cytokine	0.026
ABCB6	-0.346	transporter	0.026
PHF20L1	0.032	other	0.026
CMKLR1	-0.775	G-protein coupled receptor	0.026
PLAC1	0.166	other	0.026
UBE2D3	0.057	enzyme	0.026
EIF2B5	-0.256	other	0.026
XDH	-0.043	enzyme	0.026
IFNA7		cytokine	0.026
BAD	0.008	other	0.026
MAT2B	0.037	enzyme	0.026
TUNAR	0.414	other	0.026
SEMA4D	0.152	transmembrane receptor	0.026
MYF6		transcription regulator	0.026
ABCC2	-0.262	transporter	0.026
GRPR	-0.041	G-protein coupled receptor	0.026
mir-140		microRNA	0.026
miR-139-3p (miRNAs w/seed GGAGACG)		mature microRNA	0.026
miR-139-5p (miRNAs w/seed CUACAGU)		mature microRNA	0.026
miR-340-5p (miRNAs w/seed UAUAAAG)		mature microRNA	0.026
PDE3A	-1.318	enzyme	0.026
TOB2	0.048	other	0.026
HOXB13		transcription regulator	0.026
MGAT4A	-0.115	enzyme	0.026
ACOT8	-0.023	enzyme	0.026
DES	0.434	other	0.026
ITIH5	-0.845	other	0.026
KLF3	-0.091	transcription regulator	0.026
IFNA14		cytokine	0.026
LRRN1	0.031	other	0.026
KIF1B	0.021	transporter	0.026
IFNA4		cytokine	0.026
IFNA6		cytokine	0.026
FBXO4	-0.503	enzyme	0.026
SHCBP1	0.274	other	0.026
CCHCR1	-0.074	other	0.026
RSL1D1	-0.011	other	0.026

SNX1	0.068	transporter	0.026
CASP2	0.032	peptidase	0.026
CASP9	0.111	peptidase	0.026
CD72	-0.366	transmembrane receptor	0.026
VCAM1	-0.399	transmembrane receptor	0.026
ITGA11	0.349	other	0.026
BAMBI	0.277	other	0.026
TFF3	-0.057	other	0.026
FXYD5	-0.268	ion channel	0.026
IFNLR1	-0.261	transmembrane receptor	0.026
AZIN1	0.003	enzyme	0.026
AP2B1	-0.025	transporter	0.026
KRT10	0.002	other	0.026
IFNG		cytokine	0.0263
Fcer1		complex	0.0264
NFAT5	-0.095	transcription regulator	0.0264
HDAC6	0.006	transcription regulator	0.0264
Ctbp		group	0.0265
LINC01139	-1.225	other	0.0265
IGFBP5	-0.551	other	0.0265
HSPA9	-0.108	other	0.0265
PLG	-0.018	peptidase	0.0265
CHD4	-0.054	enzyme	0.0265
RFX5	0.054	transcription regulator	0.0265
COL18A1	0.01	other	0.027
IgG		complex	0.0272
CLOCK	-0.162	transcription regulator	0.0284
TGFBR2	-0.165	kinase	0.0287
NR3C1	-0.443	ligand-dependent nuclear receptor	0.0287
CHUK	-0.044	kinase	0.0293
STAT5A	-0.061	transcription regulator	0.0309
miR-146a-5p (and other miRNAs w/seed GAGAACU)		mature microRNA	0.0314
let-7		microRNA	0.0316
SNHG20	-0.201	other	0.0319
NFIX	-0.133	transcription regulator	0.0319
CCAT2	-0.07	other	0.0319
JMJD1C	0.143	enzyme	0.0319
PPARG	0.038	ligand-dependent nuclear receptor	0.0321
PGR	-0.818	ligand-dependent nuclear receptor	0.0326
FGF8	0.063	growth factor	0.0336
LGALS3	0.318	other	0.036
ERBB2	0.144	kinase	0.0367
SOX2-OT	0.184	other	0.0376
SMAD1	0.502	transcription regulator	0.0376
mir-373		microRNA	0.0376
AGER	0.211	transmembrane receptor	0.0376

KDM5A	-0.083	transcription regulator	0.0376
PAEP	-0.057	other	0.0376
STAT1	0.045	transcription regulator	0.0376
TP63	0.686	transcription regulator	0.0381
NFATC2	-0.387	transcription regulator	0.0389
EOMES	0.266	transcription regulator	0.0409
mir-29		microRNA	0.0424
miR-21-5p (and other miRNAs w/seed AGCUUAU)		mature microRNA	0.0424
MAPK14	0.218	kinase	0.0424
Ap2		group	0.0437
DANCR	0.135	other	0.0437
PARG	0.092	enzyme	0.0437
PGF	-0.574	growth factor	0.0437
PLAUR	0.036	transmembrane receptor	0.0437
NOTCH2	-0.161	transcription regulator	0.0437
INHBA	-0.377	growth factor	0.0448
PRKCD	0.037	kinase	0.0453
HIF1A	0.489	transcription regulator	0.0529
IL2		cytokine	0.0571
Mek		group	0.076
ESR1	-0.039	ligand-dependent nuclear receptor	0.118
TAL1	-0.1	transcription regulator	0.149


positive z-score
z-score = 0
negative z-score
no activity pattern available
-log(p-value)
0.0
0.5
1.0
1.5
2.0
2.5
3.0
3.5
4.0
4.5
Threshold
Cellular Effects of Sildenafil (Viagra)
Endocannabinoid Neuronal Synapse Pathway
GPCR-Mediated Nutrient Sensing in Enteroendocrine Cells
G Beta Gamma Signaling
Axonal Guidance Signaling
Cardiac β-adrenergic Signaling
Hepatic Fibrosis / Hepatic Stellate Cell Activation
Synaptic Long Term Potentiation
GABA Receptor Signaling
CREB Signaling in Neurons
Synaptogenesis Signaling Pathway
Netrin Signaling
Gustation Pathway
Opioid Signaling Pathway
Calcium Signaling
CCR5 Signaling in Macrophages
Androgen Signaling
Dopamine-DARPP32 Feedback in cAMP Signaling
GP6 Signaling Pathway

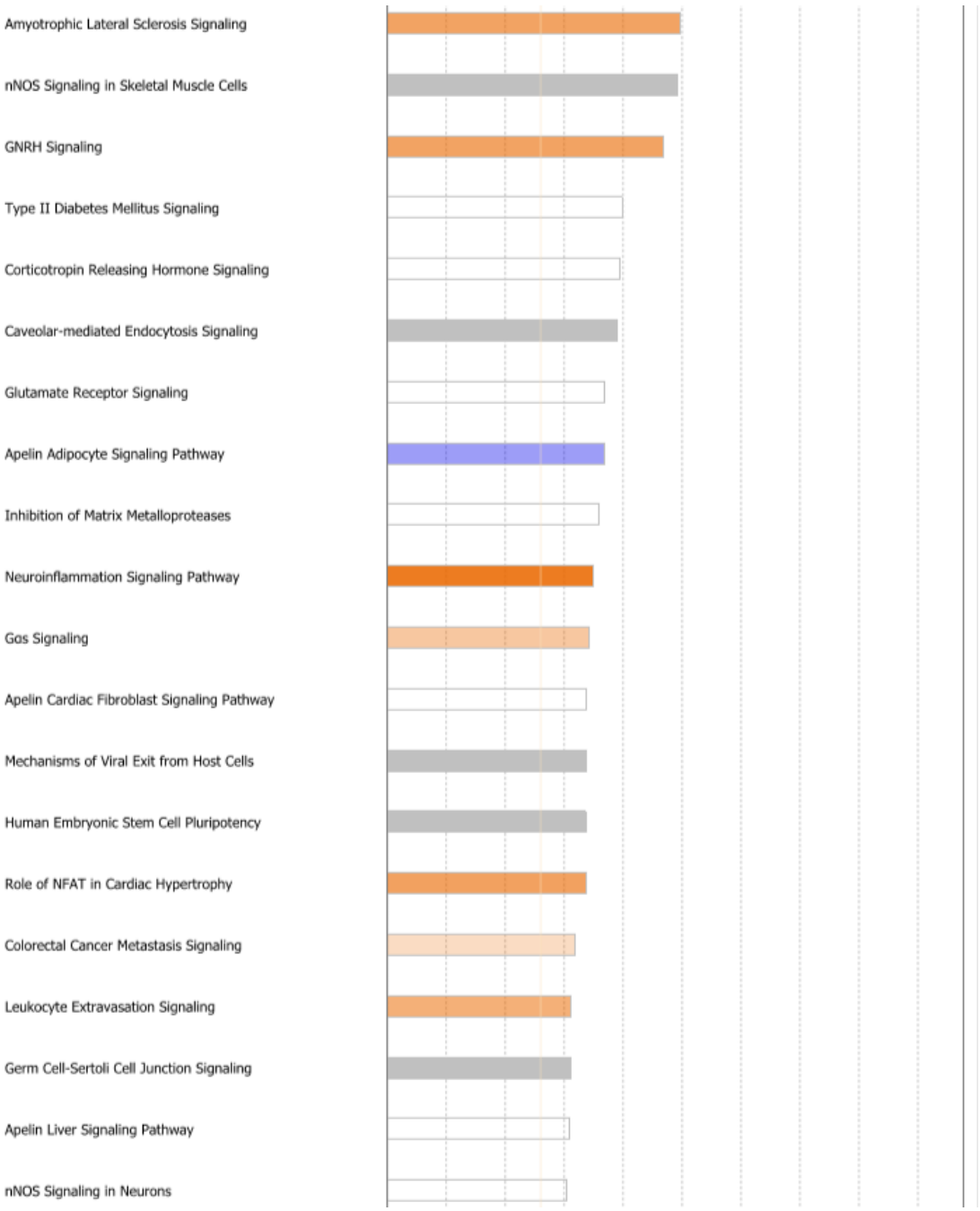
Amyotrophic Lateral Sclerosis Signaling
nNOS Signaling in Skeletal Muscle Cells
GNRH Signaling
Type II Diabetes Mellitus Signaling
Corticotropin Releasing Hormone Signaling
Caveolar-mediated Endocytosis Signaling
Glutamate Receptor Signaling
Apelin Adipocyte Signaling Pathway
Inhibition of Matrix Metalloproteases
Neuroinflammation Signaling Pathway
Gαs Signaling
Apelin Cardiac Fibroblast Signaling Pathway
Mechanisms of Viral Exit from Host Cells
Human Embryonic Stem Cell Pluripotency
Role of NFAT in Cardiac Hypertrophy
Colorectal Cancer Metastasis Signaling
Leukocyte Extravasation Signaling
Germ Cell-Sertoli Cell Junction Signaling
Apelin Liver Signaling Pathway
nNOS Signaling in Neurons

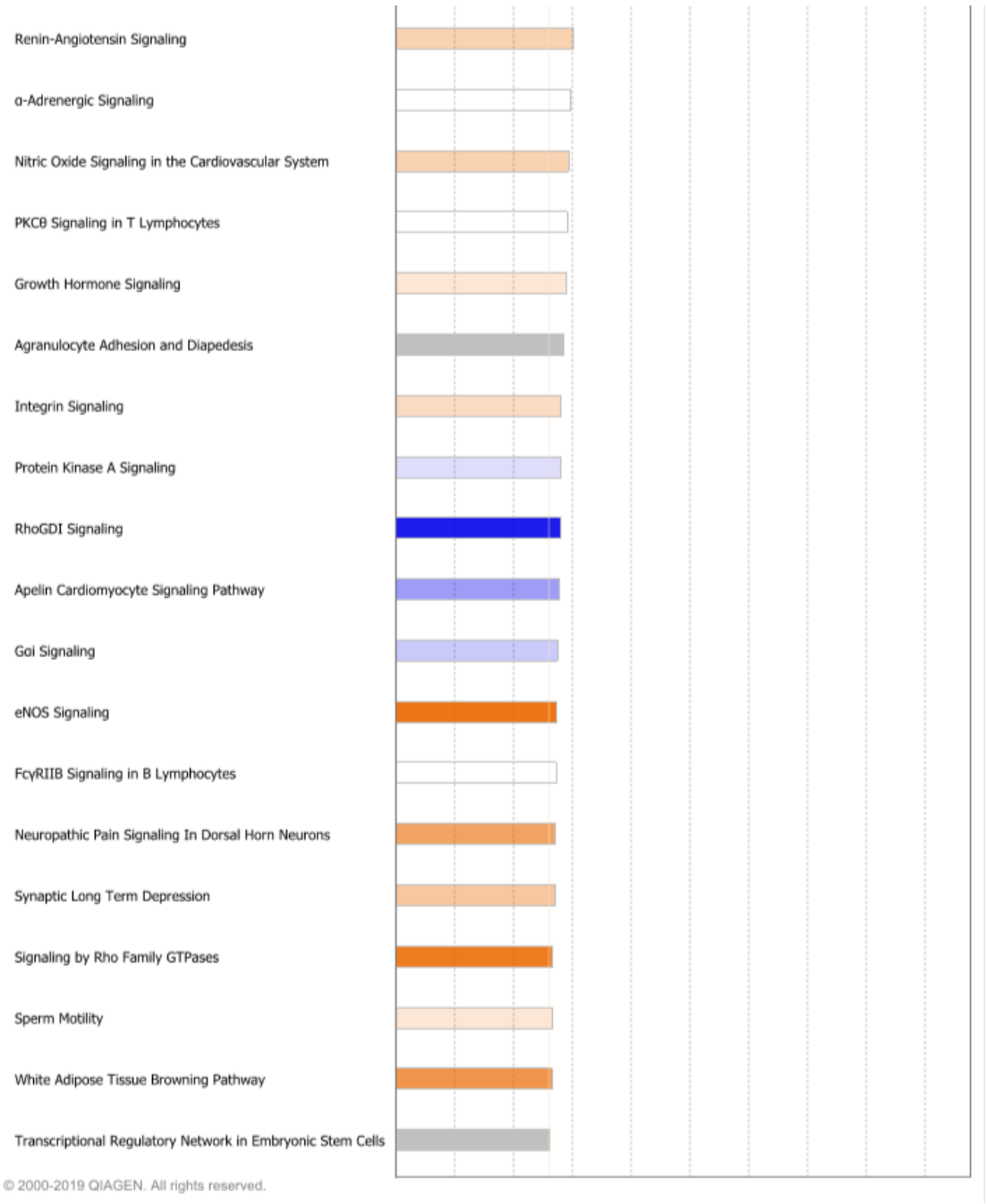

Figure S3 | RNA-seq Ingenuity Pathway Analysis – canonical pathways differentially regulated between LORD4 and LORD4C. Differentially regulated canonical pathways between LORD4 and LORD4C as revealed with IPA.